Technical Report
TR-17-15
November 2017

Long re-saturation phase of a final repository

Additional supplementary information

Patrik Sellin (editor)
Mattias Åkesson
Ola Kristensson
Daniel Malmberg
Lennart Börgesson
Martin Birgersson
Ann Dueck
Ola Karnland
Jan Hernelind

SVENSK KÄRNBRÄNSLEHANTERING AB

SWEDISH NUCLEAR FUEL
AND WASTE MANAGEMENT CO

Box 3091, SE-169 03 Solna
Phone +46 8 459 84 00
skb.se

SVENSK KÄRNBRÄNSLEHANTERING

ISSN 1404-0344
SKB TR-17-15
ID 1611368
November 2017

Long re-saturation phase of a final repository

Additional supplementary information

Patrik Sellin (editor), Svensk Kärnbränslehantering AB

Mattias Åkesson, Ola Kristensson, Daniel Malmberg, Lennart Börgesson, Martin Birgersson, Ann Dueck, Ola Karnland

Clay Technology

Jan Hernelind, 5T Engineering AB

Abstract

The current report contains the supporting work that was performed to answer the request for additional information that was requested by the Swedish Radiation Safety Authority (SSM) concerning issues related to a slow resaturation of the bentonite buffer in a KBS-3 repository.

The issues treated here are:

- An analysis of the conceptual model uncertainty associated with estimates of the saturation and homogenization of the buffer which includes comparisons with available experimental studies.
- An analysis of and discussion around possible distributions of re-saturation times for the buffer, given the local hydrogeological conditions at repository depth at the Forsmark site.
- The relevance of the saturation process and the possible influences of heterogeneous conditions within the buffer on the overall safety function.
- An analysis of the thermal effect on the mechanical and hydraulic material properties of the bentonite.
- An assessment of the possibility of adjusting the degree of saturation or to artificially add water and thereby affect/reduce the duration of the re-saturation process.

The overall summary answer is given in the first section, while the detailed assessments are presented in the following chapters.

Sammanfattning

Denna rapport innehåller det underliggande arbete som utfördes för att svara på den begäran om ytterligare information som begärdes av den svenska Strålsäkerhetsmyndigheten (SSM) rörande frågor som om en långsam återmättnad av bentoniten buffert i ett KBS-3-förvar.

De frågor som behandlas är:

- Analys av den konceptuella modellosäkerheten i samband med beräkningar av återmättnad och homogenisering av bufferten vilken inkluderar jämförelser med experimentella studier.
- Analys av och diskussion runt möjliga fördelningar av återmättnadstider för bufferten med tanke på de lokala hydrogeologiska betingelserna på förvarsdjup vid Forsmark.
- Långsiktig säkerhetsbetydelse av mättnadsgrad och eventuell inverkan av heterogena förhållanden inom bufferten.
- Analys av termisk påverkan på bentonitens mekaniska och hydrauliska materialegenskaper.
- Bedömning av möjligheten att med justering av vattenmättnadsgraden eller en artificiell tillförsel av vatten för att påverka/förkorta återmättnadsförloppet.

Svaret till SSM presenteras i det första avsnittet, medan de underliggande detaljerade analyserna presenteras i de följande avsnitten.

Contents

1 Introduction

In March 2011, SKB submitted an application under the Nuclear Activities Act for final disposal of spent nuclear fuel and an application under the Environmental Code for the KBS-3 system. An application under the Nuclear Activities Act for the encapsulation plant was submitted in 2006 and supplemented first in 2009 and thereafter in conjunction with the applications in March 2011.

The licensing is under way, and SKB has regularly answered questions and requests for supplementary information from SSM.

The current report contains the assessment work performed to answer one particular set of requests from SSM.

The issues discussed here are all related to the re-saturation of the bentonite buffer in a repository at the Forsmark site. The Formark site is expected to have a rather limited groundwater flow at repository depth. This is a clear advantage for the overall long-term performance of the repository, but it will also mean that the bentonite buffer will reach saturation rather slowly in many canister positions.

It should be noted that the material in this report was produced and first published in 2013.

The original documents are as follows:

1. **SKB, 2013.** Svar till SSM på begäran om komplettering rörande lång återmättnadsfas. SKBdoc 1385067 ver 3.0, Svensk Kärnbränslehantering AB.
2. **Åkesson M, 2013.** 1.1 Conceptual uncertainties and their influence on bentonite hydration. SKBdoc 1415874 ver 1.0, Svensk Kärnbränslehantering AB.
3. **Kristensson O, Börgesson L, Hernelind J, 2013.** 1.2 Water uptake in the CRT experiment. SKBdoc 1415870 ver 1.0, Svensk Kärnbränslehantering AB.
4. **Kristensson O, 2013.** 1.3. Description of how the CRT-model was used and how THM and TH models differ in terms of analyzing the hydration process. SKBdoc 1415872 ver 1.0, Svensk Kärnbränslehantering AB.
5. **Åkesson M, 2013**. 1.4 Bentonites other than MX-80. SKBdoc 1415875 ver 1.0, Svensk Kärnbränslehantering AB.
6. **Malmberg D, Åkesson M, Kristensson O, 2013.** 2.0+1.5 The distribution of saturation times in the Forsmark repository. The effect of hydraulic connections between deposition holes. SKBdoc 1415879 ver 1.0, Svensk Kärnbränslehantering AB.
7. **Kristensson O, 2013.** 3.1 Analysis of saturation intervals concerning long time safety during the hydration process. SKBdoc 1415873 ver 1.0, Svensk Kärnbränslehantering AB.
8. **Börgesson L, Åkesson M, Hernelind J, 2013.** 3.2 Analysis of risks and consequences of uneven wetting in a dry deposition hole. SKBdoc 1415878 ver 1.0, Svensk Kärnbränslehantering AB.
9. **Börgesson L, Hernelind J, 2013** 4.1 Analysis of how a buffer with brittle shear properties may affect the rock shear case. SKBdoc 1415876 ver 1.0, Svensk Kärnbränslehantering AB.
10. **Karnland O, Birgersson M, Dueck A, 2013.** 4.2 Analys av i vilken mån en långsam återmättnad kan förvärra försämringar av buffertens materialegenskaper pga. kemiska och strukturella omvandlingar i förhållande till ett fall med snabb återmättnad. SKBdoc 1415886 ver 1.0, Svensk Kärnbränslehantering AB.

2 Answer to SSM regarding request for additional supplementary information concerning a long re-saturation phase

This chapter contains a translation of the actual answer to the regulator. The original text can be found in SKB (2013)

The Swedish Radiation Safety Authority (SSM) has in a letter to the Swedish Nuclear Fuel and Waste Management Company (SKB) dated 2012-12-07 requested supplements to the application for the disposal of spent nuclear fuel concerning the re-saturation phase of the buffer and backfill. In the request SSM asks for additions on the following five points:

1. An analysis of the conceptual model uncertainty associated with estimates of the saturation and homogenization of the buffer that should include comparisons with available experimental studies.
2. An analysis and discussion of possible distributions of re-saturation times for the buffer given local hydrogeological conditions at repository depth at Forsmark site.
3. Safety relevance of saturation and the possible impact of heterogeneous conditions in the buffer.
4. Analysis of the thermal influence on the mechanical and hydraulic material properties of the bentonite buffer.
5. An assessment of the possibility of adjusting the degree of saturation or to artificially add water and thereby affect/reduce the duration of the re-saturation process.

The more detailed questions are given together with the answers in the following sub-sections.

2.1 An analysis of the conceptual model uncertainty associated with estimates of the saturation and homogenization of the buffer that should include comparisons with available experimental studies

2.1.1 A summary of observations from studies other than those used as the basis for SR-Site. A discussion about the conceptual uncertainties (especially thermo-osmosis and a hydraulic threshold). A quantification of how these uncertainties could affect the water saturation time

Conceptual uncertainties associated with thermal, hydraulic and mechanical processes in the vicinity of a final repository have been investigated for many years, both theoretically and through large scale experiments, in a number of EU projects and in the international DECOVALEX project. Åkesson (Chapter 3) has reviewed the available material and analyzed how the results could affect the SR-Site recalculation calculations.

The aims of the study were

- to provide a description of the FEBEX in situ experiment together with a summary of the modelling of the experiment carried out,
- to provide a description of the FEBEX Mock-up test together with a summary of the modeling of the experiment carried out; An important component here is the description of the three non-standard flow models proposed to describe the experiment (hydraulic threshold, thermo-osmosis and microstructure development),
- to make an analysis of how the models for hydraulic threshold, thermos-osmosis and microstructure development would affect the results in SR-Site analyses, as well as
- to analyze the significance of other identified uncertainties.

Evaluation of alternative models was made with analytical solutions. With a **threshold** for the hydraulic gradient in Darcy's law, the buffer will never be saturated. However, the significance of this is not great because the final saturation becomes > 99 % even with relatively low gradients. The model results presented in Sánchez and Gens (2006) also show that the time perspective for achieving a stationary state with a threshold gradient is approximately the same as the time to full water saturation without the threshold gradient. This has no significance for the buffer's hydromechanical function in the repository because swelling pressure develops at a much lower degree of saturation. This is described in Section 3.4.

A **thermo-osmosis** model also leads to full saturation not being achieved as long as there is a temperature gradient. However, the remaining unsaturation will not be great in that case either. The model results presented in Zheng and Samper (2008) also show that the time perspective for achieving a stationary state with thermo-osmosis is approximately the same as the time to reach full water saturation without thermo-osmosis.

The development of **microstructure** has been modelled as a reduction in permeability as a function of water saturation. This gives a generally slower water absorption. Unlike the models with thermo osmosis and threshold, the microstructure development model gives a final full water saturation. The significance of this process for the estimated water saturation times in SR-Site has been analyzed by employing an adjusted vapour diffusivity. The results indicate that the time of water saturation may have been underestimated in SR-Site. If SR-Site calculations would have been conducted with the lowest empirical values for vapour diffusion, the water saturation time would have increased by a factor of 3.5 for conditions of free access to water. This then affects the deposition holes where the buffer properties are controlling the water saturation time. These holes have the shortest calculated water saturation times and with this assumption, times would increase from ~ 10–20 years to ~ 35–70 years. In Forsmark, there is only a small proportion of the holes where this is the case. Figure 2-3 shows that the water saturation in the majority of the deposition holes is controlled by the properties of the rock.

During the work on alternative flow models, a few additional uncertainties were identified that could affect the water saturation rate. This concerns natural convection in the pellets slot and the temperature dependence of retention properties.

For relatively dry rock conditions, the most important transport process is diffusion of vapour, and this is the only way to transfer moisture from hot to cold parts in the used models. Therefore, the potential contribution of **natural convection** for a more pronounced moisture distribution has been identified as a conceptual uncertainty for the development of the re-saturation. The analysis shows that the natural convection is strongly dependent on the gas permeability of the pellet gap. Figure 2-1 shows the maximum height of natural convection as a function of permeability and gap. Permeability is not systematically measured for bentonite pellets, but with a maximum literature value of 10^{-7} m^2 shows that the maximum height will be 2 meters for 5 cm gap and 8 meters for 10 cm. It is therefore not impossible for the process to matter. Assuming that the equilibrium state is a constant vapour pressure throughout the deposition tunnel, a relatively large amount of water will be lost from the buffer around the canister in a case of dry tunnel and deposition holes. This would mean that the heat conductivity of the buffer decreases and that the temperature of the canister surface increases. However, this requires no condensation and swelling will occur in the pellet filling in the upper part of the deposition hole. However, the likely development is that vapour will condense in the pellet slab in the upper part of the deposition hole. The pellets in the gap will then swell and seal. Therefore, no transport of vapour to the backfill tunnel is expected.

Experimental data show that the retention properties of bentonite are temperature dependent. The general trend is that relative humidity increases with increasing temperature. However, the analysis in Åkesson (Chapter 3) shows that the effect of the process, for relevant KBS-3 conditions, is very small.

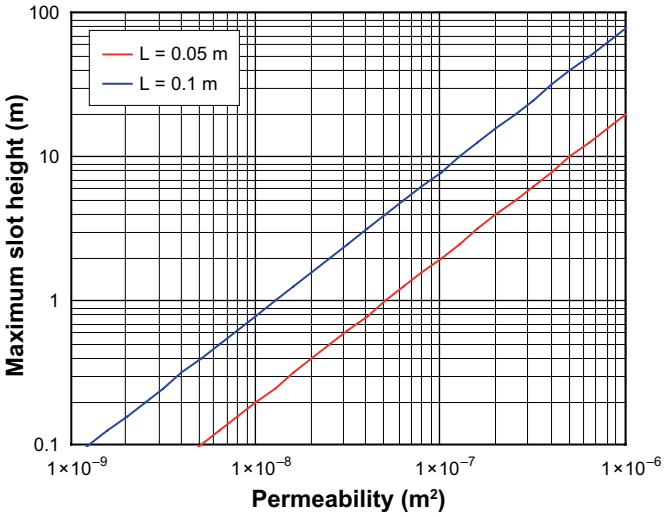

Figure 2-1. Maximum height with sustained natural convection.

2.1.2 Comparisons between measured and calculated inflows. Are there any filter effects? Can the TR-10-11 models be improved?

A comparison between measured and calculated inflows in the Canister Retrieval Test (CRT) has been conducted and reported by Kristensson et al. (Chapter 4). Measured inflows in filters and reported estimates of refilled water have been compared with the estimated values of the total void volume in the experiment. The comparison between modelled and measured total influx is well matched at the end of the experiment, while development over time does not match as well as a reasonable cause for this has been identified.

The reason for the low measured inflow of up to 680 days is probably due to the pressure in the filters being too low to keep them saturated. When the pressure was raised (day 680) the water uptake rate increased. Considering this in the model, a good match is obtained (Figure 2-2). Some other uncertainties in the experiment are also discussed and the conclusion from this is that the water uptake models seem to underestimate the real uptake somewhat and that, based on the measurement and modelling of CRT, it is not possible to identify any further process not handled in the models that would provide a slower water uptake.

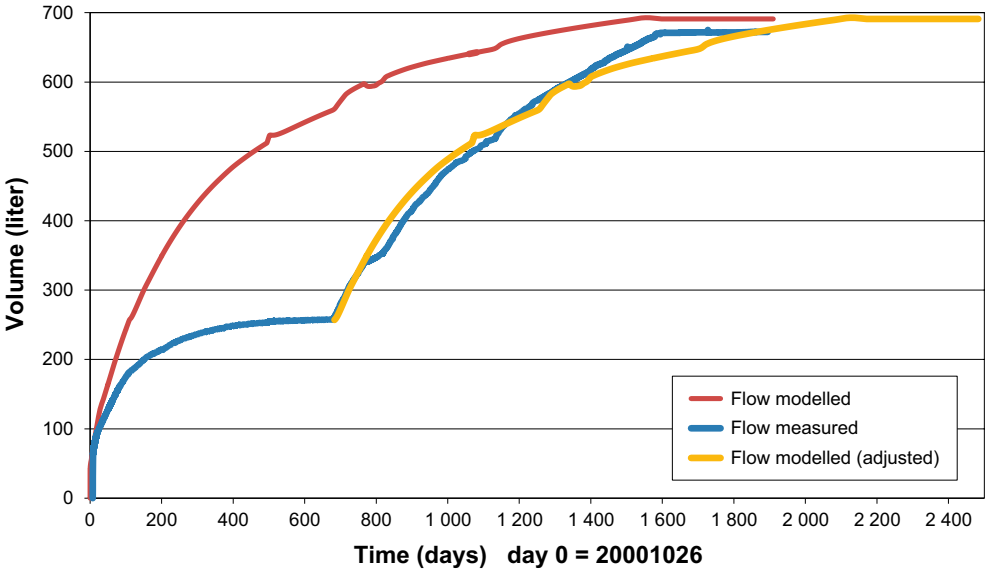

Figure 2-2. Modelled (red line) and measured (blue line) water inflow into the CRT test hole and the modelled inflow adjusted for the insufficient water supply (yellow).

2.1.3 Clarify how the CRT model has been used and explain the difference between TH and THM models

Kristensson (Chapter 5) has described the differences between the TH and THM models in CODE_ BRIGHT that may affect the water saturation process. A description of the "CRT case" which is also used as a specific case to illustrate the importance of the difference between the models is also given.

2.1.4 Compilation of data for other bentonite types than the MX-80 and discussion on the significance of the differences

Åkesson (Chapter 6) has reviewed the available data for other possible buffer and backfill materials and assessed how these data could affect the conclusions in SR-Site. Available data refers primarily to measurements of hydraulic conductivity, swelling pressure and retention characteristics from water absorption tests. In addition, data for thermal conductivity and results from homogenization tests have also been taken into account. The various materials compared are buffer materials MX-80, Deponit CA-N and Febex, and the backfill materials Ibeco RWC BF and Friedland. Two different grades and several shipments of Asha material are also included in the study. One of the materials is of buffer and the second of the backfill type.

The time scale for resaturation for a particular material is largely determined by the hydro-mechanical properties of the material in question, but also by the initial dry density and water content. Different materials can therefore exhibit optimum properties with regard to water absorption capacity for different installed initial states (density and water content). A detailed comparison of different bentonite materials with regard to the time scale for water uptake is therefore not quite straightforward. Instead, evaluated vapour diffusion data can be used to make a simple comparison. The reason for this is that the time scale for water absorption is in principle inversely proportional to diffusivity (e.g. $t_{febex} \sim t_{mx80} \times D_{mx80}/D_{febex}$). Even though the differences in vapour diffusivity were found to be quite small between different materials, it should be noted that the lowest values were for the MX-80. This means that the time scale for re-saturation for other materials would be slightly shorter than for MX-80 (the decrease would be a factor of ½ for Friedland, and ⅓ for the other analysed materials). Apart from these observations, it can be noted that the analysis showed a general coherence between different data sets and gave a verification of the material model based on independent measurements.

The temperature development of a particular bentonite material is largely determined by the thermal conductivity of the material in question. Different saturation dependent relationships assumed for the thermal conductivity of the MX-80 were compared to reported data for Febex bentonite. Febex data is generally quite similar to data for MX-80, although the relationships tend to overestimate heat conductivity in the middle of the saturation process and underestimate it at low saturation.

Homogenization of buffer and refill was analysed in the THM modeling in SR-Site (Åkesson et al. 2010b). The calculations were based on constitutive laws that utilize parameter sets derived from several different types of tests and measurements. At that stage, these tests had only been performed for the MX-80 bentonite. Therefore, based on the general lack of experimental data and the inherent uncertainties in the computation technique used, it is not possible to make a relevant comparison of the homogenization process in different materials based on numerical modeling. Scale tests, on the other hand, can be used as a fairly simple alternative method for comparisons between different materials. Relevant full-scale tests generally show a difference between the highest and lowest void ratios of 0.20–0.25 (Ibeco RWC BF) and corresponding 0.15–0.30 (Friedland). This is consistent with the homogenization calculations for the homogenisation in SR-Site, which showed a maximum difference in void ratio in the order of 0.2.

2.1.5 Impact of hydraulic interaction between several adjacent holes on the re-saturation process

If several deposition holes share the same water conducting fracture, this could affect the water saturation process. This process has been described in Malmberg et al. (Chapter 7). The main effect could be that the upstream hole is "drying out" the fracture and no water reaches the hole downstream. In order for the process to be important, the flow in the fracture must be large enough to affect the water saturation of the buffer, but not greater than that the water absorption capacity of the buffer in a hole will be able to absorb a significant portion of the flow. It is therefore only in the range of inflows between 10^{-3} and 10^{-4} L/min, in open repository conditions, which interaction may have significance at the Forsmark site. Based on Joyce et al. (2013), it is 2.6 % of the deposition holes in Forsmark that lie in this range. Of these, it is half where the fracture is divided between several holes. In an extreme case, 1.3 % of the deposition holes may lose some of their inflow from a fracture through hydraulic interaction between deposition holes. In Forsmark, it is likely that most deposition holes will be saturated by flow through the rock matrix. Adding 1.3 % of the deposition holes to this group will not affect the overall picture of the water saturation process.

Finally, it should be noted that in the assessments made for buffer saturation through inflow from the rock matrix, the repository layout is considered in the construction of the two-dimensional axisymmetric model for calculation of the saturation time. This applies both in SR-Site and in the new assessment presented by Malmberg et al. (Chapter 7). The model is designed to make no-flow boundaries between deposition holes and deposition tunnels. A detailed description of how the model was constructed can be found in Section 3.2.1 of Åkesson et al. (2010b) (and especially in Figure 3-2).

2.2 An analysis and discussion of possible re-saturation times for the buffer in view of local hydrogeological conditions at repository depth at Forsmark site

In Åkesson et al. (2010b), the water saturation process in the buffer was studied for three different "type holes":

- Hole with a water-conducting fracture.
- Hole without water-conducting fracture, but near a water-conducting fracture in the deposition tunnel.
- Hole without water-conducting fractures neither in the hole itself nor in the tunnel.

The water saturation in the backfill for different cases was also studied. The cases were chosen to cover all possible ranges of water saturation times. However, there was no attempt to link the different cases to the hydraulic situation in Forsmark and no distribution of saturation times was presented. However, in SR-Site (SKB 2011, Section 10.3.8), it was found that the conditions in Forsmark were well covered by the cases in Åkesson et al. (2010b).

Malmberg et al. (Chapter 7) has linked the water saturation models in Åkesson et al. (2010b) to the expected inflows in Forsmark based on Joyce et al. (2013). The inflow to the open repository has been used to calibrate the Code_Bright model. After that, the buffer and backfill is introduced and water saturation time is calculated. It can be noted that:

- Matrix flows are not handled in the hydrogeological model.
- Generally, the flows in the fractures that intersect deposition holes are significantly lower than the assumptions in Åkesson et al. (2010b).
- The distance between most deposition holes and the fractures that intersect the deposition tunnels is longer than in the typical cases in Åkesson et al. (2010b).

This is handled in modelling. The summarized results from the study are shown in Figure 2-3.

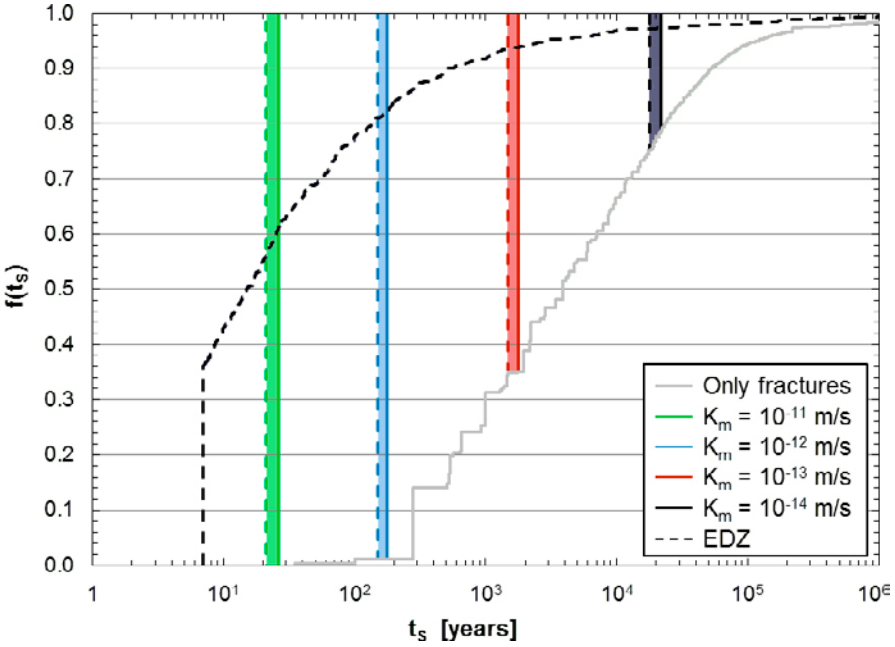

Figure 2-3. *The solid grey line identifies the cumulative distribution of saturation times, $f(t_S)$, in the Forsmark repository calculated assuming no matrix flow. The colored lines identify the time interval within which all deposition holes will reach full saturation if the matrix hydraulic conductivity has the value $K_m = 10^{-exp}$, where exp = {11, 12, 13, 14). The dashed black line identifies the distribution of saturation times if no flow resistance was present in the tunnels (see text).*

The conclusion from the study is that the assumption of the hydraulic conductivity of the rock matrix is crucial for the estimation of water saturation times in Forsmark. Measurements of matrix conductivities show that these are in the order of $K_M = 4 \times 10^{-14}$–5×10^{-12} m/s (Vilks 2007). For the values in that range it can be noted:

- **$K_m \geq 10^{-11}$ m/s:** Only a small proportion of the holes are saturated from fracture flow. The tunnel does not affect the process at all. All holes are saturated within 30 years.
- **$10^{-12} > K_m \geq 10^{-13}$ m/s:** Between 10 and 30 % of the holes are saturated with water from fractures or from the deposition tunnel. All the other deposition holes are saturated from the rock matrix and these are saturated within a period of between 200 and 2 000 years.
- **$10^{-13} > K_m \geq 10^{-14}$ m/s:** A significant proportion (30–60 %) of the deposition holes is saturated with water from fractures or from the deposition tunnel. The other deposition holes are saturated from the rock matrix and this may take more than 20 000 years.
- **$K_m < 10^{-14}$ m/s:** In practice, all deposition holes are saturated with water from fractures or from the deposition tunnel. In tunnels without fractures the saturation will take a very long time. The calculations show times of > 1 000 000 years.

In the assessment for SR-Site (Åkesson et al. 2010b) 10^{-13} m/s was employed as a "typical" matrix conductivity. With this value, according to Figure 2-3, 65 % of the deposition holes in Forsmark would be saturated in ~ 2 000 years and the largest part of the others in the 300–2 000 year range. Only a small proportion is saturated faster than 100 years.

It is obvious that the uncertainty in the estimation of water saturation time is high. The range of matric conductivities in Vilks (2007) extends over two orders of magnitude, and in principle, this scales linearly with water saturation time, since few holes are saturated from water-conducting fractures.

2.3 Long term safety significance of degree saturation and possible impact of heterogeneous conditions within the buffer

2.3.1 Analysis of the importance of different phases in the saturation process

In Åkesson et al. (2010b) 99 % was defined as "full" water saturation. The background to this is that it made possible comparisons between different water saturation cases. The value itself has no practical significance.

To illustrate the importance of different phases in the water saturation process, Kristensson (Chapter 8) has studied the safety functions of the buffer as a function of water saturation. The most relevant safety function for water saturation is the swelling pressure. In SR-Site, most safety functions are only relevant for a saturated buffer. However, in this study, no credit has been taken of this and swelling pressure has been taken into account regardless of saturation state. The conclusions from the study show the following:

- The mechanical material model is process-dependent and must be calibrated for different situations. A slow water saturation was studied, and the mechanical parameters of the pellet filling must therefore be chosen to give a representative density profile at full water saturation.
- The processes in the buffer are heterogeneous. The models show great differences between blocks and pellets, but also internally in the pellets and blocks.
- Degree of water saturation is not a suitable parameter for assessing the pressure in the buffer. The buffer can reach a given pressure for a large range of water saturation levels, absolute or relative. Near the canister, 1 MPa can be reached without any water uptake.
- The safety function indicator 1–2 MPa is reached heterogeneously in the buffer. The general trend is "down and up" and "later in the pellet".
- The hydraulic properties of the rock are crucial for the development of the swelling pressure and for the time it takes to reach the safety function indicator.

2.3.2 Risk and consequence of heterogeneous re-saturation

The deposition holes in Forsmark are expected to be practically dry. In most of the holes there will be no water conducting fractures and the cases where there are inflows, these are usually very small. The significance of a low inflow in a single point in a deposition hole has been studied by Börgesson et al. (Chapter 9).

The study is based on a geometry where the water flow occurs at a point in the buffer at the mid-height of the canister. A constant inflow or constant pressure is set as boundary conditions in that point. However, in the case of flow, this will be adjusted if it requires an unrealistic high water pressure in the rock or if there is a counter pressure from water absorption in the buffer.

Generally speaking, it is difficult to get the model to converge and to make an appropriate representation of the pellet gap. Despite this, it is possible to draw some conclusions from the study:

- In order for a point flow to yield heterogeneous conditions, water saturation must be faster than if the buffer is saturated via the rock matrix. With an assumed matrix conductivity of 10^{-13} m/s no uneven saturation will occur for water saturation times longer than ~ 1 500 years.
- The time it takes to fill all empty pores in the buffer is ~ 3 500 years for an inflow of 10^{-6} L/min and ~ 350 years for an inflow of 10^{-5} L/min. The minimum inflow rate of interest lies therefore somewhere in the middle of this range.
- If the flow is so high that the pellet gap is filled before the blocks are saturated, there will also be no heterogeneous saturation since the blocks then will be saturated from a filled gap. It takes 1.55 years to fill the gap at an inflow of 10^{-3} L/min and ~ 2 years to saturate the blocks with free access to water throughout the gap. For flows > 10^{-3} L/min, the saturation always becomes homogeneous.
- According to Joyce et al. (2013), there are approximately 400 deposition holes where the inflow is in the range of 5×10^{-5} to 10^{-3} L/min, which could cause uneven saturation.
- The mechanical analysis also reported by Börgesson et al. (Chapetr 9), however, shows that the effect of the inhomogeneities caused is small. However, a small lift of the canister and some local effects around the infusion point can be noted. The effect on the density distribution in the deposition hole is small.

An example of results is shown in Figure 2-4. Even with an extreme case where the buffer gets all water at a single point and the inflow rate is unfavorable, the water is distributed relatively well in the buffer blocks. The risk of an extremely heterogeneously saturated buffer is therefore considered negligible.

However, there are some uncertainties in the mechanical and hydraulic representation of the pellet gap and it is not clear how this affects the results. The significance of alternative models of pellet filling has been evaluated in Börgesson et al. (Chapter 9). Figure 2-5 shows calculated pore pressure in the pellet with three different representations of the hydraulic conductivity of the pellet filling.

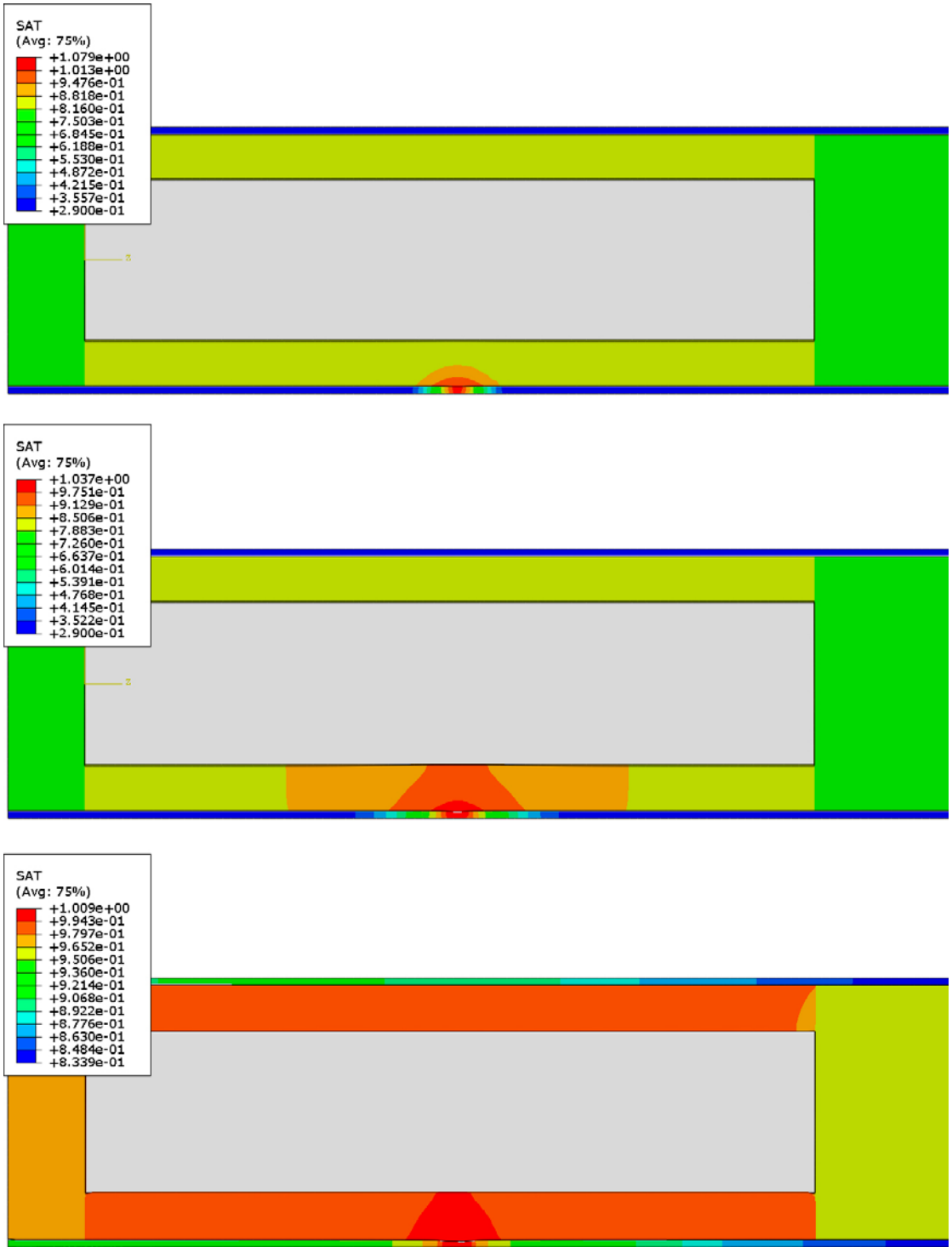

Figure 2-4. *HM-modelling of an entire deposition hole with the point inflow rate of 0.0001 L/min. Degree of saturation after 0.32 years (upper), 3.2 years (middle) and 320 years (lower).*

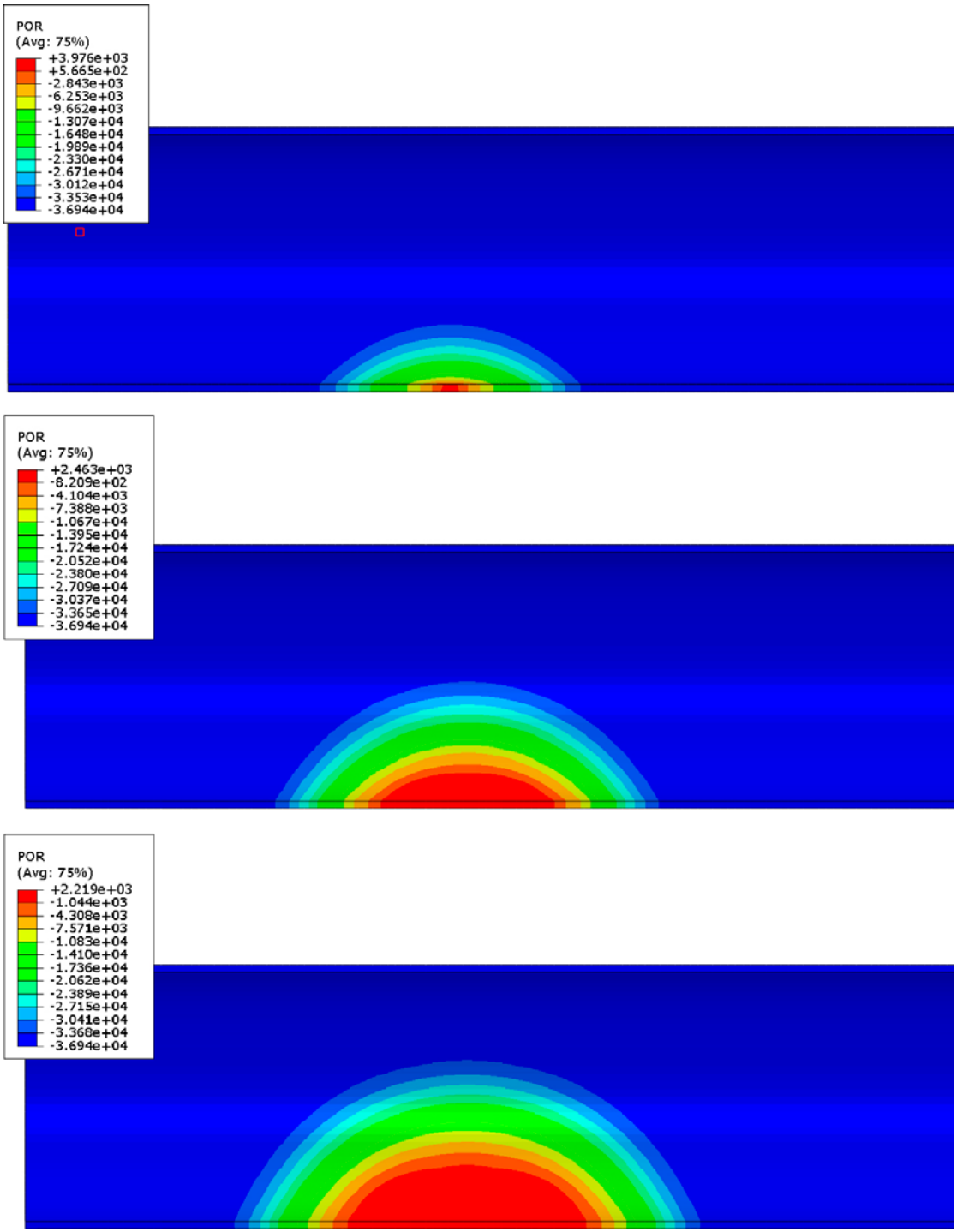

Figure 2-5. *H-modelling of pellet filled slot only with the point inflow rate of 0.0001 L/min. Pore-water pressure (kPa) after 3.2 years.*

2.4 Analysis of thermal impact on the mechanical and hydraulic material properties of the bentonite

2.4.1 Analysis of how the mechanical properties of thermally impacted bentonite affect the rock shear case

Tests on bentonite exposed to high temperatures have shown tendencies of brittle failure as opposed to results from unaffected bentonite, which show even or no decrease in strength after maximum shear stress. Figure 2-6 shows an example of such results.

The general conclusions from the experiments were that shear strength was not affected, but the failure may be brittle, i.e., abrupt shear strength reduction after maximum shear stress has been achieved. The maximum deviator stress is a measure of shear strength and it depends on the density. In case of brittle failure, a lower strain is also often seen at and the surface of the failure may also be vertical. In summary: the shear strength is not affected since the maximum deviator stress at a given density is not considered to be affected by an increased temperature. Since the test results to the left in Figure 2-6 come from three samples that have approximately the same density, but not exactly the same value, it cannot be clearly be determined from this figure whether the deviator stress increases with the temperature.

The impact of a rock shear through a deposition hole has been investigated both with laboratory tests which have been the basis for a buffer model and with a number of finite element calculations that have studied the effect of various shear cases on the canister. A number of calculation cases are reported in Börgesson and Hernelind (Section 10). The bentonite was modelled as an elastoplastic material with strain rate-dependent stress-strain relationships. Four different calculations have been made, a reference calculation with unaffected bentonite, two calculations with brittle bentonite and a fourth calculation of brittle bentonite and the shear plane of the buffer removed to simulate that shear strength has been completely lost in that zone. The material model for the reference case is identical to the material model for bentonite used for SR-Site (Åkesson et al. 2010b).

An example of results is shown in Figure 2-7 illustrating the plastic strain in the copper shell. The most obvious difference occurs in case 4 where the shear plane in the buffer is removed and the stress concentrations (as well as the plastic strain in the copper envelope) near the shear plane are greater than in the other cases. However, the maximum plastic strain is not higher and as a whole the difference between the different cases is small.

The overall conclusion is that a brittle behavior of the buffer will not have a significant effect on the consequences of a shear. This is a logical conclusion, because brittle failure does not mean increased, but instead reduced shear strength with elongation, i.e. shear resistance from the buffer decreases. Earlier calculations of the shear also show that lower shear resistance in the buffer means lower tension in the canister.

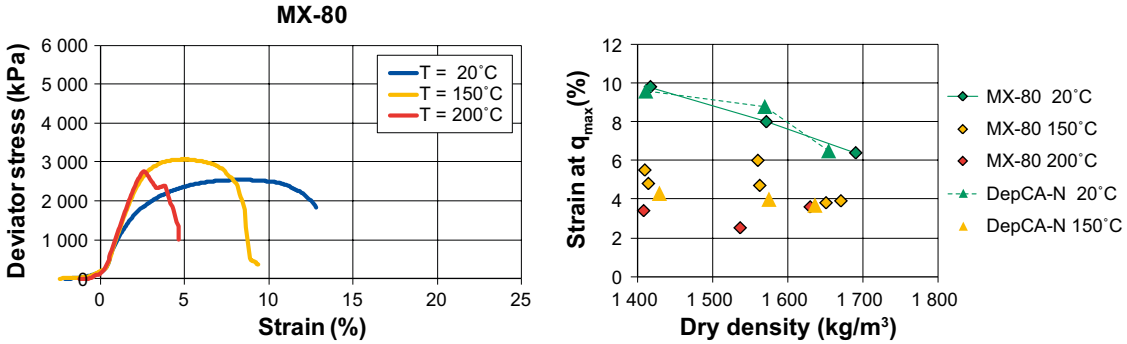

Figure 2-6. *Example of brittle failure. The left figure shows example of stress strain relations at uni-axial testing of specimen of bentonite that have been exposed to different temperatures. The right figure shows measured strain until failure as function of dry density for specimen exposed to different temperature.*

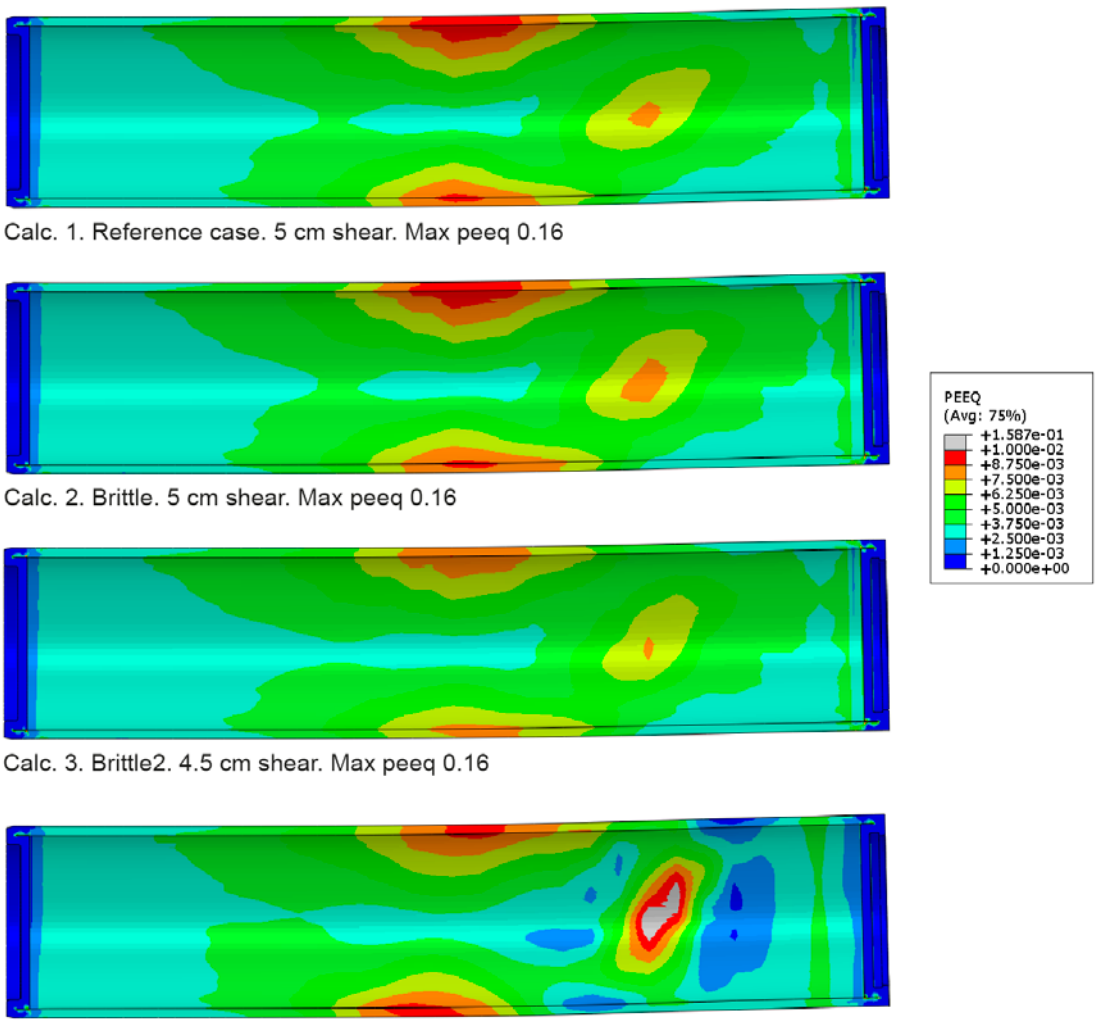

Calc. 1. Reference case. 5 cm shear. Max peeq 0.16

Calc. 2. Brittle. 5 cm shear. Max peeq 0.16

Calc. 3. Brittle2. 4.5 cm shear. Max peeq 0.16

Calc. 4. Brittle2. Shear plane removed. 5 cm shear. Max peeq 0.15

Figure 2-7. *Plastic strain (peeq) in the copper.*

2.4.2 Analysis of how slow re-saturation can change the material properties of the buffer

The bentonite in the buffer consists of mainly of the clay mineral montmorillonite together with a minor proportion of common used minerals such as quartz, feldspar, gypsum etc. The sealing properties of the bentonite are essentially linked to the montmorillonite, mainly through interaction between montmorillonite counter-ions and water.

Studies of bentonite materials under full water saturation have strongly dominated the general research efforts, as this is the common condition in natural systems. Studies for final repositories have also mainly considered a water saturated buffer. However, a few studies specifically relating to structural and/or mineralogical conversion of bentonite under unsaturated conditions have been conducted. Some studies have also touched on the special conditions, with elevated temperature and varying degrees of saturation, which may be prevailing in a final repository.

Slow water saturation generally causes transient conditions and gradients to prevail for a longer period than in the case of a rapid water saturation. High temperature conditions could potentially affect the buffer properties in a negative direction, through steam, bacterial activity, transport and enrichment of dissolved species. This is discussed and investigated in both laboratory trials and field trials. Karnland et al. (Chapter 11) has made a summary of the studies available and underway that deal with these processes.

In terms of physical properties such as shear strength, shear elongation, swelling pressure and hydraulic conductivity as a result of short-term elevated exposure (up to 150 °C) it appears that there is an tendency of increased shear strength and a significant change in maximum strain failure as a result of short-term hydrothermal treatment. However, the effect is equal to or greater for samples heated under saturated conditions compared to those heated without an external water pressure. Swelling pressure and hydraulic conductivity are not affected by short-term heating irrespective of hydraulic conditions.

Vapour transport tests in bentonite show that vapour condensed under all investigated conditions, and that water absorption from condensation water totally dominated over water absorption directly from vapour. All tests showed that water absorption decreased over time, indicating that the pellet system was sealed and that vapour transport decreased with time.

Test series of material exposed to temperatures of up to 200 °C at different water saturation levels show no clear differences due to hydrothermal treatment between unsaturated and water-saturated samples with respect to swelling capacity (Figure 2-8).

Generally, differences in measured swelling properties due to hydrothermal treatment are negligible in comparison to the differences between sodium dominated and calcium-dominated materials. The effects of short-term vapour pressure on free swelling are therefore not considered to be a problem for a KBS-3 repository. One study included experiments with bentonite at different degrees of water saturation (0, 50, 85 and 100 %) exposed to temperatures up to 150 °C. After hydrothermal treatment, the samples were saturated and swelling pressure and hydraulic conductivity was determined both at elevated temperature and at room temperature. In no case was any significant change in the properties compared to the reference materials.

Precipitation of secondary minerals in the buffer, e.g. $CaSO_4$, in a temperature and water saturation gradient has been observed in field tests. However, these reactions are reversible and the precipitated minerals will be dissolved when water saturation increases. The precipitates are therefore not expected to affect the performance of the buffer.

There is nothing in the above-mentioned studies suggesting that there would be changes in the properties caused by mineralogical changes due to short-term exposure to dry or semi-dry conditions at high temperatures. The transport capacity of dissolved species can generally be expected to be lower at low water content than at full water saturation, which counteracts most known transformation processes. SKB estimates, based on the above, that the material properties of the buffer will not be adversely affected to an extent that adversely affects long-term safety by a long water saturation phase.

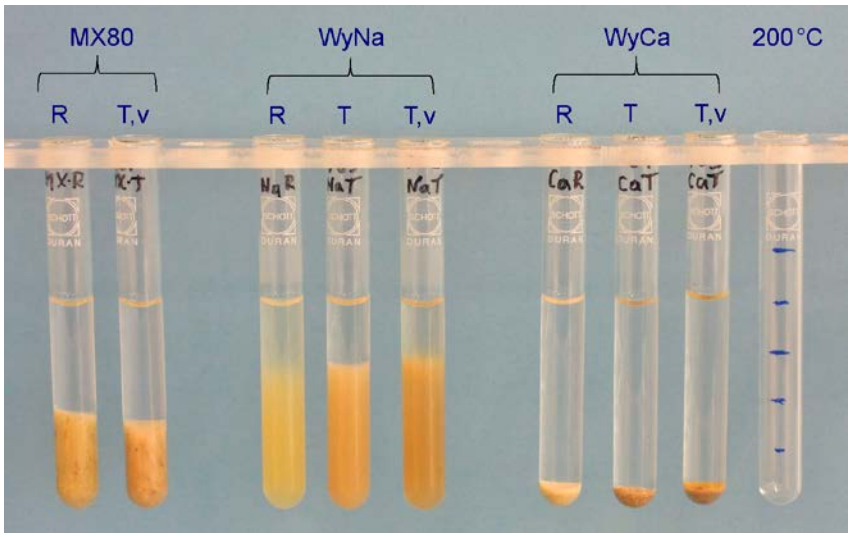

Figure 2-8. *Result from free swelling tests. All test tubes contain 1.00 grams of material expanded to the maximum volume. MX-80 bentonite was the starting material for all samples purified for some experiments and ion exchanged into sodium (WyNa) and calcium form (WyCa) respectively. R indicates reference material; T indicates material hydrothermally treated at full water saturation, and T, v indicates material hydrothermally treated in unsaturated state.*

2.5 Assessment of the possibility of adjusting/shortening the saturation process by adjusting initial water content or by an artificial supply of water

SKB has tested to water fill the pellets gap in two large-scale projects at Äspö; CRT and Lasgit. In these experiments, a concrete slab was anchored in the rock to prevent swelling of pellets and buffer blocks. This was placed on the top block as soon as possible after water was filled into the gap. Nevertheless, major deformations occurred, mainly in the pellets.

SKB has also tested the system pellets/blocks on a smaller scale, where the system had limited access to water for a week. The tests were performed without any vertical load. These tests exhibit major deformations in both blocks and pellets (Sandén and Börgesson 2010). Corresponding tests have also been performed with full-scale blocks where two annular blocks with an outer pellet-filled slot was water saturated (Åberg 2009) (Figure 2-9). The results of these tests confirm the results of the smaller tests. The assessment is that even with limited access to water unacceptably large deformations occur in the buffer with the accompanying decrease in density. The deformations become larger the more water that is supplied to the pellet filling. A prerequisite for filling water in the gap is that the buffer blocks are held in place with a vertical load. At installation in a repository, it is not possible to backfill the tunnels at such a rate which can prevent a heave of the buffer if artificial wetting is used.

Only filling the "pores" between pellets with water would add an additional 1 000 litres. The total amount of water that needs to be supplied to water the system of blocks and pellets is about 1 700 litres per deposition hole. Thus, the amount of water required to achieve water saturation is reduced to about half with artificial wetting. Since the saturation process is not linear over time, time to reach full water saturation in artificial wetting of the outer gap is not halved. The "time gain" is smaller.

Adding the water to the system of buffer blocks and pellets after the tunnel refill is in place also entails risks and problems:

1. It is difficult to show that water has reached all parts of the pellet-filled column.
2. An artificial wetting would mean that a system of tubes to get water into the system must be installed and then removed.
3. The benefit of an artificial supply of water in the pelleted column on the full wetting process is judged to be small, see the text above.

Figure 2-9. *Deformation damage in a bentonite block without vertical load in a situation with artificial water supply (Åberg 2009).*

SKB believes that it is more prioritized to quickly get a vertical load on the buffer stack, ie the backfill in place, rather than filling the slots in the deposition hole with water.

It is possible to have higher water content on the blocks at the compaction and yet achieve the same dry density as for the reference design (17 % water ratio). SKB has previously compacted blocks for large scale experiments on Äspö (Lasgit (Cuss et al. 2010)) with a high initial water ratio and degree of water saturation. Technically, it is possible to achieve a degree of water saturation of about 95 %. To achieve this, the solid blocks can be compacted with about 40 MPa to a water ratio of about 21 %. Corresponding values for the annular blocks are a compaction pressure of 80 MPa together with a water ratio of about 20 %. In connection with the Lasgit project, SKB has checked the impact of high initial water content on the water saturation process, as it was desirable to have as fast buffer saturation and homogenization as possible. In Lasgit were combined:

1. Block with high water degree of saturation.
2. Filling of the pellet slot with water.
3. Artificial wetting from filter mats in the top and bottom of the hole and filter on the surface of the canister.
4. No heating.

A prerequisite for this would be that the buffer pillar was held in place with a 300 mm thick steel cap, dimensioned for 20MPa. Lasgit was almost 4 years after installation in principle water saturated, but the pore pressure distribution (Figure 10) shows that the system was far from hydromechanical equilibrium. The different curves in the figure show the pore pressure at different points in the buffer. Because the pressure differs between the points, hydromechanical equilibrium is not achieved. The pore pressure is also not in equilibrium with the hydrostatic pressure of the surrounding rock. This shows that even if all possible measures are taken to quickly achieve full water saturation, the final results will not be equilibrium.

It is possible to produce buffer blocks with higher water ratio and maintain reference density. Future technology development may show if it is appropriate to use that type of block in the repository. However, this only has a limited effect on the water saturation process and on the thermal conductivity of the buffer.

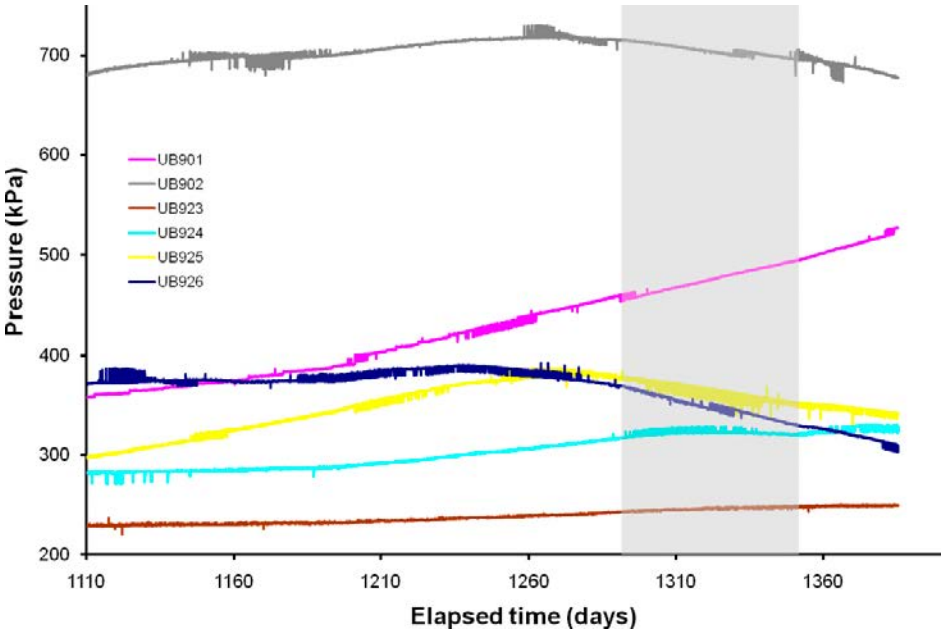

Figure 2-10. *Pore pressure inside the Lasgit bentonite in the time range of 1 110–1 360 days after the installation (Cuss et al. 2010).*

3 Conceptual uncertainties and their influence on bentonite hydration

Mattias Åkesson, Clay Technology AB, Lund, Sweden November 2013

3.1 Introduction

3.1.1 Background

Conceptual uncertainties associated with thermal, hydraulic and mechanical processes in the near field of a repository has been investigated since many years, both theoretically and through large-scale experiments, in a number of EU projects and in the international DECOVALEX project (Tsang et al. 2009). This information has, according to the judgment by SSM, not been optimally utilized in the calculations of the re-saturation phase in SR-Site. SKB should analyze the relevance of the conclusions from other extensive experiments, such as FEBEX, and include a systematic analysis of conceptual uncertainties which can influence the modelling of the evolution of the re-saturation. It has for instance been suggested that the influence of thermo-osmotic effects and the occurrence of a threshold gradient has a significant influence (Sánchez et al. 2007) in particular for those longer re-saturation times which occur in SKB's case.

3.1.2 Scope

The aim of this analysis was: i) to give an overview of different experiments which have been used for modelling tasks; ii) to give an overview of conceptual uncertainties regarding the buffer re-saturation, which have been suggested in these modelling tasks; and iii) to evaluate the relevance of these uncertainties for the re-saturation calculations within SR-Site.

The analysis has above all focused on the large-scale experiments performed within the FEBEX project, and the modelling tasks which have addressed these experiments. A description of the FEBEX *in-situ* test is presented in Section 3.2, together with a summary of performed modelling tasks. The FEBEX mock-up test and the modelling tasks related to this test are summarized in Section 3.3. This chapter also includes descriptions of three non-standard flow models (threshold gradient in Darcy's law, thermo-osmotic effects, and micro-fabric evolution) which have been analyzed within the framework of the modelling of FEBEX mock-up. An evaluation of the relevance of these non-standard flow models for the re-saturation calculations within SR-Site is presented in Section 3.4. Finally, in Chapter 5 a number of other uncertainties are described and evaluated.

3.2 FEBEX in-situ test

3.2.1 Test description

This section is based on information provided by Alonso and Alcoverro (2005) and Gens et al. (2009).

The FEBEX in-situ test has been performed (and is to some extent still running) in a granitic rock formation at the Grimsel test site in Switzerland. The FEBEX drift has a diameter of 2.28 m, and was excavated (using a TBM) in September – October 1995. The final 17.4 m of the drift was selected for the test.

The water inflow into the FEBEX drift was measured during January – May 1996, and was estimated to be 7.8 ml/min. This was found to be distributed among three types of water entry: 27 % from matrix; 51 % from well defined points; and the rest from fractures.

The mechanical installation was performed in July-October 1996. Two heaters (the outer and the inner were denoted Heater 1 and 2, respectively), with a diameter of 0.9 m and a length of 4.54 m, were installed within a buffer made of FEBEX bentonite blocks. The blocks had an initial water

content of 14.4 %, and an initial dry density of 1.7 g/cm^3. The overall dry density of the buffer, taking gaps into account, was 1.6 g/cm^3. The buffer was subjected to isothermal hydration during the first four months after the installation. The heating began on 27th February 1997. At first the heating was performed with constant power output, but on day 53 the system was switched to constant temperature mode, with a target temperature of 100 °C at the hottest point at the canister-bentonite contact. The heating from Heater 1 ended on 27th February 2002. The test was allowed to cool for 33 days, after which the outer half of the test was dismantled during a 75-days period. A new shotcrete plug was subsequently constructed, and the test of the remaining part of the experiment was continued.

3.2.2 Modelling performed within DECOVALEX

This section is based on information provided by Alonso and Alcoverro (2005) and Alonso et al. (2005).

The FEBEX in-situ test was selected as one of the modelling task (No 1) in the Decovalex III project which was carried out during 1999 to 2003. The modelling task was divided into three parts:

- A: HM modelling of the rock. The objective of this part was to predict the water inflow into the tunnel and the water pressure evolution in the rock during the tunnel excavation.
- B: THM analysis of the buffer behaviour. The objective of this part was to predict the evolution of the heating power, as well as the temperature, relative humidity and total stresses along selected sections and/or at specific points in the buffer during the first 1 000 days of operation.
- C: THM analysis of the rock. The objective of this part was to predict the evolution of the temperature, water pressure, normal stress, radial displacement at specific points and/or along selected sections in the rock during the first 1 000 days of operation.

Eight contributing teams presented modelling results for Part B (which is of main interest in this overview). A compilation of model features, couplings and some key factors used by the different teams are compiled in Table 3-1.

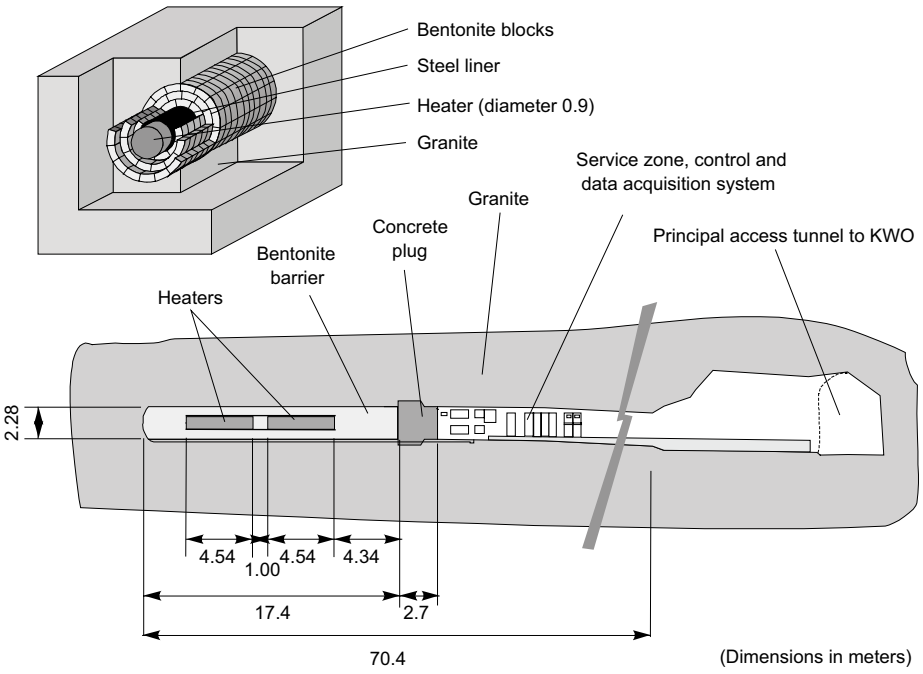

Figure 3-1. *Overview of the FEBEX in-situ test.*

Table 3-1 Consideration of couplings and some key factors by the teams.

Team	Couplings	Dimens	Liq ↔ gas	Vap. flux	$k_w(S)$	$\lambda_T(S)$	$\varepsilon_v(s)$
BGR	TH→HM*	2			■		
CNS	THM	3	■	■	■		■
DOE	TH→TM	3	■	■	■	■	■
IPS	THM	1			■		
JNC	TH	3		■	■	■	
SKB	THM	2	■	■	■	■	■
SKI	THM	3	■	■	■	■	■
STU	TH	1	■	■	■	■	

Abbreviation	Physical phenomena
liq ↔ gas	Phase change between liquid water and water vapour
vap. Flux	Vapour flux
$k_w(S)$	Saturation-dependent water permeability
$\lambda_T(S)$	Saturation-dependent thermal conductivity
$\varepsilon_v(s)$	Suction-induced deformations

M* indicates that the mechanical reduces to consider a dependency on the swelling pressure.

The chosen time frame, i.e. the first 1 000 days after the start of the heating, implied that the preceding and the subsequent time periods were excluded for modelling, and this had two consequences:

- The four months period with isothermal hydration, which followed the installation of the test, was included by some modelling teams, and this implied a better agreement with the experimental relative humidity (RH) data in the outer part of the test.
- The two year period, which followed the first 1 000 days after the heating started, was not included in the models, and this meant that the models weren't compared with the data from the dismantling of the test.

A number of observations could be made from the presented predictions:

- *Thermal problem:* The temperature predictions varied significantly among the modelling teams, although the actual recorded values tended to remain at the average of all calculations. One observed feature was the initial reduction and the subsequent increase in the power required to maintain a constant temperature at the heater-buffer contact. This was an effect of the initial drying and the subsequent re-saturation of the inner part of the bentonite. Models which did not include a saturation-dependent thermal conductivity could not reproduce this effect, and only one of the predictions matched the actual behaviour correctly.
- *Hydraulic problem:* Models which included a correct TH coupling, (i.e. with representations of the liquid/vapour phase change; and the vapour flux) were capable of reproducing the observed evolution of relative humidity. This was specially the case for the predictions of the processes at the mid-section of the heaters. The processes in the central section of the test were, however, more complex and were not accurately reproduced by the models. Preferential vapour flow paths along open joints, which may have played a role in the FEBEX test, were not considered in the used models (a related process is described and assessed in Section 3.5.2).
- *Mechanical problem:* Radial stresses recorded in the outer part of the buffer showed a continuous increase during the observation period and their value exceeded 3MPa at day 1 000, whereas the pressure sensor located in the inner part of the buffer remained essentially unloaded during the same period. Some of the presented models predicted this distribution, while other models resulted in a more homogeneous build-up of stresses within the buffer. The porosity of the buffer remained constant in global terms due to the rigid confinement offered by the granite. The intrinsic permeability of the buffer could therefore be expected to be fairly constant. This implied that a correct prediction of the relative humidity evolution did not require a mechanical coupling. This was demonstrated by one of the modelling teams.

- *Influence of the rock matrix permeability:* Measurements of different RH distributions showed that the discrete conducting features of the rock had only a minor influence on the buffer hydration, and it was concluded that the low permeability of the saturated bentonite, (1×10^{-21} m^2) compared with the granite matrix permeability (5×10^{-19} m^2), leads to a fairly homogeneous hydration of the barrier. In other words, the bentonite permeability controlled its own rate of hydration and the rock matrix was capable of providing all the required flow of water.

3.2.3 Modelling of FEBEX in-situ test by UPC

After the completion of the FEBEX task within the Decovalex III project, Sánchez and Gens (2006) and Gens et al. (2009) presented results from a modelling work which encompassed the entire five year test period of the outer part of the experiment, which therefore also could include a comparison with data from the dismantling of that part. The model consisted of a 2D axisymmetric geometry, and employed the fully coupled thermo-hydro-mechanical formulation (including gas transport) as implemented in the Code_Bright FEM code. The heat transport was calculated with Fourier's law, the advective transport of water and air followed Darcy's law, and the diffusive transport of vapour followed Fick's law. The used retention curve was a modification of the van Genuchten expression. For the mechanical behaviour a modified form of the Barcelona Basic Model was employed.

A number of observations could be made from a comparison of the model results and the data from the sensors in the bentonite:

- *Thermal problem:* The model was able to reproduce the temperature evolution generally well, although the calculated heating power was under-predicted by approximately 10 and 18 %, for Heater 1 and 2, respectively.
- *Hydraulic problem:* The model was able to reproduce the evolution of RH very satisfactory. The outer part of the bentonite displayed a monotonic increase of RH, reflecting the hydration from the rock. In the inner part, however, the RH first displayed an increase, which reflected a vapour front from even warmer parts. This was immediately followed by drying with decreasing RH. Finally, the RH exhibited a slow increasing trend, also reflecting the hydration from the rock.
- *Mechanical problem:* The model was able to resemble the general build-up of total stresses and also the final value for a number of sensors. The relatively slow build-up of stresses in the inner part of the bentonite was, however, not reproduced.

The model also simulated the cooling stage and the excavation performed prior to sampling, and the model results could be compared with data from the analyses that were performed on samples obtained during the dismantling operation:

- *Water content profiles:* The numerical analysis showed very good agreement with the measured profiles of the water content. In sections close to the heater, the water content was still below the initial value. In cool sections, however, there was a small net gain in the central part of the tunnel. Close to the rock wall, in contrast, the water content had increased significantly.
- *Dry density profiles:* The numerical analysis also showed very good agreement with the measured profiles of the dry density. Close to the rock the bentonite had expanded, exhibiting dry density values well below the initial value. In contrast, in zones near the heater and in the central part of the tunnel, the dry density had increased.

It was concluded from this modeling work that the used THM formulation was able to capture the phenomena involved as well as their interactions, and also that it has a good predictive power. It was, however, also stated that it is possible that other phenomena may start playing a more significant role (such as thermo-osmosis, chemical effects, or the double porosity fabric of the compacted bentonite) when longer periods are considered.

3.3 FEBEX mock-up test

3.3.1 Test description

This section is based on information provided by Martin and Barcala (2005) and Sánchez and Gens (2006).

The FEBEX mock-up test has been performed and is still running in the laboratory of Ciemat in Madrid. The test is performed in a cylindrical steel body with a useful length of 6 m and an inner diameter of 1.62 m. Two heaters with a length of 1.62 m and a diameter of 0.34 m were installed within a buffer made of FEBEX bentonite blocks. The blocks had an initial water content of 13.6 %, and an initial dry density of 1.77 g/cm^3. The overall dry density of the buffer, taking gaps into account, was 1.65 g/cm^3.

The experiment is equipped with an artificial hydration system by which granitic water has been used for hydration of the bentonite. Three days before the start of the test, a volume of 634 litres was injected in order to flood all the voids in gaps in the experiment. The heating and the hydration began simultaneously on 4th February 1997. At first the heating was performed with constant power output, but on day 10 the system was switched to constant temperature mode, with a target temperature of 100 °C at the heater-bentonite interface. The outer thermal boundary is set by the external climate which is maintained with air-conditioning at 20±2 °C. The water injection pressure has been between 0.5–0.6 MPa since the start.

An over-heating event occurred on day 1 391 and lasted for 40 hours. The maximum temperature in the bentonite reached 240 °C during this event.

From approximately day 900, the water uptake of the test has been significantly slower than what has been predicted, and this has motivated investigations of *non-standard flow models* (see next section). The slow water uptake coincided with a levelling out and even reduction of total stresses. An alternative explanation that a problem in the hydration system could affect the water supply to the bentonite has also been considered. However, according to Sánchez and Gens (2006), investigations have confirmed that there was no obstruction in the hydration system or geotextile, and that the water intake was nearly uniform over the entire hydration front.

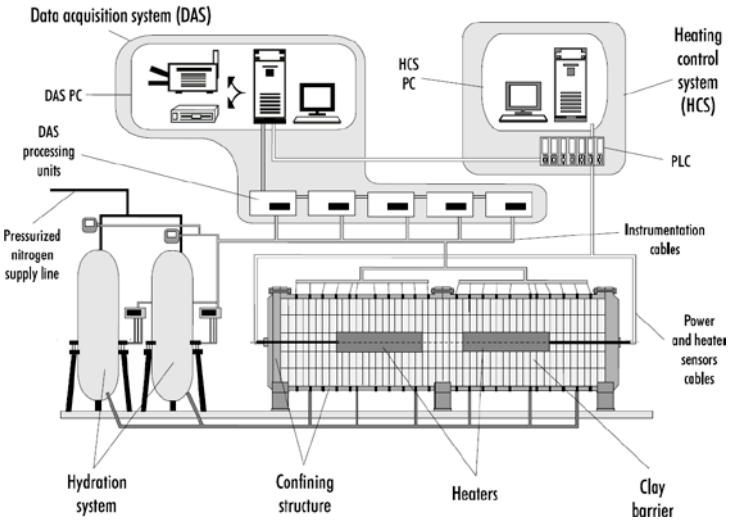

Figure 3-2. *General layout of the FEBEX mock-up test.*

3.3.2 Modelling of FEBEX mock-up test by UPC

Sánchez and Gens (2006) have presented results from a modelling work and compared this with experimental data from the operational stage with hydration and heating up to day 2 417. In addition, results from a long-term (20 years) prediction were presented.

The model consisted of a 2D axisymmetric geometry, and employed the fully coupled thermo-hydro-mechanical formulation, as implemented in the Code_Bright FEM code and very similar the one used for the in-situ test model (Section 3.2.3). The heat transport was calculated with Fourier's law, the advective transport of water and air followed Darcy's law, and the diffusive transport of vapour followed Fick's law. The used retention curve was a modification of the van Genuchten expression. For the mechanical behaviour a modified form of the Barcelona Basic Model (Alonso et al. 1990) was employed.

A comparison of results from a base case model and the data from the sensors in the bentonite showed that:

- *Thermal problem:* The model was able to reproduce the temperature evolution generally well.
- *Hydraulic problem:* The model was able to reproduce the cumulative water-uptake and evolution of RH quite well up to day 900. After that the model tended to over-estimate the hydration rate.
- *Mechanical problem:* The model was able to resemble the general build-up of total stresses up till day 900. After that the model tended to over-estimate the build-up of stresses.

The observed differences concerning the hydration rate motivated the investigation of a number of non-standard flow models. These analyses were performed with 1-D axis-symmetrical models. Two characteristic sections were considered: one represented a section in the central part of the heaters and was modelled with a temperature of 100 °C at the inner boundary, and one cold section representing the outer parts of the test was modelled with a temperature of 27 °C at the internal part of the barrier. These investigations are summarized in the following subsections.

Threshold gradient

Darcy's law describes a linear relationship between the flux and the hydraulic gradient, and this law is generally valid at low Reynolds numbers (Bear 1972). Some authors have, however, discussed a lower limit for the applicability of Darcy's law (see for instance Bear (1972) and Mitchell (1993)), and such a lower limit would imply that a threshold gradient must be exceeded before any flow can be initiated (see Figure 3-3).

In the modelling of the FEBEX mock-up test (Sánchez and Gens 2006), the following non-linear relationships between the flux and the hydraulic gradient were investigated:

- A threshold gradient (Jo) equal to 50.
- A critical gradient (Jc) close to 2000.
- A power law for the range of hydraulic gradient with non-Darcian's flow.

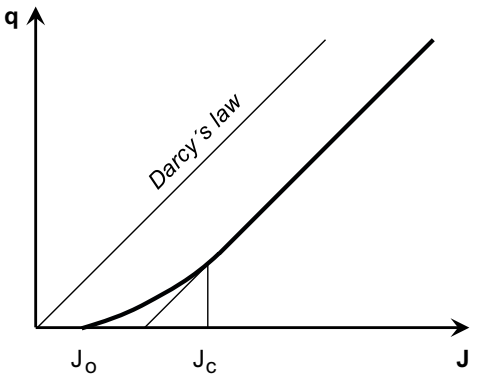

Figure 3-3. *Linear and non-linear relationships between flux (q) and hydraulic gradient (J).*

It was found that a 1D axisymmetric THM model which included this description could capture the reduction in the hydration rate observed in the mock–up test. It was, however, also noted that the used approach implied that the barrier did not reach full water saturation.

The influence of a threshold gradient was also investigated in a model of one of the FEBEX infiltration test (Sánchez et al. 2007). In this case the used threshold gradient was also set to 50, while the critical gradient was set to a value close to 1 500.

Thermo-osmosis

With thermo-osmosis is generally meant fluid flow which is caused by a temperature gradient. Such a coupled flow phenomena is supported by non-equilibrium thermodynamics (De Groot and Mazur 1984, Mitchell 1993) and is one of several coupled flow phenomena which can occur, see Table 3-2.

In the modelling of the FEBEX mock-up test (Sánchez and Gens 2006), the following equation was formulated in order to include the thermo-osmotic effect:

$$\mathbf{q}_l = -\mathbf{K}_{HH}(\nabla P_l - \rho_l \mathbf{g}) - \mathbf{K}_{HT}\nabla T \qquad (3\text{-}1)$$

The flow coefficient $\mathbf{K}_{HH}$ corresponds to $\mathbf{k} \times k_r/\mu$ used in Darcy's law, while $\mathbf{K}_{HT}$ is the phenomenological coefficient associated to the thermo-osmotic flow. For the FEBEX bentonite there were no experimental data, and for the modeling of the FEBEX mock-up a thermo-osmotic constant of 2.73×10^{-13} m^2/K/s was adopted, and this value was within the range of possible values found in the literature.

It was found that a 1D axisymmetric THM model which included this description displayed a somewhat better agreement with the RH evolution in the hot section close to the heater, but the overall tendency of the model could not be considered good. The measured trend in zones near the hydration front was not so well captured, and results from the model of the outer cold section were not influenced by the thermo-osmotic effect. It was also observed that it would be possible that the clay never reaches full saturation in the hot sections if this approach is used.

Sánchez et al. (2007) also investigated thermo-osmosis in a model of the FEBEX infiltration test. In this case, the used thermo-osmotic constant was set to 5×10^{-12} m^2/K/s. Finally, Zheng and Samper (2008) investigated thermo-osmosis in a model of the FEBEX mock-up, in which case the used thermo-osmotic constant was set to 3.62×10^{-12} m^2/K/s.

Table 3-2. Direct and coupled flow phenomena.

		Gradients	
Flow	**Hydraulic head**	**Chemical concentration**	**Temperature**
Fluid	Darcy's law	Chemical osmosis	Thermo osmosis
Ion	Streaming current	Fick's law	Soret effect
Heat	Isothermal heat transfer	Dufour effect	Fourier's law

Micro-fabric evolution

The notion of micro-fabric evolution is generally based on the following concepts (Thomas et al. 2003, Sánchez and Gens 2006): i) the main part of the water that enters the bentonite is adsorbed into the micro-pores, ii) this implies that the particles swell, and if the bentonite is restrained, this will then reduce the size of the macro-pores, iii) this will reduce the effective hydraulic conductivity of the bentonite, since only *macro-pore water is available for flow* (the validity of this third point is discussed in Section 3.4.4).

In the modeling of the FEBEX mock-up test (Sánchez and Gens 2006), this effect was considered in an approximate way by reducing the intrinsic permeability in the external zone of the barrier (until a maximum of 15 % for suctions lower than 2 MPa). It was found that this model could reproduce the observed behavior in the barrier better than the operational base case model. It was also found that the case with micro-fabric evolution reached total water saturation in a long term prediction, in contrast to the cases with threshold gradient or thermo-osmosis.

Micro-fabric (or microstructure) evolution was also investigated in models of the Canadian large-scale experiments Isothermal Test (Thomas et al. 2003, see Section 3.4.4), and the Buffer-container experiment (Thomas et al. 2009).

3.4 Evaluation of non-standard flow models

3.4.1 Introduction

The goal of the evaluation is two-fold: i) to describe the mechanisms of the suggested non-standard flow models; and ii) to assess the relevance of these models for the SR-Site calculations if they would have been included in those.

Since the flow-models are not implemented in Code_Bright, there are three potential paths that can be pursued for the evaluation of these flow models: i) modification of existing numerical tool (Code_Bright); ii) development of new devoted numerical tools; iii) use of analytical methods. The first two options have been regarded as either too complex or too far-reaching to be followed during this work. The presented evaluations have, therefore, tried to employ analytical methods and descriptions.

3.4.2 Threshold gradient

The notion of a threshold gradient implies that full saturation may never be reached.

For isothermal conditions this can easily be assessed with the following observation: for a bentonite specimen with the dimension of, say, 0.1 m, a threshold gradient of 50 implies that the pressure difference over the specimen is 5 m × 10 kPa/m = 50 kPa, when the threshold is reached. For unsaturated conditions this corresponds to a negligible suction value, and the saturation degree would thereby be very close to unity.

For non-isothermal conditions, however, there may be a substantial remaining unsaturated pore volume when the threshold is reached, and a steady-state saturation profile can be calculated for a specific hydraulic gradient at the cold end. Such a calculation can be based on the analytical solutions presented by Claesson (2007). A *coordinate-independent* relation between saturation and temperature, i.e. S(T), can be obtained for steady-state conditions with the differential equation;

$$\frac{dS}{dT} = -\frac{K_T(S,T)}{K_S(S,T)} \tag{3-2}$$

and by specifying a boundary saturation degree at the cold end ($S(T_c) = S_c$). The derivation and the details about this differential equation were presented by Claesson (2007). A *saturation profile* S(r) can subsequently be obtained for a specified temperature profile T(r).

The differential equation, Equation (3-2), was modified concerning three parts in order to resemble the results by Sánchez and Gens (2006) as far as possible:

i. The retention curve for which the following function was used together with the following parameter values: $P_0 = 28$ MPa; $\lambda = 0.18$; $P_1 = 1\,100$ MPa; $\lambda_1 = 1.1$:

$$S = \left(1 + \left(\frac{P_g - P_l}{P_0}\right)^{\frac{1}{1-\lambda}}\right)^{-\lambda} \left(1 - \frac{P_g - P_l}{P_1}\right)^{\lambda_1} \tag{3-3}$$

ii. The following permeability value at saturation was used: $k_{sat} = 1.9 \times 10^{-21}$ m^2

iii. A temperature dependent vapour diffusion coefficient was adopted:

The vapor diffusion is in the analytical solution described as driven by *vapor density gradients,* and the diffusion coefficient includes a saturation dependence:

$$g_{vap} = -D_v(S) \times \nabla \rho_v \tag{3-4}$$

In the implementation of Code_Bright, the vapor diffusion is described as driven by *vapor mass fraction gradients,* and the diffusion coefficient includes a saturation dependence, *as well as a temperature dependence*:

$$i_g^w = -\rho_g \cdot n \cdot (1-S) \cdot \tau \cdot D_0 \frac{(273+T)^{2.3}}{p_g} \cdot \nabla \omega_g^w \tag{3-5}$$

The vapor mass fraction gradient can be transformed to a vapor density gradient in the following way:

$$\omega_g^w = \frac{\rho_v}{\rho_a + \rho_v} = \frac{\rho_v}{\rho_g} \quad \Rightarrow \quad \nabla \omega_g^w = \frac{d\omega_g^w}{d\rho_v} \nabla \rho_v = \frac{\nabla \rho_v}{\rho_g} \tag{3-6}$$

In order to have the same diffusion coefficient in the analytical solution as in the Code_Bright formulation, the following function was adopted together with the following parameter values: n = 0.4; $\tau = 0.8$; $D_0 = 5.9 \times 10^{-6}$ m^2 × Pa × s^{-1} × K$^{-2.3}$; $p_g = 10^5$ Pa:

$$D_v(S,T) = -n \cdot (1-S) \cdot \tau \cdot D_0 \frac{(273+T)^{2.3}}{p_g} \tag{3-7}$$

Coordinate-independent relations between saturation and temperature, i.e. S(T), are shown in Figure 3-4 (left) for the above-mentioned material models and parameter values, as well as for the temperature interval 20–100 °C, which corresponds to the conditions in the FEBEX mock-up. Solutions for five different cold end saturation degrees are shown: 0.8, 0.9, 0.98, 0.99 and 0.998.

The temperature profile can be defined for the assumption of a constant thermal conductivity value:

$$r(T) = r_i \cdot \left(\frac{r_o}{r_i} \right)^{\frac{T_i - T}{T_i - T_o}} \tag{3-8}$$

The inner and outer radii (r_i and r_o) of the FEBEX mock-up is 0.168 and 0.795 m, respectively. This profile is shown in Figure 3-4 (right). Saturation profiles, i.e. S(r), can be obtained for the S(T) relations shown in Figure 3-4 (left) together with the temperature profile, and are shown in Figure 3-5 (left).

The hydraulic gradient can be calculated for any point along these solutions:

$$\frac{dh}{dx} = \frac{1}{\rho g} \frac{dP}{dx} = \frac{1}{\rho g} \frac{dP}{dS} \frac{dS}{dT} \frac{dT}{dx} \tag{3-9}$$

dP/dS is the derivative of the retention curve, dS/dT is the differential equation in Equation (3-2), and dT/dx is the thermal gradient. Distributions of the hydraulic gradient are illustrated in Figure 3-5 (right) for the different saturation profiles.

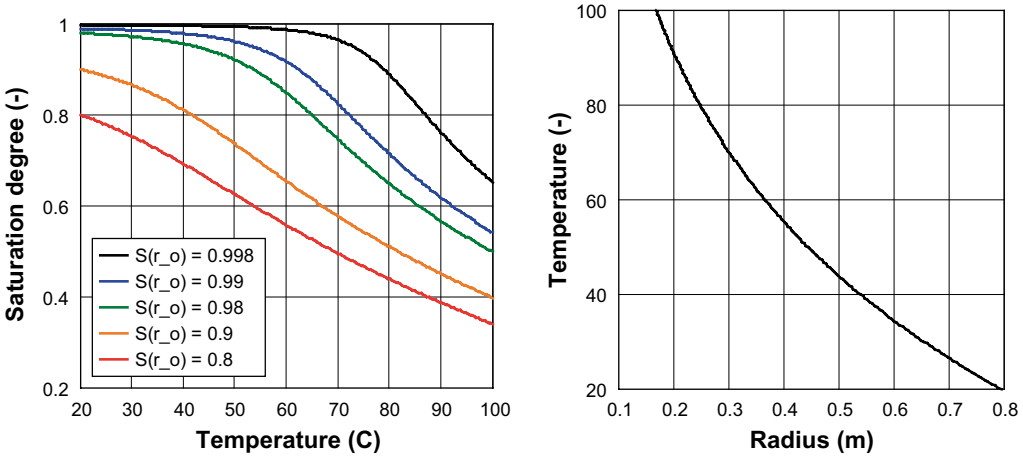

Figure 3-4. *Steady-state solutions with saturation degree vs. temperature, cold end saturation is 0.8, 0.9, 0.98, 0.99, 0.998 (left).Radial profiles of temperature (right).*

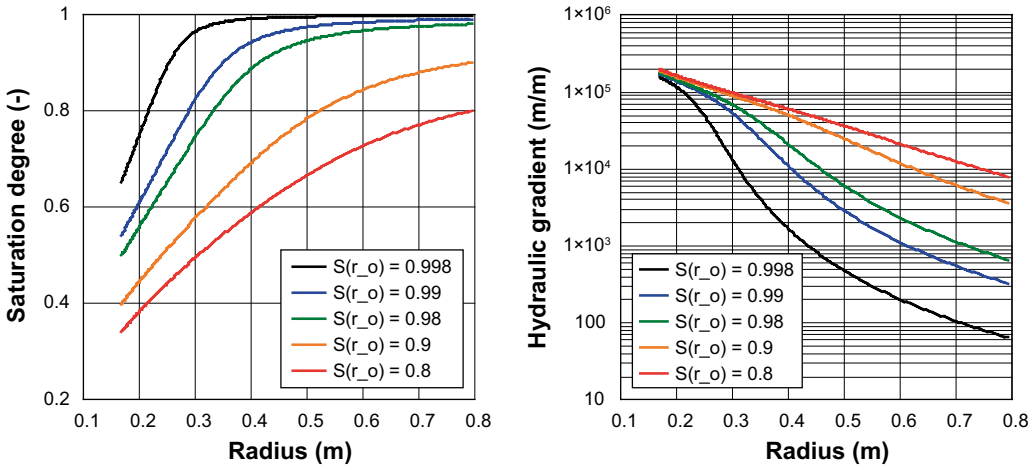

Figure 3-5. *Radial profiles of saturation degree (left) and hydraulic gradient (right) for cold end saturation degree 0.8, 0.9, 0.98, 0.99 and 0.998.*

It can be noted that the profile with a cold end saturation of 0.998 implies a hydraulic gradient of 65 m/m at the outer radius. This is approximately the threshold gradient used by Sánchez and Gens (2006). The hot end saturation degree of this profile is 0.65. This illustrates how a threshold gradient can stop the moisture transfer into the bentonite at non-isothermal conditions, although the hydraulic gradient is significantly higher inside the bentonite.

Relevance for SR-Site calculations

To conclude, it is the non-isothermal conditions that lead to a remaining unsaturated void-space. This effect was tested for a few thermal conditions characteristic for the KBS-3 buffer. For this the canister mid-height geometry of the buffer was chosen (inner and outer radii of 0.525 and

0.875 m, respectively) and sets of typical inner and outer temperatures was selected for four times (10, 30, 100 and 200 years) respectively, which were derived from Hökmark et al. (2009). The material model was identical with the FEBEX model described above. For each temperature set, a S(T)-relation, and subsequently a saturation profile, was found for which the hydraulic gradient at the cold end was exactly 50 m/m. (Figure 3-6 and Figure 3-7). It can be observed, that even though this effect implies some remaining unsaturated pore volume, it can be noted that this is very small.

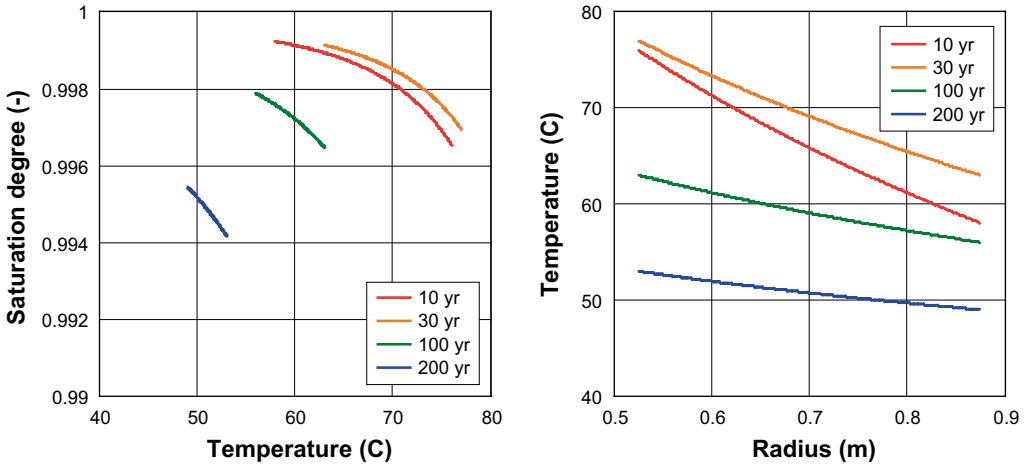

Figure 3-6. *Steady-state solutions with saturation vs. temperature (left) for radial temperature profiles typical for KBS-3 canister mid-height conditions at four different times (right).*

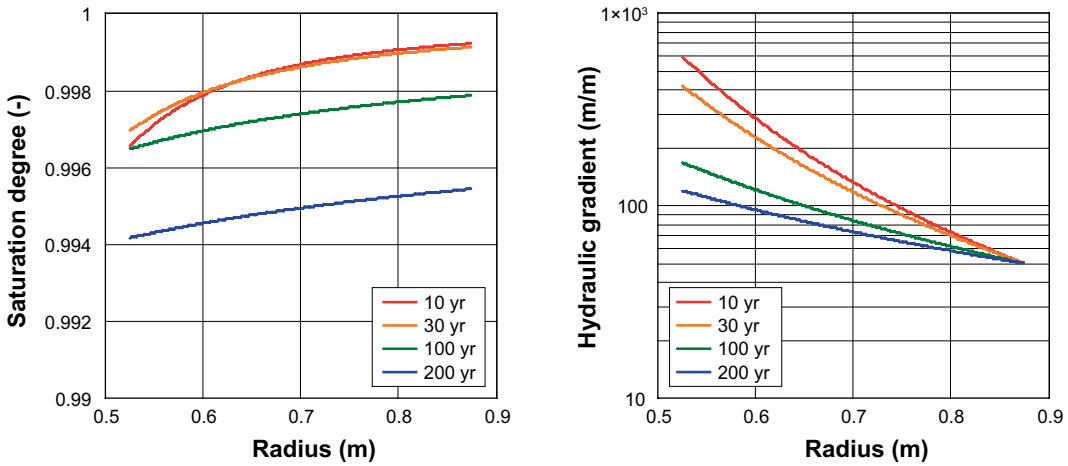

Figure 3-7. *Radial profiles of saturation degree (left) and hydraulic gradient (right) for thermal conditions shown in Figure 3-6 (right).*

Even if the steady-state conditions are very close to full saturation, this does not necessarily mean that the time scale to reach these conditions is unaffected by the threshold gradient. The model results presented by Sánchez and Gens (2006) indicate, however, that the time-scale to reach steady-state with a threshold gradient is approximately the same as the time-scale to full water saturation without a threshold gradient.

3.4.3 Thermo-osmosis

The notion of a thermo-osmotic flux term may imply that full saturation never is reached.

This effect can be fairly easily assessed for the FEBEX mock-up condition by following the modeling presented by Zheng and Samper (2008). This was based on a liquid flux, driven by gradients in liquid pressure, as well as in temperature:

$$q_l = -\frac{k_r \cdot k}{\mu}\nabla P_l - k_T \nabla T \qquad (3\text{-}10)$$

If the vapor transport is neglected, then the steady-state condition implies that q_l is equal to zero, and from this follows that:

$$\frac{dP_l}{dT} = -\frac{k_T \cdot \mu(T)}{k_r(S) \cdot k} \qquad (3\text{-}11)$$

Both sides are divided with the derivative of the inverse retention curve (dP_l/dS):

$$\frac{dS}{dT} = -\frac{k_T \cdot \mu(T)}{k_r(S) \cdot k \cdot \dfrac{dP_l}{dS}} \qquad (3\text{-}12)$$

This is a simplification of similar steady-state solutions presented by Claesson (2007), see also Equation (3-2). The retention curve was defined on the following form:

$$S(\psi) = \frac{\left(1 - 9.1 \cdot 10^{-10} \cdot \psi\right)^{1.1}}{\left[\left(1 + 5 \cdot 10^{-8} \cdot \psi\right)^{1.22}\right]^{0.18}} \qquad (3\text{-}13)$$

where ψ denotes suction (defined in Pa). This curve is shown in Figure 3-8 (left).

The derivative of the inverse retention function is given as $dP_l/dS = -d\psi/dS$. The relative permeability followed the cubic law ($k_r = S_l^3$). The temperature dependence of the viscosity was defined as:

$$\mu(T) = 0.6612 \times (T - 229)^{-1.562} \qquad (3\text{-}14)$$

where T denotes temperature (defined in K).

The value of dS/dT is in the order of -5×10^{-3} K^{-1} for the presented parameter values and for a temperature of 60 °C (Figure 3-8, left). A temperature difference between inner and outer radii of 80 °C, therefore implies a saturation difference between inner and outer radii of 0.4. An integration of the differential equation, Equation (3-12), with saturated conditions at the cold boundary, i.e. S(20 °C) = 1, results in a coordinate-independent S(T)-relation. A temperature profile can be defined under the assumption of a homogenous thermal conductivity value, see Equation (3-8), and with the radial geometry of the FEBEX mock-up (Figure 3-8, right). A saturation profile can be made by combining the S(T)-relation and the temperature profile (Figure 3-8, right).

Relevance for SR-Site calculations

To conclude, as with the threshold gradient, it is the non-isothermal conditions that lead to a remaining unsaturated void space. This effect was tested for the same thermal conditions characteristic for the KBS-3 as in Section 3.4.2. The material model was identical with the FEBEX model described above. For each temperature set, a S(T)-relation, and subsequently a saturation profile, was found for which the saturation degree as the cold end was equal to unity (Figure 3-6 and Figure 3-7). It can be observed, that this effect implies that some unsaturated pore volume will remain for a few hundred years.

Even if the steady-state conditions are fairly close to full saturation, this does not necessarily mean that the time scale to reach these conditions is unaffected by the thermo-osmosis. The model results presented by Zheng and Samper (2008) indicate, however, that the time-scale to reach steady-state with thermo-osmosis is largely the same as the time-scale to full water saturation without thermo-osmosis.

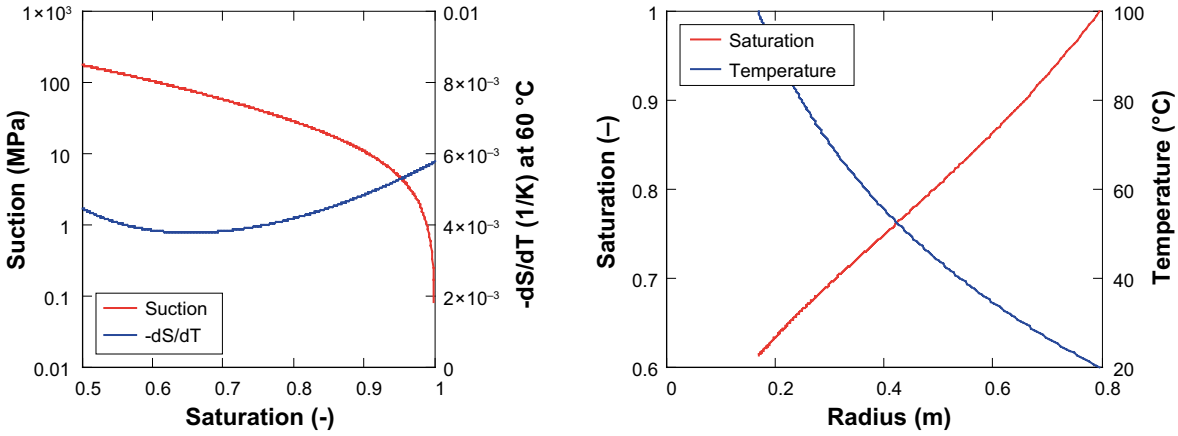

Figure 3-8. *Retention curve and dS/dT derivative (left). Radial temperature distribution and steady-state saturation profile (right).*

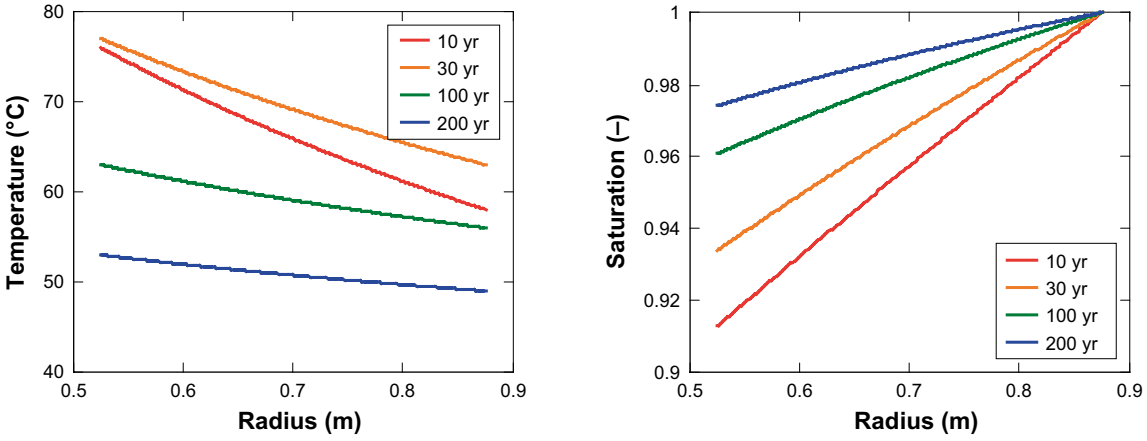

Figure 3-9. *Radial temperature distribution typical for KBS-3 canister mid-height (left) and corresponding steady-state saturation profile (right).*

3.4.4 Micro-fabric evolution

The notion of micro-structure evolution has been modeled as a reduction of the permeability value close to saturation, and this approach leads to an overall reduction in the rate of hydration. An example of an elaborate investigation of this effect was presented by Thomas et al. (2003), in a simulation of the Isothermal Test (ITT), which was one of the large-scale experiments at the Atomic Energy of Canada Limited's (AECL) underground research laboratory.

The low rate of hydration in the presented model can be illustrated through evaluation of the moisture diffusivity function, D(S):

$$D(S) = \frac{k(S)}{n \cdot \mu} \cdot \frac{dP_l}{dS} \qquad (m^2/s) \tag{3-15}$$

where k(S) = permeability function, n = porosity, μ = viscosity, dP_l/dS = derivative of the inverse retention curve.

The used retention curve was expressed as:

$$S(\psi) = \begin{cases} 1 + 2.3 \cdot 10^{-10} [1 - \exp(7.73 \cdot 10^{-6} \cdot \psi)] & \psi < 2.36 \cdot 10^6 \quad (Pa) \\ \dfrac{\log_{10}(\psi) - 8.23}{-3.38 \cdot e} & 2.36 \cdot 10^6 < \psi < 17 \cdot 10^6 \quad (Pa) \\ \dfrac{\log_{10}(\psi) - 8.74}{-5.08 \cdot e} & \psi > 17 \cdot 10^6 \quad (Pa) \end{cases} \tag{3-16}$$

The initial void ratio (e) was 0.56, which corresponds to a porosity (n) value of 0.36.

The hydraulic conductivity of the buffer material was first modeled with a saturation dependence following the approach proposed by Green and Corey (1971). The hydraulic conductivity is with this approach basically calculated as a sum of contributions from a number (m) of saturation classes (S_i) ranging from 0 to 1, with the first class (i = 1) corresponding to S = 1, and with the square of the suction value, given by Equation (3-16), in the denominator of each term:

$$K_l(S_i) = \frac{K_s}{K_{sc}} \sum_{j=i}^{m} (2j + 1 - 2i) \cdot \psi(S_j)^{-2} \tag{3-17}$$

The saturated hydraulic conductivity (K_s) was 5×10^{-12} m/s, and this value can be ensured through division with the calculated saturated conductivity value (K_{sc}) which simply is the sum in (3-17) for the first class (i = 1). Note that the division with the zero suction value for S = 1 leads to a singularity, and this can be handled with a factor close to unity for each S_i value. This relation is illustrated in Figure 3-10.

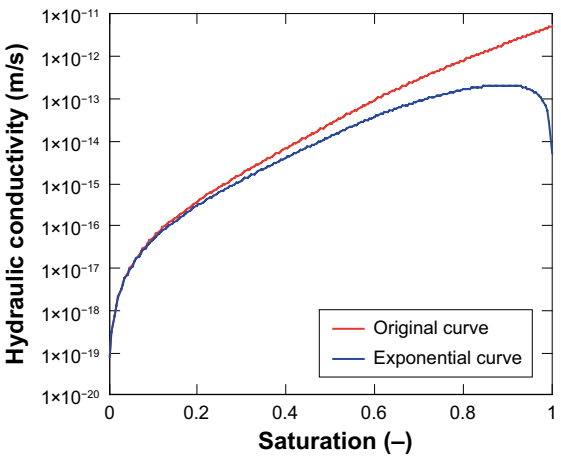

Figure 3-10. *Hydraulic conductivity vs. saturation degree.*

In order to match the experimental data, an adjusted exponential function for the hydraulic conductivity was subsequently proposed:

$$K(S)=K_l(S)\left(S_a+0.06\times S\{\exp[-100\times(1-0.06)S]\}\right) \quad (3\text{-}18)$$

The S_a is the degree of saturation of air, and can thus be replaced by (1-S). This relation is also illustrated in Figure 3-10.

The retention curve Equation (3-16) and the adjusted hydraulic conductivity curve Equation (3-18) are shown for the relevant saturation interval in Figure 3-11, upper left. These relations were used to evaluate the moisture diffusivity function according to Equation (3-15), and this relation is illustrated in Figure 3-11, upper right. The permeability function was calculated as $10^{-7}\times K(S)$, due to the factor $\mu/\rho g$. The derivative of the inverse retention function was given as $dP_l/dS = -d\psi/dS$. The evaluated function indicates that the diffusivity close to saturated conditions was as low as 2×10^{-10} m^2/s, although higher values can be noted for lower saturation degrees.

A moisture diffusivity value can easily be evaluated from the experimental data from ITT, if the hydration of the buffer material is described as a diffusion process in a cylinder (this would imply that the buffer had free access of water which may be an oversimplification to some extent).The initial and the final water content profiles (see Dixon et al. 2002) correspond to a dimensionless parameter Dt/a^2 value of approximately 0.1 for radial diffusion in a cylinder (see Crank 1975). With a radius (a) of 0.62 m and a time-scale of 6.5 years, this corresponds to a diffusivity value of 1.9×10^{-10} m^2/s. This value is basically the same as the modeled diffusivity value close to saturated conditions.

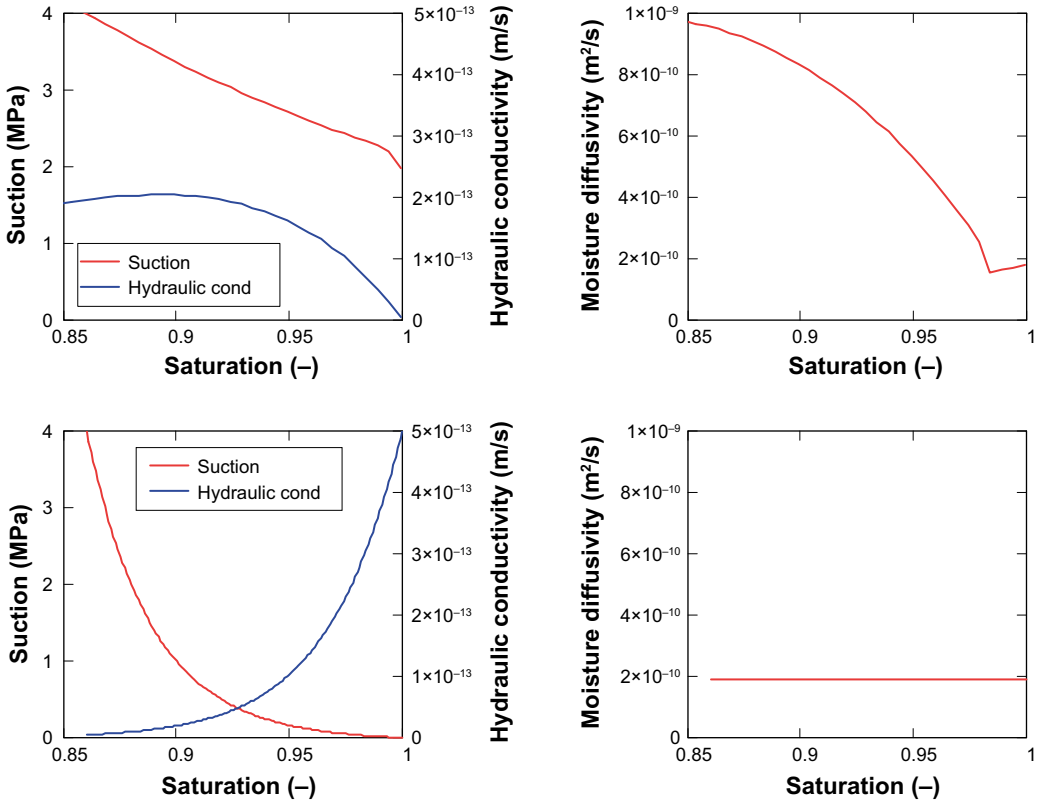

Figure 3-11. *Retention curve and hydraulic conductivity relations (left) and moisture diffusivity (right). Upper graphs show data from Thomas et al. (2003), lower graphs show data from this analysis.*

The observed diffusivity value could be reproduced with an alternative modeling approach. Equation (3-15) implies that a permeability function can be calculated for a specified D value and defined retention curve:

$$k(S) = \frac{D \cdot n \cdot \mu}{\frac{dP_l}{dS}} \tag{3-19}$$

The following function appears to be suitable as a retention curve for simple hydration problems:

$$S(\psi) = \left(\frac{\psi}{P_0} + 1 \right)^{-\lambda} \tag{3-20}$$

A specified initial point (in this case $S_{in} = 0.86$ and $\psi_{in} = 4$ MPa) implies that there is only one independent parameter. This was calibrated in order to yield a saturated hydraulic conductivity value of 5×10^{-13} m/s, as was found to be a typical value among the data from independent laboratory tests presented by Dixon et al. (2002). In this way the following parameter values were found: $P_0 = 44.8$ kPa and $\lambda = 0.0335$. Relations for retention properties, hydraulic conductivity and diffusivity are shown in Figure 3-11, lower graphs. It can be noted that the hydraulic conductivity function display an "conventional" increasing trend for increasing degree of saturation, in contrast to the micro-fabric evolution approach. It can also be noted that the suggested retention curve display a low slope close to saturation. Such a relation is supported by the final psychrometer sensors data, and the water contents measured during the dismantling operation.

Relevance for SR-Site calculations

To conclude, in contrast to the threshold and the thermo-osmosis there is no effect with a remaining unsaturated void space in the case of micro-structure evolution, but rather a reduced rate of water uptake. The main cause for this is the reduced relative permeability relation.

The physical basis for such an approach would be that only macro-pore water is available for flow (Thomas et al. 2003). It is however unclear why the effective conductivity value, Equation (3-18), close to saturation would be *orders of magnitude lower* than the measured hydraulic conductivity.

Still, the low evaluated diffusivity value seems to coincide with similar values for low density MX-80 (see Chapter 6), and this seems to support the notion that the Isothermal Test indeed displayed a low hydration rate. An overall water content of 18–22 %, would correspond to a clay water content of 36–44 % given the 50:50 sand-bentonite mixture. According to the analysis presented Chapter 9 this suggests that the mechanism behind the slow hydration rate could be that vapour diffusion limits the moisture transfer.

A simple assessment of the consequences of the micro-structure evolution for the SR-Site calculations can thus tentatively be made by comparing the moisture diffusivity value typical for the MX-80 buffer with the lower diffusivity values mentioned above.

The material model adopted for buffer hydration calculations in SR-Site, see Åkesson et al. (2010b) (homogenized approach and retention curves using the extended van Genuchten function) was used to calculate the corresponding moisture diffusivity functions with Equation (3-15) which are shown in Figure 3-12. These functions display a level of approximately 7×10^{-10} m^2/s. This can first and foremost be compared with the empirical diffusivity values presented in Chapter 6, which did not exceed the level of 5×10^{-10} m^2/s for MX-80 at buffer dry densities. This can therefore indicate a minor underestimation of the buffer hydration time-scale in SR-Site. If the SR-Site calculations would have been performed with the lowest empirical diffusivity values ($\sim 2 \times 10^{-10}$ m^2/s) then this would lead to a 3.5 times longer time for buffer-hydration (at wet rock conditions)

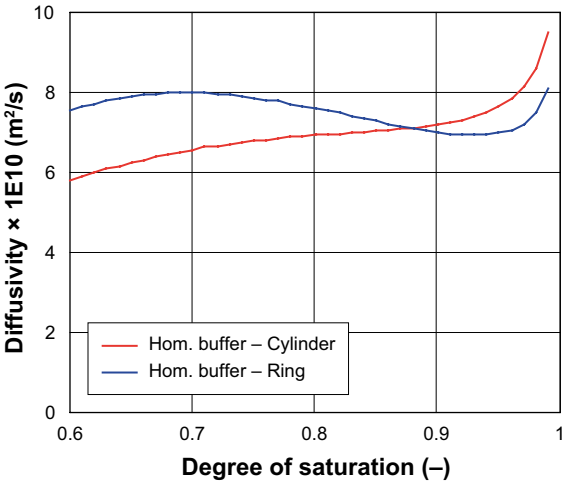

Figure 3-12. *Moisture diffusivity function based on the material model for buffer hydration calculations.*

3.5 Other uncertainties

3.5.1 Introduction

During the course of the work with the presented analysis, it was noticed that a few other conceptual uncertainties also deserved a thorough evaluation. This concerned: i) natural convection in pellets-filled slots, and ii) the temperature dependence of the retention properties. These evaluations are presented in the following subsections.

3.5.2 Natural convection in pellets-filled slots

Background

The water saturation process and the time-scale of the buffer hydration was analysed by Åkesson et al. (2010b). Among the analysed models, those with low inflow of water (low rock permeability) exhibited significant *moisture redistribution,* and this was also the case in models with no water inflow (dry rock scenario). The steady-state conditions and the time-scale to reach this state are to some extent determined by the flow coefficients. For dry rock conditions the most important transport process is the *diffusion of vapour,* and this was the only means to transfer moisture from hot to cold parts in the presented models. The potential contribution of *natural convection* to a more pronounced moisture redistribution has therefore been identified as a conceptual uncertainty for the evolution of the re-saturation. The result from a first assessment of this process is presented in this section.

Natural convection is a mechanism of heat transfer, involving the motion of a fluid (air in this case), which is the result of density differences, which in turn are caused by the exchange of heat. As a starting point, two modes of such air motions were suggested (Figure 3-13): either through a loop in the outer pellets-filled slot; or through a loop in both the inner and the outer slots, as well as through the joints between the bentonite blocks.

The complexity of the problem would be enhanced if moisture redistribution was included in these modes of air movement. Still, it is possible that the condition for the occurrence of natural conditions can be estimated with these simple descriptions.

Assessment of occurrence of natural convection

The evaluation below was based on the description of natural convection in a two-dimensional rectangular enclosure with a porous medium and isothermal side walls, presented by Nield and Bejan (2006). The geometry is shown in Figure 3-14 (left).

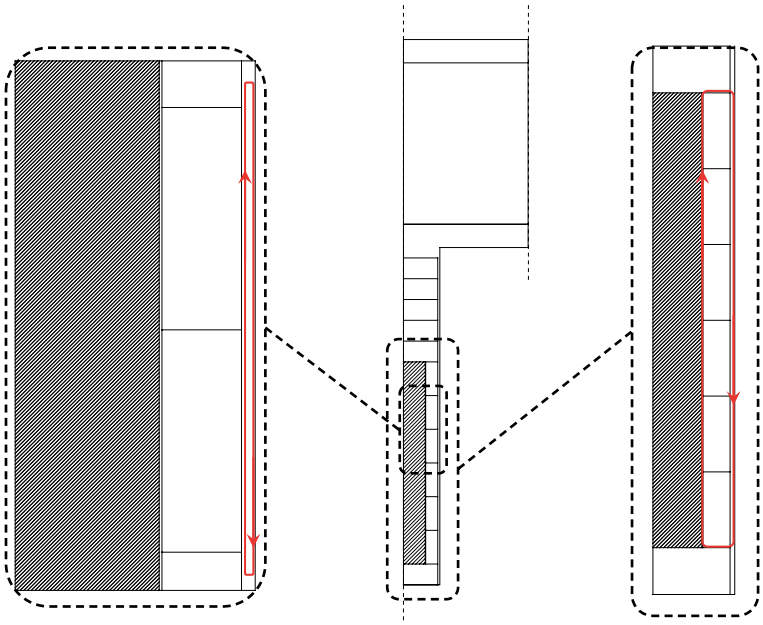

Figure 3-13. *Suggested modes of natural convection in pellets-filled slot. In outer slot only (left) and in inner and outer slot (right).*

The Rayleigh number (Ra) is a dimensionless number of significance for natural convection and is equal to the product of the Grashof and the Prandtl number. For the geometry in question it can be expressed as:

$$Ra = \frac{g\beta KH\Delta T}{\nu\alpha_m} \tag{3-21}$$

where g = gravity; β = thermal expansion coefficient; K = permeability; H = height of enclosure, ΔT = temperature difference between sides; ν = kinematic viscosity; α_m = thermal diffusivity of porous medium. It can be noted that the main uncertainty among these quantities is the K value.

A second dimensionless number of importance for natural convection is the Nusselt number (Nu), which is the ratio between total heat transfer, and conductive heat transfer. For the geometry in question a substantial amount of data (theoretical as well as experimental) has been used to adopt the following relation between Nu, Ra and the ratio of the dimensions of the enclosure:

$$Nu = 0.577\frac{L}{H}\sqrt{Ra} \tag{3-22}$$

where L = width of the enclosure (see Figure 3-14, right).

If the point on which Nu equals unity (i.e. $Ra(L/H)^2 = 3$), is regarded as the condition for natural convection to occur, then this can be used to calculate the maximum height of the slot (H_{max}) as a function of the permeability:

$$H_{\max}(K) = \frac{L^2 g\beta K\Delta T}{3\nu\alpha_m} \tag{3-23}$$

It should be mentioned that this may be a conservative approach since it was also stated by Nield and Bejan (2006) that √Ra >> H/L in order to get a *distinct* vertical boundary layers, and that this is a requirement for this type of convection.

A graph is shown (Figure 3-15) for a case with the following parameter values: L = 0.05 m (and 0.1 m); g = 9.8 m × s^{-2}; β = 0.003 K^{-1}; ΔT = 5 °K; ν = 1.9×10^{-5} $m^2 \times s^{-1}$; α_m = 3.3×10^{-7} $m^2 \times s^{-1}$. The thermal diffusivity value was based on a thermal conductivity value of 0.4 W × m^{-1} × K^{-1}. The thermal expansion and the viscosity for air were adopted for a temperature of 60 °C. These values, and the adopted temperature difference, were derived from Hökmark et al. (2009).

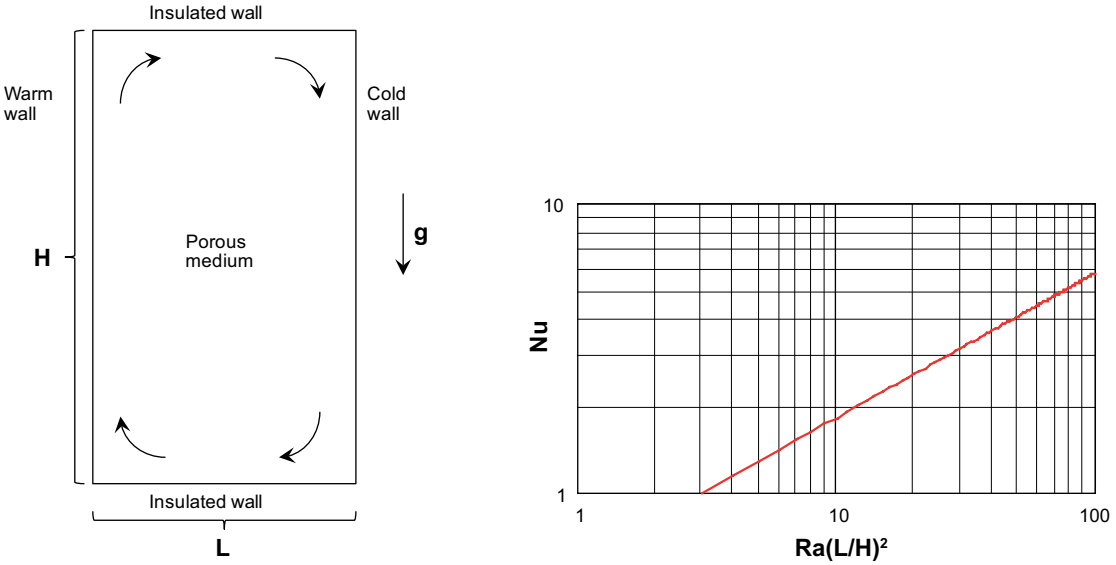

Figure 3-14. *Rectangular porus medium between heated side walls, left; illustration of Eq (3-22), right (after Nield and Bejan 2006).*

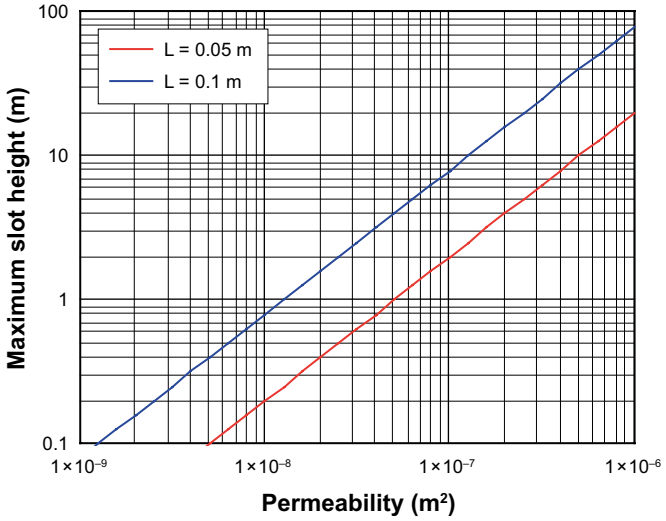

Figure 3-15. *Maximum height with sustained natural convection.*

These graphs thus show the maximum height with sustained natural convection. A lower height would imply a Nu-value higher than unity, and thus a convective heat transfer. Graphs are shown for two values of the slot width: 0.05 m, which represents the width of the pellets-filled slot, and the double value of 0.1 m. This latter analysis can be regarded as an estimate for the case with motion in both inner and outer slots, since the downward movement in this case can occupy the entire width of the pellets-filled slot, rather than only half the width.

Concluding remarks

A key property for natural convection to occur in the pellets-filled slot is apparently the (gas) permeability of pellets. This property has with the author's knowledge not been quantified experimentally. Still, an estimate can be made for "cleaned gravel" for which a permeability interval of 10^{-9} to 10^{-7} m^2 has been given (Bear 1972). If 10^{-7} m^2 is used as a conservative value for pellets, then for L=0.05 m the maximum height is 2 m, which can be regarded as fairly low in comparison to the lengths of the canister and the deposition hole. For L= 0.1 m, however, the maximum height is 8 m, which is higher than the canister. With the available information, it therefore appears to be more probable to have a sustained natural convection through both the inner and the outer slot, than through only the outer.

The presented assessment only addresses the condition for convective heat transport to occur, and hence the overall transport of air. An estimation of the actual gas flow rates, and their contribution to the moisture redistribution, appears to be far more complex. A convective transfer of vapour from hot to cold parts should imply that the equilibration of vapour pressure is more far-reaching than in the case with only diffusion of vapour. The major temperature difference between the hot parts close to the canisters and the cold parts in the tunnel ceiling, which will be prevalent during the first decades, also implies a major difference of the saturated vapour pressure in these parts. And this difference defines how far the moisture redistribution potentially can proceed. The tunnel volumes will to a large extent be backfilled with pellets which means that the accessible air-filled volumes of the backfill are substantial in comparison to the water volume of the installed buffer. Finally, the water retention properties of the bentonite describe a relation between the water content and the relative humidity. A *completely equilibrated vapour pressure* would therefore imply a major dehydration of the buffer (Figure 3-16). How much further the *actual moisture redistribution* will proceed in comparison to the case with only vapour diffusion should depend on the flow rates of the natural convection. Water uptake in the pellets-filled slot may have a retarding influence on this moisture transfer. However, experimental results from the Bastu-project (Birgersson and Goudarzi 2013) showed that only a minor fraction of the vapour passing through the investigated pellets fillings was adsorbed by the pellets.

3.5.3 Temperature dependence of retention properties

Background

Experimental data by Dueck and Nilsson (2010) and Villar and Gòmez-Espina (2007) show that the retention properties are temperature dependent. The general trend is that RH increases (suction decrease) with increasing temperature. Data by Kahr et al. (1990) suggest that this effect may be more significant for Ca dominated bentonite than for a Na dominated bentonite. This chapter describes the results from an assessment of this effect.

Assessment of the effect of temperature dependence

Kahr et al. (1990) presented a number of thermodynamic properties for systems with water and Na- and Ca-bentonites, i.e. MX-80 and Montigel, respectively.

The enthalpy change ($\overline{h}_w - h_w^\circ$, where $\overline{h}_w$ and h_w° are the partial specific enthalpy of water in the bentonite and the enthalpy of the pure water) was evaluated from measured enthalpies of immersion. The experimental data could be described as a function for the influence of the water content on the following form:

$$(\overline{h_w} - h_w^\circ) = (B + 2Cw)A \cdot \exp(-Bw - Cw^2) \qquad (J/g) \qquad (3\text{-}24)$$

For MX-80 bentonite the following parameter values were found: A=47.18; B=8.53; C=29.28, while for Montigel the following were found: A=90.14; B=8.66; C= 33.54.

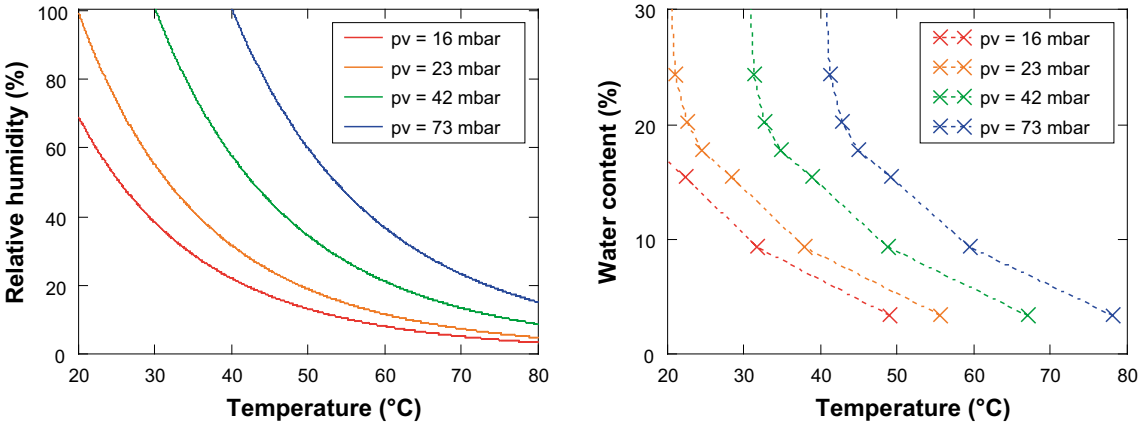

Figure 3-16. *Relations between RH and temperature (left) and water content and temperature (right) at equilibrated vapour pressures. Right graph based on water retention data for free swelling conditions and for an initial water content of 17 % (Dueck 2004).*

The difference between the free energies of water in the water-bentonite system and pure water were obtained from swelling pressure measurements, and the data could be described as a function for the influence of the water content on the following form:

$$\left(\overline{g_w} - g_w^{\circ}\right) = \exp\left(a - b \cdot w\right) \qquad (J/g) \tag{3-25}$$

For MX-80 bentonite the following parameter values were found: a=6.00 and b=17.8, while for Montigel the following were found; a=6.66 and b=18.6 (note that 1 J/g is equivalent to 1MPa for a partial specific volume of water of 10^{-3} m^3/kg) An alternative parameter set was obtained by Dueck (2007) for MX-80 with an initial water content of 10 %: a=6.3 and b=16. The following parameter values were fitted to retention data for Febex bentonite presented by Villar (2002): a=8 and b=22. All four relations are illustrated in Figure 3-17. It can be noted that the suction values presented by Kahr et al. (1990) are significantly lower than the corresponding data by Dueck (2007) and Villar (2002).

Finally, Kahr et al. (1990) provided the following relation between the enthalpy change, the difference in free energy, the absolute temperature (T), and the entropy change $(\overline{s_w} - s_w^{\circ})$:

$$\left(\overline{h_w} - h_w^{\circ}\right) = \left(\overline{g_w} - g_w^{\circ}\right) + T \cdot \left(\overline{s_w} - s_w^{\circ}\right) \tag{3-26}$$

The entropy changes are shown as functions of the water content in Figure 3-18. Both graphs are based on the original enthalpy data by Kahr et al. (1990). The left graph is also based on the original free energy data by Kahr et al. (1990). The right graph, however, is based on the retention data presented by Dueck (2007) and Villar (2002). It can be noted that the difference between the two relations (for Na- and Ca-bentonite, respectively) in the right graph appears to be smaller than the corresponding differences in the left graph.

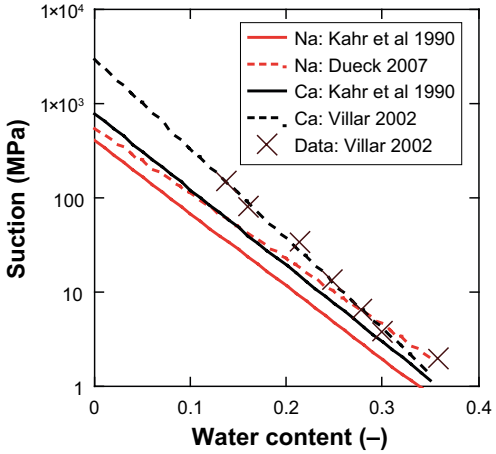

Figure 3-17. *Retention curves and experimental data (FEBEX) for unconfined conditions.*

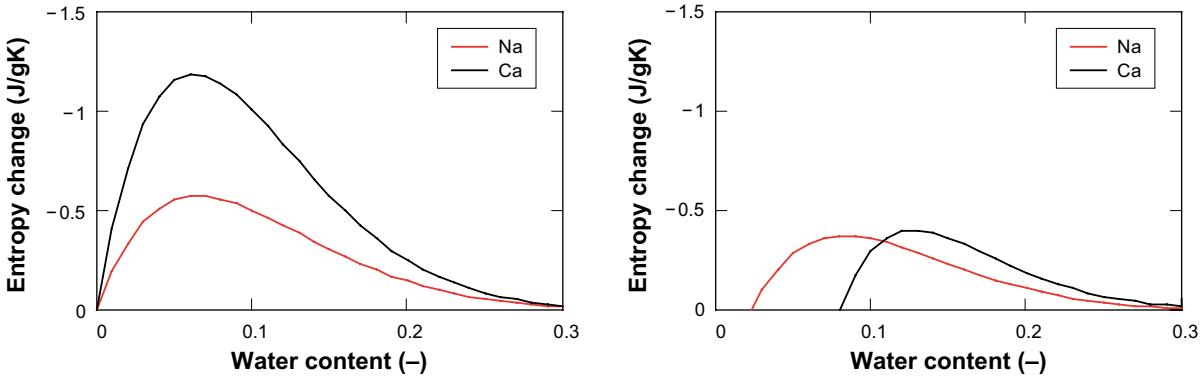

Figure 3-18. *Entropy change as a function of water content according to data by Kahr et al. (1990) (left); according to entalpy data by Kahr et al. (1990), and retention data according to Dueck (2007) and Villar (2002), respectively (right).*

The influence of the temperature on the retention properties for free swelling conditions was described by Birgersson et al. (2010) with the following expression:

$$\Psi_{free}(w,T) = \Psi_{free}(w,T_0) + \frac{\Delta s(w)\cdot\Delta T}{\nu} \qquad (3\text{-}27)$$

The entropy change $\Delta s(w) = s_{clay}(w) - s_{ref}$ corresponds to the $(\overline{s_w} - s_w^{\circ})$ described above. The temperature difference ΔT was defined as $T\text{-}T_0$. With ν is here meant the specific volume of water (10^{-3} m^3/kg) due to the used unit for Δs (J/gK) in Equation (3-26).

This description of the temperature dependence was compared with experimental retention curves for MX-80 obtained with the sorption balance technique at two different temperatures (20 and 50 °C) reported by Dueck and Nilsson (2010). Two calculations were made for each temperature: either with data solely from Kahr et al. (1990), or with enthalpy data by Kahr et al. (1990) and retention data presented by Dueck (2007). The results are shown in Figure 3-19. As expected by the entropy change data, the latter data set implies a smaller temperature dependence than the former, and this is apparently more in agreement with the experimental retention curves. Still, it should be observed that the retention curve by Dueck (2007) were obtained for an initial water content of 10 %, whereas the adsoption data by Dueck and Nilsson (2010), as well as Kahr et al. (1990) were obtained for a zero initial water content.

The relation between the suction for confined conditions and for free swelling conditions can be described:

$$\Psi_{conf}(w,T) = \Psi_{free}(w,T) - \alpha \times P \qquad (3\text{-}28)$$

Where P is the pressure and α is a compressibility factor. The value of the parameter α is usually assumed to be equal to unity, even though other values have been reported.

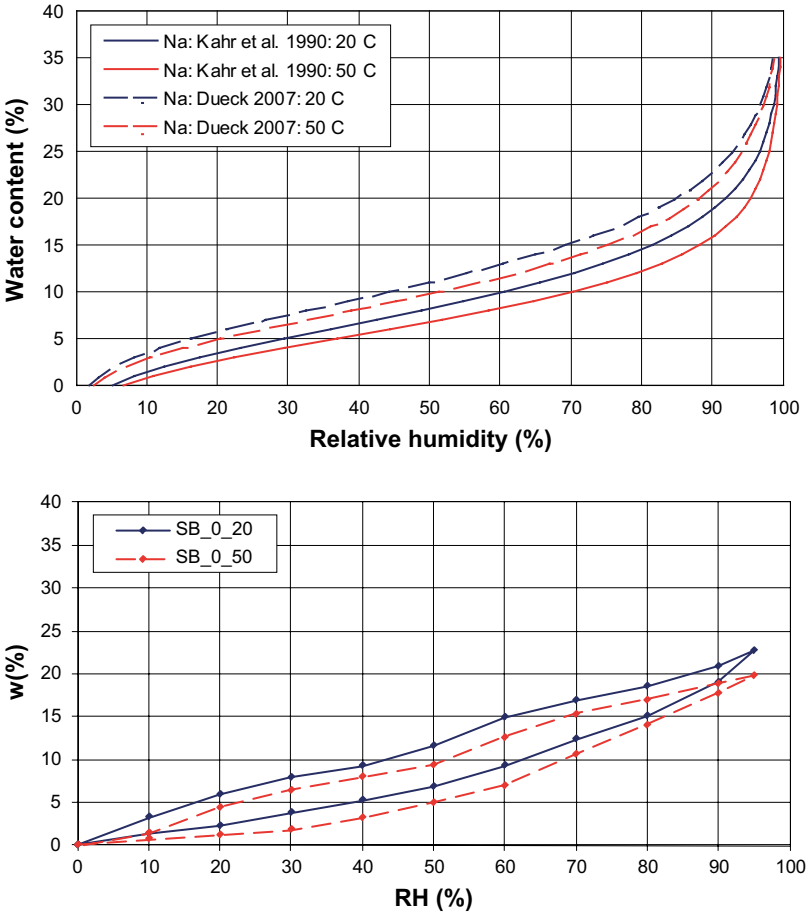

Figure 3-19. *Retention curves for MX-80 at 20 and 50 °C. Calculated with Eq (3-27) (upper graph) and determined with the sorption balance method and zero initial water content (lower graph).*

Equations (3-27) and (3-28) can be combined in order include both a temperature dependence and a pressure dependence:

$$\Psi_{conf}(w,T) = \Psi_{free}(w,T_0) + \frac{\Delta s(w)\cdot(T-T_0)}{v} - P \qquad (3\text{-}29)$$

This relation is analyzed for the case with a given pressure level (7 MPa), a zero suction value, and for temperatures between 20 and 100 °C. Such isobars are shown in Figure 3-20 for all entropy change relations shown in Figure 3-18. These relations could in principle constitute saturation profiles for which the hydration stops, and therefore corresponds to the saturation profiles in Figure 3-4 and Figure 3-8. It can be noted that the unsaturated void space would be fairly small in the cases based on the retention data by Dueck (2007) and Villar (2002), and significantly larger in the cases with the original entropy changes presented by Kahr et al. (1990).

The consequences of this effect would be even smaller for the thermal conditions in KBS-3. A typical temperature at the outer and inner radii of the canister mid-height section was 58 and 76 °C after ten years. This interval would result in a range in water content from 26.4 to 25.9 %, according to the results in Figure 3-20 for the case with Na bentonite and retention data by Dueck (2007).

Concluding remarks

The presented analysis indicates that the effects of the temperature dependence of the retention properties are very small, especially for the temperature intervals typical for KBS-3. Still, it should be observed that the presented calculations are based on measurements of enthalpies of immersion which were performed more than 25 years ago.

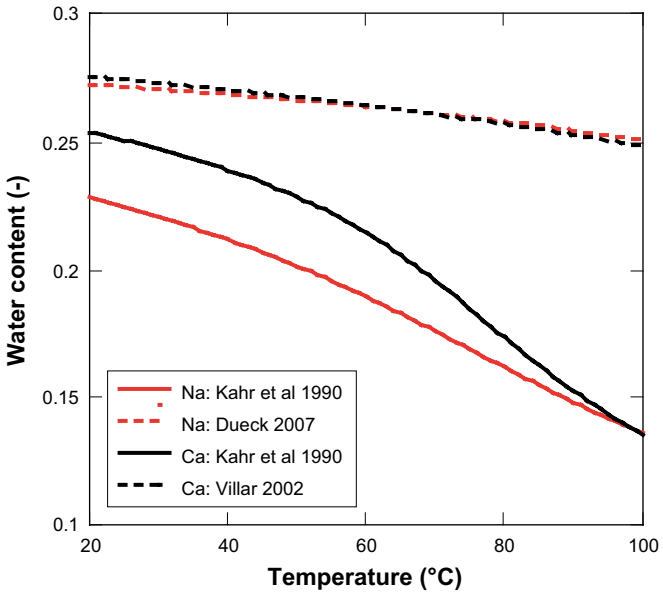

Figure 3-20. *Zero suction water content as a function of temperature at P= 7 MPa.*

4 Water uptake in the CRT experiment

Ola Kristensson, Lennart Börgesson, Clay Technology AB
Jan Hernelind, 5T Engineering AB

4.1 Introduction

The Swedish Radiation Safety Authority (SSM) requested a comparison between measured and modeled water inflow to the Canister Retrieval Test (CRT). The CRT-experiment was used as a case study when "Buffer homogenisation" was considered in Åkesson et al. (2010b, Chapter 5). SSM motivates their request by the findings reported by Benbow et al. (2012).

The study carried out regarding this subject has been divided in two sections. First, an analytical investigation is performed regarding the water uptake, where estimates are calculated under different assumptions. Thereafter follows an estimate obtained from the thermo-hydro-mechanical (THM) numerical model of the entire CRT-experiment which was described in Åkesson et al. (2010b, Chapter 5).

4.2 Analytical estimates of the water uptake

From the data in Table 4-1 and Table 4-2 together with the specified geometry an estimate of the available pore volume at installation can be calculated as shown in Appendix 1. The calculated total available pore volume, also accounting for the empty slot of 1 cm between canister and rings and a heave of the plug of 34 mm, motivated from measurements, becomes 2 264 L

Figure 4-1 shows the accumulative measured volume of artificially supplied water to the CRT-experiment. During operation, the accumulated measured filter inflow was as given by Figure 4-1 when reading the left of the scales. Thus, according to measurements, a total of 670 L was added through the filters. At installation, water was being fed into the outer pellet filled slot through tubes, which were withdrawn after usage. According to Thorsager et al. (2002) the water volume added through the tubes at installation was 950 L. The right of the scales in Figure 4-1 gives the accumulated volume of total added water, i.e. the water volume of 950 L, added at installation, is included, which ends up about 1 620 L at the end of the test. Thus, 72 % of the available pore volume was filled according to the measured and reported water volumes.

Table 4-1. Average data for buffer blocks at installation, dimensions from Thorsager et al. (2002) and other from Johannesson (2007).

Type	Dimensions [mm]	Density [kg/m^3]	Water content	Dry density [kg/m^3]	Void ratio
Cylinders	H = 504[1]	1 991	0.172	1 699	0.636
Rings	H = 510[1]	2 087	0.171	1 782	0.560
Bricks[2]	H = 123[3]	1 883	0.165	1 616	0.720

[1] The average value and an additional 3 mm representing interface volumes between blocks.
[2] The total volume including bentonite bricks, pellets, and powder.
[3] This value is obtained from subtracting the canister height from the hight of 10 rings as descibed in the table.

Table 4-2. Data for pellet filled gap at installation, from Johannesson (2007).

Type	Width [mm]	Density [kg/m^3]	Water content	Dry density [kg/m^3]	Void ratio
Pellet slot (dry)	61	1 101	0.1	1 001	1.778
Pellet slot (wet[1])	61	1 574	0.572	1 001	1.778

[1]The state when the pore volume between the pellets has been water filled.

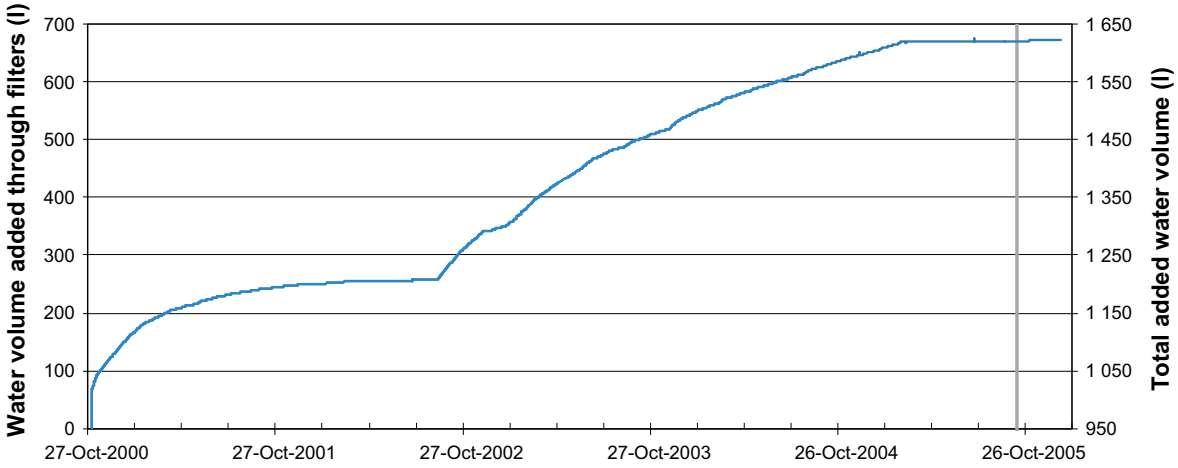

Figure 4-1. *Accumulative volume of water added through filters (left scale) and reported accumulative volume of total added water (right scale).*

If using density and water content data at installation, given in Table 4-1 and Table 4-2, and excavation (reported in Johannesson 2007) together with the specified geometry, an estimation of the added water volume may be calculated, see Appendix 1for details. An estimate of 2 036 L was obtained using the assumptions

- the heights of the blocks at excavation are similar to the estimated average block height at installation,
- the lower ring-shaped buffer blocks, R1–R5, contain the same water volume as R6, and
- the bottom buffer block, C1, contain the same water volume as C2.

The difference between the estimate and measured value is significant, 2 036–1 620 = 416 L. According to the estimate 90 % of the available pore volume was filled.

One potentially uncertain component in the total added water volume is the water volume of 950 L that was reported, (Thorsager et al. 2002), to be added when installing the pellet filled slot. If using the data in Table 4-2 together with the specified geometry, a value of 1 096 L is obtained for the available volume between the pellets, see Appendix 1for details. Also, sensor responses indicate that the open volume of 166 L between the canister and buffer rings was water filled at installation as well. If so, this gives a total volume of 1 096+166 = 1 261 L as compared to the reported 950 L. If calculating a new total added water volume based on the measured inflow from the filters and the estimated volume that was water filled (volume between pellets and the inner slot volume) we obtain 670 + 1 261 = 1 931 L which is more in line with that obtained from evaluating excavation data. According to this estimate 85 % of the available pore volume was filled.

Table 4-3 and Figure 4-2 show compilations of the discussed volumes.

Table 4-3. Compilation of the volumes discussed in the text.

Description	Volume [L]	Relative volume [%]
Estimation of available pore volume at installation	2 264	100
Water volume: Reported at pellet filling + Measured filter inflow	1 620	72
Water volume: Calculated from excavation data	2 036	90
Water volume: Calculated available “macro pore volume” in pellet filling and volume of inner slot + Measured filter inflow	1 931	85

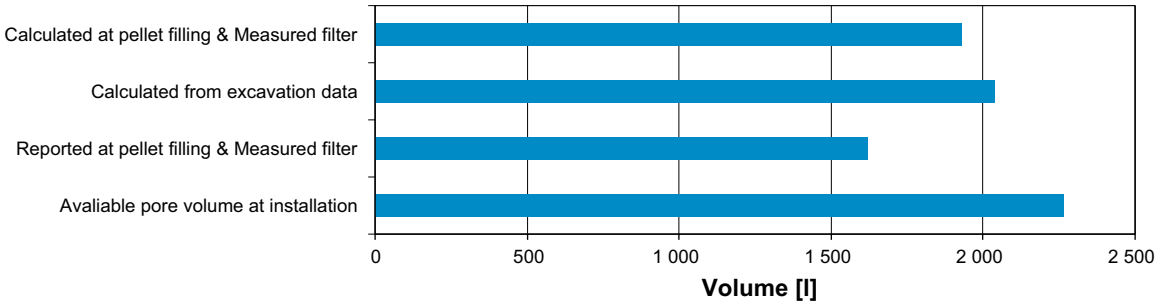

Figure 4-2. *Graphical view of the volumes discussed in the text.*

4.3 Numerical estimate of the water uptake

The THM-evolution in the Canister Retrieval Test has been modelled with both Code Bright and Abaqus (Åkesson et al. 2010b, Börgesson et al. 2016). The entire test geometry was modelled with Abaqus. The modelling included the full test time, the temperature evolution, the mechanical evolution with swelling and homogenisation of the buffer and the water uptake by the bentonite. The modelling is in detail described by Börgesson et al. (2016). The results have been compared with measured results regarding suction in the bentonite, total pressure in the bentonite and forces and displacements of the plug. The comparison showed that the agreement was rather good. Figure 4-3 shows the element model.

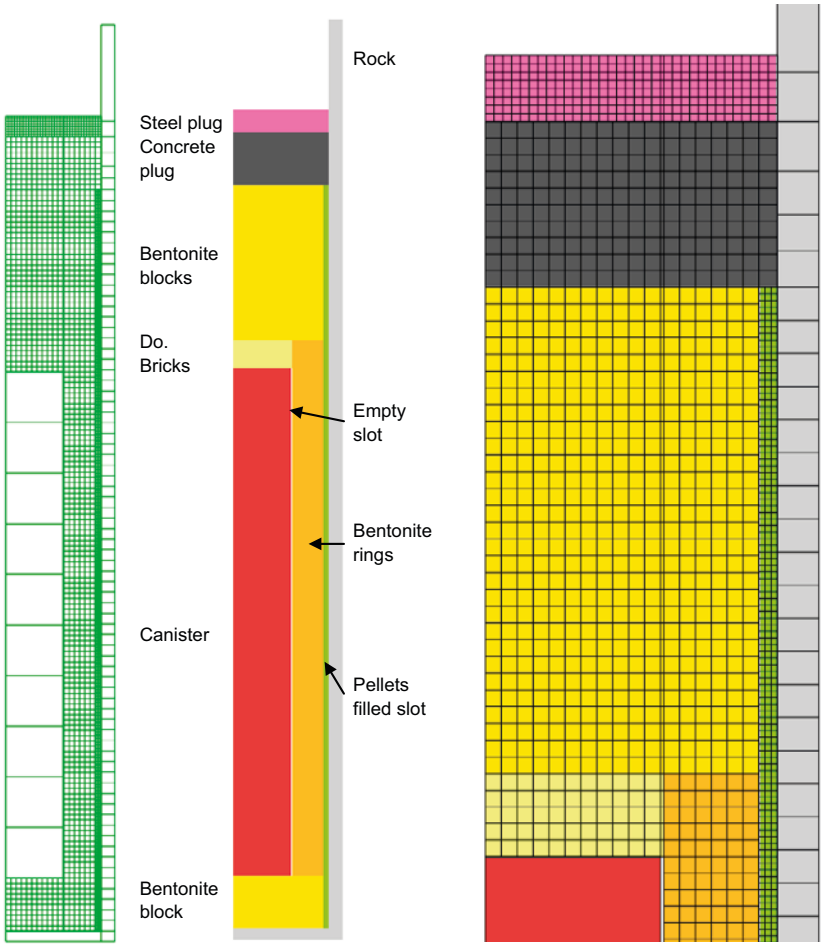

Figure 4-3. *Element mesh and property areas of the 2D model. The model is axial symmetric around the left boundary.*

An interesting comparison is the water balance of the bentonite. Does the modelled water uptake agree with the measured? Such a comparison was not done in the referred reports.

Abaqus allows for evaluation of the water flow through nodes with settled water pressure. The total water inflow from the surrounding modelled filter mats was evaluated and plotted as function of time. Figure 4-4 shows a comparison between modelled and measured inflow into the filter mats.

As seen in Figure 4-4 the agreement at the end of the test is surprisingly good. However, the history paths do not have the same nice agreement. The measured inflow rate is much lower in the beginning of the test and after about 680 days the inflow has almost stopped. The water pressure applied to the filter was up to that day limited to one meter water head above the floor of the installation drift i.e. about 50 kPa in the centre of the test hole. After 680 days the water pressure was increased to 800 kPa and the result is seen in Figure 4-4 as a strong increase in measured water inflow rate. An interesting question is why the inflow almost stopped before increasing the water pressure. The most probable explanation is that the supply of water into the filter mats was not sufficient in order keep the filter mats water saturated. Flow tests in order to flush the filter mats showed that the connectivity was for some mats rather poor unless high water pressure was applied. When after 680 days the water pressure was increased to 800 kPa the supply of water was sufficient in order to keep the filter mats water saturated and thus meet the demand of the bentonite.

If the modelled inflow is adjusted so that the measured delay caused by insufficient water supply is taken into account we get the comparison shown in Figure 4-5.

The adjustment is simply made by a parallel displacement of the modelled inflow at the total volume 260 L with about 590 days. In this way the modelled inflow restarts at the same inflow value as the measured when the filter was cleaned and the water pressure applied. This is of course not completely correct since the delay should lead to that the actual water distribution in the blocks have equalized more than in the model, which in turn should mean a slower water uptake rate in the model. This is not seen until very late when the model underestimates the water uptake rate.

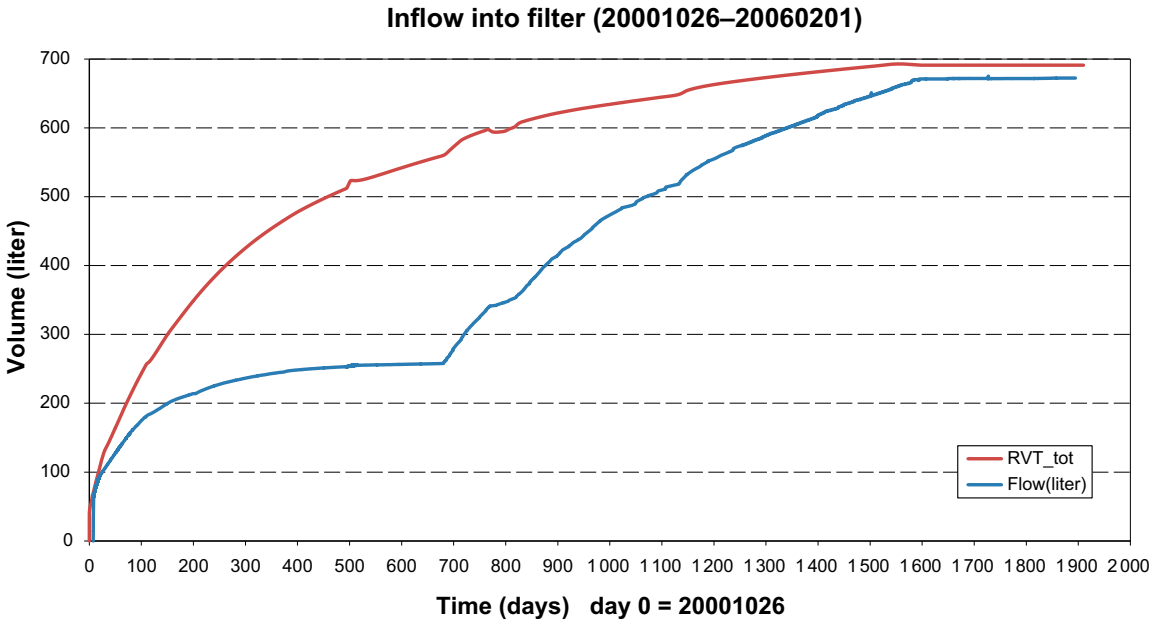

Figure 4-4. *Modelled (red line) and measured (blue line) water inflow into the CRT test hole.*

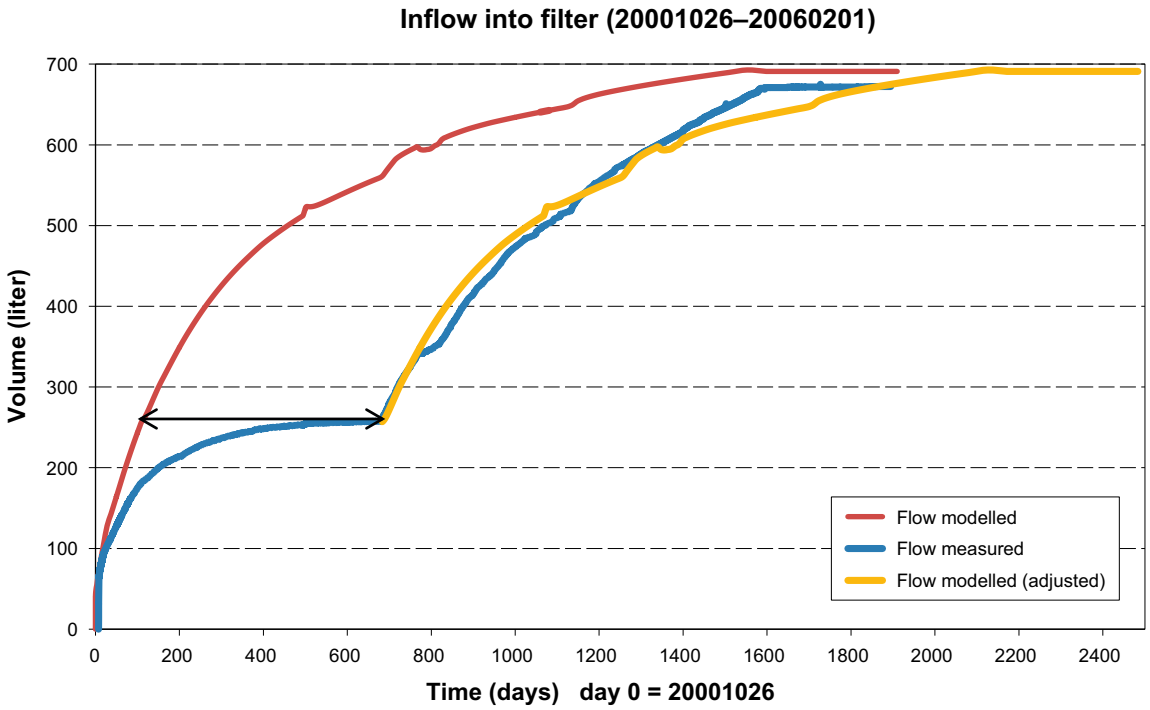

Figure 4-5. *Modelled (red line) and measured (blue line) water inflow into the CRT test hole and the modelled inflow adjusted for the insufficient water supply (yellow).*

Another interesting question is if the measured water inflow corresponds to the actual supply of water to the filters or if any water has been lost to the rock or taken up from the rock. The volumes illustrated in Figure 4-2 show that the water taken up by the bentonite calculated from the excavation data is higher or in fair agreement with the estimates done from the inflow measurements depending on if the measured volume of water filling or the calculated volume available for water filling is used. This shows that it is not probable that any water has been lost to the rock in spite of the high water pressure applied in the mats. On the other hand, the lack of available water during the first 680 days before the water pressure increase shows that it is neither probable that there is any water inflow from the rock. The rock thus seems to be very tight which is confirmed by the inflow measurements into the test hole before installation when no inflow actually could be measured. In addition, the filter mats were fastened on cement levelling that was applied on the rock wall, which hindered water exchange between the rock and the filters.

Another fact that could influence the water uptake is that the filter strips only covered parts of the rock wall surface. 10 cm wide filter strips were attached vertically with 26 cm distance. The effect of this was investigated in a pre-study. The results showed that there is an influence on the water uptake rate of the buffer, but it is rather small in comparison with if the entire surface was covered with filter (Börgesson et al. 1999). A decrease in distance between the 10 cm wide strips from the actual 26 cm to 8 cm reduced the time to saturation with 5–10 %. There is thus an overestimation in the modelled water uptake rate with about 15 % due to the strip effect. In addition to this effect, the restricted water supply during the first 680 days was not included in the model. If this restriction had been included in the modelling the predicted water inflow would have been lower as shown in Figure 4-5. It is thus probable that the model underestimates the water uptake rate of the buffer. This conclusion is also supported by the measured inflow rate, which at the end of the water supply period (after 1 600 days) is higher than the modelled since the inclination dV/dt is larger.

Summing up all the information given above the conclusion is that the water uptake models seem to slightly underestimate the water uptake rate of the buffer and that there is no indication of any buffer processes not taken into account by the models that delay the water saturation rate.

5 Description of how the CRT-model was used and how THM and TH models differ in terms of analyzing the hydration process

Ola Kristensson, Clay Technology AB

5.1 Introduction

The Swedish Radiation Safety Authority (SSM) requested a description of how the "CRT-model" was used in the study described in Åkesson et al. (2010b, Section 3.4) and how thermo-hydraulic (TH) models and thermo-hydro-mechanical (THM) models differ in terms of the water saturation process.

These notes first briefly describe general differences that may affect the water saturation process between TH and THM models expressed in the "Code_Bright formulation". There after follows a description of the "CRT-model" which also serves as a specific case describing how responses of TH and THM models differ.

5.2 Differences in water saturation process using a TH and THM formulation

Describing the hydraulics' dependency on mechanics in general, for the Code_Bright formulation used in Åkesson et al. (2010b, Section 3.4), following statements, taken from the Code_Bright user's manual (UPC 2012), are instructive:

- Water storage: Changes in porosity affect the available volume for water.
- Liquid water transport: Changes in porosity affect the hydraulic conductivity.
- Gaseous water (vapour) transport: Changes in porosity affect the vapour diffusion coefficient.

Furthermore, if using a possibility present in Code_Bright, letting the function expressing the water retention properties, here denoted by $\widetilde{S}_l$, include a dependency on porosity, n, i.e.

$$S_l = \widetilde{S}_l(P_g - P_l, n),$$

additional mechanical dependencies to the ones listed above become activated. This feature was, however, not utilized in Åkesson et al. (2010b, Section 3.4), but is never the less considered highly relevant for our systems and therefore here discussed. So, with $\widetilde{S}_l$ dependent on porosity, changes in porosity of course affect the degree of water saturation directly. In addition, the degree of water saturation is also included in the water storage capacity and vapour diffusion coefficient which then will be affected indirectly by changes in porosity through the presence of degree of water saturation.

5.3 Description of the usage of the "CRT-model"

Turning towards describing the "CRT-model", it should be mentioned that CRT is an abbreviation of Canister Retrieval Test, an experiment realized at the Äspö Hard Rock Laboratory in Sweden. In Section 5.4 of Åkesson et al. (2010b), regarding "Buffer homogenisation", CRT was used as a case for which the homogenization process was studied by performing plane axisymmetrical THM simulations. The model regarded most representative was denoted CRT 6b.

In Section 3.4 of Åkesson et al. (2010b) model CRT 6b was recycled, but in an attempt to facilitate readability somewhat, it was now called THM CRT, since TH versions (TH CRT I and TH CRT H) without the mechanics also were used, as described below. This information, about the connection between CRT 6b and THM CRT, was unfortunately missing in Åkesson et al. (2010b). Detailed information about model THM CRT can be found in Åkesson et al. (2010b, Section 5.4).

With that said, we turn to describing the actual purpose for using the THM model of CRT in Section 3.4 of Åkesson et al. (2010). The analysis in Åkesson et al. (2010b, Section 3.4), where the CRT-model was utilized, served as motivation for being able to use two global TH-models with different "immobile mechanical representations", i.e. different density distributions, rather than performing one full global THM-simulation, and still being able to consider effects from the homogenization process. Performing detailed coupled THM-simulations on a global scale can be very challenging in terms of computational demand and numerical stability and that is why it was desirable to use two TH-models with different immobile mechanical representations at the global scale to circumvent these issues.

The strength of the coupling between TH and M in the buffer materials cannot be said to be insignificant, most parameters have some dependency on density (porosity), and therefore, the pair of two extreme immobile mechanical representations are used to account for this dependency. As mentioned, the immobile mechanical representations are represented by two extreme density fields, either equal to the *Initial* state as obtained at installation or a fully *Homogenized* state, i.e. the pellet slot density equals that of the buffer block.

The conceptual idea behind the model setup in the study within Section 3.4 of Åkesson et al. (2010b) is schematically described in Figure 5-1. In a deposition hole buffer, present at a *global* scale, THM-processes in a disc at canister mid-height (visualized to the left of the hatched vertical line in Figure 5-1) are considered to be sufficiently accurate represented by a plane axisymmetric model at a *local* scale (visualized to the right of the hatched vertical line in Figure 5-1). For this to be true the boundary conditions prescribed on the local model have to be representative for the processes on the global scale.

The most general of the three local representations used in the analysis is the THM CRT model where the homogenization process is simulated, as indicated in Figure 5-1. TH parameters/variables may thereby vary with the mechanical process and this may significantly affect the TH-process.

The two TH-models, indicated by the top and bottom schematic geometries in Figure 5-1, are obtained from either using the initial state density field, as in model TH CRT I, or a density field where full homogenization of the buffer has been assumed, as in model TH CRT H. Note that the fully homogenized state most likely differs from the final state obtained at full saturation as indicated in Figure 5-1. Thus, full homogenization cannot generally be assumed for a fully water saturated state.

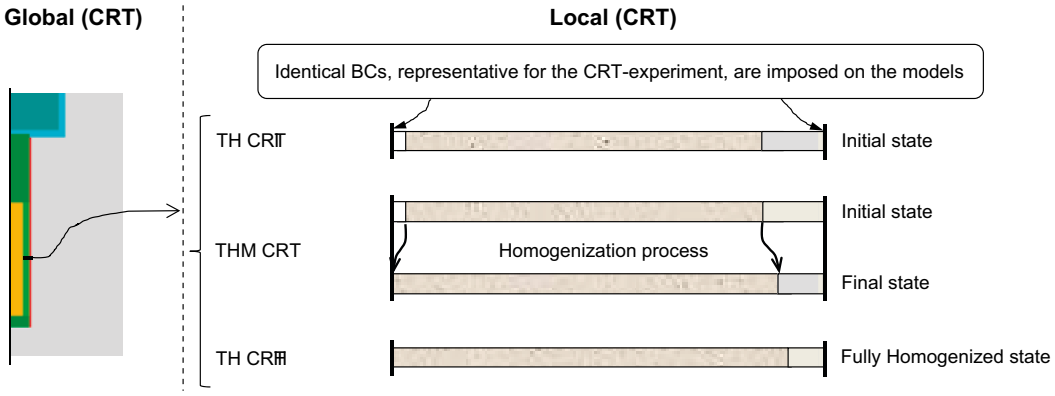

Figure 5-1. *Schematic description of the relation between models used in Section 3.4 of Åkesson et al. (2010b). An imagined global model of the CRT-experiment is visualized to the left. To the right three local models, representing an axisymmetric disc at canister mid-height of the global model, are visualized. The local models are, from top to bottom, TH CRT I(nitial), THM CRT, and TH CRT H(omogenized). To the right of the schematic geometries of the local models the states considered are indicated. When using the THM-model the effect from the homogenization process is considered directly. When using the pair of TH-models and evaluating their responses together, an indirect consideration of the homogenization is possible.*

Figure 3-9 in Åkesson et al. (2010b) is repeated below in Figure 5-2. It shows water saturation histories at three radial positions (r = 585, 685 and 785 mm) for the THM-model and the two TH-models. As can be seen, in the studied example, the THM responses are "bounded" by the responses of the TH-simulations. There is a significant difference between the THM and the TH-models, in this special case most so for the TH-model with the homogenized mechanical assumption. With the notation used in the legends in Figure 5-2 the relation between the saturation times, t_{sat}, of the models can be expressed,

t_{sat} (TH CRT Initial) < t_{sat} (THM CRT) < t_{sat} (TH CRT Homogenized),

which in Åkesson et al. (2010b) were taken as motivation for being able to use two global TH-models with different immobile mechanical representations, with saturation times bounding the THM-model's saturation time.

It should also be mentioned that the comparison of the three CRT models described above was not considered totally fair towards the homogenized TH-model. In Section 3.4.2 in Åkesson et al. (2010) the CRT models were altered somewhat to make them more comparable and as a result, both TH-models' saturation times became closer to what the THM-model produced.

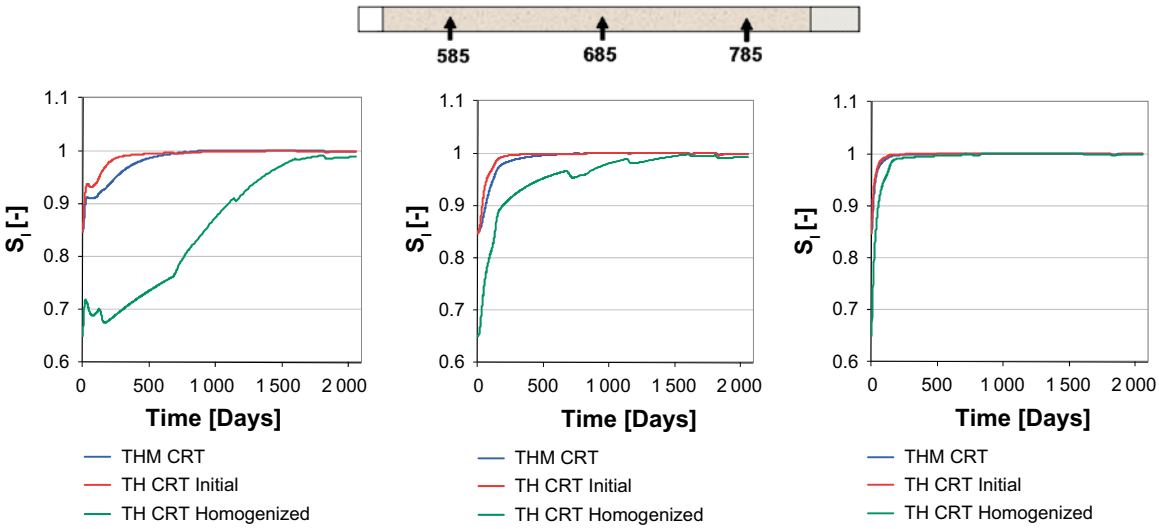

Figure 5-2. *Water saturation evolution at three different radii (585, 685 and 785 mm), Figure 3-9 in Åkesson et al. (2010b).*

6 Bentonites other than MX-80

Mattias Åkesson, Clay Technology AB, Lund, Sweden

6.1 Introduction

6.1.1 Background

SKB has been asked to comment the fact that different bentonite types may be more or less favourable in the perspective of the resaturation phase.

6.1.2 Scope

The aim of this analysis was: i) to present the available data concerning hydro-mechanical properties for bentonites other than MX-80; and ii) to evaluate whether these properties can lead to other modelling results than those which were presented in SR-Site.

With available data is primarily meant results from measurement of hydraulic conductivity, swelling pressure, retention properties and from water uptake tests. In addition, data on thermal conductivity and some results from homogenization test are also included in the presentation. With bentonites other than MX-80 is primarily meant Deponit Ca-N, Ibeco RWC BF, Asha, Friedland and Febex. A compilation of sources of hydro-mechanical data for different bentonites is shown in Table 3-2.

A simple way to estimate the water-uptake capacity for different materials is to evaluate the moisture diffusivity from water uptake tests. Moisture diffusivities can also be evaluated from hydraulic conductivity values and retention properties. The consistency between different data sets can in this way be corroborated, while the material model can be verified from independent measurements.

Table 6-1. Sources of hydro-mechanical data for different bentonites.

Bentonite	Hydraulic conductivity	Swelling pressure	Retention properties	Water-uptake test	Thermal cond.	Homogen. test*
MX-80	Relation: TR-10-44	Relation: TR-10-44	TR-10-55 Dueck 2004	IPR-01-34	Relations: TR-10-44	–
Deponit Ca-N	TR-06-30 TR-11-06	TR-06-30 TR-11-06	–	–	–	–
Asha	TR-06-30 TR-11-06 R-13-08	TR-06-30 TR-11-06 R-13-08	R-08-136	R-08-136	–	–
Ibeco RWC BF	R-10-44 R-13-08	R-10-44 R-13-08	R-10-44	R-10-44	–	R-10-44
Friedland	TR-06-30 R-08-136	TR-06-30 R-08-136	R-08-136	R-08-136	–	R-08-136
Febex	Villar 2002	Villar 2002	Villar 2002	This study	Villar 2002	–

* Tests with same material for block and pellets.

6.2 Hydraulic conductivity

Hydraulic conductivity data for different materials have been reported from a number of studies: Karnland et al. (2006) (TR-06-30) presented results for a large number of bentonites, among which the data for Friedland, Deponit Ca-N and Asha (Kutch) are of interest in this study; Johannesson et al. (2010) (R-10-44) presented results for Ibeco RWC BF; Svensson et al. (2011) (TR-11-06) presented results for reference material of Asha and Deponit Ca-N; Sandén et al. (2014) (R-13-08) presented results for Ibeco RWC BF and Asha (two different shipments); finally, Villar (2002) presented results for Febex. All data from these analyses (dry density higher than 1 000 kg/m^3) are compiled in Figure 6-1.

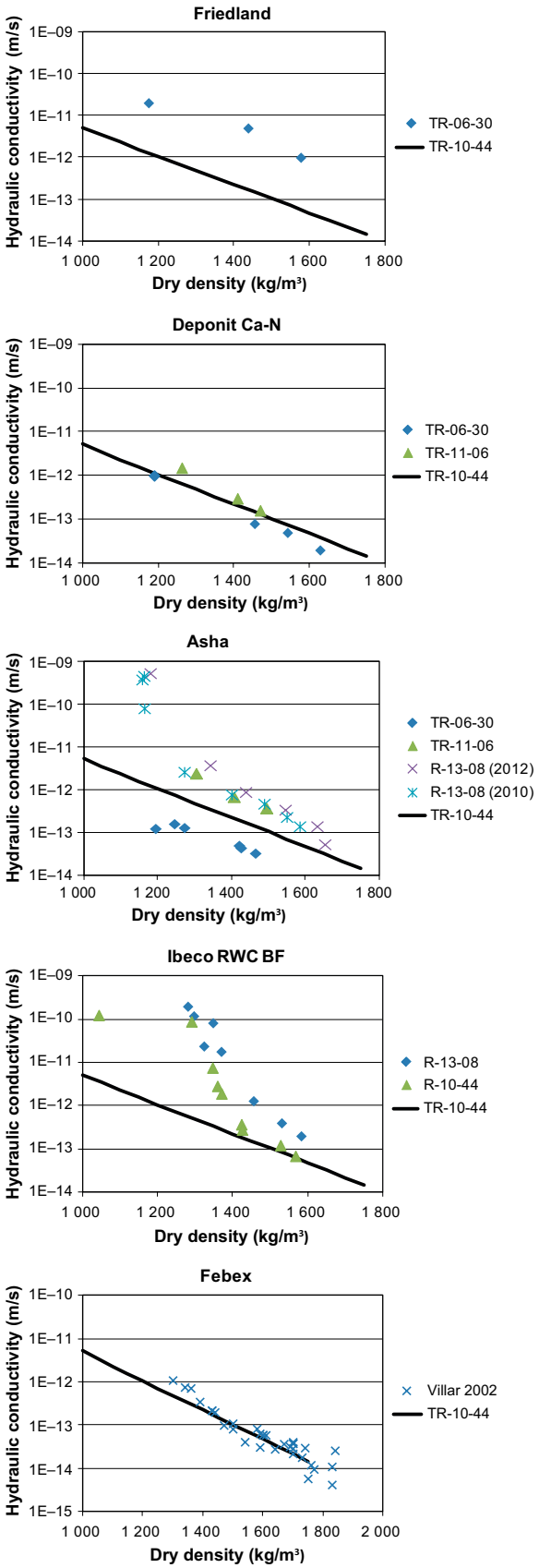

Figure 6-1. *Hydraulic conductivity data for different materials. A relation adopted for MX-80 data (marked TR-10-44) is shown for comparison.*

A relation adopted for MX-80 data by Åkesson et al. (2010a) is shown for comparison. For a dry density level of 1 500–1 600 kg/m^3 the following approximate observations can be made:

- For Friedland material, the hydraulic conductivity values were more than one order of magnitude higher than for MX-80;
- For Asha (in three different studies) and for Ibeco RWC BF (in one study), the hydraulic conductivity values were 2–3 times higher than for MX-80;
- Deponit Ca-N, Ibeco RWC BF (in one study) and Febex material displayed approximately the same hydraulic conductivity values as MX-80;
- Finally for Asha (in one study) the hydraulic conductivity values were 2–3 times lower than for MX-80.

6.3 Swelling pressure

Swelling pressure data for different materials have been reported from a number of studies: Karnland et al. (2006) (TR-06-30) presented results for a large number of bentonites, among which the data for Friedland, Deponit Ca-N and Asha (Kutch) are of interest in this study; Johannesson et al. (2010) (R-10-44) presented results for Ibeco RWC BF; Svensson et al. (2011) (TR-11-06) presented results for reference material of Asha and Deponit Ca-N; Sandén et al. (2014) (R-13-08) presented results for Ibeco RWC BF and Asha (two different shipments); Johannesson and Börgesson 2002 (IPR-02-50) presented results from oedometer tests on Friedland; finally, Villar (2002) presented results for Febex. All data from these analyses (dry density higher than 1 000 kg/m^3) is compiled in Figure 6-2. A relation adopted for MX-80 data by Åkesson et al. (2010a) is shown for comparison. For a dry density level of 1 500–1 600 kg/m^3 the following approximate observations can be made:

- For Friedland material, the swelling pressure values were one order of magnitude lower than for MX-80;
- For Ibeco RWC BF (in one study), the swelling pressure values were 2–3 time lower than for MX-80;
- Asha (in three different studies), Deponit Ca-N, Ibeco RWC BF(in one study) and Febex material displayed approximately the same swelling pressure values as MX-80;
- Finally for Asha (in one study), the swelling pressure values were 2–3 times higher than for MX-80.

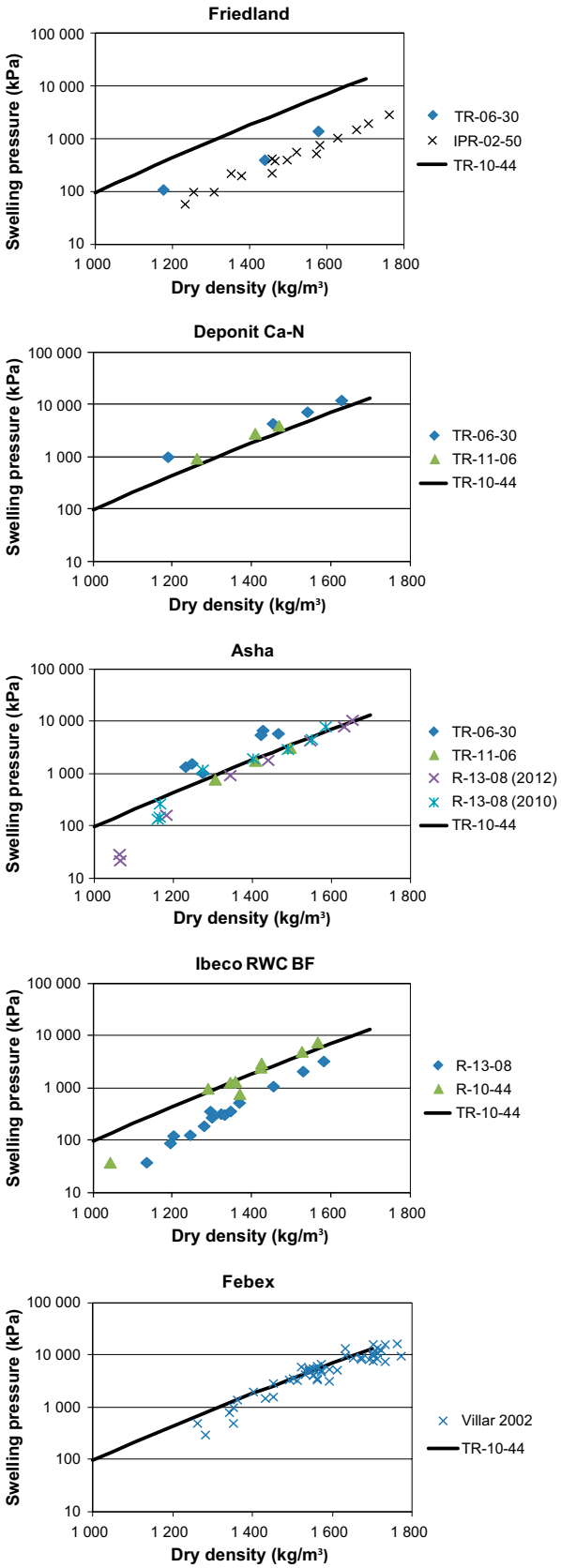

Figure 6-2. *Swelling pressure data for different materials. A relation adopted for MX-80 data (marked TR-10-44) is shown for comparison.*

6.4 Retention properties

Water retention data for different materials have been reported from a number of studies: Johannesson et al. (2008) (R-08-136) presented results for Asha and Friedland; Johannesson et al. (2010) (R-10-44) presented results for Ibeco RWC BF; finally, Villar (2002) presented results for Febex. All data from these analyses, i.e. water content versus relative humidity (RH), are compiled in Figure 6-3. In addition, two sets of data for MX-80, presented by Dueck and Nilsson (2010) (TR-10-55) and Dueck (2004) are shown for comparison.

For an approximate level of water content of 17 % the following observations can be made:

- Febex, Asha & Ibeco RWC BF equilibrate at a lower RH than MX-80.
- Friedland equilibrates at a higher RH than MX-80.

For an approximate level of water content of 25 % the following observations can be made:

- Asha equilibrates at a lower RH than MX-80.
- Febex and Ibeco RWC BF equilibrate at approximately the same RH as MX-80.
- Friedland equilibrates at a higher RH than MX-80.

6.5 Water uptake tests

Water uptake tests have been reported from a number of studies: Börgesson (2001) (IPR-01-34) presented results for MX-80; Johannesson et al. (2008) (R-08-136) presented results for Asha and Friedland; and Johannesson et al. (2010) (R-10-44) presented results for Ibeco RWC BF. Results from these tests are compiled in Figure 6-4 to Figure 6-6. Finally, two water uptake tests were performed on Febex benonite within this study, see Appendix 2. An evaluation of the results from all the tests is presented in Section 6.7.

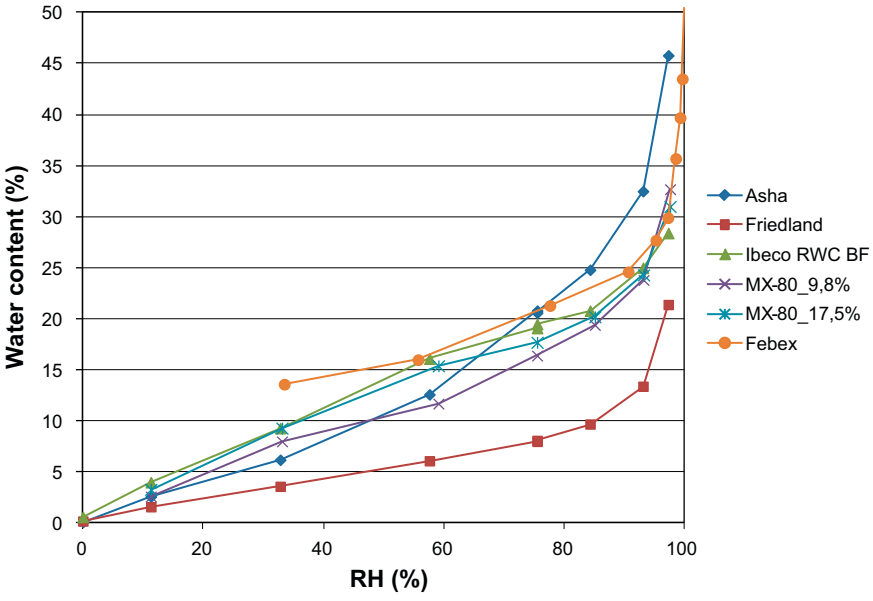

Figure 6-3. *Retention data for different materials.*

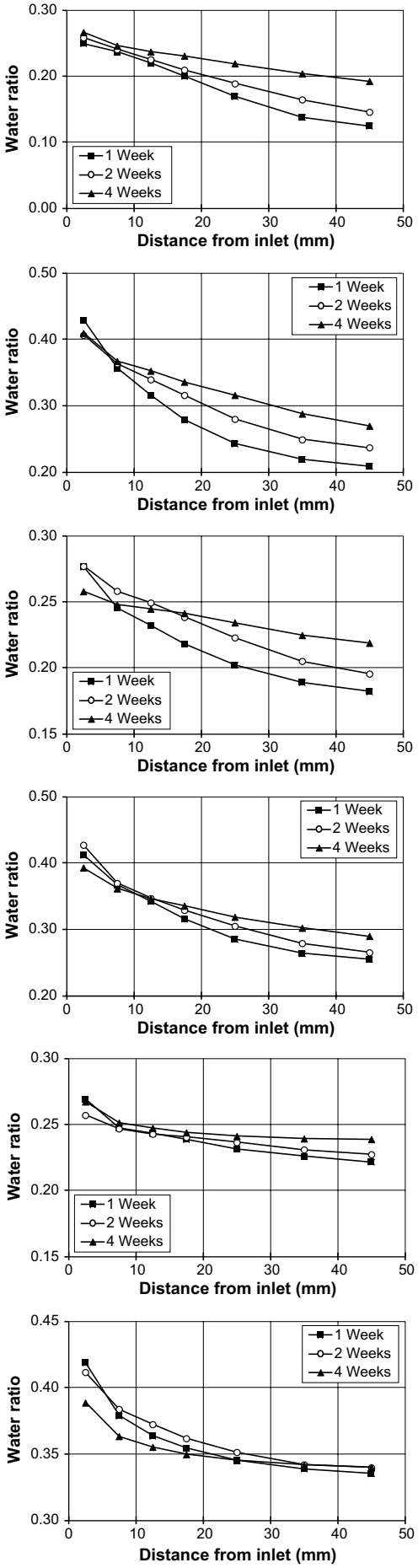

Figure 6-4. *Water-uptake tests: MX-80.*

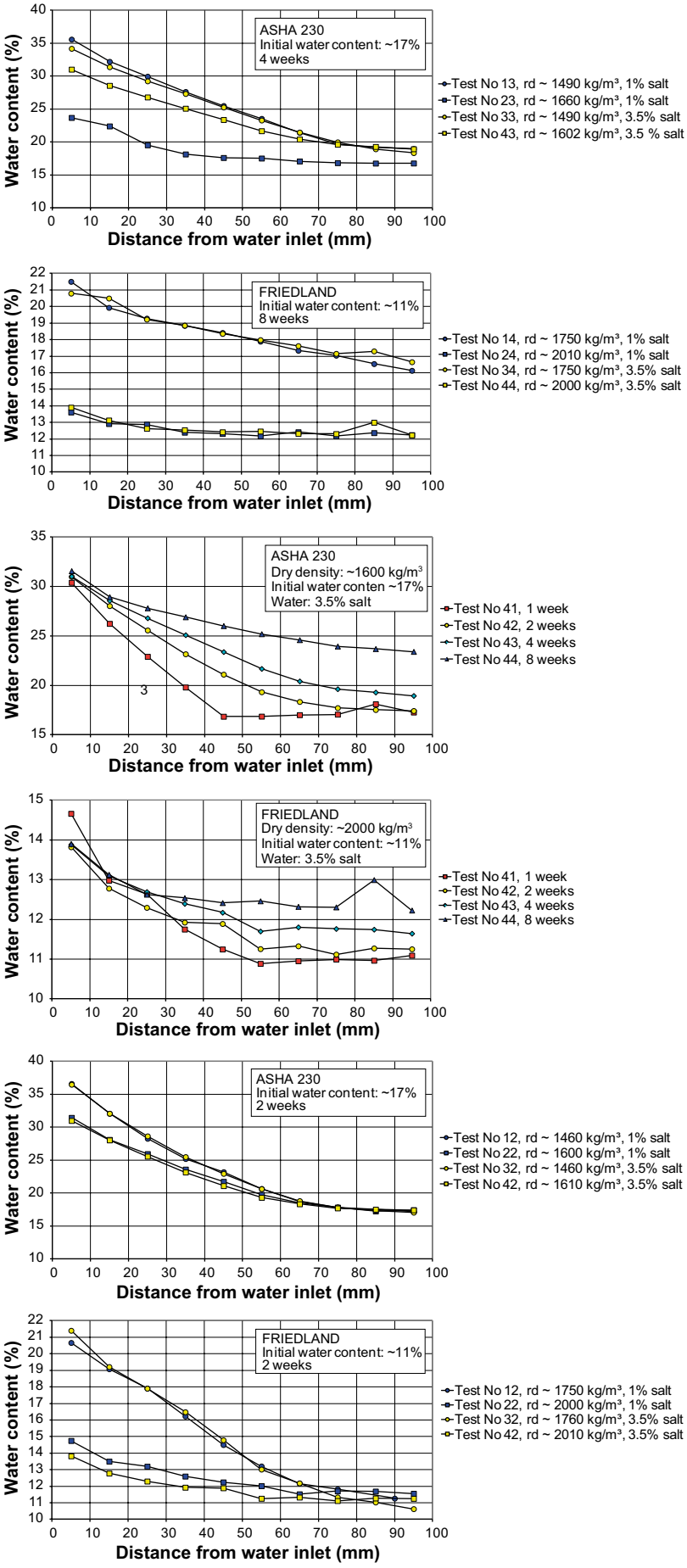

Figure 6-5. *Water-uptake tests: Asha (left); Friedland (right).*

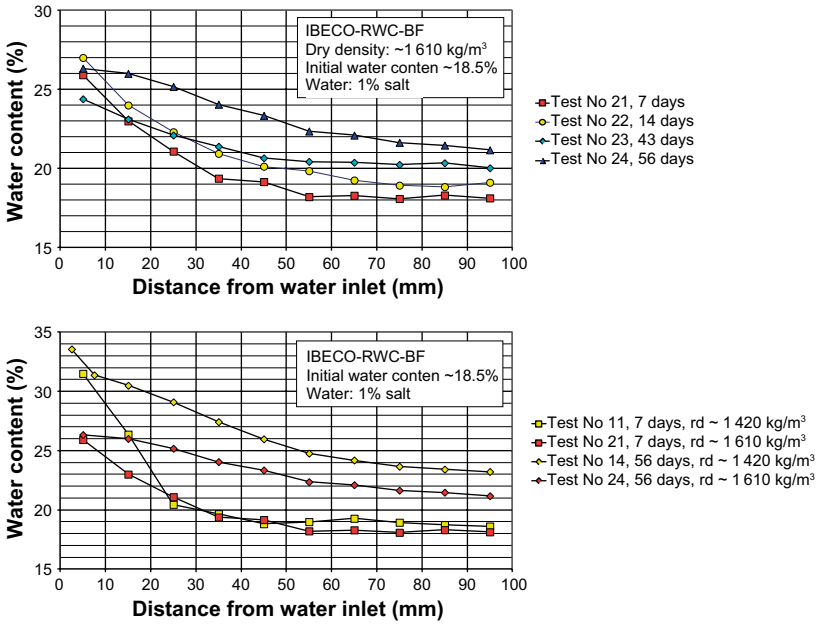

Figure 6-6. *Water-uptake tests: Ibeco RWC BF.*

6.6 Thermal conductivity

Thermal conductivity data has been reported from measurements performed by Villar (2002) on Febex bentonite. The data from this analysis is compiled in Figure 6-7 as a function of the degree of saturation. Three different relations adopted for MX-80 data by Åkesson et al. (2010a) are shown for comparison. The Febex data are generally quite similar to the MX-80 data relations, although the relations tend to overestimate the thermal conductivity at mid- saturation range, and underestimate the thermal conductivity at low saturation degrees.

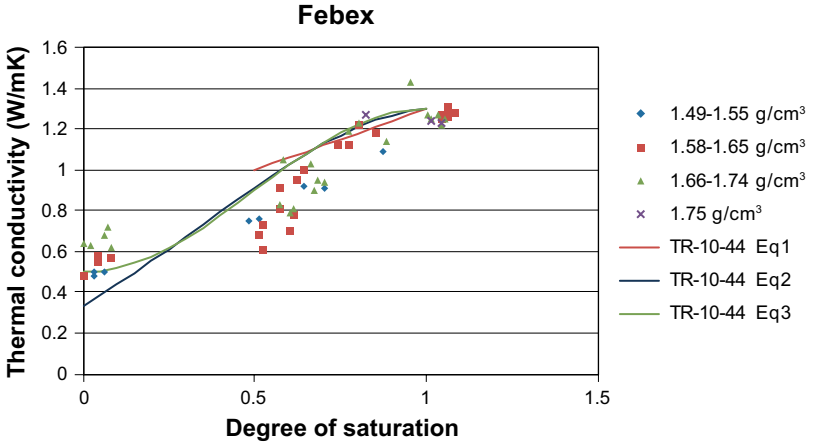

Figure 6-7. *Thermal conductivity. Adopted functions for MX-80 (lines) and experimental data for Febex (symbols).*

6.7 Evaluation of hydraulic properties

6.7.1 Diffusivity evaluation from water-uptake tests

Diffusivity (D) values were evaluated from the water-uptake tests presented in Section 6.5 and Appendix 2. Each evaluation was based on three different water contents (Figure 6-8, left): initial value (w_i), boundary value (w_f), and temporal value (w_x) at a specified time and coordinate. The initial value was generally measured with adequate precision. Different approaches can be applied for the boundary value, such as the calculated from the average dry density of the specimen, or from the measured water content in the sample adjacent to the water inlet. The latter approach was applied in this analysis. The temporal value was based on one specific measurement.

The evaluations were based on an analytical solution for diffusion in a plane sheet (Crank 1975):

$$\frac{w-w_i}{w_f-w_i}=1-\frac{4}{\pi}\sum_{n=0}^{\infty}\frac{(-1)^n}{2n+1}\exp\left\{-D(2n+1)^2\frac{\pi^2 t}{4l^2}\right\}\cos\frac{(2n+1)\pi x}{2l} \qquad (6\text{-}1)$$

where t is the time, l is the length of the specimen, and x is the distance from the hydrated boundary, and a diffusivity value was sought with this function for each set of specified water contents. In order to optimize the precision, the samples used for the temporal values (w_x) were chosen as distant as possible from the hydrated boundary. Moreover, only tests for which the increase in water content (w_x–w_i) exceeded 1 % were included in the evaluation. This was thus a very simple evaluation technique, which yielded only one constant D value from each test.

Evaluated moisture diffusivity values are plotted versus the temporal water contents (w_x) in Figure 6-8 (right). It can be noted that the evaluated diffusivity values are well-defined and display a fairly small variability. The values for Friedland ($6.5–8.4\times10^{-10}$ m^2/s) are clearly higher than all the other materials, whereas the values for and Asha, Febex and to some extent also Ibeco RWC BF ($5.1–6.7\times10^{-10}$ m^2/s) is higher than MX-80 at e=0.7 ($3.6–5.3\times10^{-10}$ m^2/s).

The diffusivity values from tests performed on specimen with high density MX-80 (e=0.7) exhibit an increasing trend for increasing water content, which is consistent with other studies (Kahr et al. 1986). However, tests performed on low density MX-80 specimen (e=1.0) rather indicate that the diffusivity value tends to decrease at increasing water contents. Similar trends were found in a theoretical analysis of moisture diffusivities for unsaturated conditions (Chapter 9).

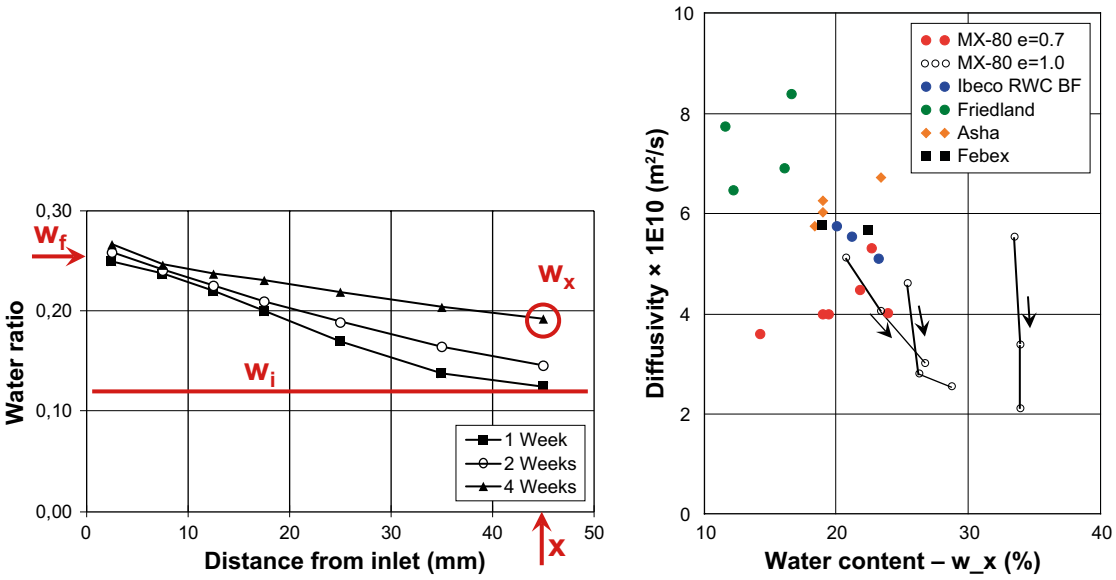

Figure 6-8. *Water-uptake tests (left); evaluated diffusivity values (right).*

6.7.2 Diffusivity evaluation from hydraulic conductivity and initial RH

The moisture diffusivity can be evaluated as a function of the saturation degree from the intrinsic permeability, k, the relative permeability relation, $k_r(S_l)$, the derivative of the retention curve, dP_l/dS_l, a homogenous porosity, n, and the water viscosity, μ:

$$D(S_l) = \frac{k \cdot k_r(S_l)}{n \cdot \mu} \cdot \frac{dP_l}{dS_l} \qquad (m^2/s) \tag{6-2}$$

A commonly used type of retention curve is the van Genuchten function:

$$S_l(P_l) = \left(1 + \left(\frac{P_g - P_l}{P_0} \right)^{\frac{1}{1-\lambda}} \right)^{-\lambda} \tag{6-3}$$

Two such curves were adopted for backfill blocks (Åkesson et al. 2010a) and were subsequently used for hydration calculations and evaluations of moisture diffusivity functions (Åkesson et al. 2010b), see Base case and Modified case in Figure 6-9. An alternative retention curve is the square law:

$$S_l(P_l) = \frac{1}{\sqrt{1 + \frac{P_g - P_l}{P_0}}} \tag{6-4}$$

This function is implemented in Code_Bright, and in combination with the cubic power law for the relative permeability it implies a *constant diffusivity value*. Such a curve is illustrated in Figure 6-9 with the same initial point as for the backfill blocks. It can be noted that the square law only has one parameter and that this is specified as soon as the initial point is defined.

The inverse function of square law can be expressed as:

$$P_l(S_l) = P_g - P_0 \cdot \left(\frac{1}{{S_l}^2} - 1 \right) \tag{6-5}$$

The derivative of this function is simply:

$$\frac{dP_l}{dS_l} = \frac{2P_0}{{S_l}^3} \tag{6-6}$$

The sole parameter P_0 is specified from the initial point (ψ_{init}, S_{init}):

$$P_0 = \frac{P_g - P_l}{\frac{1}{{S_l}^2} - 1} = \frac{\psi_{init}}{\frac{1}{{S_{init}}^2} - 1} \tag{6-7}$$

The expressions for the derivative (6-6) and the parameter (6-7) can be substituted in the evaluation of diffusivity (6-1):

$$D = \frac{k \cdot {S_l}^3}{n \cdot \mu} \cdot \frac{2P_0}{{S_l}^3} = \frac{2k}{n \cdot \mu} \cdot \frac{\psi_{init}}{\frac{1}{{S_{init}}^2} - 1} \tag{6-8}$$

This can be rearranged as a relation between the hydraulic conductivity (K) and the initial RH for different D values:

$$K(RH_{init}) = \frac{\rho g}{\mu} \cdot k = \frac{\rho g \cdot n \cdot D}{2 \cdot \psi(RH_{init})} \cdot \left(\frac{1}{{S_{init}}^2} - 1 \right) \tag{6-9}$$

where Ψ(RH) denotes Kelvin's psychrometric law. This function is illustrated in Figure 6-10 which was prepared for the properties of backfill blocks according to Åkesson et al. (2010a). The graphs were made for an initial water content of 17 % and a dry density of 1 700 kg/m^3. An initial RH of 71 % and a hydraulic conductivity of 2×10^{-14} m/s correspond to a diffusivity of 6×10^{-10} m^2/s, which is exactly the same result as in Figure 6-9.

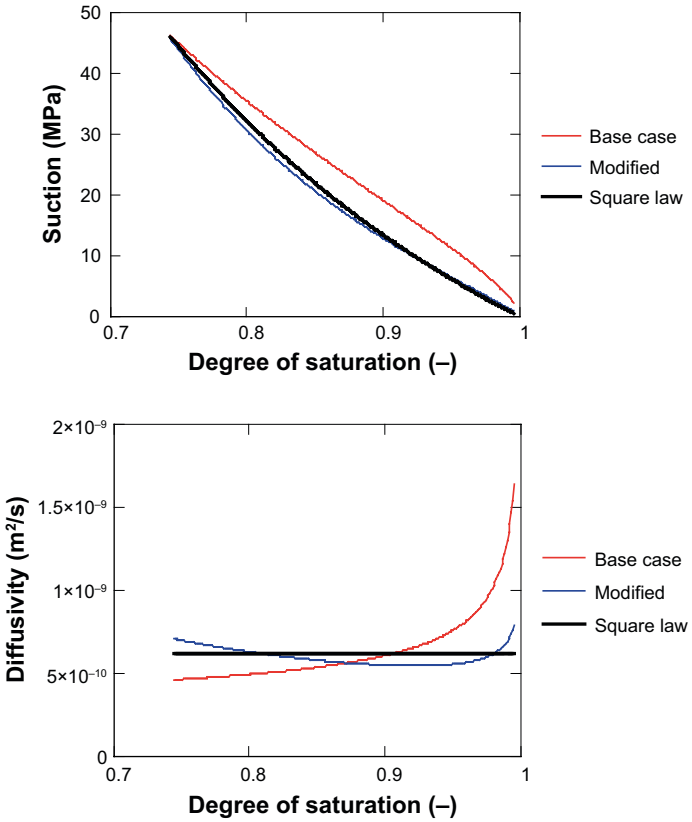

Figure 6-9. *Retention curves, adopted for backfill blocks of MX-80 (left), and evaluated diffusivity relations (right).*

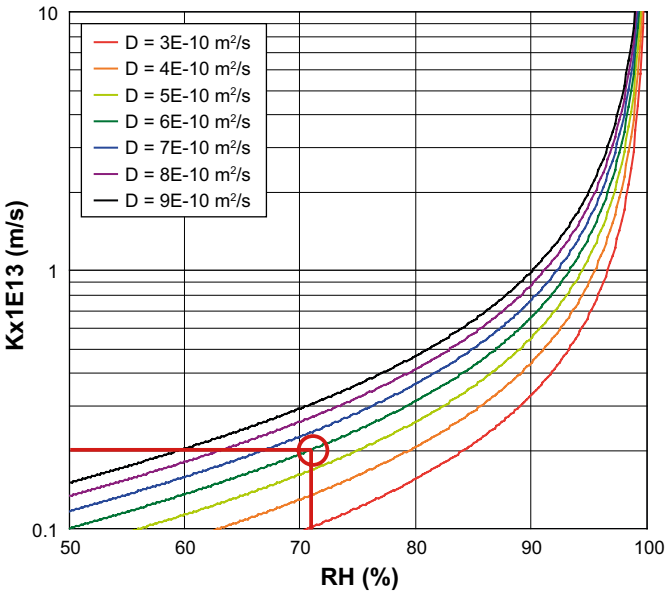

Figure 6-10. *Hydraulic conductivity vs. initial RH for different D values. Data corresponding to backfill blocks with MX-80 ($w = 17$ %; $\rho_d = 1\,700$ kg/m^3; $\rho_s = 2\,780$ kg/m^3).*

Specific water uptake tests were evaluated with this approach:

An evaluation of MX-80 specimens is shown in Figure 6-11. The specific tests are shown in the top left graph in Figure 6-4 (2 and 4 weeks tests). The hydraulic conductivity for the dry density in question is 5×10^{-14} m/s according to the adopted curve, and the retention data indicates that the initial RH was 58 % for the water content in question. Together, this data set corresponds to a diffusivity level of 4×10^{-10} m^2/s, which is basically the same value as from the direct evaluation of the water-uptake tests in question.

An evaluation of Asha specimens is shown in Figure 6-12. The specific tests are shown in the left middle graph in Figure 6-5 (test 43 and 44). The retention data indicates that the initial RH was 67 % for the water content in question, and the directly evaluated diffusivity was ~6×10^{-10} m^2/s. Together, this data set corresponds to a hydraulic conductivity level of 4×10^{-14} m/s, and this appears to be consistent with the available hydraulic conductivity data for Asha, although it is in-between results from different studies.

An evaluation of Friedland specimens is shown in Figure 6-13. The specific tests are shown in the right top graph in Figure 6-5 (test 14 and 34). The retention data indicates that the initial RH was 89 % for the water content in question, and the directly evaluated diffusivity was 7–8×10^{-10} m^2/s. Together, this data set corresponds to a hydraulic conductivity level of 2×10^{-13} m/s and this appears to be consistent with the available hydraulic conductivity data for Friedland.

An evaluation of specimens with Ibeco RWC BF is shown in Figure 6-14. The specific tests are shown in the left graph in Figure 6-6 (test 23 and 24). The retention data indicates that the initial RH was 72 % for the water content in question, and the directly evaluated diffusivity was 5–6×10^{-10} m^2/s. Together, this data set corresponds to a hydraulic conductivity level of 2–3×10^{-14} m/s and this appears to be only slightly lower than the available hydraulic conductivity data for Ibeco RWC BF.

Finally, an evaluation of Febex specimens is shown in Figure 6-15. The specific tests are shown in Appendix 2. The retention data indicates that the initial RH was 40 % for the water content in question, and the directly evaluated diffusivity was slightly lower than 6×10^{-10} m^2/s. Together, this data set corresponds to a hydraulic conductivity level of 3×10^{-14} m/s and this appears to be fairly consistent with the available hydraulic conductivity data for Febex, although in the lower range.

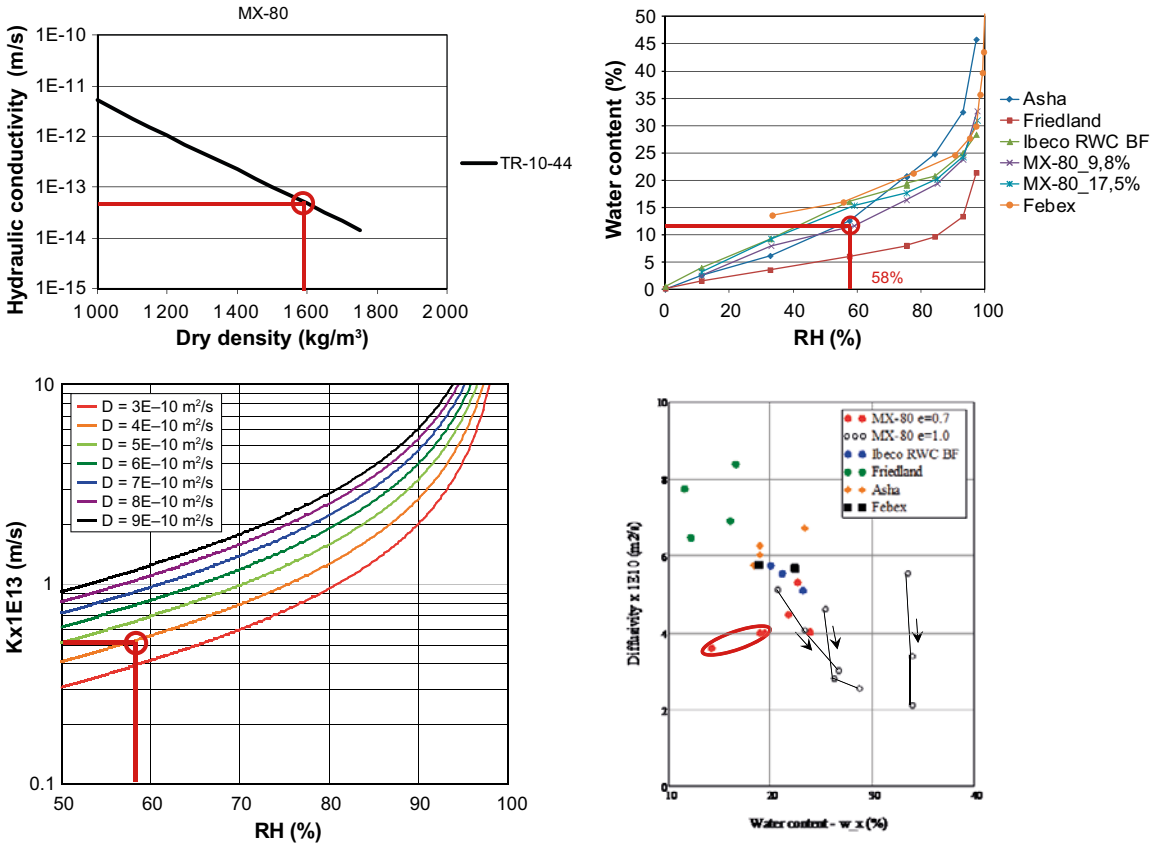

Figure 6-11. *Evaluation of water-uptake tests with MX-80 bentonite ($w = 11.5$ %; $\rho_d = 1\,590$ kg/m^3; $\rho_s = 2\,780$ kg/m^3).*

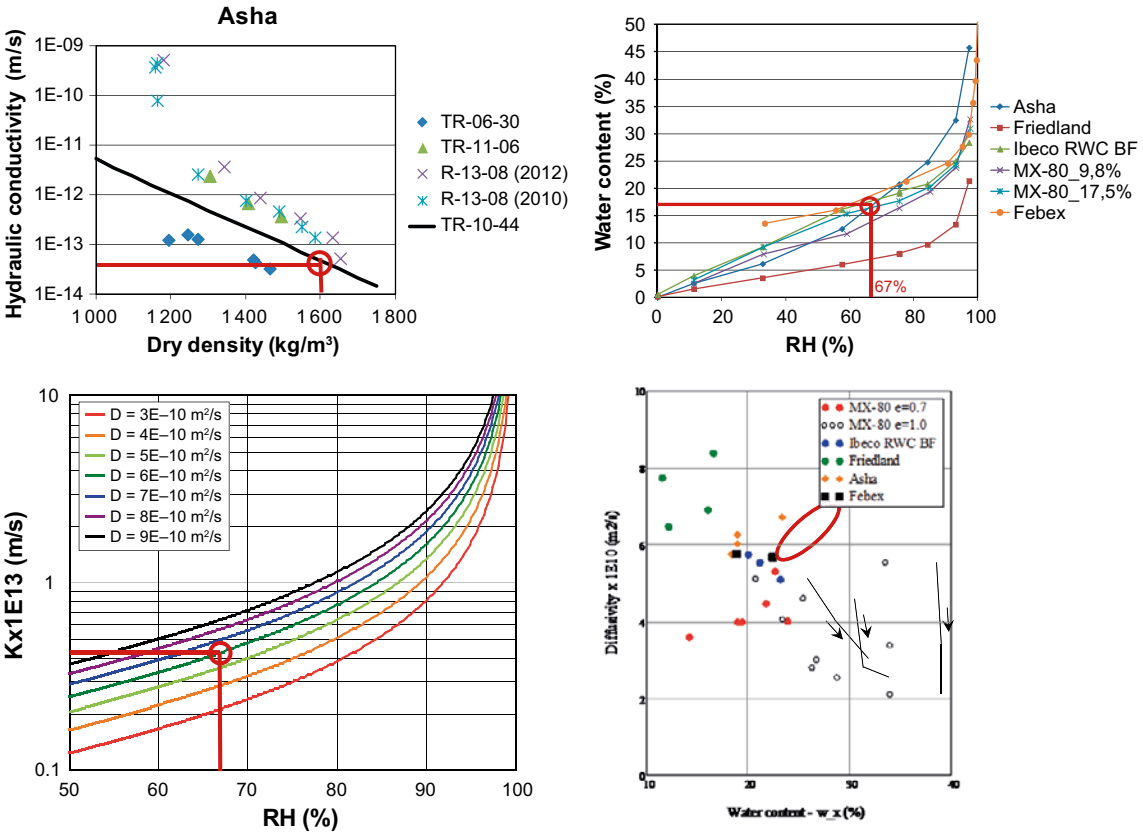

Figure 6-12. *Evaluation of water-uptake tests with Asha bentonite ($w = 17$ %; $\rho_d = 1\,600$ kg/m^3; $\rho_s = 2\,900$ kg/m^3).*

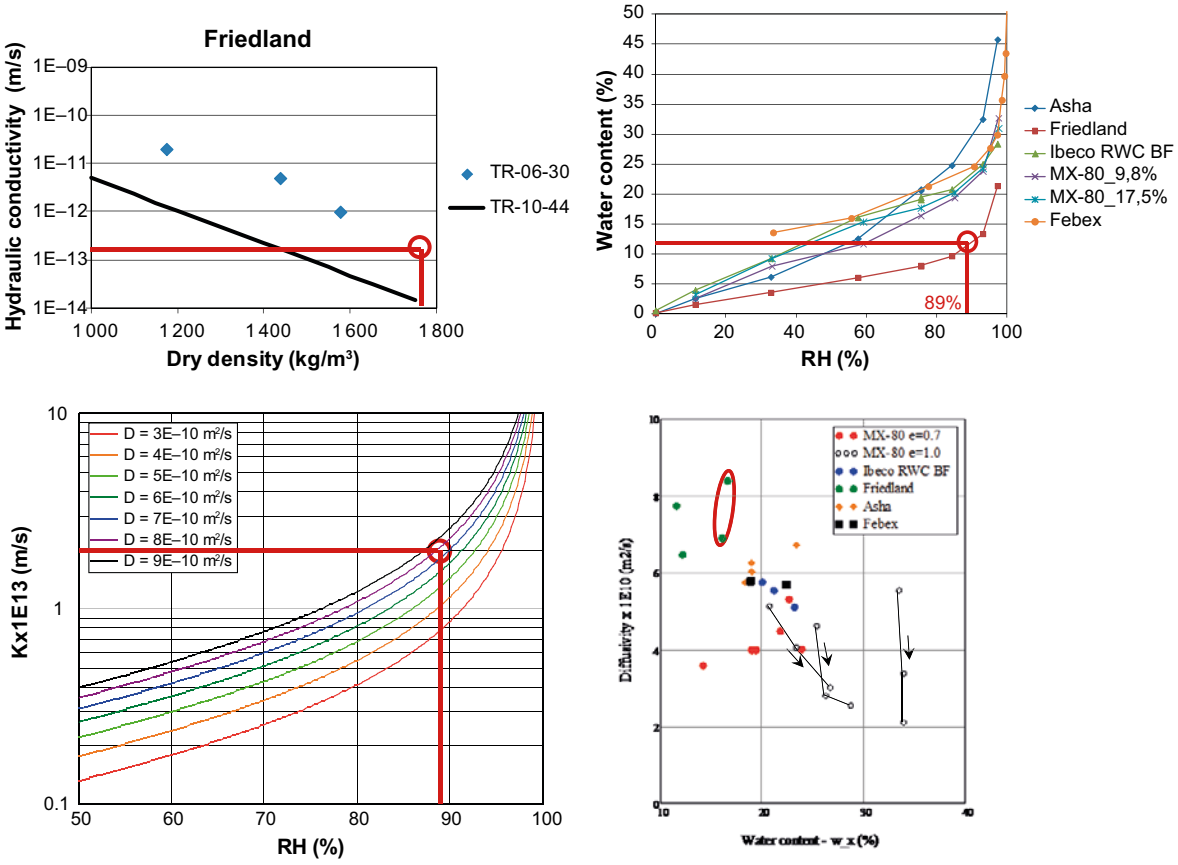

Figure 6-13. *Evaluation of water-uptake tests with Friedland bentonite ($w = 11.8$ %; $\rho_d = 1\,750$ kg/m^3; $\rho_s = 2\,780$ kg/m^3).*

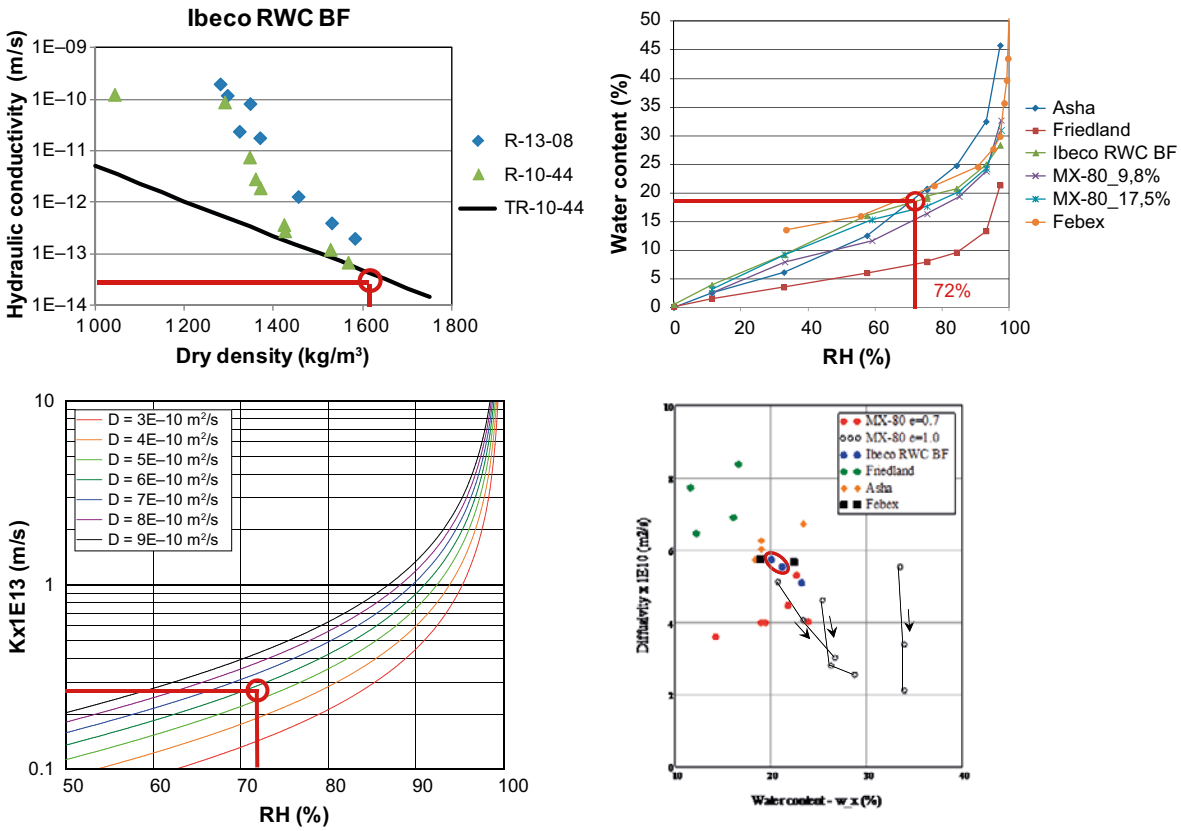

Figure 6-14. *Evaluation of water-uptake tests with Ibeco RWC BF bentonite ($w = 18.5$ %; $\rho_d = 1\,610$ kg/m^3; $\rho_s = 2\,780$ kg/m^3).*

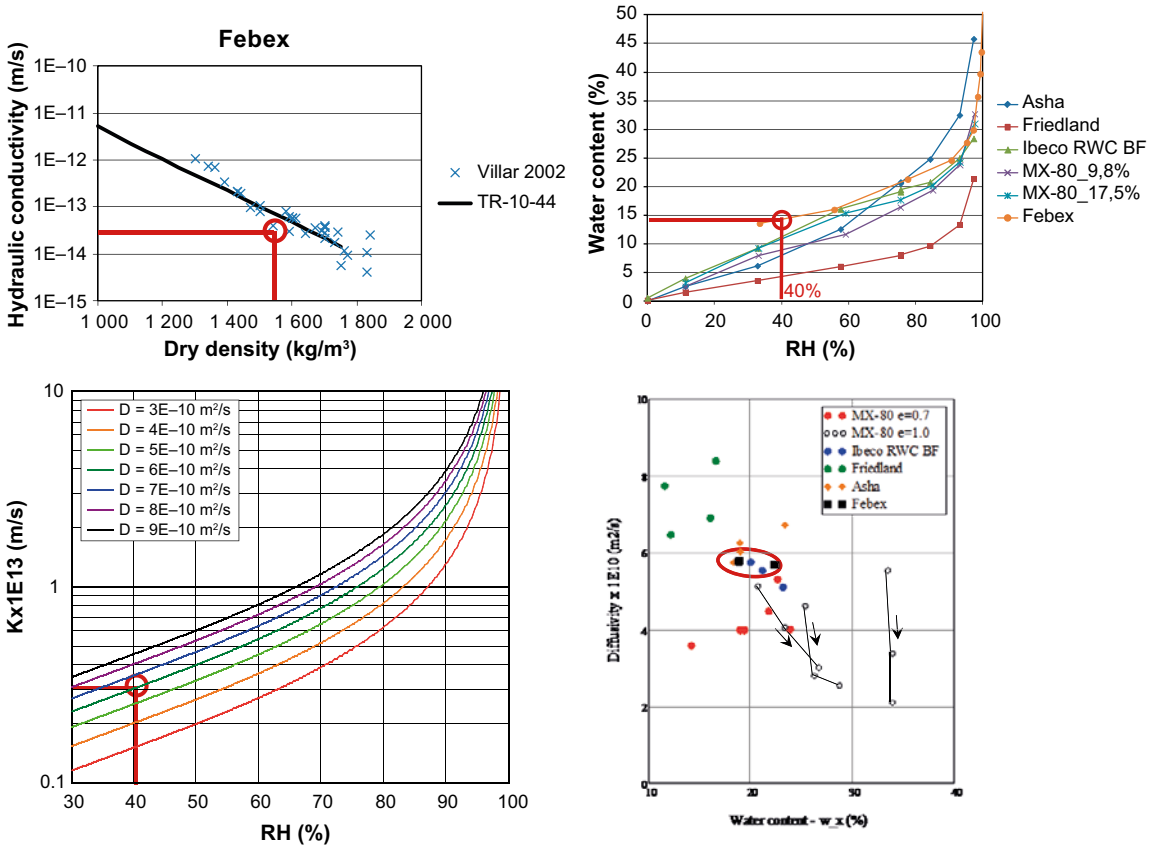

Figure 6-15. *Evaluation of water-uptake tests with Febex bentonite ($w = 14.3$ %; $\rho_d = 1\,551$ kg/m^3; $\rho_s = 2\,753$ kg/m^3).*

Taken together, this analysis demonstrates a general consistency between the data sets on hydraulic conductivity and retention properties on one hand, and data sets from water uptake tests on the other. It also contributes to a verification of the material model, especially regarding the relative permeability relation ($k_r(S_l)=S_l^3$). Evaluated hydraulic conductivity values which were slightly lower than measured data (Figure 6-14) or in the lower range (Figure 6-15) can be increased by increasing the exponent in the relative permeability law and correspondingly by modifying the retention curve in order to obtain a constant moisture diffusivity value.

6.8 Homogenization processes

6.8.1 Homogenization calculations in SR-Site

The THM modeling of buffer, backfill and other system components (Åkesson et al. 2010b) performed for SR-Site included homogenization calculations for the buffer as well as for the backfill. In general, these models consisted of a combination of blocks and pellets and therefore displayed large difference regarding dry density in the initial conditions. Moreover, the FEM program Code_Bright was used for these modeling tasks, and the used constitutive laws were based on the Barcelona Basic Model (Alonso et al. 1990). The sets of parameters which were adopted for these constitutive laws, were based on several types of tests and measurements (Åkesson et al. 2010a): i) compression tests with uniaxial strain at constant suction; ii) swelling tests with uniaxial strain at constant axial load; iii) swelling pressure measurements; iv) shear strength measurements (triax tests); and v) tensile strength measurements (beam tests). Still, all these tests had exclusively been performed on MX-80 bentonite.

Corresponding tests for other materials have basically been limited to swelling pressure measurements (see Section 6.3), although a few shear strength measurements (triaxial tests) have also been performed on specimen with Deponit Ca-N (Dueck et al. 2010). Given the general lack of experimental data, and the inherent uncertainties of the used calculations technique (see Åkesson et al. 2010b), it therefore appears as if a comparison of different material with respect to the homogenization process is currently beyond the horizon, at least by the *means of numerical modelling*. As will be shown in the next section, however, it appears as if *scale tests* can be quite useful for this type of comparisons.

6.8.2 Homogenization tests

Homogenization tests have been used during the course of different characterizations of backfill candidate materials. These tests are generally performed with a high density compacted specimen (block) in combination with a low density pellets filling in a confined volume, and in which the bentonite can take up water and equilibrate mechanically. Such tests have been performed with different combinations of materials for the blocks and pellets, respectively. Tests performed with one single material for both block and pellets, have so far only been conducted for Ibeco RWC BF (Johannesson et al. 2010) and Friedland (Johannesson et al. 2008). Final void ratio distributions for tests in which the initial thickness of the blocks and pellets was varied are shown in Figure 6-16. These profiles generally display a difference between the highest and lowest void ratio of 0.20–0.25 for the tests with Ibeco RWC BF, and correspondingly 0.15–0.30 for the tests with Friedland. This is well in agreement with the backfill homogenizations calculations in SR-Site (Åkesson et al. 2010b), which showed a maximum difference in void ratio of slightly more than 0.2.

The homogenization process is currently a fairly major research topic, with an ongoing project and an associated modelling task within the EBS Taskforce. Still, these activities are limited to saturated conditions, in contrast to the process considered here.

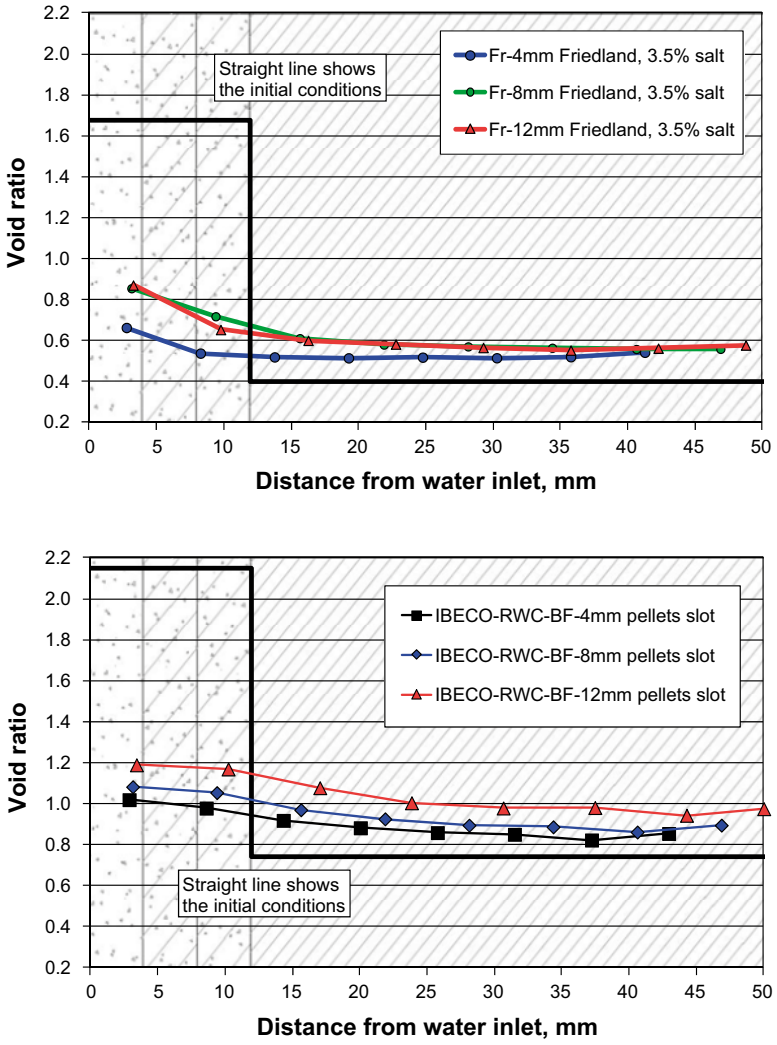

Figure 6-16. *Water content (upper), dry density (lower) plotted as function of the distance from the water inlet for the three specimens.*

6.9 Concluding remarks

Time-scale of buffer and backfill hydration

The time-scale of hydration for a certain material is to a large extent determined by the hydro-mechanical properties for the material in question, but also by the initial dry density and water content. In addition, different materials may display optimal properties for different initial conditions. A detailed comparison of different bentonite materials with respect to the time-scale of hydration is therefore not very straightforward. Instead, the evaluated moisture diffusivity data in Figure 6-8 (right) can be used to make a simple comparison of materials. The reason for this is that the time scale of hydration is basically inversely proportional to the diffusivity (e.g. $t_{febex} \sim t_{mx80} \times D_{mx80}/D_{febex}$). Although the variability of the moisture diffusivity was found to be fairly small, it can be noted that the lowest values were found for MX-80. This implies that the time-scale of hydration for other materials would be slightly shorter than for MX-80 (the reduction would be approximately 1/2 for Friedland, and 1/3 for the other analysed materials). Apart from these observations it can be noted that the presented analysis demonstrated a general consistency between the different data sets, and a verification of the material model from independent measurements.

Buffer temperature evolution

The temperature evolution for a certain bentonite material is to a large extent determined by the thermal conductivity for the material in question. Different saturation dependent relations adopted for the thermal conductivity of MX-80 was in this analysis compared with reported data for Febex benonite. The Febex data is generally quite similar to the MX-80 data relations, although the relations tend to overestimate the thermal conductivity at mid- saturation range, and underestimate the thermal conductivity at low saturation degrees.

Homogenization of buffer and backfill

The homogenization of buffer and backfill was analyzed with THM modeling in SR-Site. These calculations were based on constitutive laws which make use of parameter sets which were adopted from several types of tests and measurements. So far, this has only been performed for MX-80. Given the general lack of experimental data, and the inherent uncertainties of the used calculations technique, it therefore appears as if a comparison of different material with respect to the homogenization process by the *means of numerical modelling* is currently beyond the horizon. *Scale tests,* on the other hand, appears to be a valuable quite simple alternative method which can be used for comparisons of different materials. Scale tests of relevance have generally displayed a difference between the highest and lowest void ratio of 0.20–0.25 (Ibeco RWC BF), and correspondingly 0.15–0.30 (Friedland). This is well in agreement with the backfill homogenizations calculations in SR-Site which showed a maximum difference in void ratio of slightly more than 0.2.

7 The distribution of saturation times in the Forsmark repository and the effect of hydraulic connections between deposition holes

Daniel Malmberg, Mattias Åkesson, Ola Kristensson, Clay Technology AB, Lund, Sweden

7.1 Distribution of saturation times

As part of the evaluation of SKB's license application, SSM has requested that the distribution of the buffer's saturation time in all the deposition holes is analysed. Here we use data from groundwater models of the Forsmark repository, and couple this with thermo-hydraulic models of the buffer saturation process in deposition holes and hydraulic models of the saturation process in the tunnel backfill to estimate the distribution of saturation times.

7.1.1 Background – Summary of results from SR-site

In task 3 of the SR-site THM modelling report (Åkesson et al. 2010b) several models were constructed to estimate the maximum and minimum saturation time for three different types of deposition holes. These were:

- Deposition holes intersected by a single fracture at the mid-height of the canister (CMH-fracture).
- Deposition holes with no fractures, but where the tunnel just above the deposition hole is intersected by a single fracture (T-fracture).
- Deposition holes with no nearby fractures, and no nearby tunnel fractures (unfractured rock).

The models simulated thermo-hydraulic (TH), but not mechanical processes in the buffer, thus neglecting the consequences of the swelling of the bentonite buffer. To estimate the uncertainty introduced with this simplification, two models were constructed for each case: one with the buffer in the installation state and one with the buffer in a radially homogenized (extreme final) state. The assumption, supported by the findings in Task 3 of Åkesson et al. (2010b) is that the actual time to reach full saturation is bounded by the saturation times found in these two models.

Furthermore, in Task 2 of Åkesson et al. (2010b) the saturation time of the tunnel backfill was investigated using hydraulic models. Of primary interest for the present study is the models used to analyse the saturation time when water is only transported to the tunnel via fractures.

In Åkesson et al. (2010b) no attempt to couple the results of Task 2 and 3 with the expected distribution of fractures intersecting deposition holes and deposition-hole tunnels in the Forsmark repository were done. Thus, the distribution of saturation times for all deposition holes was not evaluated. Here such an evaluation is presented; the data on the expected inflow characteristics are taken from groundwater models of the Forsmark repository prior to installation (Joyce et al. 2013). These are similar to the models of the excavation phase presented as part of SR-Site (Svensson and Follin 2010), but in difference to those, where a continuum model was used to describe the flow properties of the rock, Joyce et al. (2013) have implemented a discrete fracture network. This means that individual fractures are represented, and thereby also the fracture intersections with deposition holes and tunnels. The statistical fracture model used is taken from the modelling of the operational phase during periods with temperate climate conditions presented in Joyce et al. (2010).

7.1.2 Groundwater models fracture statistics

We use groundwater models of the Forsmark repository where the period after excavation but before installation of the canister with spent fuel and the clay buffer (i.e. the inflows are measured during atmospheric conditions in the tunnels/deposition holes) was simulated, and analyse the fracture statistics (such as the fraction of deposition holes intersected by fractures, the fracture inflows and the distance from each deposition hole to nearby tunnel-intersecting fractures).

These open-repository fracture flows are then used to calibrate Code_Bright models, where at first atmospheric conditions are prescribed in both the deposition hole and the tunnel. Thereafter, the tunnel backfill/deposition-hole buffer is introduced and the saturation time calculated.

When studying the properties of the fracture population in the groundwater models, three main differences with the models in Åkesson et al. (2010b) can be identified:

1) no matrix flow is included in the groundwater models,
2) most fractures intersecting deposition holes and tunnels have considerably lower inflows than what was used in Åkesson et al. (2010b),
3) most deposition holes are not intersected by fractures and are situated quite far away from the nearest tunnel fracture. Thus, to estimate the saturation-time distribution, the tunnel-fracture separations analysed (6m and 24m) in Åkesson et al. (2010b) appears to have been too small.

These three points are discussed in further detail below.

1. Matrix flow

The perhaps most influential uncertainty in this work is the rock-matrix flow. Measurements on intact (unfractured) borehole cores from Forsmark (Vilks 2007) suggest that intact rock samples on the decimetre-size scale have hydraulic conductivities between $K_M = 5 \times 10^{-12}$–4×10^{-14} m/s. However, in the groundwater models, all water is assumed to be transported in fractures. While the matrix flow may be unimportant when studying the transport of radionuclides out of the repository (as is the main goal of the groundwater models), it can, depending on its magnitude, almost completely set the distribution of saturation times, t_s, in the repository.

As the value of the matrix conductivity in Forsmark is uncertain, the distribution of saturation times has here been calculated assuming no matrix flow (i.e. water to the deposition holes and tunnels only enters through fractures). Then, Code_Bright models with different values of the matrix conductivity ($K_M = 10^{-11}$–10^{-14} m/s) have been used to calculate the saturation time $t_S(K_M)$ if water only enters via the matrix. The cumulative distribution of saturation times for a particular value of K_M is then assumed to be identical to that with no matrix flow for $t < t_S(K_M)$ and equal to 1 for $t > t_S(K_M)$.

2. Fracture inflows in the groundwater models

The cumulative distribution of inflows in deposition-hole-intersecting fractures, q_{DH}, is shown in the left panel of Figure 7-1. About 60 % of all these fractures have $q_{DH} < 10^{-4}$ L/min. In Åkesson et al. (2010b), the saturation time was calculated for $q_{DH} = 0.1$ L/min and 10^{-3} L/min, respectively.

The cumulative distribution of inflows through tunnel-intersecting fractures (q_{TF}) is shown in the right panel of Figure 7-1. As can be seen, the tunnel-fracture inflows vary between approximately $q_{TF} = 10^{-6}$ and $q_{TF} = 10$ L/min. It is important to note that in the groundwater models used here, grouting is not included and tunnel-intersecting fractures with inflows higher than the prescribed limit of *0.1* L/min (SKB 2010b) are included. If grouting were included this could change the inflows into the tunnels by reducing the inflow through high-flowing fractures and possibly (by redistribution of flow) increasing the inflow through low-flowing fractures. Hence, depending on how high-flowing fractures are handled in the Forsmark repository, the tunnel-backfill-saturation process could, in some tunnels, be rather different than the estimates presented in this report.

The models of the tunnel backfill saturation process presented in Åkesson et al. (2010b) were set up using fractures with open-repository inflows equal to 0.1 L/min and 10^{-3} L/min only, hence to better represent the inflows expected in the repository we have here also included tunnel-intersecting fractures with $q_{TF} = 10^{-5}$ L/min.

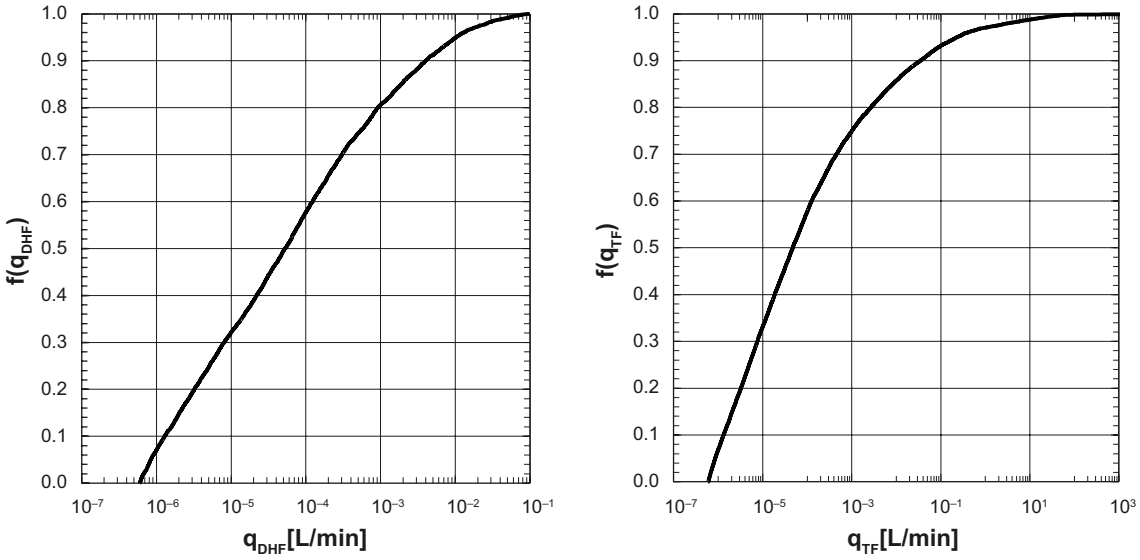

Figure 7-1. *Cumulative distribution of inflows (during atmospheric conditions in the repository) through deposition-hole intersecting fractures (left panel), and through tunnel-intersecting fractures (right panel), as determined in the groundwater models of the Forsmark repository.*

3. Fracture separation

The majority (about 90 %) of deposition holes in the groundwater models are not intersected by fractures[1]. Furthermore, the vast majority of these deposition holes are situated far away from the nearest tunnel fracture.

To quantify the tunnel-fracture separation, L (see Figure 7-2), we can construct the cumulative distribution. In this report we will use the quantity *L/2*, i.e. the fracture separation divided by 2, as this is the quantity which is varied in the Code_Bright models presented in Åkesson et al. (2010b) and below.

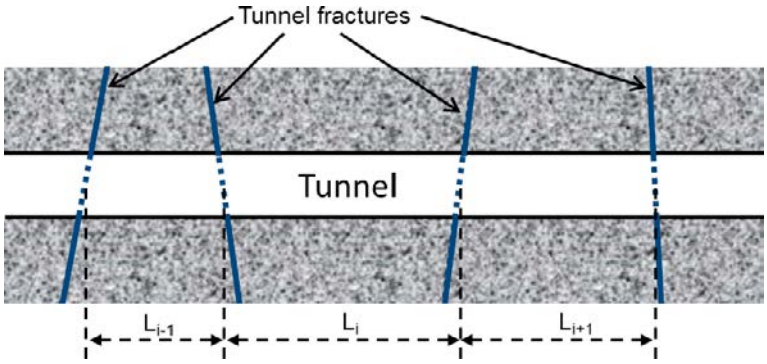

Figure 7-2. *The tunnel-fracture separation, L, is defined as the separation between two fractures, as measured from the point where they intersect the deposition-tunnel central axis.*

[1] This statement is only correct if EDZ (Excavation Damaged Zone) fractures are not included. In SR-site it is assumed that no significant EDZ will be present in Forsmark, and the same is assumed here. In Section 1.5 a short discussion on the possible effects of a highly unrealistic EDZ is included.

The cumulative distribution of *L/2* can be constructed in two different ways: 1) by analysing the fracture separations from the point of view of an observer sequentially positioned in each and every tunnel, or 2) from the point of view of an observer sequentially positioned in each and one of the deposition holes. In the first case, each fracture separation is only counted once and it results in the distribution identified by the black solid line in Figure 7-3. In the second case, each large fracture separation will be counted many times, as more deposition holes are situated between fractures with large separations than between fractures with small separations. The resulting distribution is the red solid line in Figure 7-3, which reaches a value of one at $L/2 \approx 260$m. When analysing the saturation-time distribution, the interesting statistic is the second one.

It should be noted that we have only considered the value of *L/2* for the two fractures situated closest to the deposition hole; if these have very low inflows, fractures further away have to be considered when analysing the tunnel-backfill-saturation time at a given position. In principle this could lead to that larger separations than $L/2 = 260$m should be considered; however, with the data analysed here this was not the case.

As is seen, the majority (about 80 %) of deposition holes are situated between fractures with $10 \text{ m} \le L/2 \le 100$ m, whereas in Åkesson et al. (2010b) only $L/2 = 3$ and 12 m were considered.

When considering the saturation time of the tunnel backfill, at any given deposition point, it is to a first approximation set by 1) the separation between the two nearest surrounding fractures (*L/2*), 2) the inflow through these fractures (q_{TF}), and 3) the distance to the nearest fracture (d_{min}). In practice this method gives too slow saturation times, as more distant but higher flowing fractures can lead to a shorter saturation time, which partially can be handled by analysing all fractures/fracture pairs in the tunnel (this is further explained in Section 7.1.5).

The distance to the nearest fracture (d_{min}) is of little significance when L/2 is small, but dominant when L/2 is large. This can be illustrated using the models of the tunnel backfill saturation phase which were presented in Task 2 in Åkesson et al. (2010b). As part of that task, the saturation of the tunnel backfill was studied in the case where water only entered through equidistant fractures.

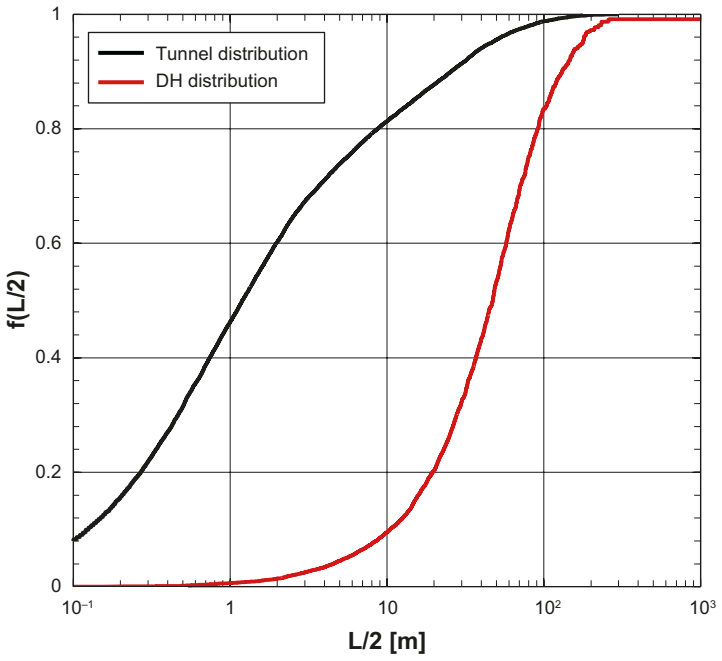

Figure 7-3. *Distribution of tunnel-fracture separations, where the tunnel-fracture separation, L, has been divided by a factor of 2. The black line shows the distribution from the point of view of an observer standing in the tunnels and the red line shows the distribution from the point of view of an observer standing in the deposition holes.*

Two fracture separations were investigated (L/2= 3 and 12 meters) using the geometry seen in Figure 7-11. The saturation profile at several different points in time after installation is shown in Figure 7-4 (left panel: L/2 = 3m, right panel: L/2 = 12m). As can be seen, the saturation profile in the two cases is rather different. When the fractures are relatively close to each other (L/2 = 3m, left panel) the saturation profile is rather shallow, and the entire buffer segment between the two fractures reach full saturation at approximately the same time. However, for larger fracture separations, a clear "saturation front" is seen in the tunnel backfill, with the parts close to the fracture reaching full saturation much faster than the parts further away.

7.1.3 Estimate of saturation time for different deposition holes

The saturation time of each deposition hole will here be calculated assuming none (or very small) matrix flow. The effect of the matrix flow is then taken into account when constructing the total distribution of saturation times.

We start by dividing the deposition holes into four different classes:

1) Deposition holes which are intersected by one or more fractures, which set the saturation time.
2) Deposition holes with no fractures, which are situated in between two tunnel fractures with small separation.
3) Deposition holes with no fractures, which are situated in between two tunnel fractures with large separation.
4) Deposition holes with no fractures, which are situated in a tunnel with no fractures.

Considering the deposition holes in class 1, the modelling done in Åkesson et al. (2010b), where the saturation time was calculated due to water inflow through a fracture intersecting the deposition hole at mid height of the canister, gives a good estimate of the saturation time if the fracture inflow under atmospheric conditions is around 10^{-4} L/min or higher and a significant matrix flow is present. However, as can be seen in the left panel of Figure 7-1, the majority of deposition-hole-intersecting fractures have much lower inflows. Thus, to properly cover the range of inflow configurations found in the groundwater models, we must update the models from Åkesson et al. (2010b) by including a very low matrix flow, and add a model with a low-flowing fracture.

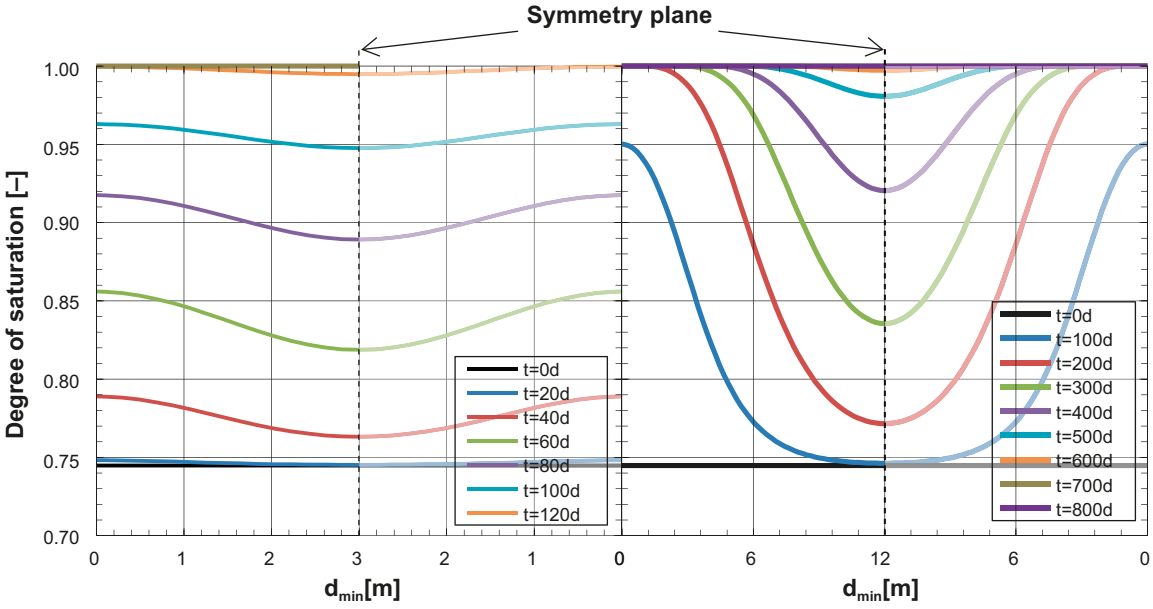

Figure 7-4. *Saturation profiles at the center of the tunnel backfill at different points in time after installation. The models are constructed with a symmetry plane in between the two fractures (see Figure 7-11), which, in these two models, were calibrated such as to give 10^{-3} L/min each under atmospheric conditions in the tunnel. The left panel depicts the evolution when the two fractures are separated by a distance of 6m, while the right panel depicts the evolution when the fractures are separated by 24m.*

It should be pointed out that some of the deposition holes that belong to class 1 will have such a low fracture inflow that the saturation time is actually set by nearby tunnel fractures (i.e. the deposition hole is saturated by water entering via the tunnel backfill). Here this is handled by comparing the saturation time as calculated from deposition-hole-intersecting fractures and tunnel-intersecting fractures separately, with the assumption that the shortest one is valid. In reality the two inflows will add up, potentially leading to significantly shorter saturation times. The number of deposition holes which this is the case for is, however, low, and thus have small impact on the shape of the cumulative distribution curve of saturation-times.

Concerning deposition holes belonging to class 2 and 3, we can estimate the saturation time by calculating the time it will take until the tunnel backfill is saturated above the deposition hole. Models for two fracture separations were analysed in Task 2 of Åkesson et al. (2010b); these are here supplemented by 18 additional models, which better cover the range of fracture inflows and fracture separations present in the groundwater models.

Deposition holes belonging to class 4 will be saturated either through matrix flow or, alternatively, by water passing through the tunnel plug into the deposition tunnel from the transport tunnels. In the latter case, we have no way of estimating the time until saturation in this report, and thus when zero matrix flow is assumed, the saturation time of the class 4 deposition-holes will be set to infinity. This is, however, of little importance for the saturation-time distribution, as the fraction of deposition holes belonging to class 4 is less than one per cent.

7.1.4 Additional models

As mentioned above, several new models were constructed (with respect to those presented in Åkesson et al. 2010b) to better represent the inflow characteristics in the groundwater models. Below we first discuss the additional models of the deposition-hole saturation process, where after we describe the additional models of the tunnel-backfill saturation process.

Additional models of the deposition-hole saturation process

The hydration of the buffer in a deposition hole intersected by a single fracture was analysed in Task 3 of Åkesson et al. (2010b). Two fracture transmissivities were used, corresponding to fracture inflows under atmospheric conditions of $q_F = 0.1$ L/min and $q_F = 10^{-3}$ L/min. The simulations also included matrix flow, with $K_m = 10^{-11}$ m/s and $K_m = 10^{-12}$ m/s, respectively. Two combinations of these fracture transmissivities and matrix conductivities were modelled: $q_F = 0.1$ L/min with $K_m = 10^{-11}$ m/s and $q_F = 10^{-3}$ L/min with $K_m = 10^{-12}$ m/s. For the purposes here, however, we would like to know the time until full saturation in the buffer for $q_F = 0.1$ L/min, 10^{-3} L/min and 10^{-5} L/min in the case of a very small matrix flow.

The models presented use the same geometry and mesh, as well as material parameters and initial/boundary conditions, as was used in Åkesson et al. (2010b). For completeness they are briefly described below; for a more in-depth description, as well as motivation for the values used the reader is directed to Task 3 in Åkesson et al. (2010b).

Material parameters

The constitutive laws used are:

Liquid and gas density

$$\rho_l = 1002.6 \cdot \exp[4.5 \cdot 10^{-4}(p_l - 0.1\ \text{MPa}) - 3.4 \cdot 10^{-4}T] \quad (7\text{-}1)$$

$$\rho_g = \frac{0.018 p_v}{8.3143\ (273.15 + T)} \cdot RH \quad (7\text{-}2)$$

$$p_v = 130675 \cdot \exp\left[-\frac{5239.7}{273.15 + T}\right] \quad (7\text{-}3)$$

$$RH = \exp\left[\frac{-0.018 \cdot (p_g - p_l)}{8.3143 \cdot\ (273.15 + T) \cdot \rho_l}\right] \quad (7\text{-}4)$$

Conductive heat flux

$$\boldsymbol{i}_{\mathrm{c}} = -\lambda \nabla T \tag{7-5}$$

$$\lambda = \lambda_{\mathrm{sat}} \cdot S_{\mathrm{l}} + \lambda_{\mathrm{dry}} \cdot (1 - S_{\mathrm{l}}) \tag{7-6}$$

Retention behaviour, Van Genuchten

$$S_{\mathrm{l}} = \left[1 + \left(\frac{S_{\mathrm{l}}}{P_0}\right)^{1/(1-\lambda)}\right]^{-\lambda} \tag{7-7}$$

$$S_{\mathrm{l}} = p_{\mathrm{g}} - p_{\mathrm{l}}$$

Flow through porous medium

$$\boldsymbol{q}_{\mathbf{l}} = -\frac{k \cdot k_{\mathrm{rl}}}{\mu_{\mathrm{l}}} \nabla \boldsymbol{p}_{\mathrm{l}} \tag{7-8}$$

Buffer materials: $k_{\mathrm{rl}} = S_{\mathrm{l}}^3$ (7-9)

Rock materials: $k_{\mathrm{rl}} = \sqrt{S_{\mathrm{l}}}\left[1 - \left(1 - S_{\mathrm{l}}^{1/\lambda}\right)^{\lambda}\right]^2$ (7-10)

$$\mu_{\mathrm{l}} = 2 \cdot 10^{-12} \exp\left(\frac{1808.5}{273.15 + T}\right) \tag{7-11}$$

Vapour diffusion

$$\boldsymbol{i}_{\mathrm{g}}^{\mathrm{w}} = -\left[n \rho_{\mathrm{g}} (1 - S_{\mathrm{l}}) D_{\mathrm{m}}^{\mathrm{w}}\right] \nabla \omega_{\mathrm{g}}^{\mathrm{w}} \tag{7-12}$$

$$D_{\mathrm{m}}^{\mathrm{w}} = \tau \cdot 5.9 \cdot 10^{-6} \frac{(273.15 + T)^{2.3}}{p_{\mathrm{g}}} \tag{7-13}$$

The models simulate thermo-hydraulic, but not mechanical processes in the buffer. This introduces an uncertainty in the saturation time, as the swelling of the buffer and its effect on the void ratio distribution and hydraulic properties of the clay are not included. To estimate the effect of this simplification two "mechanical" states of the buffer were modelled; 1) the initial state and 2) the homogenised state. In 1) the buffer is modelled in the state it had just after installation, while in 2) it is modelled in a theoretical final state, where the buffer has swelled (radially) and homogenised in that direction. The parameters used to describe the buffer in the initial state models are summarised in Table 7-1, while the parameters in the homogenised models are found in Table 7-2.

Table 7-1. Data used for initial state MX-80 materials. Directly adopted from the values used in Åkesson et al. (2010b).

Parameter		Buffer ring n=0.36 w=17 %	Buffer cylinder n=0.61 w=17 %	Buffer pellets n=0.61 w=17 %	Backfill block n=0.39 w=17 %	Backfill Pellets n=0.61 w=17 %
Thermal conductivity	λ_{dry} λ_{sat} (W/mK)	0.7 1.3	0.7 1.3	0 1.3	0.7 1.3	0 1.3
Specific heat	c (J/kgK)	800				
Solid density	ρ_s (kg/m^3)	2780				
Intrinsic permeability	k (m^2)	1.2×10^{-21}	2.0×10^{-21}	5.2×10^{-19}	2.1×10^{-21}	5.2×10^{-19}
Relative permeability	k_{rl} (–)	S_r^3				
Vapour diffusion tortuosity	τ (–)	1				
Water retention curve	P_0 (MPa) λ (–)	67.2 0.48	43.5 0.38	0.508 0.26	37.2 0.34	0.162 0.19

Table 7-2. Data used for homogenized MX-80 materials. Directly adopted from the values used in Åkesson et al. (2010b).

Parameter		Homog. Buffer cylinder n=0.419 w=17 %	Homog. Buffer ring n=0.435 w=17 %	Homog. Backfill n=0.454 w=17 %
Thermal conductivity	λ_{dry} λ_{sat} (W/mK)		0.7 1.3	
Specific heat,	C (J/kgK)		800	
Solid density	ρ_s (kg/m^3)		2780	
Intrinsic permeability	k (m^2)	4.2×10^{-21}	6.0×10^{-21}	8.9×10^{-21}
Relative permeability	k_{rl} (–)		S_r^3	
Vapour diffusion tortuosity	τ (-)		1	
Water retention curve,	P_0 (MPa) λ (-)	15.19 0.25	8.93 0.22	

To determine the properties of the Homogenized Backfill the tunnel geometry was obtained as an average of the measures of the "Theoretical section" and the "Maximum fall out" as defined in the Backfill Production Report (SKB 2010a). The "Averaged" geometry was then used to find suitable properties of the homogenized tunnel backfill materials: backfill blocks and pellets.

The parameters used to model the rock and canister materials are found in Table 7-3. The value of the rock intrinsic permeability deserves some discussion. The goal of this modelling is to quantify the saturation time due to fracture wetting without significant matrix flow. Thus, in principle the intrinsic permeability of the rock should be set as low as possible. However, setting too small a value leads to unrealistically high liquid pressures in the rock around the deposition hole, due to the increased temperature that causes the water to expand (see Equation 7-1) in combination with the low permeability, which prevents the water to flow away from the warm zone. Using the value 10^{-21} m/s is a good compromise which leads to a very low matrix flow, while avoiding high pressures in the rock.

Table 7-3. Data used for the rock, fracture and canister materials. Directly adopted from the values used in Åkesson et al. (2010b).

Parameter		Rock n=0.003	Fracture n=0.99	Canister n=0.0001
Thermal conductivity	$\lambda_{dry} = \lambda_{sat}$ (W/mK)	2.8	2.8	90
Specific heat	C (J/kgK)	770	770	480
Solid density	ρ_s (kg/m^3)	2277	2277	7500
Intrinsic permeability	k (m^2)	10^{-21}	4.3×10^{-15} 4.3×10^{-17} 4.3×10^{-19}	–
Relative permeability	k_{rl} (-)	λ= 0.6*	S_r^3	–
Vapour diffusion tortuosity	τ (-)	1	1	–
Water retention curve	P_0 (MPa) λ (-)	1.74 0.6	1.74 0.6	–

* van Genuchten is used, see Equation 7-7.

Geometry, initial and boundary conditions

The geometry is a two-dimensional axisymmetric representation of a single deposition hole, with the backfilled tunnel and nearby host rock; it is shown in Figure 7-5.

The initial conditions prescribed are taken from Åkesson et al. (2010b). They are:

Parameter Unit	Initial liquid pressure [MPa]	Porosity [-]	Initial temperature [°C]
Rock/Fracture	4–5.2[1)]	0.003	15
Buffer rings	−46	0.36	15
Buffer blocks	−46	0.38	15
Buffer pellets	−46	0.64	15
Backfill blocks	−46	0.39	15
Backfill pellets	−46	0.64	15
Canister	−46	0.0001[2)]	15

[1)] Linear vertical distribution between upper (4MPa) and lower (5.2MPa) boundary.

[2)] When using Code_Bright all materials must have a porosity. As the canister in reality has zero porosity a very low value is prescribed here.

Two types of thermal boundary conditions are used, a heat flux on the canister and a prescribed temperature on the upper and lower boundaries (on the vertical boundary adiabatic thermal conditions are prescribed). In Åkesson et al. (2010b), all models were saturated within 3 000 years. For some models analysed here this was not the case, hence the boundary conditions had to be evaluated for considerably longer time periods (t = *30 000* years).

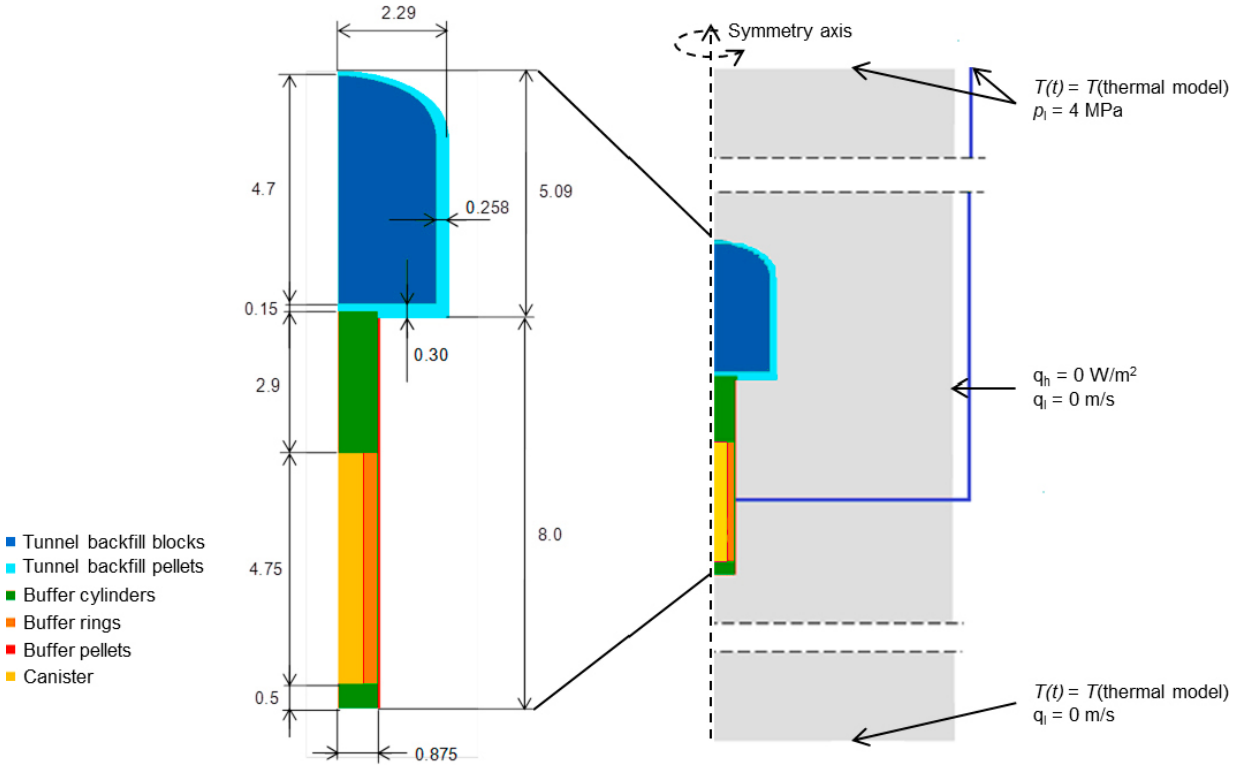

Figure 7-5. *Geometry and boundary conditions used to model the saturation process in a deposition hole intersected by a single fracture at canister mid height. The figure is adapted from figures 3-3 and 3-6 in Åkesson et al. (2010b).*

The canister heat load is prescribed on two vertically orientated concentric cylinders within the canister material. 1/3 of the total heat load is prescribed at the radial distance $r = 0.105$ m and 2/3 of the total heat load at $r = 0.315$ m. This is done to mimic the real case, where four fuel elements are placed in the inner part and eight in the outer part of the canister.

The heat load (i.e. the canister power) is prescribed according to the expression reported in Hökmark et al. (2010):

$$P(t) = P(0)\sum_{i=1}^{i=i_{\max}} a_i \exp(-t/t_i), \qquad (7\text{-}14)$$

where $P(0) = 1\,700$ W, $i_{max} = 7$ and the parameters a_i and t_i have the values shown in Table 7-4. We here assume that it is valid for $t \leq 30\,000$ years, the graph in Figure 7-6 shows the values during this time span.

The temperature prescribed on the upper and lower boundaries are taken from a thermal model of the entire repository used in the THM report concerning the geosphere, as presented in Hökmark et al. (2010). That model simulated the entire repository with surrounding rock mass, assuming a canister distance of 6m −6.8m (depending on the position within the repository) and a rock thermal conductivity equal to 3.57 W m^{-1} K^{-1}. The temperature change 60 m above/below the repository level is shown in Figure 7-7 (red and blue solid lines). As can be seen the evolution is almost identical, hence the same temperature could be prescribed on both boundaries (black dashed line in Figure 7-7). Data for t > 10 000 years have not been directly evaluated at ±60 m above/below the deposition holes, but the temperature evolution on the deposition-hole wall in similar models is available in Hökmark et al. (2010). The results suggest that the temperature reaches its original value (T = 15 °C) about 100 000 years after installation of the spent fuel, and that the trend, as plotted on a semi-log plot, is close to linear between 10 000 and 100 000 years. As such the temperature boundary condition has been extrapolated as is shown in Figure 7-7. It should be noted that the temperature at the boundary is less than 4 °C above its original value of 15 °C in this time interval. As such, any small errors in the temperature boundary condition should have a very small effect on the thermo-hydraulic evolution in the buffer.

Table 7-4. Decay function coefficients and the corresponding canister power graph.

i	1	2	3	4	5	6	7
t_i	20	50	200	500	2 000	5 000	20 000
a_i	0.060	0.705	−0.055	0.250	0.025	−0.009	0.024

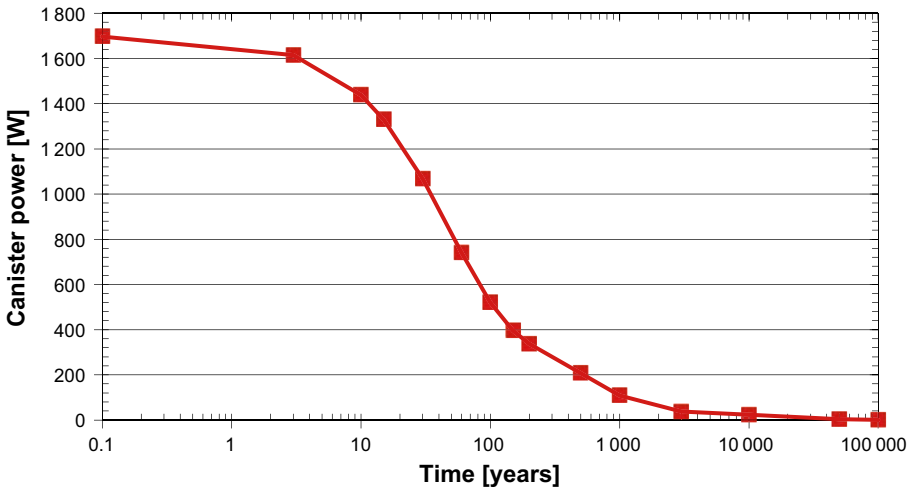

Figure 7-6. *Canister power as calculated using Equation 7-14.*

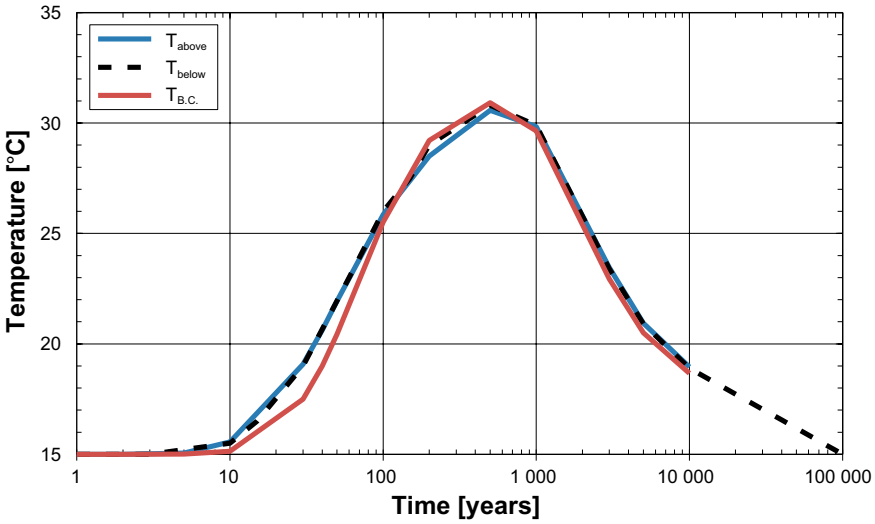

Figure 7-7. *Temperature change at the upper (red line) and lower (blue line) boundary of the model, taken from a thermal simulation of the entire repository presented in Hökmark et al. (2010). The dashed black line is the temperature boundary condition prescribed on the boundary in the Code_Bright models.*

The hydraulic boundary condition was evaluated from a hydraulic model of the entire repository, presented in Åkesson et al. (2010b). It showed that at both the upper and lower boundaries of the model used to simulate the evolution of a single deposition hole, the liquid pressure was close to hydrostatic at all times. Furthermore, evaluation of the single-deposition-hole model showed that a no-flow condition on the lower boundary gave a correct evolution. As such, the only hydraulic boundary condition used in the model is that a liquid pressure of 4 MPa is prescribed on the upper boundary of the geometry.

Parameter variations explored

The main parameter to be investigated here is the fracture transmissivity, T_F. However, it is more correct to state that the importance of variations in fracture inflow was explored, as the values of these, as measured under atmospheric conditions, were used to calibrate the transmissivity. Aside from different fracture transmissivities, one extra (with respect to the models presented in Åkesson et al. 2010b) value of the matrix hydraulic conductivity was modelled, $K_m = 10^{-14}$ m/s. The different models analysed are summarised in Table 7-5 below.

Table 7-5. Additional models constructed to explore the effect of deposition-hole intersecting fractures on the buffer's saturation time.

Model name	Matrix conductivity K_m [m/s]	qF [L/min]	I/H[1)]
Km14_qF1_I	10^{-14}	0.1	I
Km14_qF1_H	10^{-14}	0.1	H
Km14_qF3_I	10^{-14}	10^{-3}	I
Km14_qF3_H	10^{-14}	10^{-3}	H
Km14_qF5_I	10^{-14}	10^{-5}	I
Km14_qF5_H	10^{-14}	10^{-5}	H
Km14 _I	10^{-14}	–	I
Km14 _H	10^{-14}	–	H

[1)] I = **I**nstallation state, H = **H**omogenised state.

Results

In accordance with Åkesson et al. (2010b), the saturation time (here defined as the time from buffer installation until the buffer reaches 99 % saturation) was measured in four pre-determined points (P1–P4) as well as in the last point to reach full saturation. The positions of points P1–P4 are illustrated in Figure 7-8. It should be noted that due to limitations of the post-processor used, the saturation has to be measured on the second node from the edge of the buffer material (the same is true for the models presented in Åkesson et al. 2010b).

In Figure 7-9 the time to reach full saturation in the six models with $K_m = 10^{-14}$ m/s and a single fracture is shown. The saturation times are rather long, with a time to saturation of *679–1 579* years for $q_F = 0.1$ L/min up to *2 035–2 551* years when $q_F = 10^{-5}$ L/min. Furthermore, it can be observed that the results of the models with $q_F = 0.1$ and 10^{-3} L/min are rather similar, hence in these cases the buffer limits the fracture flow.

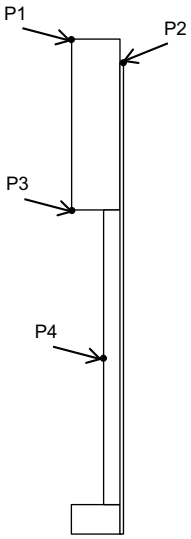

Figure 7-8. *Schematic overview of the position of the four points in the buffer where the saturation time is recorded in each model.*

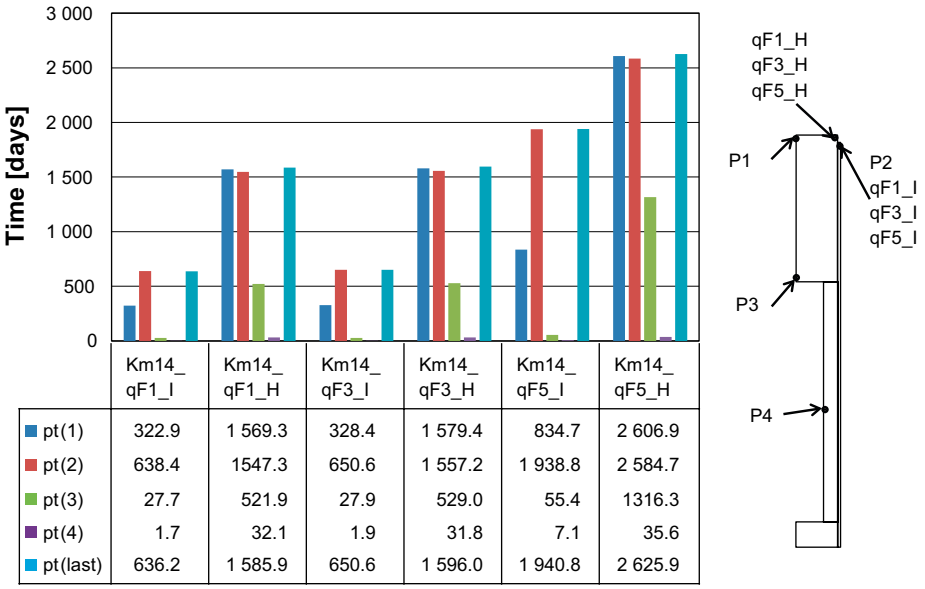

	Km14_ qF1_I	Km14_ qF1_H	Km14_ qF3_I	Km14_ qF3_H	Km14_ qF5_I	Km14_ qF5_H
pt(1)	322.9	1 569.3	328.4	1 579.4	834.7	2 606.9
pt(2)	638.4	1547.3	650.6	1 557.2	1 938.8	2 584.7
pt(3)	27.7	521.9	27.9	529.0	55.4	1316.3
pt(4)	1.7	32.1	1.9	31.8	7.1	35.6
pt(last)	636.2	1 585.9	650.6	1 596.0	1 940.8	2 625.9

Figure 7-9. *Time to 99 % saturation [in years] in models with a matrix conductivity equal to 10^{-14} m/s and a fracture flow of $q_F = 0.1$ L/min (qF1_I, qF1_H), $q_F = 10^{-3}$ L/min (qF3_I, qF3_H) and $q_F = 10^{-5}$ L/min (qF5_I, qF5_H). A description of the parameter variations between the models is shown in Table 7-5.*

Another important aspect here is when we define the deposition hole to be saturated. As is seen in Figure 7-9, points 3 and 4 are in general saturated much faster than points 1 and 2. Hence, if we defined the saturation time as the time until saturation just around the canister the result would be rather different from if we define it as the time until the buffer in the entire deposition-hole is saturated. Following the procedure used in Åkesson et al. (2010b) we will here use the latter definition, i.e. the saturation time is defined as the time it takes to saturate the buffer in the entire deposition hole.

In Figure 7-10, the saturation time due to only matrix flow is shown for $K_M = 10^{-11}$, 10^{-12}, 10^{-13} and 10^{-14} m/s. Only the models with 10^{-14} m/s were done as part of this report, the results for the other six cases are taken from Åkesson et al. (2010b). The models have been re-named to fit the nomenclature in this report, although their original names are also included in Figure 7-10. As can be seen the saturation time scales rather well with the matrix conductivity, a decrease of K_M with a factor of 10 leads to an increase in saturation time of roughly a factor of 10.

It is also important to compare the saturation time for $K_M = 10^{-14}$ m /s and no fracture (*17 742–21 872*) with the maximum saturation time seen when including fractures (*1 941–2 626* for $q_F = 10^{-5}$ L/min). This indicates that the matrix plays a very small role in saturating the buffer in the fracture models.

Additional models of the tunnel-backfill saturation process

Setup

The models presented here to analyse the tunnel-backfill saturation process used the same type of geometry and the same material parameters (with the exception of one additional value of the fracture transmissivity) as the models in Åkesson et al. (2010b). An example of the geometry is shown in Figure 7-11, where the model with *L/2 = 3* is shown.

Several different models were constructed, varying the fracture half separation, *L/2*. The values of *L/2* were chosen so as to represent the cumulative distribution of *L/2* (*f(L/2)*, see red solid line in Figure 7-3). The values of *L/2* modelled, and the corresponding value of *f(L/2)* are listed in Table 7-6. As can be seen the distribution is better mapped for *f(L/2) > 0.80*; this is motivated by the large variations in saturation time in this region.

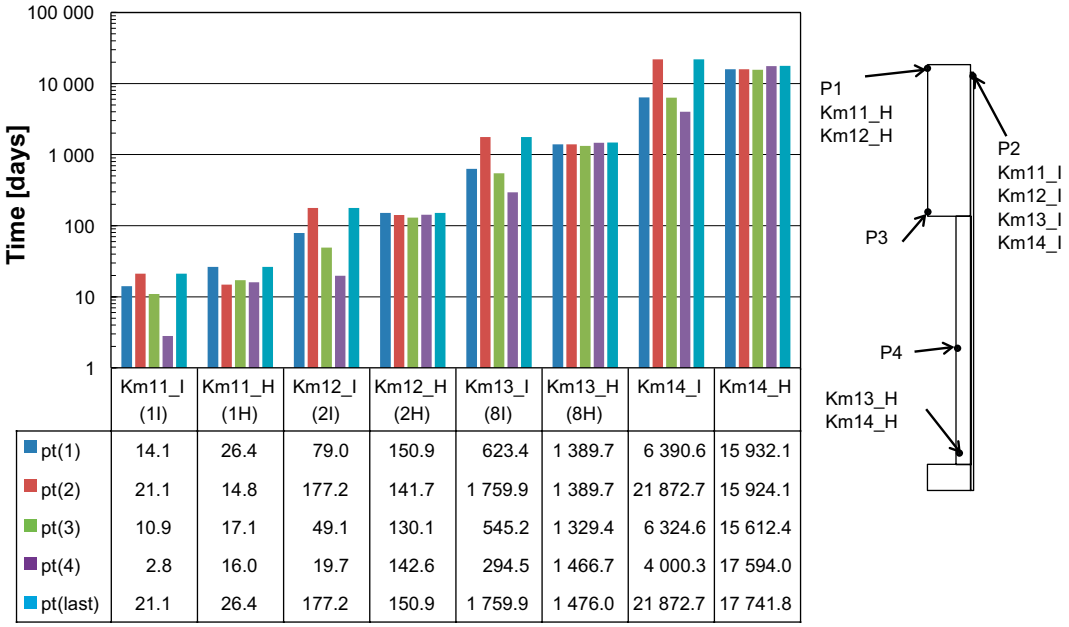

	Km11_I (1I)	Km11_H (1H)	Km12_I (2I)	Km12_H (2H)	Km13_I (8I)	Km13_H (8H)	Km14_I	Km14_H
pt(1)	14.1	26.4	79.0	150.9	623.4	1 389.7	6 390.6	15 932.1
pt(2)	21.1	14.8	177.2	141.7	1 759.9	1 389.7	21 872.7	15 924.1
pt(3)	10.9	17.1	49.1	130.1	545.2	1 329.4	6 324.6	15 612.4
pt(4)	2.8	16.0	19.7	142.6	294.5	1 466.7	4 000.3	17 594.0
pt(last)	21.1	26.4	177.2	150.9	1 759.9	1 476.0	21 872.7	17 741.8

Figure 7-10. *Time to reach 99 % saturation [in years] in the deposition-hole buffer in models with only matrix flow (i.e without a fracture). The models with matrix conductivity equal to 10^{-13} m/s and above were done as part of Åkesson et al. (2010b) and the results are taken directly from that report. The model identifiers used in that report are included inside parenthesis in the figure.*

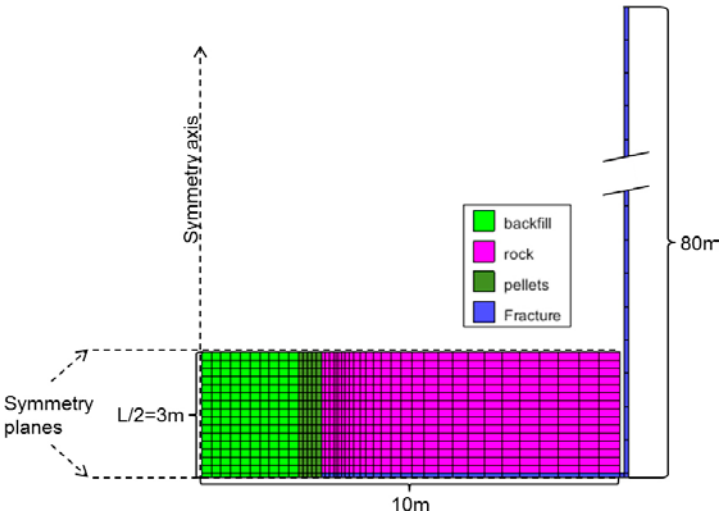

Figure 7-11. *Geometry used when modelling fracture wetting of the tunnel backfill. In this particular model the inter-fracture distance (L) was 6m. To achieve a relevant liquid pressure at the intersection of the no-flow boundary (r = 10m) the fracture length is set to 80m. A more in-depth description of the geometry shown here and how it was constructed can be found in Section 2.3 of Åkesson et al. (2010b).*

Table 7-6. Range of L/2 modelled and the corresponding values of the cumulative distribution function of L/2.

L/2 [m]	f(L/2)
3	0.03
20	0.20
38	0.40
60	0.60
90	0.80
130	0.90
170	0.95
260	0.99

The only difference in geometries between the models is that the backfill, pellets and rock materials were extended away from the fracture to the corresponding fracture half separation. The material parameters are summarized in Table 7-7. The constitutive laws used are the same as the hydraulic constitutive laws summarised in Equation 7-1 to 1-11.

The models of the tunnel backfill saturation process done for this report are summarized in Table 7-8. There, q_{TF} is the tunnel fracture inflow in L/min as measured during atmospheric conditions.

Results

The results from the models were quantified by measuring the time until $S_l = 0.99$ at distance d_{min} from the fracture at $r = 2.55$ m (i.e. in the pellets column). Here $d_{min} = n \times 6$ m, where n goes from 1 up to n_{max}, such that $(L/2–6) \leq n_{max} \times 6$ m $< L/2$. In the cases where $n_{max} \times d_{min} \neq L/2$, the time until $S_l = 0.99$ at $L/2$ m from the fracture in the pellets column ($r = 2.55$ m) was also measured and recorded.

In Figure 7-12, the results from models with $q_{TF} = 10^{-3}$ L/min (solid lines) and $q_{TF} = 0.1$ L/min (dashed lines) are shown. As can be seen, the results for the two fracture inflows are rather similar. The cause is that for such high inflows, the bentonite limits the inflow, as it effectively acts as a seal on the fracture.

Table 7-7. Material parameters used when modeling the tunnel-backfill saturation process. Directly adopted from the values used in Åkesson et al. (2010b).

Parameter		Backfill block e=0.635 w=17 %	Backfill Pellets e=1.780 w=17 %	Homog. Backfill e=0.74 w=17 %	Homog. Backfill e=0.91 w=17 %	Rock matrix	Fracture material
Porosity	**n (–)**	0.388	0.64	0.425	0.476	0.003	0.003
Intrinsic permeability	**k (m^2)**	2.1×10^{-21}	5.2×10^{-19}	4.8×10^{-21}	1.5×10^{-20}	5×10^{-20}	[1]
Relative permeability	**k_r (–)**	S_r^3	S_r^3	S_r^3	S_r^3	vG†: λ = 0.6	vG[2]: λ = 0.6
Water retention curve	**P_0 (MPa)**	37.2	0.162	11.6	3.45	1.74	1.74
	λ (–)	0.34	0.19	0.23	0.20	0.6	0.6

[1] Three variations: 2.5×10^{-15} m^2 (0.1 L/min) , 2.5×10^{-17} m^2 (10^{-3} L/min) and 2.5×10^{-19} m^2 (10^{-5} L/min)
[2] vG: van Genuchten relative permeability law, see Equation 7-10.

Table 7-8. Overivew of models of the tunnel backfill saturation process.

L/2	q_{TF}		
	10^{-5}	10^{-3}	10^{-1}
3	TB_Q5_L3	TB_Q3_L3	TB_Q1_L3
20	TB_Q5_L20	TB_Q3_L20	TB_Q1_L20
38	TB_Q5_L38	TB_Q3_L38	TB_Q1_L38
60	–	TB_Q3_L60	TB_Q1_L60
90	–	TB_Q3_L90	TB_Q1_L90
130	–	TB_Q3_L130	TB_Q1_L130
170	–	TB_Q3_L170	TB_Q1_L170
260	–	TB_Q3_L260	–

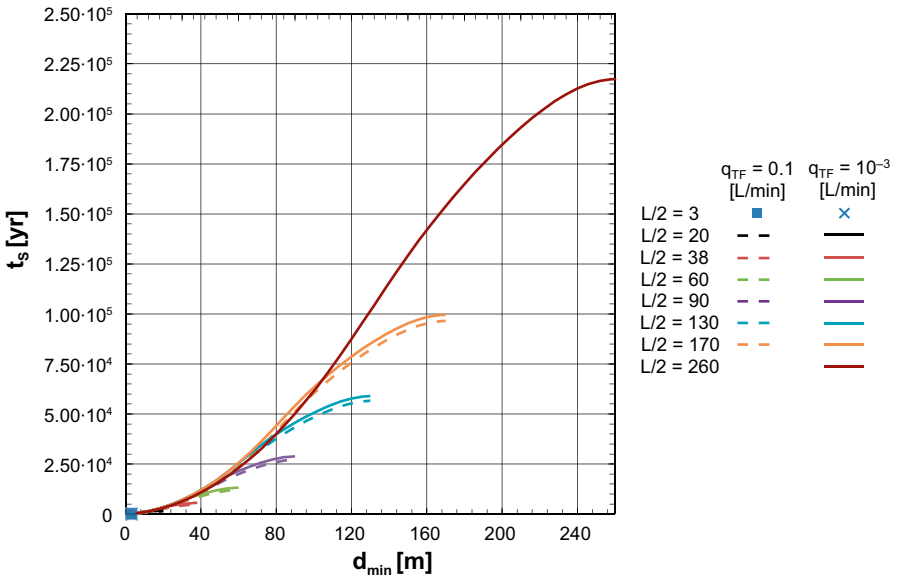

Figure 7-12. *The graph shows the saturation time as a function of distance to the nearest fracture, for seven different fracture separations. Solid lines correspond to a fracture inflow (under atmospheric conditions) q_{TF} = 0.1 L/min, and dashed lines to $q_{TF} = 10^{-3}$ L/min.*

Not included in Figure 7-12 are the results from the three models with $q_{TF} = 10^{-5}$ L/min (see Table 7-8). For such a low inflow one might assume that the saturation time is entirely controlled by the flow in the fracture, i.e. the bentonite can, at all times during the hydration process, take in all the water which the fracture provides per unit time. Hence, the buffer does not limit the inflow from the fracture. Under such conditions, the saturation time can to a good approximation be calculated analytically, by dividing the total available pore volume in the buffer with the steady-state fracture flow:

$$t_S = \frac{V_p}{q_{TF}} . \tag{7-15}$$

Here, V_p is the total available pore volume. We are, however, interested in the saturation time as a function of L/2, and hence we re-write Equation 7-15 on the form:

$$t_S = \frac{A_T \times 2 \times L/2}{q_{TF}}, \tag{7-16}$$

where A_T is the available pore area of the deposition tunnel. Taking the value $A_T = 5.9$ m^2 (which is valid for the case of maximum fallout (see e.g. Åkesson et al. 2010b) we find:

$$t_S = 2.245 \times 10^{-2} \times \frac{L/2}{q_{TF}} \tag{7-17}$$

where q_{TF} is measured in units of L/min. If we assume that q_{TF}, as measured during atmospheric conditions, is unchanged by the tunnel backfill, we can thus calculate t_S given q_{TF} using Equation 7-17.

The results from the three models with $q_{TF} = 10^{-5}$ L/min are shown in Figure 7-13. Also shown is the saturation time for each value of *L/2* as calculated using Equation 1-17. As is seen, the agreement is very good between the analytical solution and the numerical models. This reinforces the assumption made when deriving Equation 7-17, that the fracture flow, for such low inflows, is not significantly changed by the presence of the tunnel backfill.

Furthermore, the numerical simulations with $q_{TF} = 10^{-5}$ L/min show that the tunnel backfill reaches full saturation on a rather similar time-scale at all distances from the fracture (see Figure 7-13), hence t_S is independent of the distance d_{min} between the fracture and the deposition hole, and hence to a good approximation only depends on the fracture half separation, *L*/2.

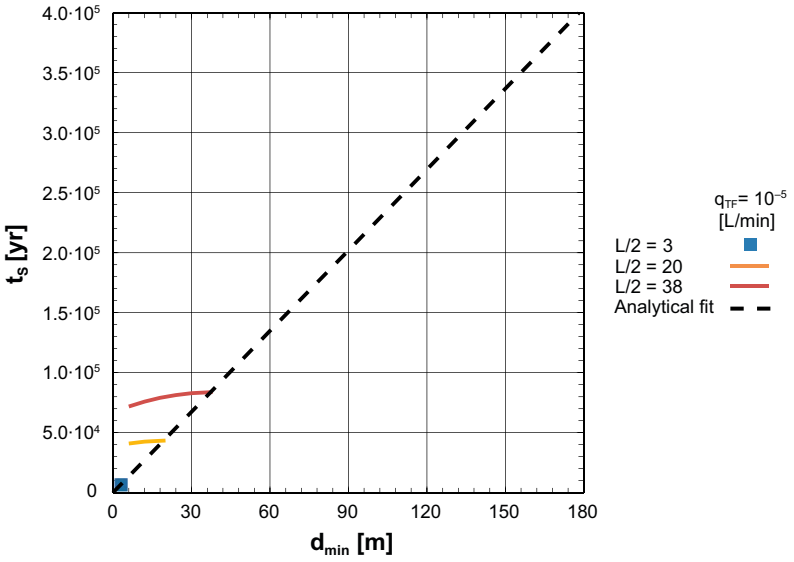

Figure 7-13. *The graph shows the saturation time as a function of distance to the nearest fracture, for three different fracture separations. Solid lines correspond to a fracture inflow (under atmospheric conditions) of q_{TF} = 0.1 L/min. The dashed line is an evaluation of Equation 7-17, which is used to determine the saturation time at distance L/2 from the fracture.*

The perhaps biggest limitation of the models presented here and in Åkesson et al. (2010b), with respect to calculating the saturation-time distribution is that we, because of the assumed symmetry, are not able to directly simulate the saturation process between two fractures with significantly different inflows. This is a common situation in the groundwater models and as such needs to be handled.

Comparing the saturation times for the same values of L/2 for fractures with different inflows it can clearly be seen that the models with $q_{TF} = 10^{-3}$ L/min (Figure 7-12) are saturated much faster than the models with $q_{TF} = 10^{-5}$ L/min (Figure 7-13).

Two examples of this are shown in Figure 7-14. In the left-hand graph, the ratio of saturation times for models with fracture inflow between $q_{TF} = 10^{-5}$ L/min (blue line) -10^{-6} L/min (red line) and $q_{TF} = 10^{-3}$ L/min is shown. As can be seen, the difference in saturation time between the different fractures is greatest for small values of L/2, whereas it decreases significantly at larger values.

In the right-hand graph, the saturation time of models with $q_{TF} = 10^{-5}$ L/min (blue lines) -10^{-6} L/min (red lines) are shown, where t_S have been normalised to the saturation time from the model with $q_{TF} = 10^{-3}$ L/min and $L/2 = 170$ m (dashed lines) and $L/2 = 260$ m (solid lines). The critical point here is that for fractures with $q_{TF} \leq 10^{-6}$ L/min the inflow is so low that if a fracture with $q_{TF} \leq 10^{-3}$ L/min is present anywhere in the tunnel, the latter will set the saturation time close to the low-flowing fractures, even if these are situated only a few meters apart. For fractures with $q_{TF} = 10^{-5}$ L/min the situation is somewhat more complicated, as these, if relatively closely spaced, can dominate the saturation process if the high-flowing fracture is far away.

However, we can conclude that for pairs of fractures where one has an inflow of $q_{TF} \geq 10^{-3}$ L/min and the other fracture's inflow is considerably lower, the saturation process is completely dominated by the high flowing fracture. Thus, without simulating the situation, the best approximation is to ignore the low-flowing fracture and calculate the saturation time due to the presence of the high-flowing fracture only. This is done by taking L/2 as the distance between the fracture and the tunnel entrance or end (depending on which side of the fracture the deposition holes is situated) and taking the distance between the deposition hole and the fracture, d_{min}, into account when reading off the saturation time from the models of the tunnel-backfill saturation (Figure 7-12).

In the situation where no high-flowing fractures are present, and hence the saturation time above a deposition hole situated in between two low-flowing fractures needs to be calculated, the approach used below is to take the average inflow of the two fractures and use this in Equation 7-17.

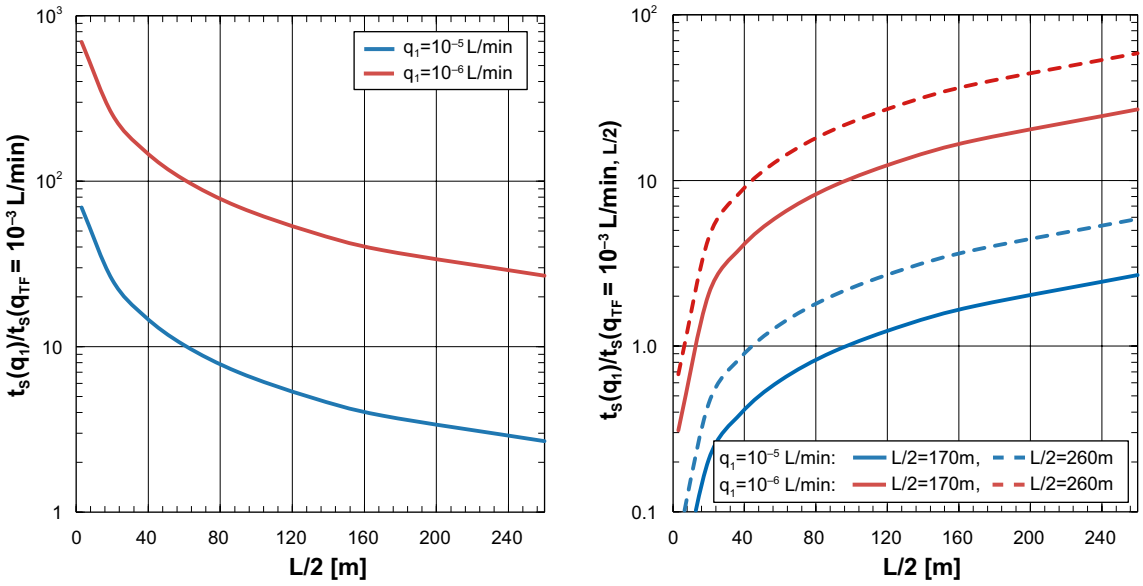

Figure 7-14. *The left-hand graph shows the ratio of saturation times as function of L/2 for different fracture flows (blue lines: $q_F = 10^{-5}$ L/min, red lines: $q_F = 10^{-6}$ L/min). The right-hand graph shows the saturation time for a fracture with inflow q_F, normalized to the saturation time measured for a fracture with $q_{TF} = 10^{-3}$ L/min and L/2 = 170 m (solid lines) and L/2 = 260 m (dashed lines).*

7.1.5 Distribution of saturation timescale

Using the model results presented above we are able to construct the expected distribution of saturation times. As a baseline we first construct the distribution assuming that no matrix flow is present. It is constructed using the following algorithm:

1) For each fracture realisation (i.e. the four different equi-probabilistic groundwater realisations r0, r2, r3 and r5 in Joyce et al. 2013) all deposition holes are looped over.
2) Each deposition hole is checked for intersecting fractures
   i. if there are intersecting fractures with an inflow higher than *0.1* L/min, the deposition hole is discarded,
   ii. if there are fractures with an inflow below *0.1* L/min, the saturation time t_{S_DHF} is taken from the results of the corresponding Code_Bright model.
3) Then, the saturation time in the pellets column of the tunnel backfill just above the deposition hole, $t_{S\_TF}(x_{DH})$ is analysed. This is done by looping over all tunnel fractures individually and calculating $t_{S\_TF}(x_{DH})$ in two ways:
   i. Under the assumption that the fracture in question is the only one intersecting the tunnel and thus *L/2* is the distance between the fracture and the tunnel entrance/end.
   ii. By pairing up the fracture in question with all other fractures in the tunnel separately. Here it is vital to take into account the difference in inflow between the fractures. Given two fractures with inflow q_{TF1} and q_{TF2} we use the following approach:
      a) If both q_{TF1} and q_{TF2} are greater than 10^{-4} L/min the saturation time is taken from the results presented in Figure 7-12.
      b) If both q_{TF1} and q_{TF2} are less than 10^{-5} L/min the saturation time is calculated using Equation 7-17 and by setting $q_{TF} = (q_{TF1} + q_{TF2})/2$. The tunnel is then assumed to reach full saturation simultaneously between the two fractures.
      c) If one fracture has an inflow greater than 10^{-4} L/min while the other doesn't, the ratio q_{TF1}/q_{TF2} is evaluated. If $0.1 < q_{TF1}/q_{TF2} < 10$, the saturation time is again calculated by taking the average inflow between the two fractures, now using the results presented in Figure 7-12. However, if $q_{TF1}/q_{TF2} > 10$ or $q_{TF1}/q_{TF2} < 0.1$ the fracture pair is discarded.

   The actual tunnel-backfill-saturation time at the position of the deposition hole is then taken to be the minimum value found.
4) The saturation time of the deposition hole is then taken as $t_S = \min(t_{S\_DHF}, t_{S\_TF})$
5) If no fractures intersect the tunnel or the deposition hole, the saturation time is set equal to infinity.

The resulting saturation time is calculated for all deposition holes in all four groundwater model realisations of the Forsmark repository, and the cumulative distribution is then calculated. The result is the grey solid line in Figure 7-15. As can be seen the distribution has a tail towards very long saturation times, these deposition holes are situated in tunnels with very few and low flowing fractures. A small fraction (less than one per cent) of the deposition holes has an infinitely long saturation time; these are the deposition holes situated in tunnels with zero intersecting fractures.

It is, however, unrealistic to exclude matrix flow when calculating the distribution of saturation times. Measurements of the hydraulic conductivity on borehole cores from Forsmark suggests that unfractured rock samples have hydraulic conductivities between $K_M = 5 \times 10^{-12}$–4×10^{-14} m/s under the conditions which prevail at repository depth. The saturation time of a deposition hole in the absence of fractures (i.e. through matrix flow only) has been calculated for $K_m = 10^{-11}$, 10^{-12}, 10^{-13} and 10^{-14} m/s using Code_bright models (see Section 7.1.4). These results are included in Figure 7-15 as the coloured intervals, which are bounded by the lower (dashed lines) and upper (solid lines) limits on the saturation time as calculated from the installation and homogenised models, respectively.

For a given value of K_m, the cumulative distribution, $f(t_S)$, has the shape of the "Only fractures" distribution (grey solid line) for $t < t_S(K_M)$, while for $t \geq t_S(K_M)$ it equals one.

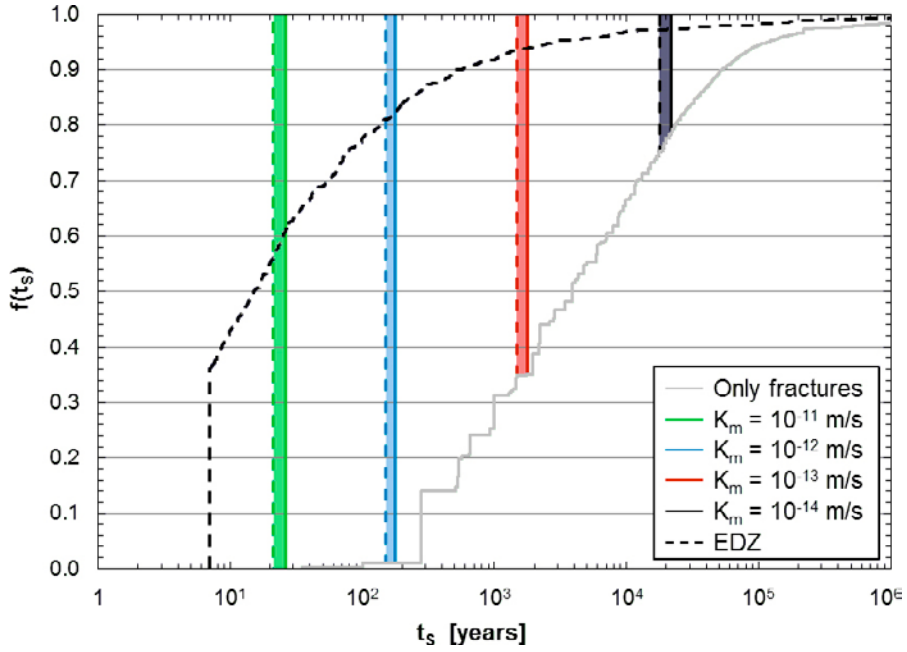

Figure 7-15. *The solid grey line identifies the cumulative distribution of saturation times, $f(t_S)$, in the Forsmark repository calculated assuming no matrix flow. The colored lines identify the time interval within which all deposition holes will reach full saturation if the matrix hydraulic conductivity has the value $K_m = 10^{-exp}$, where exp = {11, 12, 13, 14). The dashed black line identifies the distribution of saturation times if no flow resistance was present in the tunnels (see text).*

While this treatment is somewhat inaccurate since, if it is significant, the matrix flow will contribute to the fracture wetting and thereby change the shape of $f(t_S)$ for $t<t_S$, the error introduced should be relatively small.

Finally, given the rather long saturation times of a large fraction of deposition holes, it can be useful to estimate how quickly the saturation process would go if the water entering the tunnels via fractures had direct access to all parts of the tunnel instantaneously. An extremely transmissive and fully connected (along the tunnel axis) Excavation Damaged Zone (EDZ) could in theory lead to this situation. However, in Forsmark this will not be the case, as the design and construction of the repository will not allow for a highly connected EDZ to be present. More specifically the current design criteria specify that the "Excavation-induced damage should be limited and not result in a connected effective transmissivity, along a significant part (i.e. at least 20–30 m) of the disposal tunnel and averaged across the tunnel floor, higher than 10^{-8} m^2/s" (SKB 2010a). As an upper bound on how fast all deposition holes in theory could be saturated it is, however, still an interesting exercise.

If water entering through tunnel fractures is redistributed along the entire tunnel instantaneously, the saturation time of all deposition holes is to a first approximation given by the available pore volume in the deposition holes divided by the total tunnel inflow. However, this is only valid in tunnels with high inflows. If the total inflow is low, the water has time to redistribute within the bentonite, thereby leading to moisture equilibrium. The result is that the saturation time is given by the total available pore volume in the tunnel (i.e. tunnel-backfill pore volume + deposition-hole pore volume). Then the saturation time can be calculated as:

$$t_s = \frac{V_{p,tunnel}}{q_{tunnel}} \,. \qquad (7\text{-}18)$$

Here $V_{p,tunnel}$ is the total available pore volume in the tunnel and q_{tunnel} is the total inflow (through all fractures intersecting the tunnel in question) into the tunnel.

The available pore volume in the tunnel is taken to be the average volume of all tunnels (including deposition holes) and it is equal to 1.247×10^6 L (see Appendix 3). Calculating the saturation time using Equation 7-18, with the data on fracture inflows as given in the groundwater models of Joyce et al. (2013) as input, result in a saturation time less than 6.9 years for approximately 35 % of all deposition holes. This time is shorter than the saturation time of a deposition hole with free access to water (see Åkesson et al. 2010b) and thus not valid. In these cases, the saturation time is therefore set equal to 6.9 years. The resulting distribution is shown as the black dashed line in Figure 7-15. It can be considered as an upper limit on how fast the deposition holes in the repository could become fully saturated in the absence of matrix flow. As can be seen in Figure 7-15, even for this extremely unrealistic case a significant fraction of deposition holes still takes a very long time to saturate.

7.1.6 Conclusions

The distribution of saturation times expected in the Forsmark repository has been analysed using a combination of 1) fracture data from groundwater models of the site and 2) Code_Bright models of the saturation process of both the deposition-hole buffer and the tunnel backfill. The resulting distribution is shown in Figure 7-15.

As can be seen in Figure 7-15 the flow properties of the so-called matrix flow are crucial when determining the distribution of saturation times. Measurements of the hydraulic conductivity of the matrix (Vilks 2007) suggest that it lies between $K_M = 5 \times 10^{-12}$–4×10^{-14} m/s. In this range of values the effect can be summarised as:

- **High matrix conductivity ($K_m \geq 10^{-11}$ m/s):** only a tiny fraction of the deposition holes are saturated through direct fracture flow and none through water entering the deposition hole via the tunnel backfill. All deposition holes will have reached full saturation within approximately 27 years or less.
- **Intermediate matrix conductivity ($10^{-12} > K_m \geq 10^{-13}$ m/s):** between 10 % and 30 % of the deposition holes are saturated trough fracture flow or via water entering via the tunnel backfill. The remaining deposition holes are saturated primarily via matrix flow, all deposition holes are saturated between approximately 177 and 1 760 years.
- **Low matrix conductivity ($10^{-13} < K_m \geq 10^{-14}$ m/s):** A significant fraction (30–60 %) of all deposition holes are saturated via fracture flow or by water entering via the tunnel backfill. All deposition holes will have reached full saturation within approximately 22 000 years.
- **Extremely low matrix conductivity ($K_m < 10^{-14}$ m/s):** If the matrix conductivity would be extremely low almost all deposition holes will be saturated through fracture flow. Deposition holes situated in tunnels where there are no fractures will reach full saturation at a very late time, possibly after 10^6 years.

7.2 Task 1.5: Hydraulic connection between deposition holes

As part of the evaluation of SKB's license application, SSM has requested a clarification of the impact that hydraulically connected deposition holes may have on, for example, the saturation time. By hydraulic connection we here refer to the situation where two or more deposition holes are intersected by the same fracture. To analyse this question we must first answer two questions: 1) for which types of fractures is a hydraulic connection between two or more deposition holes important and 2) how common are such deposition holes in the Forsmark repository.

7.2.1 Relevant fracture flows

The main effect of the hydraulic connection is here assumed to be that the buffer in deposition holes upstreams in the fracture effectively dries out the fracture, significantly decreasing the fracture flow downstream. To approximately quantify when this effect may become important we must look at two aspects:

1) *The minimum required fracture flow:* In order for the hydraulic connection to be important it must be that the fracture intersecting the deposition holes have a high enough flow to be important for the saturation of the deposition hole.
2) *The maximum fracture flow that can be absorbed by a single deposition hole:* If the fracture flow is considerably higher than the flow which the bentonite can take up per unit time, the potential decrease in fracture flow due to water uptake in other deposition holes will not change the hydration evolution in the deposition hole considered.

We analyse these two limits on the fracture flow in further detail below.

The minimum required fracture flow

As a lower limit on the fracture flow which is interesting in this context, we can compare the saturation time due to fracture flow with the saturation time due to matrix flow. The magnitude of the matrix flow is set by the hydraulic conductivity of the matrix. The actual value of the matrix hydraulic conductivity in the Forsmark repository is, however, uncertain; a topic which was discussed in more detail in Section 7.1.2 above. As a reference we here assume that, on the scale used in the Code_Bright models of a single deposition hole as presented in Section 7.1.4, it is not lower than $K_m = 10^{-13}$ m/s.

The saturation time for $K_m = 10^{-13}$ m/s was calculated in Task 3 of Åkesson et al. (2010b). The saturation time is, however, not given as a single value, but rather as a minimum and maximum time, where the uncertainty arises from the swelling of the bentonite, which is not included in the models. The saturation time for $K_m = 10^{-13}$ m/s is calculated to be between 1 476 and 1 760 years.

In Section 7.1.4, the saturation time due to a single fracture flow is calculated. In these models, the matrix conductivity was set equal to $K_m = 10^{-14}$ m/s. Such a low value means that the matrix flow is extremely small, without the presence of a fracture it results in a saturation time between 17 742 and 21 873 years. Hence, when including a fracture in models with $K_m = 10^{-14}$ m/s the deposition hole is primarily hydrated through the fracture. The results of these models are:

Table 7-9. Time to 99 % saturation in the deposition-hole buffer (see also Section 7.1.4).

K_m [m/s]	$q_{F,0}$ [1)] [L/min]	t_s [years]
10^{-13}	[2)]	1476–1760
10^{-14}	[2)]	17 742–21873
10^{-14}	10^{-1}	636.2–1585.9
10^{-14}	10^{-3}	650.6–1 596.0
10^{-14}	10^{-5}	1 940.8–2 625.9

[1)] The fracture flow as measured during atmospheric conditions in the deposition hole.
[2)] No fracture was included in these models.

The results show that in deposition holes with fracture inflows less than 10^{-3} L/min (under atmospheric conditions), the saturation time is similar to that of a deposition hole which is not intersected by a fracture, but where $K_m = 10^{-13}$ m/s. Thus, in these holes the effect of any connections with other deposition holes does not significantly change the saturation evolution.

The maximum fracture flow

In the case of high fracture flows, the bentonite will very quickly reach full saturation just in front of the fracture. After that the inflow from the fracture cannot proceed faster than the rate at which water can be transported inside the bentonite to unsaturated parts of the buffer. This effectively puts a limit on the maximum inflow that a fracture can provide during the saturation process of the buffer. This effect is clearly seen in the model results presented in Table 7-9. The saturation time in the presence of a fracture with inflow (under atmospheric conditions) of 0.1 L/min is very similar to the saturation time in the presence of a fracture with inflow equal to 0.001 L/min. This can be further

seen if we plot the volumetric liquid flux through the fracture from all three fracture models included in Table 7-9; this is shown in Figure 7-16. The liquid flux is almost identical in the two models with $q_{F,0} = 0.1$ and 10^{-3} L/min, whereas it is considerably lower in the model with $q_{F,0} = 10^{-5}$ L/min. This suggests that the inflow is limited by the bentonite in the first two cases, but not in the latter.

Furthermore, it can be noted that the inflow into the bentonite is significantly lower than the open fracture inflow in the models with $q_{F,0} \geq 10^{-3}$ L/min, hence such fractures should not dry out even if connected to multiple deposition holes.

Range of relevant open fracture inflows

We may thus conclude that the case where a fracture intersects multiple deposition holes can only have a significant effect on the saturation process if the fracture flow, as measured during open conditions, is approximately between 10^{-3} and 10^{-4} L/min, assuming that $K_m \geq 10^{-13}$ m/s in the Forsmark repository, as is indicated by measurements of the hydraulic conductivity of bore hole samples taken at the site (Vilks 2007).

7.2.2 Prevalence of hydraulically connected deposition holes

To understand how common it will be that several deposition holes are intersected by a given fracture, we can use groundwater models of the Forsmark repository. In these, a fracture network has been generated given the data obtained from the surface-based site investigations at Forsmark. Here the fracture realisations r0, r2, r3 and r5 (which are equi-probabilistic realisations of the same DFN) from Joyce et al. (2013) have been used. More specifically we use the inflows and statistics on fractures intersecting deposition holes from these four realisations.

A first estimate of the prevalence of hydraulically connected deposition holes is given by the fraction of deposition holes that are intersected by one or more fractures. Taking all the data available from the groundwater models, neglecting EDZ fractures, and excluding deposition holes that share a fracture with four or more other deposition holes in the same deposition tunnel (as motivated by the Extended Full Perimeter Intersection Criterion) we find that about 10 % of all deposition holes are intersected by fractures.

However, as we are only really concerned with fractures where $10^{-4} < q_F < 10^{-3}$ L/min, this fraction falls to 2.6 %. Half (1.3 %) of these deposition holes are intersected by a fracture which intersects at least one or several deposition holes.

7.2.3 Effect of hydraulic connections

The fraction of affected deposition holes (1.3 %) is thus small enough that even if the effect on their saturation process were significant, the distribution of saturation times would hardly be affected.

Looking at the effect on the saturation time for an individual deposition hole we can again consider the numbers in Table 7-9. A deposition hole intersected by a single fracture with a flow of $q_F = 10^{-3}$ L/min is saturated about twice as fast as compared to the case with no fracture but with a rock matrix conductivity of $K_m = 10^{-13}$ m/s. Hence, for a given deposition hole intersected by a fracture which also intersects other deposition holes, the maximum effect, which occurs if a relatively high flowing fracture ($q_F = 10^{-3}$ L/min) is entirely dried out by the buffer in other deposition holes and hence all the water enters via matrix flow, is at most a doubling of the saturation time.

The effect of hydraulic connections between deposition holes is thus, in the most extreme case, that the deposition holes in question are saturated via matrix or through tunnel backfill flow rather than through fracture flow. Since, as is discussed in Section 7.1, the majority of the deposition holes in the Forsmark repository will be saturated via matrix flow or by water entering via the tunnel backfill, deposition holes with hydraulic connections, where the saturation process is slowed down significantly, will behave as if they belong to one of these categories instead.

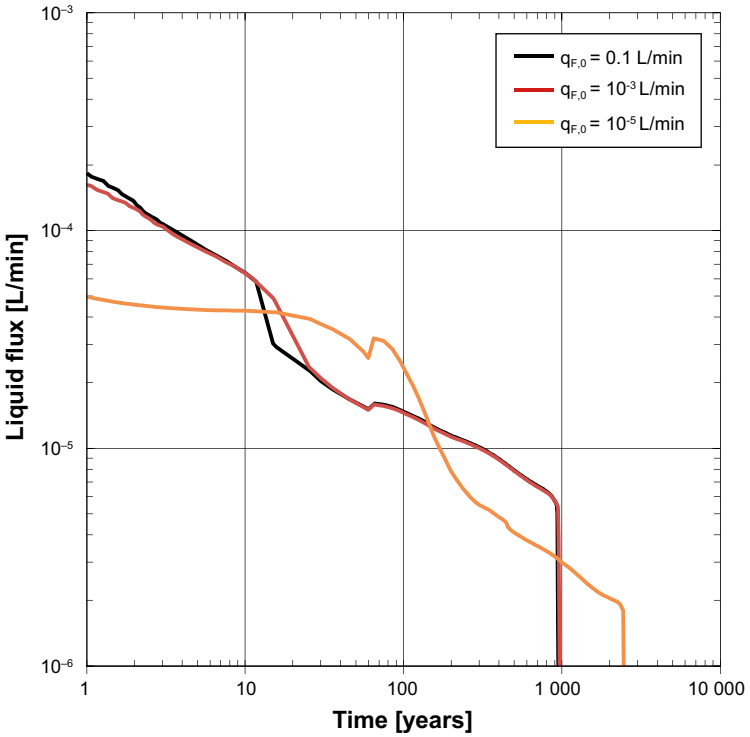

Figure 7-16. *The flow through the fracture as function of time after installation of the buffer in the Code_Bright models discussed in Section 7.1.4.*

8 Analysis of saturation intervals concerning long time safety during the hydration process

Ola Kristensson, Clay Technology AB

8.1 Introduction

The Swedish Radiation Safety Authority (SSM) points out that in Åkesson et al. (2010b), the buffer saturation process has not been directly evaluated in the light of long term safety (SSM2011-2426-81). Therefore, SSM requests an analysis where intervals in the saturation process are coupled to long time safety. SSM suggests that intervals in degree of saturation should be coupled to conditions/ events that promote long term safety such as: build up of pressure to reduce microbial activity, and closure of open gaps close to the canister and deposition hole (DH) wall.

The objective of the analysis in Åkesson et al. (2010b, Chapter 3) was "*Analyzing the time scale of buffer hydration"*, where buffer stands for the engineered barrier system within a DH. A number of different cases were studied by using pairs of thermo-hydraulic (TH) models. The TH-models were considered in pairs in order to somewhat account for effects of mechanics (M) without performing full THM-simulations. One of the TH-models in the pairs had properties corresponding to initial conditions and the other properties corresponding to fully homogenized conditions. This strategy was chosen in order to avoid dealing with about 15 detailed and fully coupled THM-simulations on a global scale since this type of modelling often is very challenging in terms of computational demand and numerical stability.

For enabling a structured comparison of the saturation process between models, the duration until the degree of saturation reached 99 % was listed for five points in the buffer for all models. Four of the points were geometrically specified and the fifth point was the last point within the buffer reaching 99 % degree of saturation. It should be noted that the fifth point may coincide with the other points.

In order to meet the request of SSM, providing an analysis where intervals in the saturation process are coupled to long time safety, local 1D axisymmetrical THM simulations are utilized to translate SKB's safety function criteria, expressed in pressure, into new criteria expressed in degree of saturation. These criteria are then applied on the global TH-models in order to evaluate the fulfillment of the safety functions.

The notes start with identifying relevant safety functions and their criteria as defined by SKB, and thereafter the strategy used to accomplish the analysis is outlined. Next, the processes coupled to homogenization, which occurs in the local models, are discussed and this is followed by describing how the new criteria were developed and refined. After this, the new criteria are applied to two cases considered in Åkesson et al. (2010b, Chapter 3), and the safety function fulfillment is discussed. Finally a summary of and conclusions drawn from the analysis are given.

8.2 Safety functions and corresponding criteria

Conditions/events that promote long time safety as suggested by SSM (build up of pressure to reduce microbial activity, closure of open gaps close to the canister and DH-wall) are related to the so called safety functions, safety function indicators, and safety function indicator criteria for the buffer as described in the SR-Site main report. The *Safety functions for the initial temperate period after closure*, their indicators, and indicator criteria for the buffer are (SKB 2011, Figure 8-2 and Section 10.3.16):

Buff1. Limit advective transport

i. Hydraulic conductivity $< 10^{-12}$ m/s

ii. Pressure > 1 MPa

Buff2. Reduce microbial activity

Density; high

Buff3. Damp rock shear movements

Density < 2 050 kg/m^3

Buff4. Resist transformations (requirement on temperature)

Temperature < 100 °C

Buff5. Prevent canister sinking

Pressure > 0.2 MPa

Buff6. Limit pressure on canister and rock

i. Pressure < 15 MPa

ii. Temperature > −4 °C

When it comes to Buff2, the criterion of a "high enough density", as specified in the SR-Site main report, has here to be expressed numerically in order to be able to be evaluated. So here, a criterion where density > 1 800 kg/m^3, as specified in "Buffer and backfill process report for the safety assessment SR-Can" (SKB 2006), will be used. It should be noted that this is not what is specified in (SKB 2011) and that there, it is pointed out that this type of criteria might not be a "true" indicator for the safety function.

The safety functions given above assume fully water saturated conditions, as stated in the SR-Site main report (SKB 2011, Section 10.3.8):

"*The safety functions for the buffer and backfill assumes a fully water saturated state. This should mean that the buffer and backfill need to be saturated to perform properly. However, no performance is needed from the buffer as long as the deposition hole is unsaturated, since no mass-transfer between the canister and the groundwater in the rock can take place in the unsaturated stage. The water saturation process itself has therefore no direct impact on the safety functions of the buffer and backfill.*"

Thus, with this in mind, analyzing the saturation process in the light of safety functions as defined by SKB might not be very meaningful. According to SKB's definitions it is only the final state of the saturation process, the saturated state, that matters for safety and for which the safety function indicator criteria have been designed.

It should, however, be mentioned that the condition of microbes at unsaturated states has not yet been scrutinized in detail. There is an ongoing project ("Gradientförsök") which addresses this issue, but no conditions are yet available, so currently an evaluation regarding this is not possible. Thus, dependent of the outcome of the ongoing microbe-project, safety function Buff2 might not only assume fully water saturated conditions, and might be extended with additional criteria.

Going back to what is given at the time when these notes are written, and studying the safety functions and theirs criteria, it can be seen that all but Buff4 (only given as a temperature criterion) are connected to restrictions on pressure (p) or density (ρ) at full saturation,

Buff1. Limit advective transport

$p > 1$ MPa

Buff2. Reduce microbial activity

$\rho > 1\,800$ kg/ m^3

Buff3. Damp rock shear movements

$\rho < 2\,050$ kg/m^3

Buff5. Prevent canister sinking

$p > 0.2$ MPa

Buff6. Limit pressure on canister and rock

$p < 15$ MPa

, respectively.

Among the criteria, the upper limits on pressure and density, given by Buff3 and Buff6, are more or less avoided by a suitable choice of initial state of the EBS and these are therefore not analyzed here.

The lower limits could be more relevant to investigate in the present context since the time when these limits are reached during the simulated saturation process may be studied. Again, however, it should be remembered that the "true" criteria as defined by SKB assume fully water saturated conditions. This is particular so for Buff5 since creep of the buffer material at unsaturated states must be considered insignificant and the criteria of this safety function will therefore not be evaluated. Thus, left to be studied are Buff1 and Buff2.

If adopting a highly simplified view on the hydro-chemo-mechanical processes in the buffer, by omitting path dependence present both in retention and mechanical behavior and also dependence on chemistry within the system, a "typical" one-to-one relation between density and pressure at full water saturation (a so called "swelling pressure curve") may be used. The lower density limit of 1 800 kg/m^3 may then be expressed as being approximately equal to a limit in pressure of 2 MPa (SKB 2006). Thus, the criteria to be investigated may be reformulated as:

Buff1: $p > 1$ MPa in order to limit advective transport

and

Buff2: $p > 2$ MPa in order to reduce microbial activity.

It is again stressed that the criterion related to Buff2 is not according to what is given in SKB (2011). The criterion used, obtained from SKB (2006), was chosen in order to have a numerical value for the analysis.

8.3 Strategy for the analysis

If to study when the criteria (pressures) are reached, the natural step would be to perform THMC-simulations, because pressure, within the system we look at, depends on all these processes. This is, however, out of scope of the present work, and would be a totally different task, much beyond the intention of the "original" described in Åkesson et al. (2010b, Chapter 3). There, the main objective was to analyze the time scale of buffer hydration, which was performed by direct consideration of TH processes and indirect consideration of mechanical effects, i.e. pressure is not available from these models.

Therefore, in the next chapter, plane axisymmetric THM-models, similar to those described in Åkesson et al. (2010b, Sections 3.4 and 5.4), will be used to develop criteria for Buff1 and Buff2 expressed in degree of liquid saturation, S_l. The new criteria, expressed in liquid degree of saturation, may then be applied on the global TH-models presented in Åkesson et al. (2010b, Chapter 3). The translation from "pressure criteria" to "degree of saturation criteria" is performed by evaluating the pressure criteria in the local THM-models and then trying to find a relation to degree of liquid saturation.

If omitting chemical aspects, except what may implicitly be regarded when choosing constitutive relations and parameter values, the problem formulation necessary for studying the present issue is in line with what already has been dealt with in Åkesson et al. (2010b, Section 3.4 and Chapter 5). There, plane and axisymmetrical THM-simulations were performed for a model representing a disc of buffer, similar to the KBS-3V design, at canister mid-height.

In this context it also seems relevant to remind about another part of the supplementary material to SR-Site requested by SSM, *Task 1.3 Description of how the "CRT-model" was used and how THM and TH models differ in terms of analyzing the hydration process*, since it relates to the studies undertaken in Sections 3.4 and 5.4 of Åkesson et al. (2010b).

The global and local models used in this study and their specific features are given in Table 8-1 and Table 8-2, respectively. Detailed information about the global and local models can be found in Åkesson et al. (2010b, Section 3.2) and Åkesson et al. (2010b, Section 5.4), respectively.

Table 8-1. Global models used in this study.

Model name	Model identification	GiD-dir.
2I	Initial state model, $K_R = 10^{-12}$ m/s	THsat13.gid
2H	Totally Homogenized state model, $K_R = 10^{-12}$ m/s	THsat14.gid
8I	Initial state model, $K_R = 10^{-13}$ m/s	THsat20I2.gid
8H	Totally Homogenized state model, $K_R = 10^{-13}$ m/s	THsat20H4.gid

Table 8-2. Local models used in this study. Model identification by the deviation in the pellet slot material representation from that of model CRT 6b in Section 5.4 of Åkesson et al. (2010b).

Model name	Model identification	GiD-dir.
TEP_new_12	K_{min} = 1 MPa, $k_{s0} = 0.1$, $\alpha_i = 0$	TEP_new_12.gid
TEP_new_14	K_{min} = 1 MPa, $\alpha_i = 0$	TEP_new_14.gid

8.4 Development of new criteria expressed in S_l

The purpose of the local THM models is to provide information for the development of representative criteria for Buff1 and Buff2 expressed in degree of liquid saturation, S_l. The first step is to formulate a first version of criteria based on obtained magnitudes of degree of liquid saturation when the pressure obtain the values 1 MPa and 2 MPa. In the next step, the times until the degree of liquid saturation criteria are fulfilled in global TH models (at canister mid-height) are compared with the times for which the pressure criteria of Buff1 and Buff2 are fulfilled for the local THM models. Based on the outcome of the comparison, the degree of liquid saturation criteria are evaluated and refined.

A schematic sketch illustrating the relation between the used models in this study is shown in Figure 8-1. To the left of the vertical hatched line we have models on a global scale. In theory, the most general model is a THM-model (which we here do not have access to), and somewhat less general are the available pairs of TH-models with immobile mechanical representations (Initial or Homogenized) presented in Åkesson et al. (2010b, Chapter 3). In the following, the pairs (2I, 2H) and (8I, 8H) will be considered. To the right of the vertical hatched line in Figure 8-1 the local scale THM-models are illustrated. As indicated in Figure 8-1, the local models will only be representative for a disc of buffer at canister mid-height, if the prescribed BCs are representative for the "global conditions" at this position.

The solutions of one pair of global TH-models, (2I, 2H), are utilized for designing BCs used in the local models. The global TH-models are described in detail in Åkesson et al. (2010b, Sections 3.2 and 3.3). In short, these models are considered a pair of base case models without explicit fracture representation and a lower choice of hydraulic rock conductivity ($K = 10^{-12}$ m/s). The extracted BCs at canister mid-height are: (1) radial heat flux at the canister surface, (2) temperature at the hole wall, and (3) liquid pressure at the hole wall, all three are shown in Figure 8-2.

As can be seen in Figure 8-2, the chosen conditions for the two models are quite alike. Thus, the mechanical representations of the buffer seem not to affect the TH-processes on the "outside" of the buffer to a great deal. Due to the similarities between the models' conditions, only the responses of 2H are used when designing BCs. In Figure 8-2, symbols indicate points between which linear interpolation was made when forming the BCs.

Model CRT_6b, described in Section 5.4 of Åkesson et al. (2010b), was used as the starting point for the local models. In these, however, the parameters of the mechanical material model of the pellet slot material had to be altered, as compared to CRT_6b, to produce a representative porosity profile at full water saturation, relevant for slow water saturation processes. To obtain estimates of representative averaged porosities for the block and pellet slot, the graph in Figure 5-14 in Åkesson et al. (2010b), repeated below in Figure 8-3, was used. The graph presented in Figure 8-3 was produced using the analytical model described in Section 5.3 of Åkesson et al. (2010b). The input to the analytical model was chosen as; block void ratio $e^b = 0.72–0.73$, pressure ratio $\alpha = 0.8–0.9$, and an assumption of a "parallel wetting process", which can be considered representing a slow wetting process. The obtained output, a range in pellet slot void ratio, became $e^p = 0.75–0.78$. Two local realizations, as defined according to Table 8-2, were developed in models denoted TEP_new_12 and TEP_new_14.

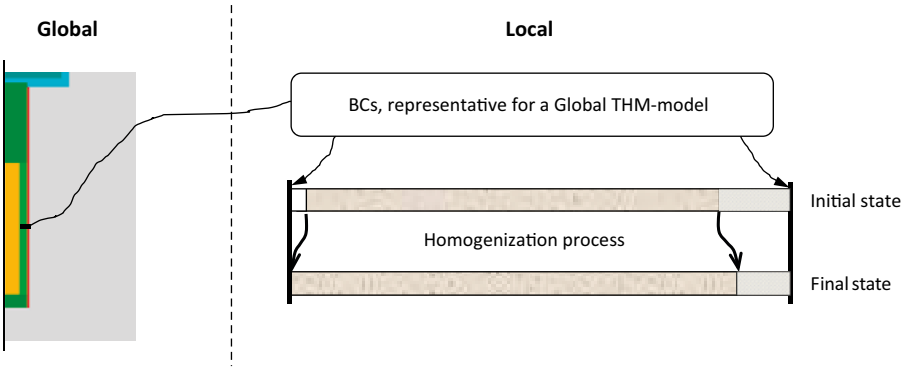

Figure 8-1. *Illustration of the relations between models used in this study. Global models are visualized to the left. To the right, a schematic local model geometry, to represent an axisymmetric disc at canister mid-height, is visualized. To the right of the schematic local geometry the states considered are indicated.*

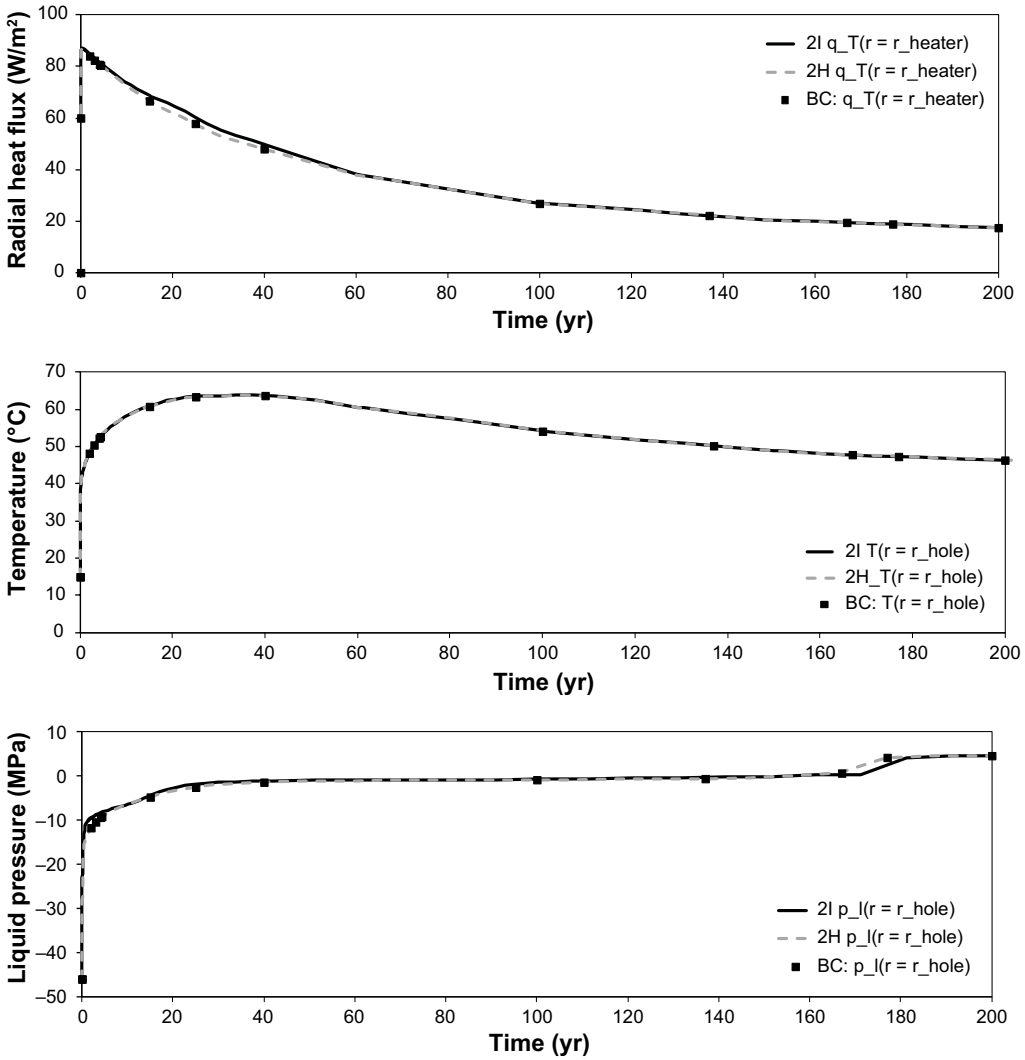

Figure 8-2. *Responses for the global models and corresponding boundary conditions for local models: radial heat flux at the canister surface (top), temperature at the hole wall (mid), and liquid pressure at the hole wall (bottom).*

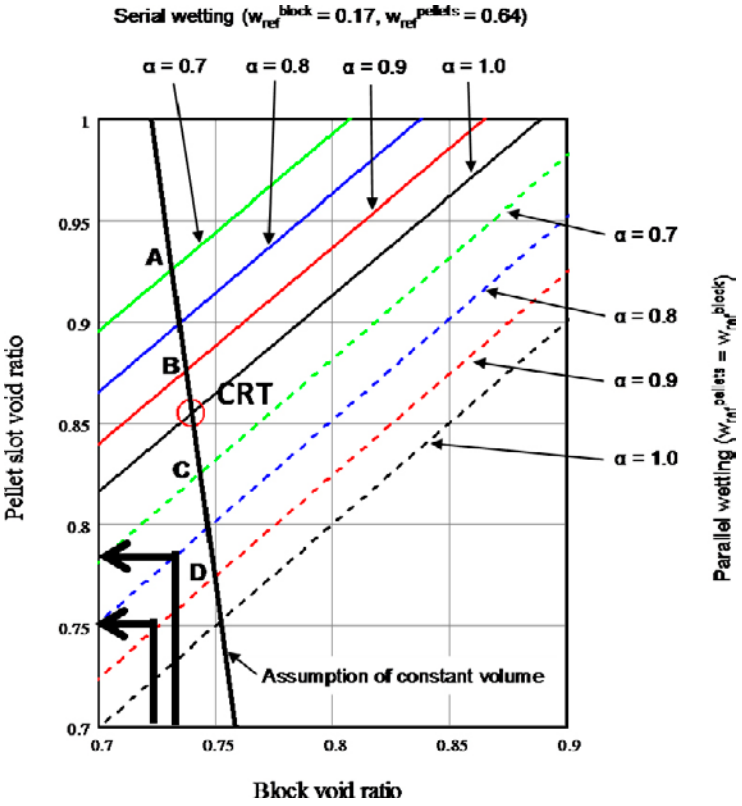

Figure 8-3. *Compilation of solutions using the analytical model described in Section 5.4 of Åkesson et al. (2010b). The black thick arrows indicate the pellet slot void ratios, e^p = 0.75 and e^p = 0.78, obtained from applying the input (e^b = 0.72, α = 0.9, parallel wetting) and (e^b = 0.73, α = 0.8, parallel wetting), respectively. This graph is a part of Figure 5-14 in Åkesson et al. (2010b).*

Before addressing the criteria translation from pressure to degree of saturation, we take the opportunity to study the mechanical process in the models in order to visualize the homogenization process and also where and when Buff1 and Buff2 are fulfilled in the models. It could also be mentioned that a mesh dependency study was performed for model TEP_new_12 by using three times the number of elements radially in the pellet slot and block volumes in a new model (TEP_new_12_fine). No significant mesh dependency could be seen as shown in 0.

8.4.1 Local model responses

The graph at the top in Figure 8-4 shows void ratio profiles obtained after completed simulations together with the initial void ratio profile. Also, two arrows indicate the change in position and void ratio for two points in the TEP_new_12 model. Comparing with the initial state, the buffer has evolved into a considerably more homogenized state. The pellet slot material has been compressed by the "more strongly" swelling block material. The left arrow, showing initial and final state of a point in the block close to the initially open inner slot, indicates the swelling character in this part of the buffer. The right arrow, belonging to the pellet slot, indicates the compression taking place in this part of the buffer.

The lower part of Figure 8-4 is a blow-up of the final state in terms of void ratio. Beside the numerical models results, given as profiles (symbols) and volume averages (black lines),

$$\mathrm{VA}(\cdot) \equiv \frac{1}{V}\int (\cdot)\,dV, \tag{8-1}$$

over the block and pellet slot, also the analytical solutions, obtained from using the information in Figure 8-3, are given (grey thick lines). The pellet slot representations as described in Table 8-2 were chosen as to generate volume averages in close agreement with the analytical solutions, and as can be seen this is also the case.

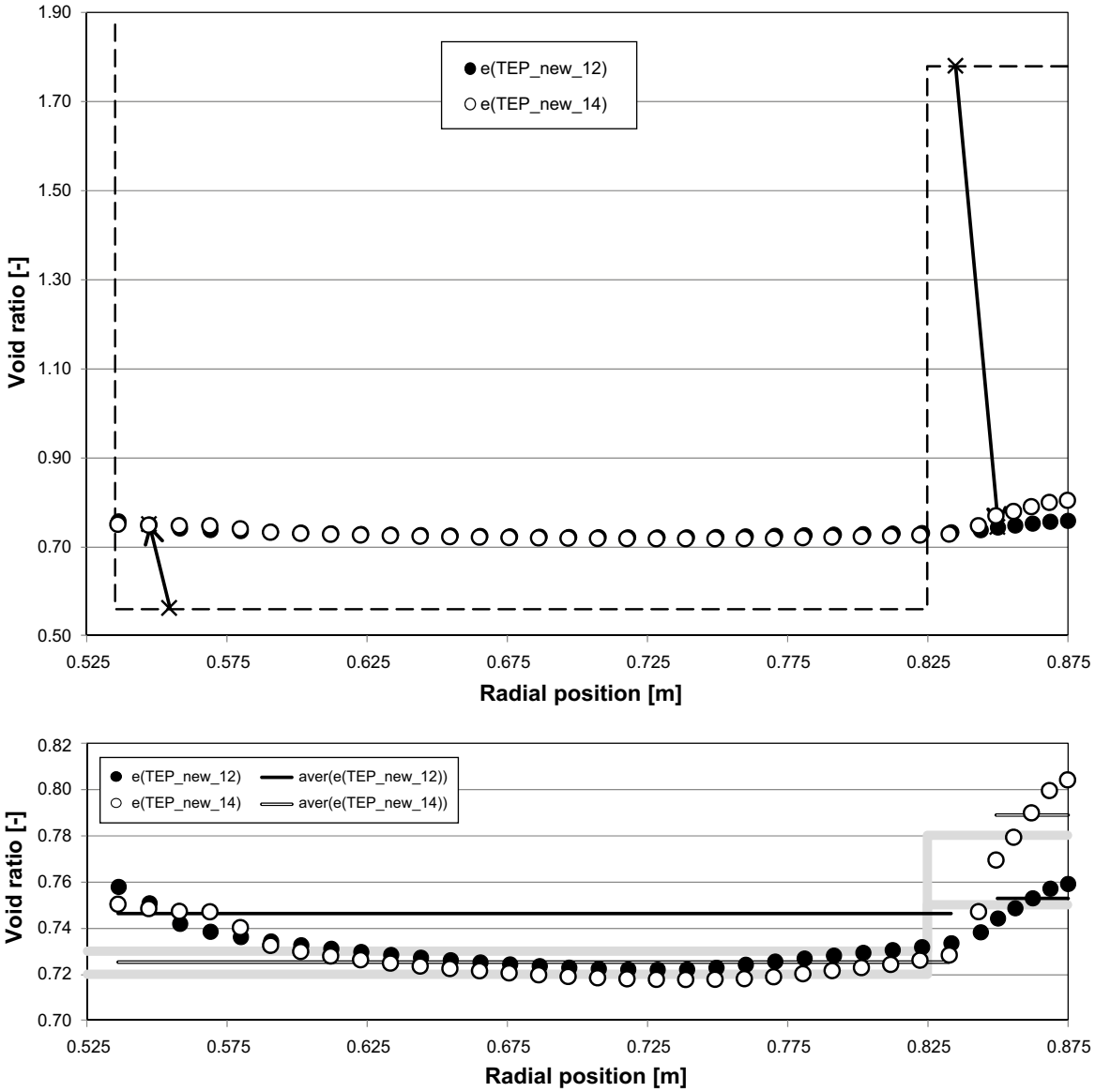

Figure 8-4. *Void ratio profiles obtained for the two local models at full simulation time. The initial profile (hatched line) and the two solutions (symbols) are shown at top where the arrows indicate initial and final states for two different nodes belonging to TEP_new_12. The bottom graph shows a close up at the final state for both models (symbols) with the analytical solution (grey thick line) also indicated as well as the volume averages (thin lines) over block and pellet slot for the model solutions.*

One more check of the agreement between the analytical and numerical solutions can be performed by comparing the pressure ratio $\alpha = p_p/p_b$. In the analytical solution the pressure ratio, given by the ratio of volume averages of pressure over the pellet slot and block, was chosen as $\alpha = \{0.8, 0.9\}$. For both local models $\alpha = 0.85$ which clearly agrees well with the input to the analytical model.

To visualize the closure of the open gap close to the canister and the homogenization process of the buffer, Figure 8-5 shows the path of material particles (grey lines), initially positioned with equal distances, for both local models. The interfaces (inner empty gap, block) and (block, pellet slot) are also indicated (solid black lines). An isoline consisting of (time, position)-pairs, for which the deformation is 0.99 of the final deformation is also given in Figure 8-5 (hatched line with symbols). Solution data are given in Table 8-3.

When studying the particle paths, it can be seen that the deformation of the block material can be thought of as belonging to two modes: (1) swelling into the pellet slot and (2) inner slot closure. Initially, an instant rapid compression of the pellet slot can be seen when the outer part of the block

takes up water and expands. When water reaches further in, the open inner slot begins to close and finally the block has expanded all the way to the canister. The two "deformation modes" listed above act in different directions, thereby the visible kink on the particle paths at the time when the inner slot closes.

As for the character of the final stage of deformation it can be somewhat understood by studying the appearance of the isoline. The most obvious feature is that the material close to the canister is the first to cease deforming with the extreme at the inner slot closing after 11–14 yr. At radii < 0.625 m there is, with increasing radius, a gradual halt of the deformation from 11–14 yr to about 154 yr, which also is the maximum value for the entire buffer. For radii > 0.625 m the halt of the deformation is taking place "more simultaneous", in a time range about 120–145 yr.

To visualize when and where Buff1 and Buff2 are fulfilled in the models, Figure 8-6 shows isolines with elements (time, initial radial position) for which $p \approx 1$ MPa (solid) and $p \approx 2$ MPa (hatched). Solution data regarding this analysis are also given in Table 8-3.

The most conspicuous feature of both isolines is the distinct difference for block and pellet slot. The pellet slot material reach the pressure levels significantly later as compared to neighboring points in the block material. If this is in accordance with reality or just a manifestation of the adopted material representation is, however, not known. Another obvious general feature is the evolution of attaining the pressure levels, first occurring in the outer part of the block material and then progressing inwards. As can be seen, there is some divergence from this trend for $p \approx 1$ MPa in the inner part of the block material close to the initially open inner slot.

It is again stressed that the behavior described above concerns models, and that it is unknown to what degree this agrees with what occur in reality.

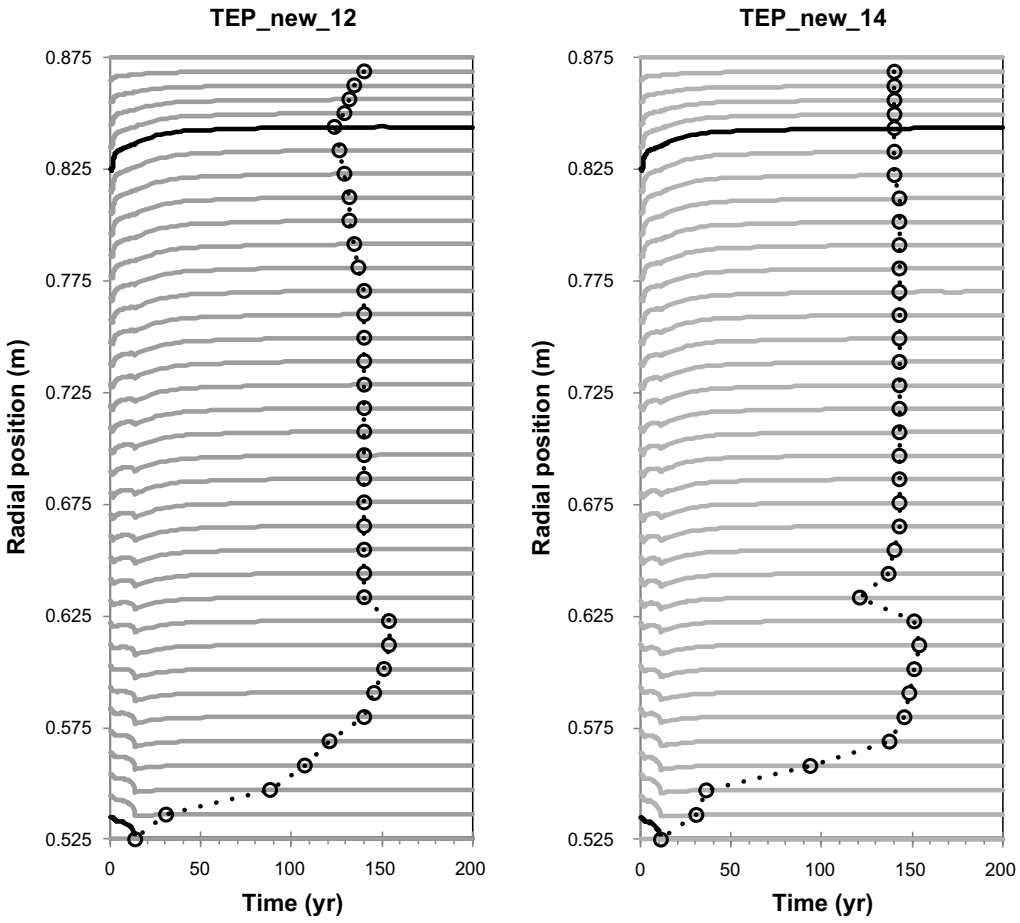

Figure 8-5. *Local models deformation evolution (solid lines) and isoline consisting of (time, position)-pairs for which the deformation is 0.99 of the final is indicated (hatched),i.e.* $t(|u_r|) \approx 0.99 \times |u_r(t = 200)|$.

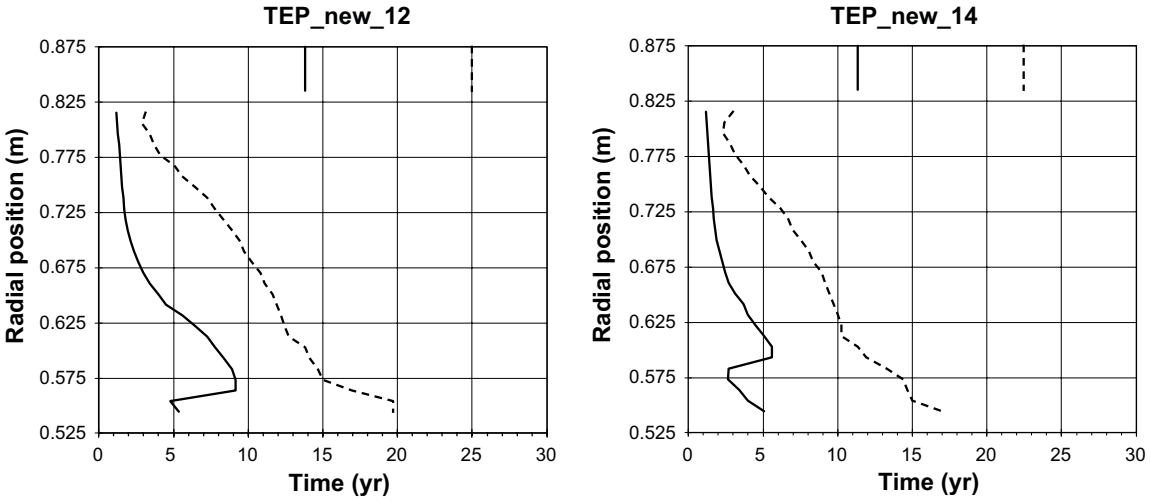

Figure 8-6. *Local model isolines consisting of (t,r_0)-pairs for which $p \approx 1$ MPa (solid) and $p \approx 2$ MPa (hatched).*

Finally, in order to develop new Buff1 and Buff2 criteria expressed in terms of degree of liquid saturation, the relation of this variable to pressure has to be established. To facilitate this, a procedure similar to what was done when producing the graphs in Figure 8-6 is utilized. This is based on visualization of when and where Buff1 and Buff2 are fulfilled in the models, again using isolines for which $p \approx 1$ MPa and $p \approx 2$ MPa, but this time the isolines consist of (degree of liquid saturation, initial radial position)-pairs, see Figure 8-7. In the graphs the initial state of the block and pellet slot material is also indicated for reference. Solution data regarding this analysis are given in Table 8-3.

Again, as also was the case when studying the graphs in Figure 8-6, the block and pellet slot materials show distinct differences. In Figure 8-7 the pellet slot material attains the criteria at a considerable lower degree of saturation as compared to the block material and the isolines also span over a large range which indicate that S_l is not an ideal indicator for pressure in these systems. The lower pressure isoline of the block material has a peculiar feature in the inner part. The lower pressure level (1 MPa) is actually obtained for S_l equal to the initial value S_l^0. Most likely, this comes from the character of the homogenization process where the dry and stiff inner part of the block is compressed by swelling of outer parts and therefore the pressure increases despite no local water uptake in the inner part. This also indicates that S_l is not an ideal indicator for pressure in these systems.

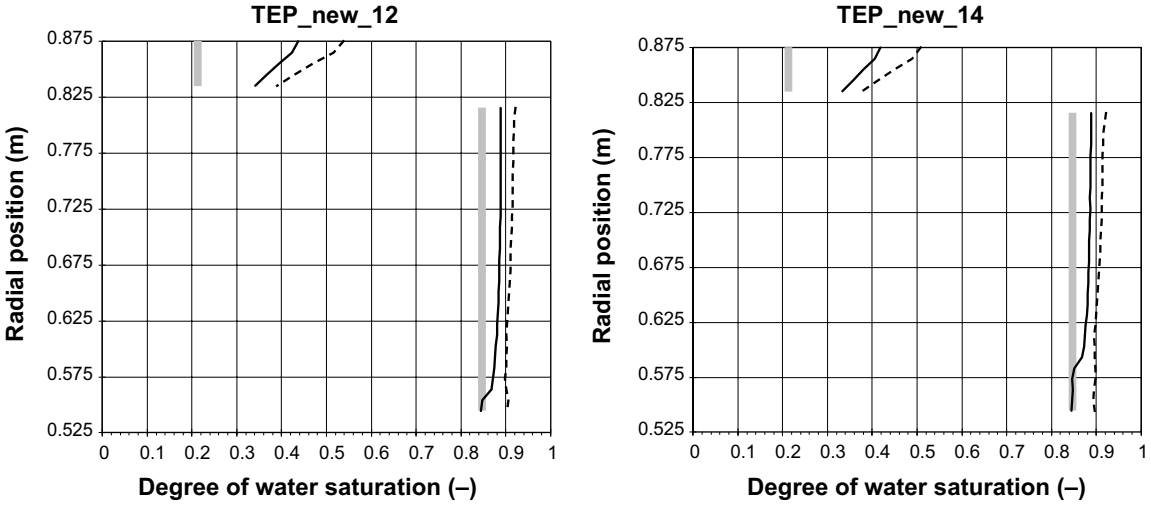

Figure 8-7. *Local model isolines consisting of (S_l,r_0)-pairs for which $p \approx 1$ MPa (solid black) and $p \approx 2$ MPa (hatched) and initial state (grey).*

Table 8-3. Solution data for the local models.

Criterion	Model: TEP_new_12		Model: TEP_new_14	
	Block	Pellet slot	Block	Pellet slot
$\lvert u_r \rvert \approx 0.99 \times \lvert u_r(t=200) \rvert$	t = {14, 154} yr	t = {124, 140} yr	t = {11, 154} yr	t = 140 yr
$p \approx 1$ MPa	t = {1.2, 9.2} yr S_l = {0.85, 0.89} VA(S_l)= 0.88	t = 14 yr S_l = {0.34, 0.44} VA(S_l) = 0.39	t = {1.2 , 5.6} yr S_l = {0.85, 0.89} VA(S_l) = 0.88	t = 11 yr S_l = {0.33, 0.42} VA(S_l) = 0.38
$p \approx 2$ MPa	t = {2.9, 20} yr S_l = {0.90, 0.92} VA(S_l) = 0.91	t = 25 yr S_l = {0.39, 0.54} VA(S_l) = 0.47	t = {2.3, 17} yr S_l = {0.89, 0.92} VA(S_l) = 0.91	t = 23 yr S_l = {0.39, 0.54} VA(S_l) = 0.45

8.4.2 Development of new criteria

First, just to remind the reader, the overall objective is to define intervals in degree of saturation coupled to conditions/events that promote long term safety. The safety functions defined by SKB may be related to criteria expressed in terms of pressure. The task here then is to translate the pressure criteria to criteria given in terms of degree of saturation.

With the former discussion related to the results in Figure 8-7 in mind, clearly, there exist potential objections for using S_l as a general indicator of pressure. A one-to-one correspondence certainly not exists. In order to reach the objective set out for, a concept of intervals in degree of saturation corresponding to a certain magnitude in pressure will be used.

Since the global and local models do not correspond exactly in terms of initial degree of saturation, S_l^0, relative degree of saturation,

$$S_l^{rel} \equiv \frac{S_l - S_l^0}{1 - S_l^0}\ , \tag{8-2}$$

will be used when formulating the criteria. In order to obtain criteria manageable when evaluating the global models, they will be formulated in terms of volume averages of relative degree of saturation, VA(S_l^{rel}), over the block material and pellet slot material. During the investigation it was found convenient to work in terms of VA(S_l), given in Table 8-3, and S_l^0 instead of VA(S_l^{rel}) using the relation,

$$\mathrm{VA}\left(S_l^{rel}\right) = \frac{1}{1 - S_l^0}\left(\mathrm{VA}(S_l) - S_l^0\right). \tag{8-3}$$

The chosen criteria formulated in terms of a range in VA(S_l^{rel}) defined by minimum and maximum values. These values are obtained from evaluating the S_l^{rel}-response of the local models. A single criterion is defined by,

criterion ≡ {minimum, maximum}

minimum ≡ VA(S_l^{rel})−(max(S_l^{rel})−VA(S_l^{rel}))

maximum ≡ max(S_l^{rel})

When calculating the criteria based on the expressions above, the values given in Table 8-4 are obtained.

Table 8-4. First version of new Buff1 and Buff2 criteria expressed in terms of relative degree of liquid saturation for the block and pellet slot materials.

	Criterion expressed in p	Criterion expressed in VA(S_l^{rel})	
		Block	Pellet slot
Buff1	≈ 1 MPa	{0.145, 0.278}	{0.165, 0.285}
Buff2	≈ 2 MPa	{0.302, 0.487}	{0.225, 0.414}

Figure 8-8 shows the criteria graphically, indicated by the grey solid and grey hatched lines, for Buff1 (solid grey) and Buff2 (hatched grey), respectively. The criteria are shown together with the same information as Figure 8-7, but now expressed in terms of S_l^{rel}. As the criteria are designed, they exclude the "tail" of low values of saturation in the block material close to the canister. The criteria are considered on the conservative side in the sense that they most likely overestimate the time until Buff1 and Buff2 are fulfilled.

8.4.3 Evaluation and refinement of new criteria

The first versions of the new criteria, expressed in VA(Slrel), are here to be evaluated. Time intervals when the new Slrel criteria are reached in the global models, 2I and 2H, are compared with time intervals when the criteria expressed in p are reached in the local models, TEP_new_12 and TEP_ new_14. The analysis is performed at canister mid-height of the global models in order to obtain as clear comparison to the local models as possible.

In Figure 8-9 the global model response in terms of volume averages of relative degree of liquid saturation formed over the block and pellet slot at canister mid-height, as well as the first version criteria as listed in Table 8-4 are shown. As for the pellet slot it was discretized using two elements radially, thus three nodes where two belong to interfaces and the mid node belong to the pellet slot material solely. The volume average is therefore taken as the result at the mid-node. The time intervals obtained from applying the criteria in Table 8-4 on the evolution curves in Figure 8-9 are listed in Table 8-5.

Table 8-5. Obtained times (in years) when the adopted S_l criteria are fulfilled for global models 2I and 2H.

	Model: 2I		Model: 2H	
	Block	Pellet slot	Block	Pellet slot
Buff1	t={1.8, 3.4}	t={5.8, 16}	t={5.5, 12}	t={0.058, 0.22}
Buff2	t={3.7, 6.8}	t={13, 23}	t={13, 22}	t={0.26, 2.3}

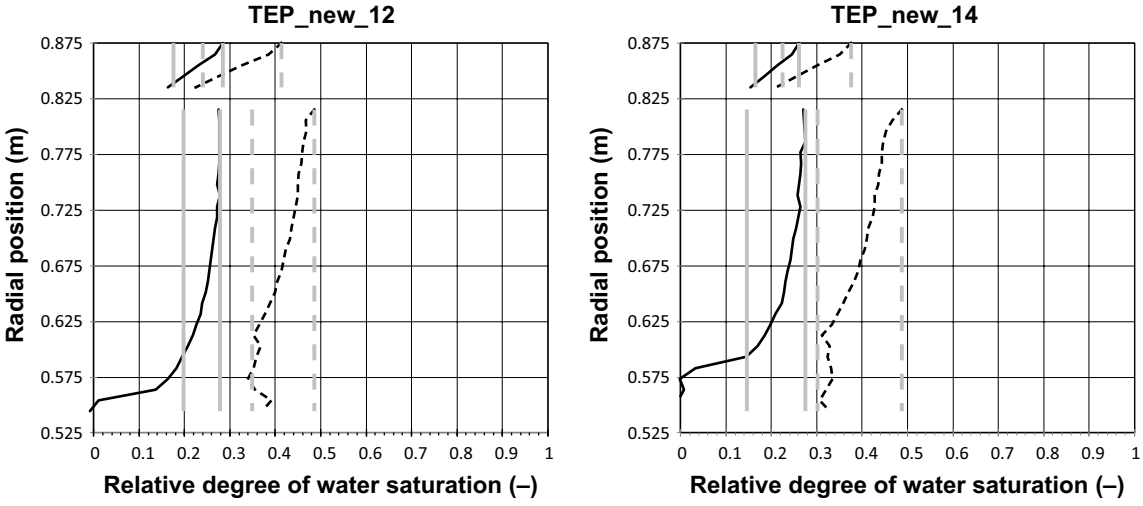

Figure 8-8. *Local model isolines consisting of (S_l^{rel},r_0)-pairs for which p ≈ 1 MPa (solid black) and p ≈ 2 MPa (hatched black). Also, the adopted minimum and maximum limits are indicated in solid and hatched grey lines, for Buff1 and Buff2, respectively.*

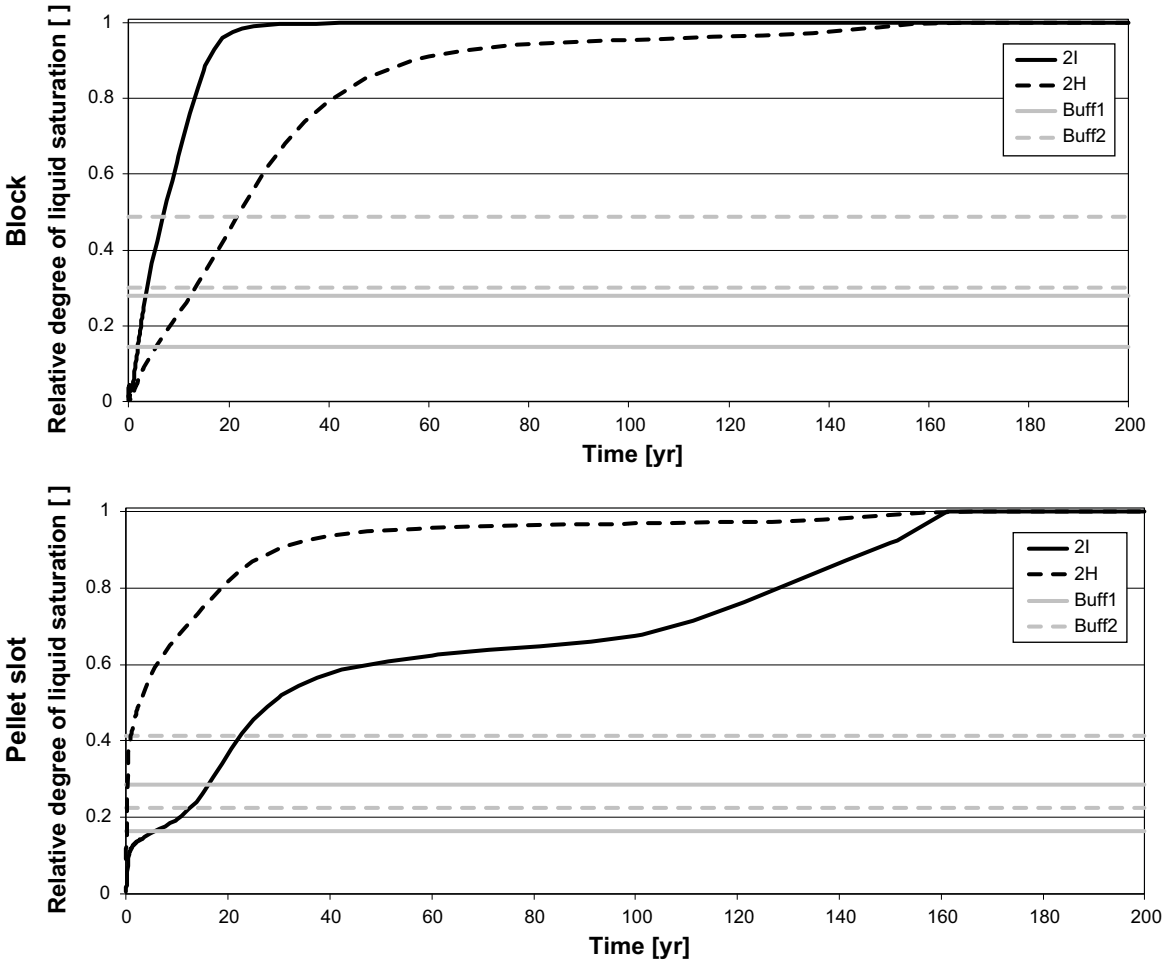

Figure 8-9. *Evolution of volume averages of relative degree of liquid saturation, $VA(S_l^{rel})$ for global models 2I and 2H are shown together with the first version of S_l criteria. The volume averages over the pellet slot and buffer are formed at canister mid-height.*

Plotting the time intervals when the p and S_l criteria are reached in the block and pellet slot materials for the local models (in grey) and global models (thin black lines), gives the diagrams shown in Figure 8-10. In addition, the thick black lines indicate combined considerations of both global models, i.e. overall maximum and minimum values for both global models.

For the block material, the global models together with the first version criteria produces time intervals for Buff1 and Buff2, which are in good agreement with those of the local models. Therefore, no adjustments are made to the first version criteria for the block material.

For the pellet slot material, the global models together with the first version criteria do not match the results of the local models well for either Buff1 or Buff2. For Buff1 the homogenized global model (2H) severely underestimates the time until Buff1 is reached, whereas the time interval of the initial state model (2I) includes the local time interval. For Buff2, however, the time until fulfilment is significantly underestimated by 2H and somewhat underestimated by 2I. An adjusted criterion is therefore regarded necessary for the pellet slot material.

To get better correspondence between the global and local time intervals for the pellet slot material without complicating things too much, the maximal criterion of Buff2 is chosen equal to that of the block material ($VA(S_l^{rel}) > 0.487$) and only the initial state model (2I) is considered in the "combined" consideration.

The result from these adjustments can be seen when studying Figure 8-11 and the final version of the criteria, used in the evaluation, is shown in Table 8-6.

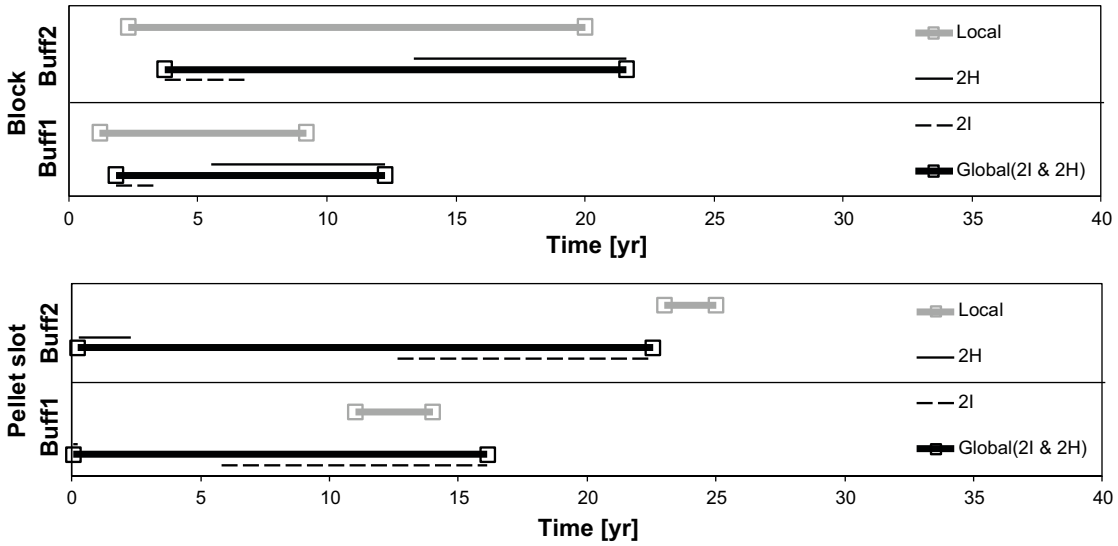

Figure 8-10. *Time intervals when the first version criteria are reached for the local models (grey) and global models, 2I (thin black solid) and 2H (thin black hatched). The thick black solid lines indicate the time intervals resulting from using the combined result of both global models. Note that the criteria generating the above are expressed in pressure for the local (THM) models and in degree of liquid saturation for the global (TH) models.*

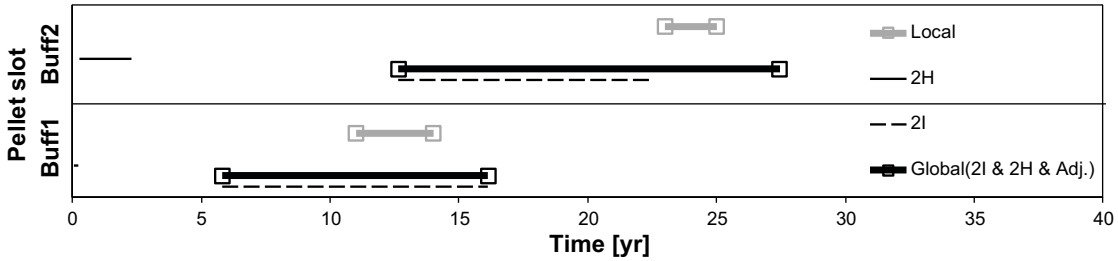

Figure 8-11. *Time intervals when the adjusted pellet slot criteria limits are reached for the local models (grey) and global models, 2I (thin black solid) and 2H (thin black hatched). The thick black solid lines indicate the time intervals resulting from using the adjusted pelllet slot criteria where only the time interval of 2I is considered. Note that the criteria generating the above are expressed in pressure for the local (THM) models and in degree of liquid saturation for the global (TH) models.*

The adjustments described above might seem rough, but it should be remembered that the homogenized global model has a very oversimplified representation of the pellet slot material and by disregarding this one may say that a higher degree of accuracy has been obtained. Also, when using the adjusted criteria, the global time intervals include the corresponding local time intervals and obtain lower limits closer to the local model intervals.

Table 8-6. Final version of adjusted Buff1 and Buff2 criteria expressed in terms of relative degree of liquid saturation for the block and pellet slot materials.

	Criterion expressed in p	Criterion expressed in VA(S_l^{rel})	
		Block	Pellet slot*
Buff1	≈ 1 MPa	{0.145, 0.278}	{0.165, 0.285}
Buff2	≈ 2 MPa	{0.302, 0.487}	{0.225, 0.487}

* Only the results of the initial state model are to be considered for the pellet slot material.

8.5 Investigation of fulfilment of Buff1 and Buff2 in global TH models

The fulfilment of the criteria is studied at a number of positions in the DH-buffer as shown in Figure 8-12. There are five positions at different heights: below canister, mid canister, above canister, top of buffer, and top of deposition hole, and three "radial positions" (or rather cross-sectional areas): inner block (IB), outer block (OB), and pellet slot (P), for which the criteria are evaluated. It is assumed that due to the geometric and structural similarity at different heights, the criteria found relevant at canister mid-height, shown in Table 8-6, also can be used to obtain reasonable estimations at other positions as well. Moreover, the influence of the open slot, not present in the buffer below and above the canister, was suppressed when designing the new criteria. This should bring the state for which the criteria were designed "closer to" what the cylinder-shaped blocks "experience".

Two different cases have been considered, first, the case with a hydraulic conductivity of the rock equal to $K_R = 10^{-12}$ m/s, represented by models 2I and 2H, and secondly, a case with a hydraulic conductivity of the rock equal to $K_R = 10^{-13}$ m/s, represented by models 8I and 8H. Since the criteria were developed using a 1-D model which was calibrated to represent a slow wetting process, it is here assumed that the criteria, verified for $K_R = 10^{-12}$ m/s, are valid for systems using the lower hydraulic conductivity, $K_R = 10^{-13}$ m/s, as well.

For the case where $K_R = 10^{-12}$ m/s (model 2I and 2H), the results are given in graphical and tabulated form in Figure 8-13 and Figure 8-14 for Buff1 and Buff2, respectively. The shaded regions with different outlines (solid, hatched, and dot-hatched) for the different buffer volumes as defined in Figure 8-12 (IB, OB, and P, respectively) represent what will be called "criteria fulfilment surface" (CFS).

As clearly seen in Figure 8-13 and Figure 8-14 when studying the appearance of the pellet slot CFS, there is a general trend, for both Buff1 and Buff2, in that the criteria are fulfilled "from the bottom to the top" in the pellet slot. The time intervals of the pellet slot are also generally later in time when comparing with the other material volumes at the same height, the only exception being at the bottom for Buff1.

Another common feature for Buff1 and Buff2 is the shift to the right of the inner block CFSs' (thus, its later occurrence in time) as compared to the outer block's, with the exception at the top position for both Buff1 and Buff2. The overall shape of the CFSs is also similar between Buff1 and Buff2. A distinct kink in the inner block's CFS, delaying the fulfilment, is present in the position above the canister for Buff1 and Buff2. On the other hand, at the same position, the outer block CFSs are shifted towards an earlier fulfilment.

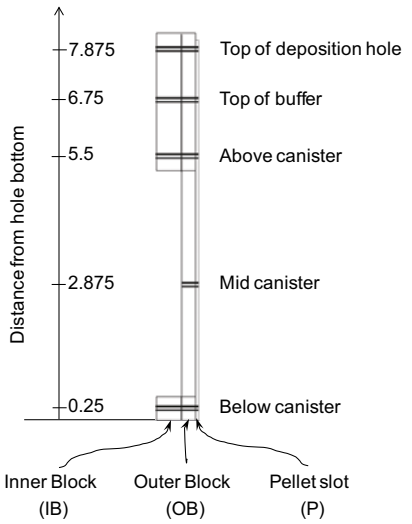

Figure 8-12. *Positions and notation regarding where the criteria are evaluated for the global models.*

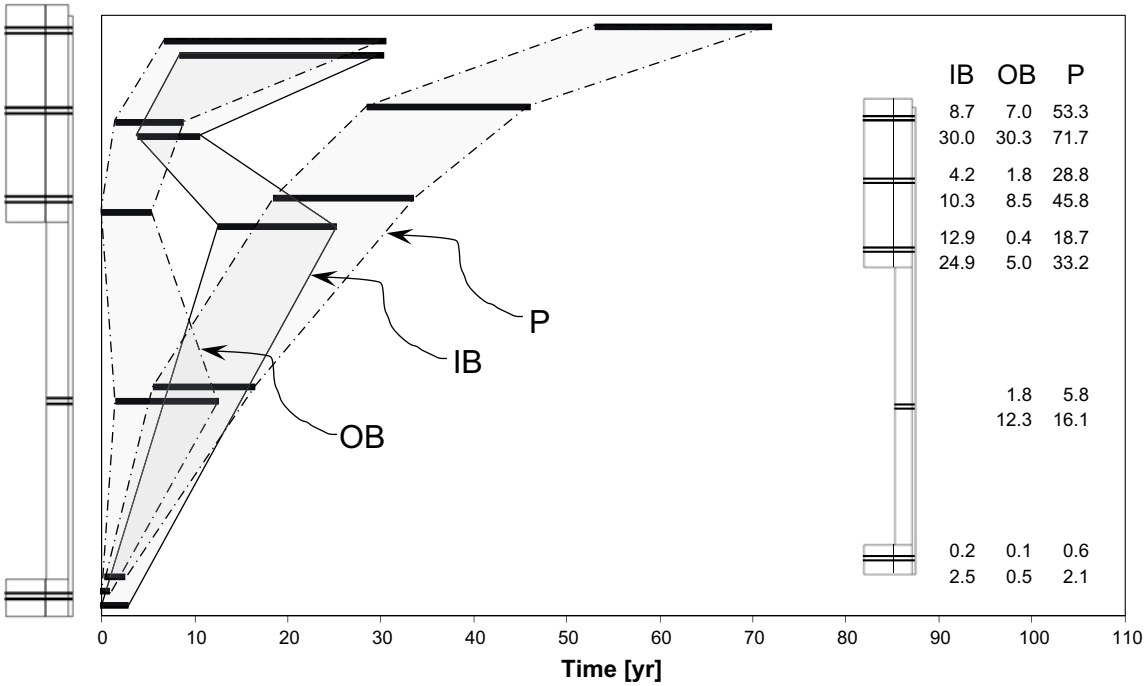

Figure 8-13. *Compilation of estimated time intervals for which safety function Buff1 are reached at the indicated positions for models with rock conductivity 10^{-12} m/s and no fractures, i.e. 2I and 2H in Åkesson et al. (2010b, Chapter 3). In the table to the right the start (top) and end (bottom) of the time interval are given for each of the positions.*

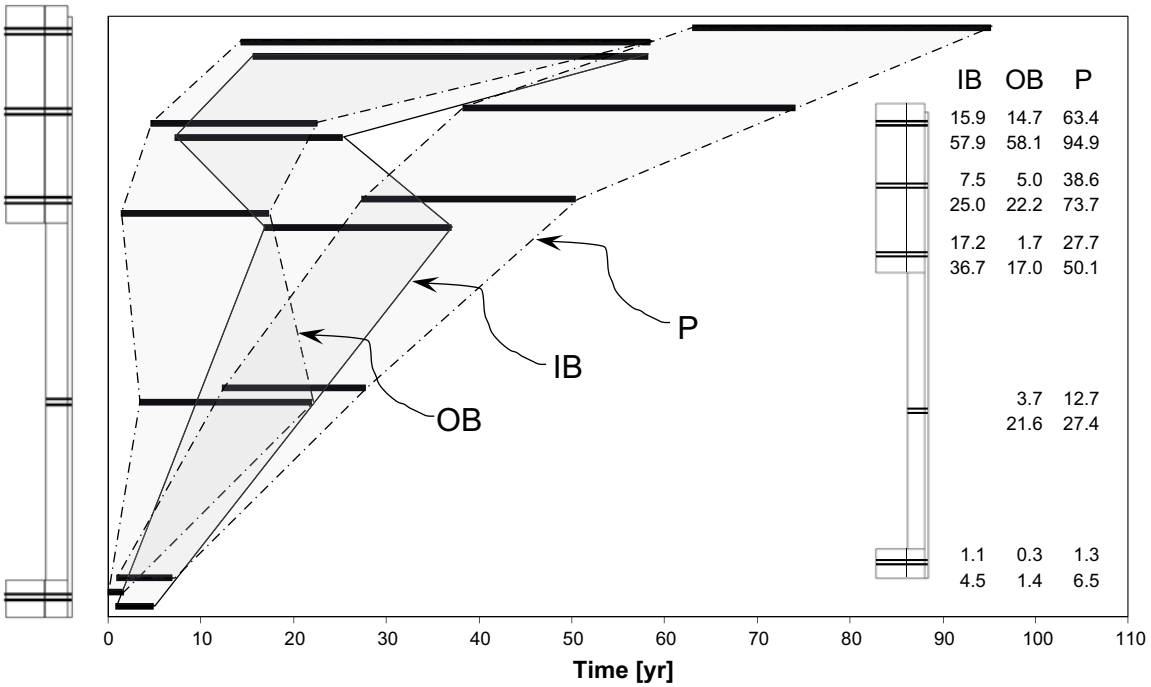

Figure 8-14. *Compilation of estimated time intervals for which safety function Buff2 are reached at the indicated positions for models with rock conductivity 10^{-12} m/s and no fractures, i.e. 2I and 2H in Åkesson et al. (2010b, Chapter 3). In the table to the right the start (top) and end (bottom) of the time interval are given for each of the positions.*

If trying to elaborate on the reason behind the CFS shape at the canister top, it could be said that the material in the inner block volume on top of the canister will generally be relatively dry due to the proximity to the heat source and distance to the water bearing rock. The water will be transported outwards in form of vapour that counteracts the inward liquid water transport from the rock. Therefore, the water uptake in the inner block material will be restrained and the material in the outer block may have an influx of water in terms of vapour which will enhance the water uptake.

As also can be seen, the criteria fulfilment occurs late at the top of the deposition hole. This comes from the proximity to the tunnel backfill, "competing" with the buffer about the water.

If considering the case where $K_R = 10^{-13}$ m/s (model 8I and 8H) the results given in Figure 8-15 and Figure 8-16 for Buff1 and Buff2, respectively, are obtained. As can be seen, the CSFs have a lot in common with those of the case where $K_R = 10^{-12}$ m/s:

- For the pellet slot the criteria are fulfilled late in time and from the bottom to the top.
- The inner block CFS is to the right (later in time) as compared to the outer block CFS.
- A rightward kink (a "delay") of the inner block CFS can be seen above the canister.

There are, however, some special features for the $K_R = 10^{-13}$ m/s case as well. The position of the pellet slot CFS is further to the right (later in time) as compared to the block volumes and the shape is also somewhat different from what is seen for $K_R = 10^{-12}$ m/s. It could also be mentioned that the Buff1 criterion giving the end point of the pellet slot interval below the canister (225.2 yr) was crossed the first time at 11.2 yr, but a subsequent drying of the material made the saturation level go down below the criterion again. The same happened in the pellet slot at the same position but for the Buff2 criterion which gives the start point of the interval (144.9 yr), the time at the first fulfilment of the criterion was 5.9 yr.

Finally, in Figure 8-17, all results are compiled for facilitating comparisons between the $K_R = 10^{-12}$ m/s and $K_R = 10^{-13}$ m/s case.

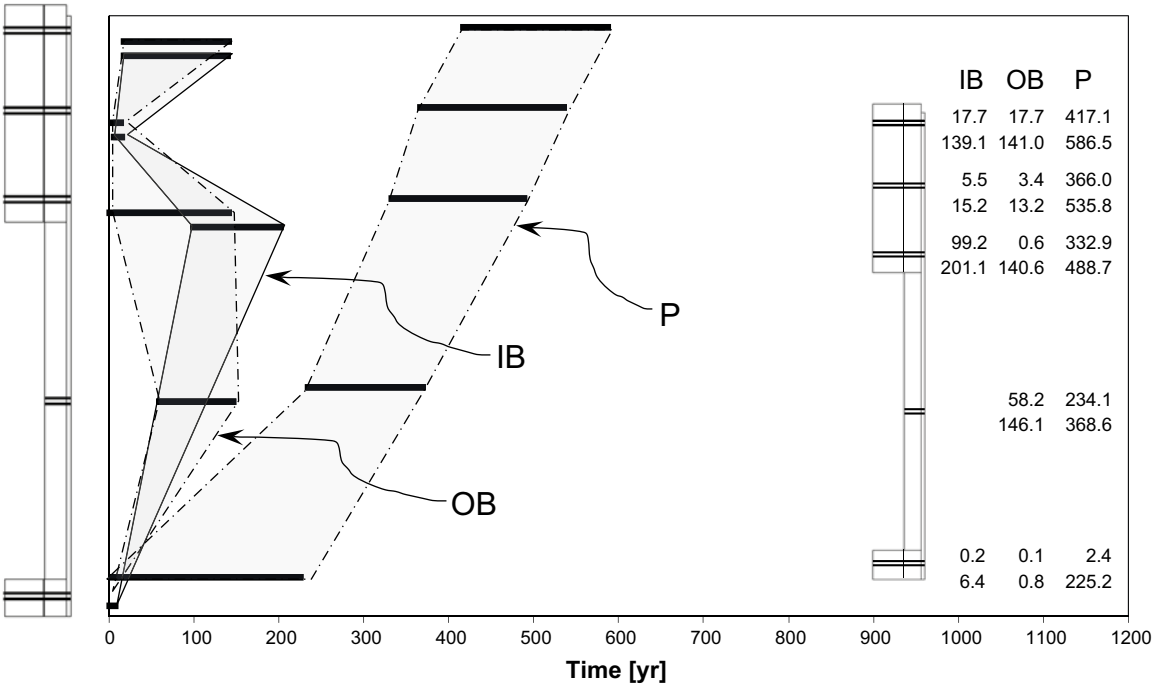

Figure 8-15. *Compilation of estimated time intervals for which safety function Buff1 are reached at the indicated positions for models with rock conductivity 10^{-13} m/s and no fractures, i.e. 8I and 8H in Åkesson et al. (2010b, Chapter 3). In the table to the right the start (top) and end (bottom) of the time interval are given for each of the positions.*

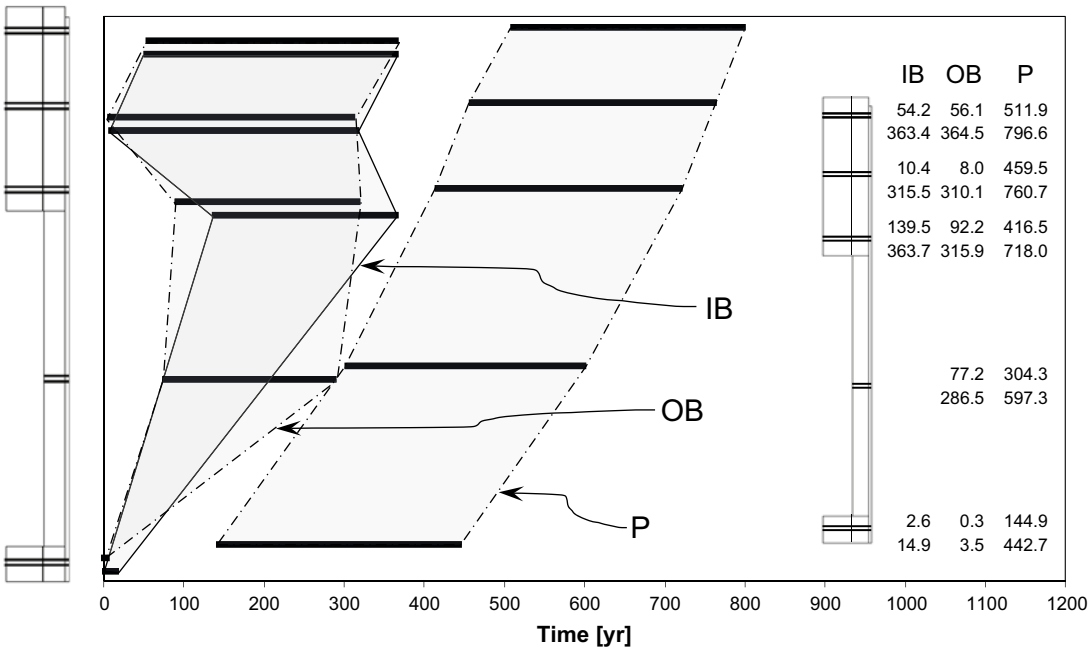

Figure 8-16. *Compilation of estimated time intervals for which safety function Buff2 are reached at the indicated positions for models with rock conductivity 10^{-13} m/s and no fractures, i.e. 8I and 8H in Åkesson et al. (2010b, Chapter 3). In the table to the right the start (top) and end (bottom) of the time interval are given for each of the positions.*

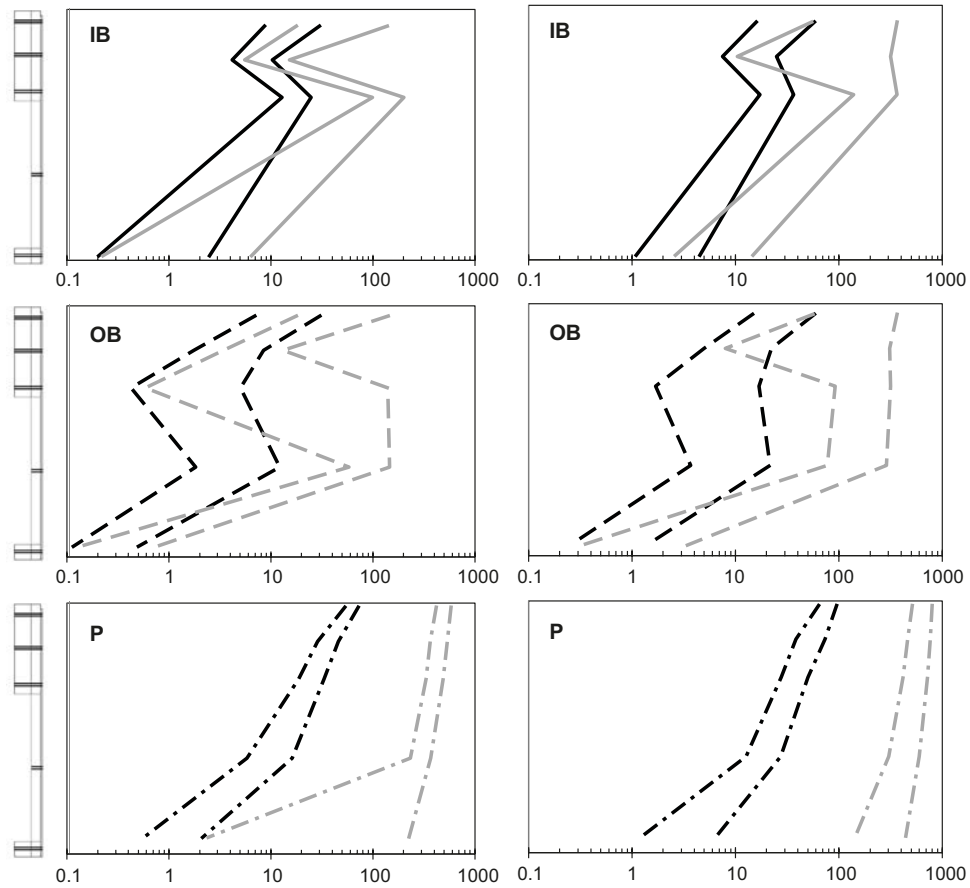

Figure 8-17. *Compilation of estimated time intervals (given by the horizontal distance between similar lines) for which safety functions Buff1 (left column) and Buff2 (right column) are reached in different buffer volumes (Inner Block = IB, Outer Block = OB, and Pellet slot = P) at different height from the deposition hole bottom. Results are shown for cases with rock conductivity 10^{-12} m/s (black lines) or 10^{-13} m/s (grey lines) and no fractures, i.e. (2I, 2H) and (8I, 8H) in Åkesson et al. (2010b, Chapter 3), respectively.*

8.6 Summary and conclusions

Here, an attempt to meet SSM's request of an analysis where intervals in the saturation process are coupled to long time safety (SSM2011-2426-81) is carried out. SSM suggested that intervals in degree of saturation should be coupled to conditions/events that promote long term safety such as: build up of pressure to reduce microbial activity, and closure of open gaps close to the canister and deposition hole (DH) wall.

These conditions/events that promote long time safety are related to the so called safety functions, their safety function indicators, and corresponding safety function indicator criteria for the buffer as described in the SR-Site main report (SKB 2011). Criteria considered relevant for this study, related to "Limiting advective transport" and "Reduce microbial activity", were expressed in terms of pressure.

Local 1D axisymmetrical THM simulations were performed and utilized to translate the criteria, expressed in pressure, into new criteria expressed in intervals of degree of saturation, as requested by SSM, see Table 8-6 repeated below.

Table 8-6 repeated: Final version of adjusted Buff1 and Buff2 criteria expressed in terms of relative degree of liquid saturation for the block and pellet slot materials.

	Criterion expressed in p	Criterion expressed in VA(S_l^{rel})	
		Block	Pellet slot*
Buff1	≈ 1 MPa	{0.145, 0.278}	{0.165, 0.285}
Buff2	≈ 2 MPa	{0.302, 0.487}	{0.225, 0.487}

* Only the results of the initial state model are to be considered for the pellet slot material.

These criteria, given in terms of intervals of volume averages of relative degree of saturation, were then applied on two sets of TH-models, described in Åkesson et al. (2010b, Chapter 3), and the safety functions' fulfillment process in a DH-buffer was then studied, see Figure 8-13 to Figure 8-17.

Below follows a list of conclusions from the investigation:

- The current safety functions given by SKB are only defined for fully water saturated conditions. The present study disregards this and only considers the safety function criteria expressed in pressure without taking into account the level of saturation.
- The used mechanical material representation is process dependent and has to be calibrated for different situations. Here a slow wetting process was considered and mechanical parameters of the pellet slot had to be chosen as to generate a representative density profile at full water saturation.
- Processes in the buffer are heterogeneous. The models show large differences between the block and pellet slot materials as well as within the block and pellet slot materials.
- Degree of water saturation is not found to be an ideal indicator for pressure in the buffer system. The buffer attains a specified pressure for quite a large range of degree of water saturation, absolute or relative. That is why the criteria in Table 8-6 are given in terms of intervals.
- Safety function criteria are fulfilled heterogeneously within the buffer. The general trend is "from the bottom to the top" and "later in the pellet slot".
- For the cases investigated, the hydraulic conductivity of the rock material is a crucial characteristic of the system, which significantly affects the time until fulfillment of the safety functions.
- The general "relative" trend of the safety function fulfillment process for the two different rock hydraulic conductivities studied has strong similarities.

9 Analysis of risks and consequences of uneven wetting in a dry deposition hole

Lennart Börgesson, Mattias Åkesson, Clay Technology AB
Jan Hernelind, 5T Engineering AB

9.1 Introduction

The deposition holes and tunnels in the Forsmark repository are foreseen to be very dry with none or a single inflow point in most of the deposition holes. The question of how a low inflow rate in single points in a deposition hole affects the wetting and homogenisation of the buffer has been raised and is analysed in this chapter.

In general uneven wetting is not expected to yield any homogenisation problems since the swelling and homogenisation processes are nor very stress path dependant. If the buffer starts swelling at one point the influence on the unswelled parts are not very strong and possible displacements of the buffer is small due to the confinement of the buffer inside the rock surface. The displacements that take place are to a large part expected to be reversed by the late swelling of the other parts of the buffer. However, research concerning this question is on-going.

This report includes a theoretical study of the moisture transport in dry pellet filling and the consequences for the wetting. It also includes simulations of some critical cases with uneven wetting.

9.2 Inflow scenarios

9.2.1 General

The expected inflow distribution in the deposition holes in the Forsmark repository has been analysed and reported (Svensson and Follin 2010, Joyce et al. 2013). According to Joyce at al. (2013) the total number of deposition holes with an inflow rate higher than 10^{-5} L/min is about 1 350 out of 6 916 holes. The majority of the deposition holes thus has a very low inflow rate.

The water inflow from a single fracture or channel in the rock into a deposition hole is only of interest if the water supply from the matrix is lower than from the fracture. The hydraulic conductivity of the rock matrix in Forsmark is thus an important input parameter to the analysis. It has been measured for a large number of rock core samples by Vilks (2007). Almost all tests showed a hydraulic conductivity of the matrix of between 2×10^{-12} m/s and 1×10^{-13} m/s. Only a few tests at high external pressure resulted in a hydraulic conductivity below 1×10^{-13} m/s.

9.2.2 Matrix flow in the rock

The distribution of inflow between matrix flow and fracture flow at low inflow rate is not clear. It may be a matter of definition but for the wetting of the buffer it is interesting to study the effect of having a low inflow rate into a point of the deposition hole without considering the matrix flow. In order to get the perspective, modelled time to full water saturation in the case of only matrix flow and a low rock matrix hydraulic conductivity is in the order of 1 500 years at $K_{rock} = 10^{-13}$ m/s and 15 000 years at $K_{rock} = 10^{-14}$ m/s (Åkesson et al. 2010b).

9.2.3 Free water inflow

A number of time limits can be set for bounding the time it may take to fill up the pellet filling with water and for saturating the buffer blocks. The available pore space is defined by the density and degree of saturation of the different bentonite parts and the geometry of the deposition hole, the canister and the bentonite blocks and rings. Table 9-1 shows the bentonite properties (taken from the modelling of the CRT in Åkesson et al. 2010b) and Figure 9-1 shows the geometry used for the calculations. The geometry is not totally identical to the geometry shown in the production report of the buffer (SKB 2010b), but the difference is not significant for the results.

Table 9-1. Basic properties of the bentonite parts.

Section	Density (kg/m^3)	Water ratio	Dry density (kg/m^3)	Void ratio	Degr. of saturation
Solid block	1 991	0.172	1 699	0.636	0.751
Ring shaped block	2 087	0.171	1 782	0.560	0.849
Pellets (17 %)	1 162	0.186	993	1.78	0.29

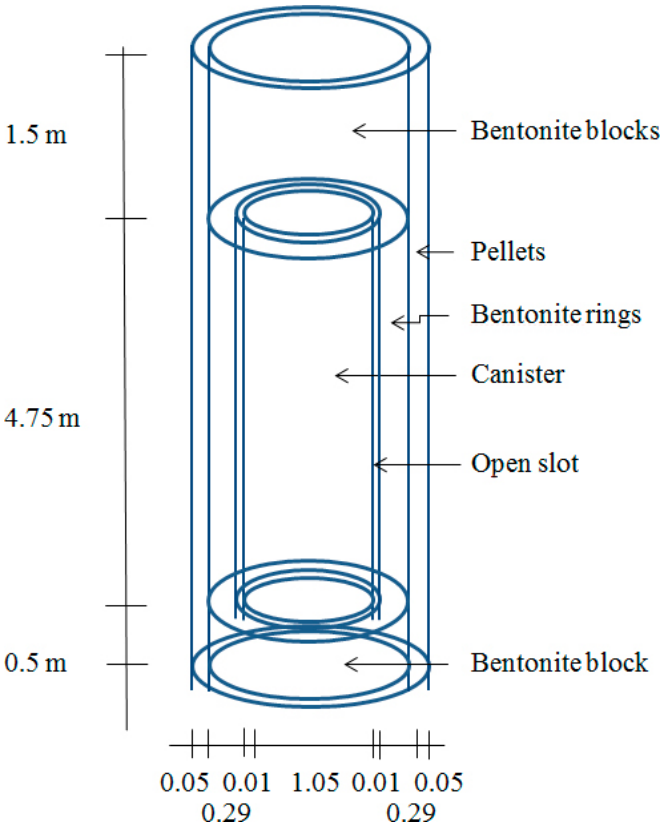

Figure 9-1. Geometry of the deposition hole with the canister and the bentonite.

Volume calculations

Pellets

Volume of pellets:

$V_p = H \times D \times \pi \times \Delta r = 6.75 \times 1.7\pi \times 0.05 = 1.80\ m^3$

where H = height, D = diameter, Δr_p = aperture of pellet filled slot

Available pore space in pellets:

$V_{pp} = n \times V_p = V_p \times e/(1+e) = 1.15\ m^3$

where n = porosity, e = void ratio

Empty pore space:

$V_{ppe} = V_{pp} \times (1 - S_r) = 0.817\ m^3$

Solid blocks

Volume of blocks:

$V_b = H \times \pi \times D^2/4 = 2.0 \times \pi \times 1.65^2/4 = 4.28\ m^3$

where H = height, D = diameter, Δr = aperture of pellet filled slot

Available pore space in blocks:

$V_{pb} = n \times V_b = V_b \times e/(1+e) = 1.66\ m^3$

where n = porosity, e = void ratio

Empty pore space:

$V_{pbe} = V_{pb} \times (1 - S_r) = 0.414\ m^3$

Rings

Volume of rings:

$V_p = H \times (D_o^2 - D_i^2) \times \pi/4 = 6.75 \times (1.65^2 - 1.07^2) \times \pi/4 = 8.36\ m^3$

where H = height, D_o = outer diameter, D_i = inner diameter

Available pore space in rings:

$V_{pr} = n \times V_p = V_p \times e/(1+e) = 3.00\ m^3$

where n = porosity, e = void ratio

Empty pore space:

$V_{pre} = V_{pr} \times (1 - S_r) = 0.453\ m^3$

Inner slot

Volume of inner slot:

$V_s = H \times D \times \pi \times \Delta r_s = 4.75 \times 1.06 \times \pi \times 0.01 = 0.158\ m^3$

where H = height, D = diameter, Δr_s = aperture of inner slot

Total empty volume is thus

$V_{te} = 1.842\ m^3$ whereof

$V_{ppe} = 0.817\ m^3$

Inflow 0.0001 L/min yields 35 years to saturate the buffer. See Table 9-2.

Table 9-2 Time to fill all empty space in the pellets filled slot and time to saturate the entire buffer in case of constant water inflow rate.

Inflow (L/min)	Time to fill pellets slot (years)	Modelled time (years)	Time to fill all voids (years)	Modelled time (years)
1.0×10^{-3}	1.55		3.5	
1.0×10^{-4}	15.5	≈150/1 500	35	≈1 500
1.0×10^{-5}	155		350	
1.0×10^{-6}	1 550	1 500–2 000	3 500	
1.0×10^{-7}	15 500		35 000	

The times calculated refer to the case that the inflow rate is constant irrespective of the water pressure required. In the modelling (se later) the reduced inflow that will be the case if a water pressure is generated in the fracture is taken into account.

9.2.4 Water distribution in a pellet filling

A critical process for the wetting is how the water is distributed in the pellet filling. The water transport properties in pellet filling are complicated and the water distribution caused by water inflow difficult to predict, not always repeatable and to some extent random. There is also an influence of pellet type, bentonite type and salt concentration. However, there are some patterns observed that can be used to formulate a "model" although very primitive and uncertain. The pellet type to be used in the deposition holes is not finally decided. The model is mainly based on results on the tests made on roller compacted pellets made of MX-80 according to the reference design as described in the production report of the buffer (SKB 2010b) but may probably also be used for extruded pellets although it seems as the limits are moved towards higher inflow rates for those pellets. The limits between the different patterns are not clear but a successive transition is assumed.

$q \geq 0.1$ L/min

At very high inflow rates, the water inflow is faster than the individual pellets can absorb so the free water will fill up the empty pore space and by gravity flow downwards. The deposition hole will be filled like a bathtub.

$q = 0.01$ L/min

At fairly high inflow rates, the flow is spread equally in all directions and thus fills the slot circularly with the inflow point as centre and with increasing radius with time. There might though be a tendency for upwards movements. When the water reaches a free surface it seems as the continuing flow mainly goes to the surface.

$q = 0.001$ L/min

At low inflow rates, the flow seems to move upwards in a rather narrow channel. Once it reaches a free surface of the pellet filling the water stays there and continues to flow out on the surface. The reason for the upwards flow is not clear. The phenomenon is empirically observed but it is not yet clear if it fundamentally correct to assume that it always will take place.

$q = 0.0001$ L/min

At very low inflow rates, the inflow pattern seems to go back to something between the pattern at 0.001 L/min and 0.01 L/min. An elliptic pattern seems to be formed with a tendency to move upwards and with the major axis directed vertically.

$q \leq 0.00001$ L/min

At extremely low inflow rates, the water seems to follow a diffusion like behaviour and spread as concentrical circles, similar to that at 0.01 L/min.

The "model" is illustrated in Figure 9-2.

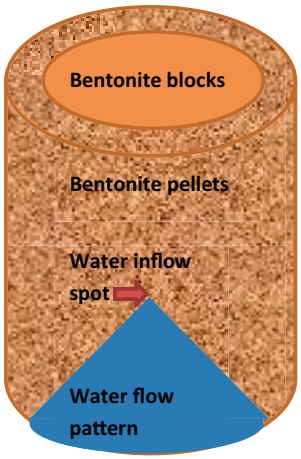

$q \geq 0.1$ L/min

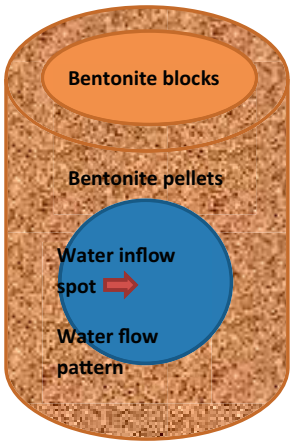

$q = 0.01$ L/min

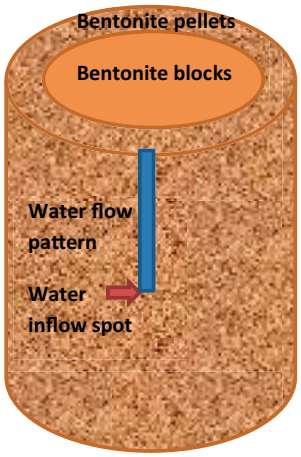

$q = 0.001$ L/min

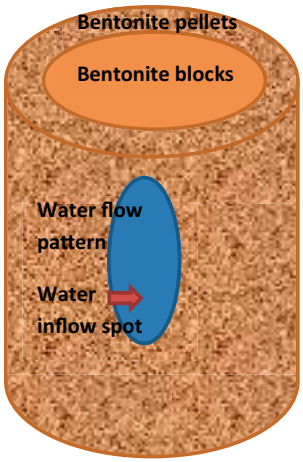

$q = 0.0001$ L/min

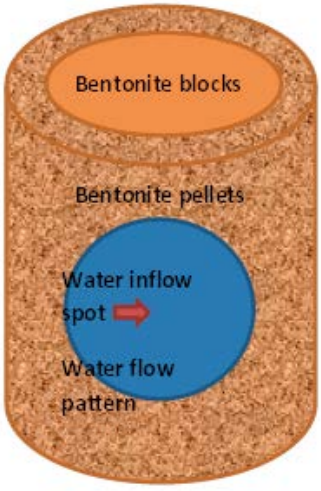

$q \leq 0.00001$ L/min

Figure 9-2. *Simple "model" of water flow distribution in the pellet filled slot in the deposition holes. The limits between the different patterns are not clear but a successive transition is assumed.*

The flow behaviour is important to understand in order to be able to predict how heterogenic the bentonite blocks are wetted at very low inflow rates from single fractures in dry deposition holes. The "model" presented is very uncertain but is judged sufficient for the purposes of the present study.

Since the flow rates of interest at dry rock conditions is below 0.0001 L/min, water uptake from a single point in a deposition hole can be assumed to behave in a diffusion like pattern, the last picture in Figure 9-2, with equal distribution of moisture in all directions.

9.3 Water transport in a pellet filled slot at very low inflow rates, modelled as a diffusion process with free access of water

9.3.1 Moisture diffusivity in pellets-filled slots

Introduction

The apparently slow water-uptake in bentonite pellets has raised the question whether moisture transfer in pellets may be governed by vapour diffusion. An analysis has therefore been performed with the aim to quantify the moisture transfer flow coefficients for different dry densities and water contents, in general, and for typical pellets conditions, in particular. The results from this analysis are presented in this chapter.

The bentonite is regarded as a system of two phases: water-saturated grains and gas-filled voids, in which the moisture is transferred as liquid or as vapour, respectively. Both these fluxes are described as driven by gradients in water content, and moisture diffusivity values for liquid as well as vapour can be quantified in this way.

An effective diffusivity value is finally estimated for the bentonite as a whole, and for this the phases are assumed to behave as a composite medium arranged either in series or in parallel (Figure 9-3). The relative distribution of these phases is assumed to be equal to the fraction of grains and gas-filled voids, respectively.

It is found that the moisture diffusivity value for the two phases appears to coincide at a moisture content of approximately 20–30 %. Below this level the effective diffusivity appears to be limited by liquid transfer whereas the vapour transfer can be limiting above the level.

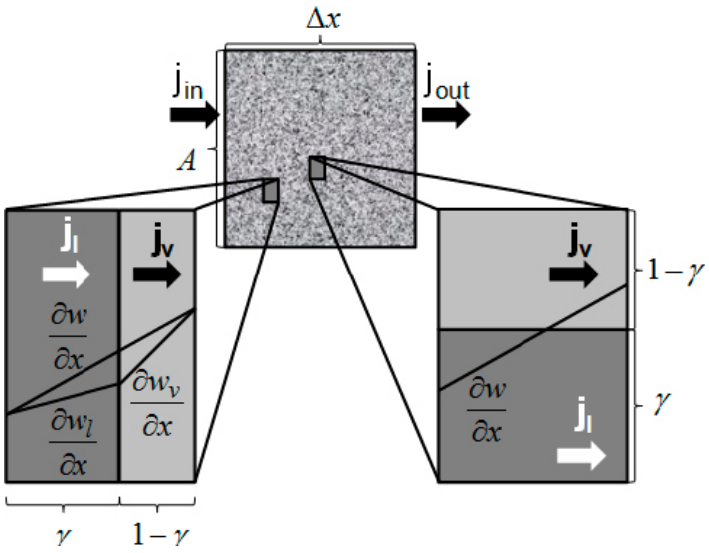

Figure 9-3. *Schematic outline of fluxes in and out of elementary volume, and fluxes in liquid and vapour phase arranged in series or in parallel.*

Mass flux and mass conservation

The mass flux (j) is given by gradients in water content (w):

$$j = -D' \cdot \frac{\partial w}{\partial x} \tag{9-1}$$

where the unit of the coefficient D' is $kg \times m^{-1} \times s^{-1}$.

The next step is to consider an elementary volume with section area A and length Δx (see Figure 9-3). The condition of mass conservation implies that the increase of the water mass in the volume equals the difference between the inflow flux (j_{in}) and outflow flux (j_{out}) through the section area. The mass increase is expressed in terms of a time derivative of the water content:

$$A \cdot \Delta x \cdot \rho_d \cdot \frac{\partial w}{\partial t} = A \cdot (j_{in} - j_{out}) \tag{9-2}$$

where ρ_d is the dry density of the bentonite. The right hand side is developed as:

$$A \cdot (j_{in} - j_{out}) = A \cdot \left[j - \left(j + \frac{\partial j}{\partial x} \Delta x \right) \right] = -A \cdot \Delta x \cdot \frac{\partial j}{\partial x} = A \cdot \Delta x \cdot \frac{\partial}{\partial x} \left(D' \cdot \frac{\partial w}{\partial x} \right) \tag{9-3}$$

Both sides are then divided with dry mass of the volume ($A \times \Delta x \times \rho_d$), which results in Fick's second law:

$$\frac{\partial w}{\partial t} = \frac{\partial}{\partial x} \left(\frac{D'}{\rho_d} \cdot \frac{\partial w}{\partial x} \right) = \frac{\partial}{\partial x} \left(D \cdot \frac{\partial w}{\partial x} \right) \tag{9-4}$$

The moisture diffusivity D is thus obtained by dividing the coefficient D' with the dry density.

Liquid and vapour mass fluxes

The mass flux through vapour diffusion (j_v) is in Code_Bright described as driven by gradients in vapour mass fraction (ω). This gradient can be developed in terms of gradients in water content:

$$j_v = -\rho_g \cdot D^o \cdot \frac{T^{2.3}}{p_g} \cdot \frac{\partial \omega}{\partial x} = -\rho_g \cdot D^o \cdot \frac{T^{2.3}}{p_g} \cdot \frac{d\omega}{dw} \cdot \frac{\partial w}{\partial x} = -D_v' \cdot \frac{\partial w}{\partial x} \tag{9-5}$$

where ρ_g is the gas density, D^o is a diffusion parameter set to 5.9×10^{-6} ($m^2\ s^{-1}\ K^{-2.3}$ Pa), T is the absolute temperature and p_g is the gas pressure. The negative ratio between the mass flux and the water content gradient in vapour is denoted D_v'. Note that this flux is found in the gas phase, and the factor used normally in unsaturated porous medium, $\tau \times n \times (1-S)$, is assumed to be equal to unity. The derivative dω/dw is developed in Equation (9-10) below. The moisture diffusivities for vapour transfer can thus be expressed as:

$$D_v = \frac{\rho_g}{\rho_d} \cdot D^o \cdot \frac{T^{2.3}}{p_g} \cdot \frac{d\omega}{dw} \tag{9-6}$$

Mass flux through water-saturated grains (j_l) is given by Darcy's law and gradients in water activity (liquid pressure, p_l), which is equal to the negative gradient in suction (ψ). This can be developed in terms of gradients in water content:

$$j_l = -\rho_w \frac{k}{\mu} \frac{\partial p_l}{\partial x} = \rho_w \frac{K(w)}{\rho_w \cdot g} \frac{d\psi}{dw} \frac{\partial w}{\partial x} = -D_l' \cdot \frac{\partial w}{\partial x} \tag{9-7}$$

where ρ_w is the water density, k is the permeability, μ is the viscosity, and g is gravity. Hydraulic conductivity, K, is described as a function of water content, see Equation (9-13) below. The negative ratio between the mass flux and the water content gradient in grains is denoted D_l'. The moisture diffusivities for liquid transfer can thus be expressed as:

$$D_l = -\frac{K(w)}{\rho_d \cdot g} \frac{d\psi}{dw} \tag{9-8}$$

Material models and derivatives

The derivative of the vapour mass fraction with respect to water content in Equation (9-6) can be calculated with the chain rule:

$$\frac{d\omega}{dw} = \frac{d\omega}{dp_v}\frac{dp_v}{d\psi}\frac{d\psi}{dw} \tag{9-9}$$

The relation between the vapour mass fraction and the vapour pressure (p_v) gives the first derivative:

$$\omega \approx \frac{p_v}{p_g}\frac{M_w}{M_a} \quad \Rightarrow \frac{d\omega}{dp_v} \approx \frac{M_w}{p_g M_a} \tag{9-10}$$

where M_w and M_a are the molar masses for water and air, respectively. The relation between the vapour pressure and suction value is given by Kelvin's law and gives the second derivative:

$$p_v = p_v^{sat} \cdot \exp\left[-\frac{\psi(w)\cdot M_w}{\rho_w RT}\right] \quad \Rightarrow \frac{dp_v}{d\psi} = -p_v^{sat} \cdot \frac{M_w}{\rho_w RT} \cdot \exp\left[-\frac{\psi(w)\cdot M_w}{\rho_w RT}\right] \tag{9-11}$$

Where p_v^{sat} is the saturated vapour pressure, and R is the general gas constant. The retention curve gives the third derivative, and also for the liquid transfer diffusivity in Equation (9-8). The retention curve used here follows the model for MX-80 presented by Dueck (2007):

$$\psi(w) = \exp[a - bw] - \frac{w - w_{in}}{w_{sat} - w_{in}} \cdot \exp[a - bw_{sat}] \quad (MPa) \tag{9-12}$$

The following parameter values are used for a case with initial water content of 10 %:

$a = 6.3$ and $b = 16$.

Finally, the following relation for the hydraulic conductivity of MX-80 was adopted by Åkesson et al. (2010a) and used for the liquid transfer diffusivity in Equation (9-8):

$$K(w) = 2.4 \cdot 10^{-13} \cdot \left(\frac{w\cdot\rho_s}{\rho_w}\right)^{5.33} \tag{9-13}$$

Liquid and vapour transfer in series or in parallel

The condition for moisture transfer in series is illustrated in Figure 9-3. Since the liquid and vapour fluxes have to be equal, this implies the following relation between the water content gradients in the gas phase and in the grains:

$$j_v = j_l \quad \Rightarrow \quad -D_v\frac{\partial w_v}{\partial x} = -D_l\frac{\partial w_l}{\partial x} \quad \Rightarrow \quad \frac{\partial w_v}{\partial x} = \frac{D_l}{D_v}\frac{\partial w_l}{\partial x} \tag{9-14}$$

The overall water content gradient is estimated by weighting the gradients in the phases with respect to the volume fractions of the phases, and with the relations of the gradients in the phases according to Equation (9-14). In this way a relation between the overall gradient and the gradient in the grains is obtained.

$$\frac{\partial w}{\partial x} = \gamma\cdot\frac{\partial w_l}{\partial x} + (1-\gamma)\cdot\frac{\partial w_v}{\partial x} = \frac{\partial w_l}{\partial x}\left[\gamma + (1-\gamma)\cdot\frac{D_l}{D_v}\right] \tag{9-15}$$

γ is defined as the ratio between the specific grain volume and the specific total volume $(1+w\times\rho_s/\rho_w)/(1+w_{sat}\times\rho_s/\rho_w)$. The overall flux is the same as the flux through the grains, and together with Equation (9-15) this yields an expression for the effective moisture diffusivity:

$$D_l\frac{\partial w_l}{\partial x} = \frac{D_l}{\gamma + (1-\gamma)\cdot\frac{D_l}{D_v}}\frac{\partial w}{\partial x} = \frac{1}{\frac{\gamma}{D_l} + \frac{1-\gamma}{D_v}}\frac{\partial w}{\partial x} = D_{ser}\frac{\partial w}{\partial x} \quad \Rightarrow \quad D_{ser} = \frac{1}{\frac{\gamma}{D_l} + \frac{1-\gamma}{D_v}} \tag{9-16}$$

A corresponding effective diffusivity can be evaluated for a parallel arrangement:

$$D_{par} = \gamma \cdot D_l + (1-\gamma) \cdot D_v \qquad (9\text{-}17)$$

Quantification of diffusivity functions

Evaluated diffusivities, in vapour, liquid, series and parallel are shown for two different cases in Figure 9-4, for water contents in the intervals 13–25 % (corresponding approximately with buffer dry density), and 10–64 % (i.e. typical for pellets-filled slots).

In the first case, D_l displays an increasing trend for increasing water contents, whereas D_v, in contrast, displays a decreasing trend. The values coincide at the level of 5×10^{-10} m^2/s at a water content of approximately 25 %. The effective diffusivity for arrangements in series is quite close to the D_l values, whereas the corresponding values for parallel arrangements are significantly higher for the lower water contents. Both effective diffusivity functions can be regarded as in fairly good agreement with empirical data (see Chapter 6).

In the second case, the diffusivity functions are basically the same as in the first case for water content levels below 25 %. One exception is $D_{parallel}$ which is much higher in the second case. For higher water contents, the D_l displays a maximum of 7×10^{-10} m^2/s at 30–35 % and above that decreases down to 2×10^{-10} m^2/s at 64 %. The D_v, in contrast, displays a strong decreasing trend and falls below 1×10^{-10} m^2/s at water contents above 35 %. The effective diffusivity for arrangements in series is closer to the D_v-values, whereas the corresponding values for parallel arrangements are closer to the D_l-values.

Apart from these direct observations, the following comments can be made concerning the presented approach:

- The effective diffusivity of the serial arrangement tends to be governed by the phase with the lowest diffusivity, i.e. the liquid transfer at w < 25 % and the vapour transfer at w > 25 %.
- The validity of the evaluated results is limited by the ranges for which the used parameters were adopted. The hydraulic conductivity relation was indented to be used for dry density values corresponding to water contents of 20–64 %, although the empirical data in both ends were quite scarce. Similarly, the retention curve was based on experimental data with water contents of 2–35 %. This latter function may be extended with swelling pressure data which was adopted for the same range as the hydraulic conductivity. Therefore, the material model appears to be least founded for water contents below 20 %, although the high end values of D_l may also be updated if more hydraulic conductivity data are considered.
- Retention curve was based on a linear pressure build-up, although alternative functions may also be considered.
- The serial arrangement implies no continuity of the phases, whereas the parallel implies a perfect continuity. The possibility that continuities occurs at the low and high end of the water content range may be considered.

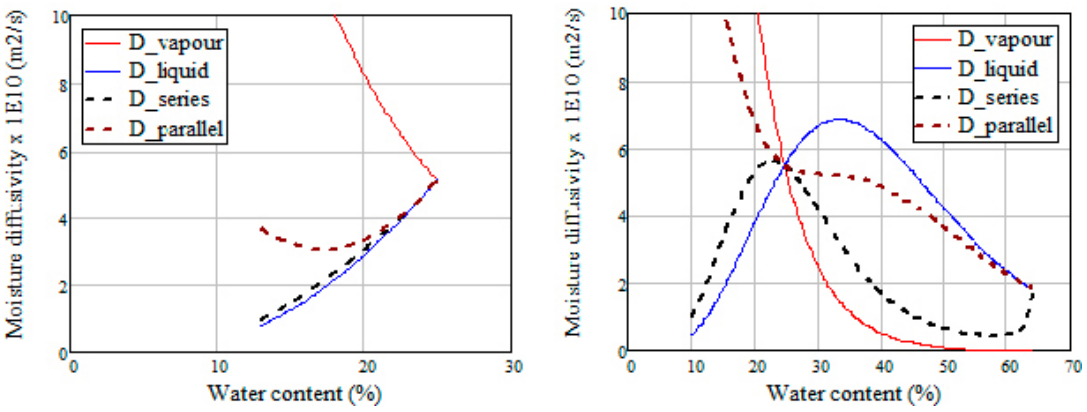

Figure 9-4. *Evaluated diffusivity as a function of water content; liquid phase (red thin line); in vapour phase (blue thin line); series (black dotted line) and parallel (brown dotted line). Left graph shows results for water contents between 13–25 %. Right graph shows results for 10–64 %.*

9.3.2 Water-uptake calculation

Geometrical considerations

A simple case of water-uptake into the pellets-filled slot around the buffer, in which water enters the filling in one point at the mid-height, is illustrated in Figure 9-5. The cylindrical shape is first folded up into a rectangular panel with the water inlet at the centre. This is in turn simplified as a circular panel with the same area as the rectangular panel, again with the inlet as the centre. Finally, this form is identical with a 1D axisymmetric geometry. The height and the circumference of the pellets-filling correspond to an area of 43 m^2, which in turn corresponds to an outer radius of 3.7 m. The thickness of the filling is 0.05 m. A small inner radius is finally adopted, and this was in this analysis set to 0.01 m, thereby representing a channel with approximately the same dimensions as the voids in the pellets filling.

Tool for water-uptake calculations

In order to have an efficient and transparent tool for evaluating the water-uptake a MathCad algorithm was prepared, in which the water transport is described by a saturation dependent moisture diffusivity function D(S), and in which the diffusion equation is solved with an explicit finite-difference method.

The 1D radial geometry of the water-uptake tests are discretized in n elements according to Figure 9-6 (left). The index *i*, with values between 0 and n−1, denote the element. The radial width of each element is $\Delta r = (R_{out}-R_{in})/(n-1)$, except for the inner and outer elements which have half this width. The numerical scheme used to calculate the saturation profile for a point in time, with index *j*, is illustrated in Figure 3-4 (right). The time step between two successive point in time is denoted Δt.

The diffusion equation for radial diffusion can be developed in the following four terms:

$$\frac{\partial S}{\partial t} = \frac{1}{r}\cdot\frac{\partial}{\partial r}\left(rD\frac{\partial S}{\partial r}\right) = D\frac{\partial^2 S}{\partial r^2} + \frac{D}{r}\cdot\frac{\partial S}{\partial r} + \frac{\partial D}{\partial r}\cdot\frac{\partial S}{\partial r} \tag{9-18}$$

These terms with partial derivatives are estimated with the following corresponding finite differences:

$$\begin{cases} \dfrac{\partial S}{\partial t} & \approx & \dfrac{S_{j,i} - S_{j-1,i}}{\Delta t} \\ D\dfrac{\partial^2 S}{\partial r^2} & \approx & D(S_{j-1,i})\cdot\dfrac{S_{j-1,i+1} - 2S_{j-1,i} + S_{j-1,i-1}}{\Delta r^2} \\ \dfrac{D}{r}\cdot\dfrac{\partial S}{\partial r} & \approx & \dfrac{D(S_{j-1,i})}{R_{in} + i\cdot\Delta r}\cdot\dfrac{S_{j-1,i+1} - S_{j-1,i-1}}{2\cdot\Delta r} \\ \dfrac{\partial D}{\partial r}\cdot\dfrac{\partial S}{\partial r} & \approx & \dfrac{D(S_{j-1,i+1}) - D(S_{j-1,i-1})}{2\cdot\Delta r}\cdot\dfrac{S_{j-1,i+1} - S_{j-1,i-1}}{2\cdot\Delta r} \end{cases} \tag{9-19}$$

Note that the radius of element *i* is expressed as $R_{in} + i \times \Delta r$. For convenience, the following constant is defined:

$$R = \frac{\Delta t}{\Delta r^2} \tag{9-20}$$

Based on Equations (9-18)–(9-20), the following expressions can be derived for the saturation degree in all elements, except for the inner and outer elements:

$$\begin{aligned} S_{j,i} = {} & S_{j-1,i} + R\cdot D(S_{j-1,i})\cdot[S_{j-1,i+1} - 2S_{j-1,i} + S_{j-1,i-1}] \\ & + \frac{\Delta t}{2\Delta r}\frac{D(S_{j-1,i})}{R_{in} + i\cdot\Delta r}\cdot[S_{j-1,i+1} - S_{j-1,i-1}] \\ & + \frac{R}{4}[D(S_{j-1,i+1}) - D(S_{j-1,i-1})]\cdot[S_{j-1,i+1} - S_{j-1,i-1}] \end{aligned} \tag{9-21}$$

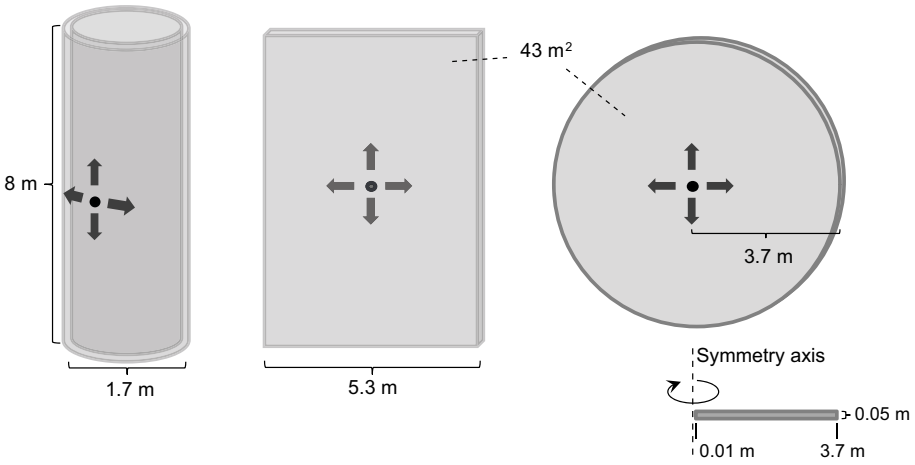

Figure 9-5. *Simplification of pellets geometry into a 1D axisymmetric geometry.*

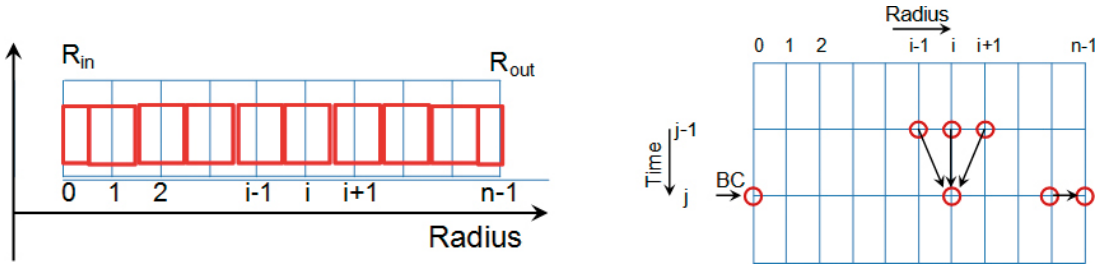

Figure 9-6. *Discretization of geometry in n elements with index i, shown as red boxes (left). Numerical scheme used to update the saturation profile (right). Points in time are denoted with index j.*

The saturation degree of the outer element is the same as for the adjacent element ($S_{j,n-1} = S_{j,n-2}$), and for the inner element this is given as a boundary condition, which is full saturation ($S_{j,0} = 1$).

The following parameters and geometries were defined for the current problem:

- Inner radius: 0.01 m.
- Outer radius 3.7 m.
- Thickness: 0.05 m.
- Porosity: 0.64.
- Initial saturation: 0.156; based on a water content of 10 %.

The discretization in time and space was adjusted for each specific calculation.

Time-scale for water-uptake in pellets-filled slot

The water-uptake in the outlined geometry was modelled for two different moisture diffusivity functions.

In the first case a constant value of 2×10^{-10} m^2/s was used. This value was chosen since it represents an approximate mean value of the evaluated diffusivity relation for a serial arrangement (see Figure 9-3). The geometry was discretized in 50 elements, and the calculation was performed for the time span of 25 kyears, which was discretized in 60 000 time steps. The time until a saturation degree of 0.99 was reached in the last element was found to be 22 kyears. Results are shown in the left graphs in Figure 9-7.

It can be mentioned that an independent analytical solution for this problem was obtained from Carslaw and Jaeger (1959). This calculation resulted in a slightly slower hydration, and the time to reach a saturation degree of 0.99 at the outer boundary was 25 kyears. This difference may possibly be due to the rough mesh of the numerical solution. Even if the geometry was divided in 50 elements, these elements may still be too large in comparison to the inner radius. The accuracy of the method can nevertheless be considered as sufficiently good at this stage.

In the second case, the following diffusivity function was adopted in order to mimic the evaluated diffusivity relation for a serial arrangement (see Figure 9-8):

$$D_f(w) = [0.4 + 64(w - 0.09) \cdot \exp[-28 \cdot (w - 0.09)^2]] \cdot 10^{-10} \quad (m^2/s) \qquad (9\text{-}22)$$

The geometry was discretized in 30 elements, and the calculation was performed for the time span of 100 kyears, which was discretized in 250 000 time steps. The time until a saturation degree of 0.99 was reached in the last element was found to be 91 kyears. Results are shown in the right graphs in Figure 9-7.

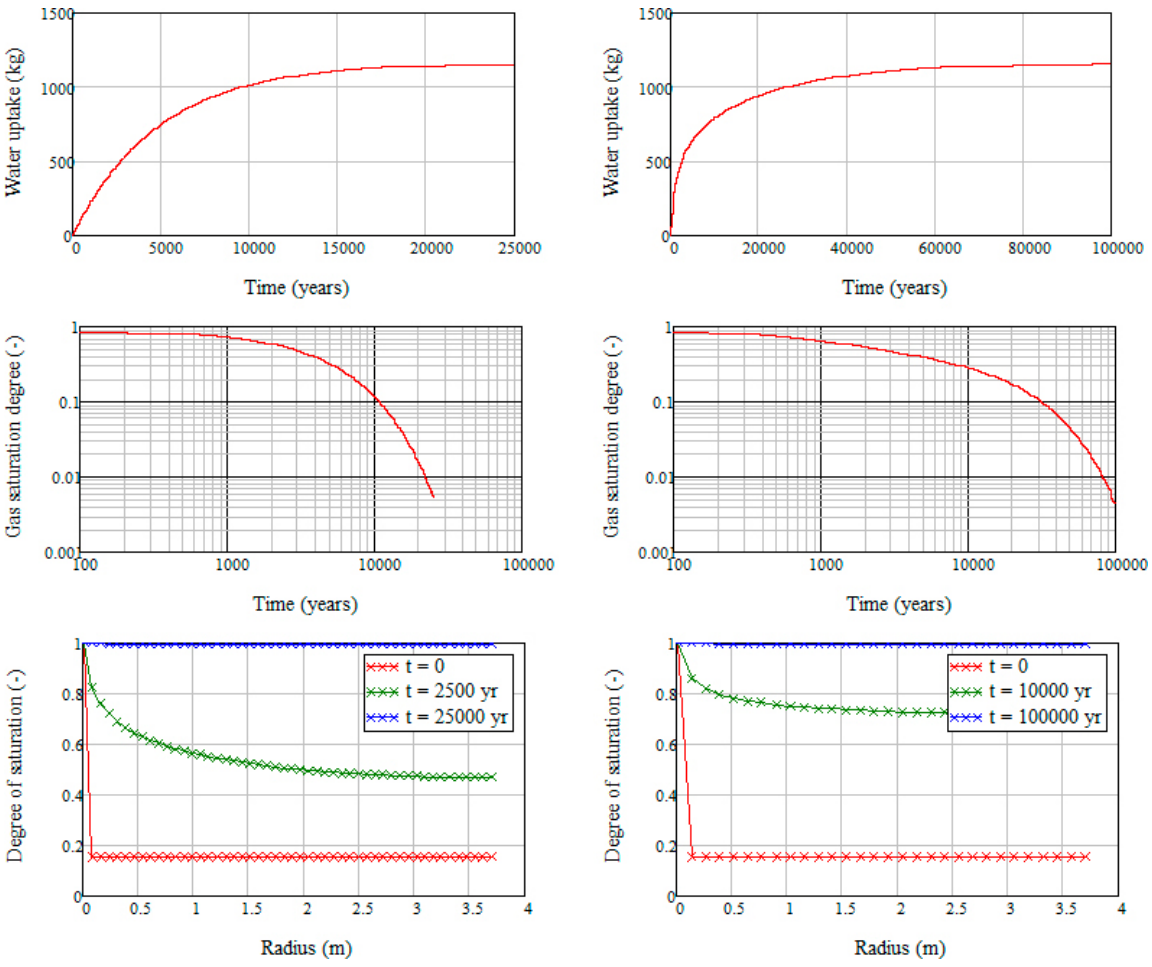

Figure 9-7. *Model results for a case with constant diffusivity of 2×10^{-10} m^2/s (left) and with a water content dependence according to Equation (9-22) (right): cumulative water uptake (upper), gas saturation (1−S) in the outer element (middle) and saturation profiles (lower).*

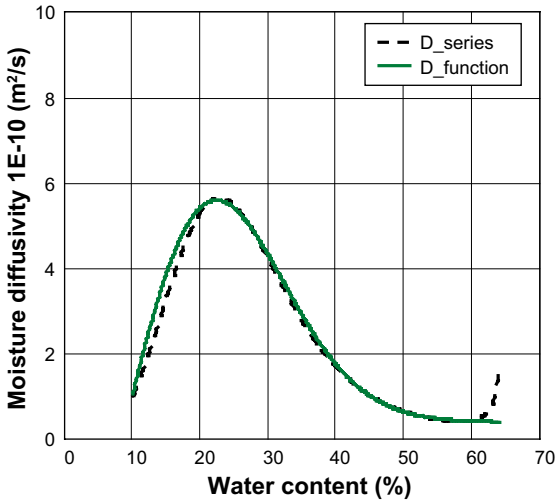

Figure 9-8. *Adopted diffusivity function (green solid) mimicking evaluated diffusivity for phases in series (black dotted line).*

9.4 FEM modelling of the wetting and homogenisation of the buffer at heterogeneous water inflow distribution

9.4.1 General

In order to study the wetting process and the subsequent homogenisation at heterogeneous inflow distribution, a case with one inflow point has been modelled assuming constant water inflow rate.

In a first attempt, a 3D model of a deposition hole with bentonite blocks, rings and pellets and a canister was analysed with a number of calculations using the finite element coda Abaqus and a completely coupled THM processes. These calculations were not successful since convergent solutions could not be reached. In order to try to simplify the calculation all nodes were locked so that the mechanical swelling and homogenisation were disregarded. Also these calculations were problematic but in the end successful. Then the pellet filled slot alone was studied and a number of calculations with different inflow rates were successful.

Finally some simulations with another boundary condition of the water inflow were performed.

9.4.2 Finite element code Abaqus

The code Abaqus has been described in previous reports and will not be further described here. See e.g. Åkesson et al. (2010b).

9.4.3 Element mesh

The dimensions of the different parts of the modelled system are shown in Figure 9-1. The one cm slot between the canister and the bentonite rings are also included.

The geometry and the element mesh are shown in Figure 9-9 together with some result points.

9.4.4 Material models

The basic properties of the three bentonite parts are shown in Table 9-3. The material models of the bentonite blocks and rings are identical to the models used in Åkesson et al. (2010b) for modelling the Canister Retrieval Test, CRT, with Abaqus (Section 5.13.2). The model of the bentonite pellets differs however, since the pellets filled slot was water filled in CRT but is dry in the present model (no artificial water filling will be done according to the reference concept).

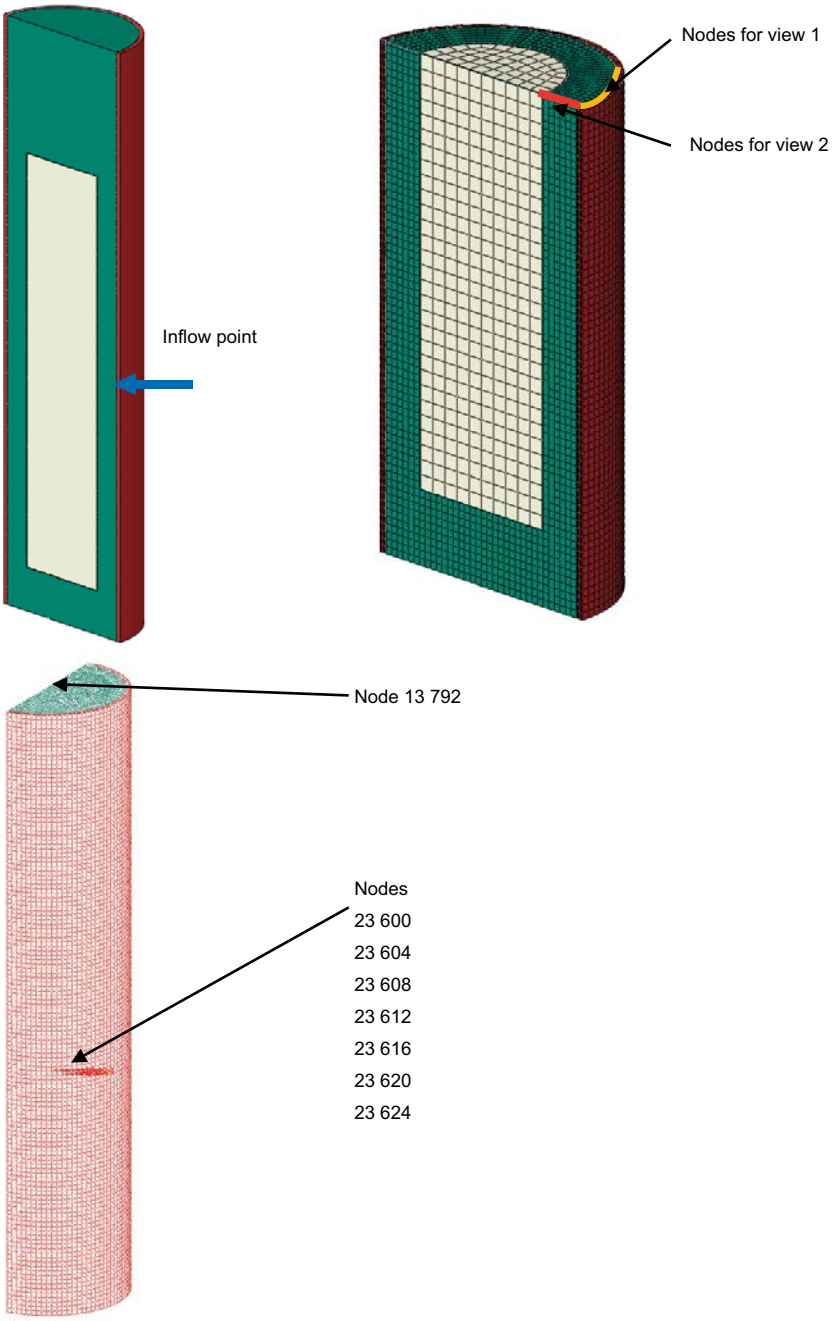

Figure 9-9. *Element geometry and half of the element mesh (upper). The vertical surface is a symmetry plane. Some nodes that are used to plot results are also shown.*

A hydro-mechanical model of a pellets filled slot that can be used in finite element calculations together with the established models of highly compacted bentonite has not been formulated before and there is a need for further tests and model development. As seen in Figure 9-2, the behaviour is very different depending on the water inflow rate. The model used here refers to very slow water inflow rates ($q_f \leq 0.0001$ L/min) and is not verified.

Pellets properties

$e_0 = 1.78$

Hydraulic

The retention curve is derived from the same relation between the water ratio and suction that is used for the other bentonite parts (see Åkesson et al. 2010b) and shown in Table 4-1.

Table 9-3 Retention curve of the pellet filling.

Sr %	Suction kPa
10.66	295088
29.00	36925
39.00	27366
50.00	19977
60.00	14623
70.00	10616
77.00	7526
83.00	5075
86.00	4230
88.00	3449
90.00	3080
91.00	2724
92.00	2380
93.50	1887
94.50	1571
95.50	1266
96.50	969
97.50	682
98.10	514
98.30	458
98.50	403
98.70	349
98.90	294
99.10	240
99.30	186
99.40	159
99.50	133
99.60	106
99.70	79
100.00	0

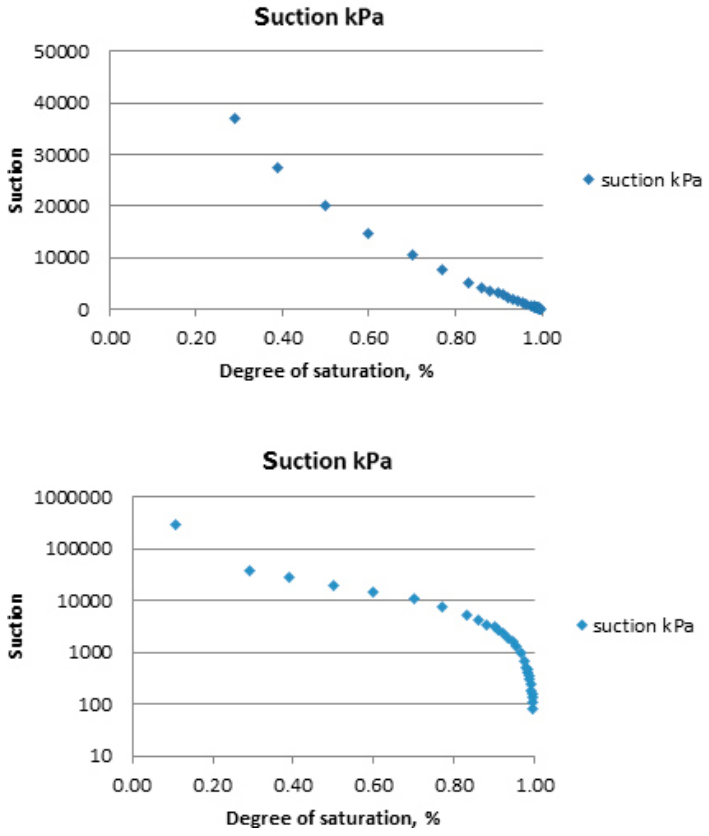

Hydraulic conductivity:

$$K = S_r^a \times K_0 \qquad (9\text{-}23)$$

The relation between the hydraulic conductivity and the void ratio is described in Table 9-4. This relation corresponds to the actual hydraulic conductivity of the bentonite and is called the reference model.

Table 9-4. Relation between hydraulic conductivity and void ratio for the pellet filling (reference model).

e	K_0 (low inflow rate) $\alpha = 3.0$
1.78	1.0×10^{-12}
1.60	2.0×10^{-12}
1.40	4.0×10^{-12}
1.20	8.0×10^{-13}
1.00	2.75×10^{-13}
0.80	1.0×10^{-13}

Equation 9-23 with $\alpha = 3.0$ and the hydraulic conductivity described in Table 9-4 correspond to a standard model of bentonite used for water unsaturated compacted bentonite. A pellet filling is more complicated since there are two types of water transport ways, in the open space between the separate pellets and in the highly compacted separate pellets. This means that the water transport probably behaves in different ways dependant on the inflow rate. At high inflow rate the water can flow freely in the open large pores between the pellets yielding a very high hydraulic conductivity while at very low inflow rate (that is modelled here) water needs to either be transported in the separate pellets (like in highly compacted bentonite) or by diffusion in the pore air between the pellets, which means that the low hydraulic conductivity shown in Table 9-4 probably is relevant. These processes are analysed in Section 9.3.

However, the low density of the pellet filling leads to that there is no resistance to high water pressure. There will be piping if the water pressure exceeds a couple of hundred kPa until the bentonite blocks have swelled so much that the pellet filling has been consolidated to a high density. In order to handle the problem with piping some alternative material models have been tested with high hydraulic conductivity close to water saturation. Table 9-5 shows the models.

Table 9-5 Alternative models for the hydraulic behaviour of pellet filling. Hydraulic conductivity K as function of degree of saturation S_r.

Alternative model 1 e = 1.78		Alternative model 2 e = 1.78	
S_r	K	S_r	K
< 0.90	Equation 4-1	< 0.90	Equation 4-1
0.90	1.0×10^{-12}	0.90	1.0×10^{-12}
0.91	1.0×10^{-11}	0.91	1.0×10^{-10}
0.92	1.0×10^{-10}	0.92	1.0×10^{-8}
0.93	1.0×10^{-9}	0.93	1.0×10^{-6}
0.94	1.0×10^{-8}	0.94	1.0×10^{-4}
0.95	1.0×10^{-7}	0.95	1.0×10^{-2}
0.96	1.0×10^{-6}	0.96	1.0
1.00	1.0×10^{-6}	1.00	1.0

The change to high hydraulic conductivity is done in order to simulate that piping will occur when the water pressure in the fracture gets positive and that can only take place when the pellet filling is close to water saturation. The piping will probably stop when the bentonite blocks have compressed the pellet filling to a high density yielding a high swelling pressure.

Mechanical

The mechanical processes are modelled in an identical way as the other bentonite parts but with different parameter values. The models are described in Åkesson et al. (2010b).

Porous elastic

$\kappa = 0.21$

$\nu = 0.4$

Moisture swelling

Moisture swelling controls the average total stress to be linear between 0 and 50 kPa between the degree of saturation 29 and 100 % as follows:

$S_r = 0.29 \rightarrow \sigma_t = 0$ kPa

$S_r = 1.0 \rightarrow \sigma_t = 50$ kPa

Initial conditions

$S_r = 0.29$

$u = -36\,925$ kPa

$\sigma_t = 0$

Contact surfaces

Contact surfaces are applied on all contacts between bentonite materials and their non-bentonite contacts.

$\phi = 8.5°$ at all contacts

9.4.5 Modelling strategy

As shown in Figure 9-9 the inflow takes place in one point in the symmetry plane at the midpoint of the canister. The inflow is modelled in a special way. A constant inflow rate q_f is forced to the inflow point. However, since the water pressure in the rock cannot exceed about 4 MPa that condition is applied. Another factor that is important is that the inflow rate q_f is related to free inflow into the empty deposition hole. If there is a resistance to inflow that creates a water pressure larger than zero at the inflow point the inflow rate will be decreased since the hydraulic gradient over the fracture decreases. The effect of this is not known and not automatically taken into account since the rock is not modelled. Instead a procedure according to Equations 4-2 and 4-3 that reduces the inflow rate proportionally to the pore water pressure at the inflow point is applied.

$$q = q_f \times (4.0 - u_i)/4.0 \qquad (9\text{-}24)$$

$$q = q_f \text{ if } u_i < 0 \qquad (9\text{-}29)$$

where

q = water inflow rate

q_f = water inflow rate at free inflow ($u_i = 0$)

u_i = water pressure at the inflow point

In addition, the flow is thus limited to q_f if the pore pressure in the inflow point is negative.

9.4.6 Modelling results – constant inflow rate

General

A large number of different calculations have been done with a constant inflow rate modelled according to Section 9.4.5. Convergence problems and questions about the hydraulic behaviour of the pellet filling have dominated the work. Three different types of results will be shown:

1. HM-calculation.
2. HM-calculation with fixed nodes in the pellet filled slot.
3. H-calculations of only the pellet filled slot.

The hydraulic behaviour of the pellet filling has also been considered with different K-values in order to have a wetting behaviour that better reflects the actual behaviour. The two alternative models shown in Table 9-5 have been used and the results compared.

HM-calculation of the entire deposition hole – 0.0001 L/min

The element mesh shown in Figure 9-9 and the material models described in Section 4.4 were used for this calculation and the inflow rate was 0.0001 L/min. The reference model of the hydraulic conductivity was used in this calculation i.e. Equation 9-23 and Table 9-4.

It was not possible to run the calculation to full saturation due to convergence problems. The last point of time where results are available is after 10^{10} seconds or 320 years.

Figure 9-10 shows the degree of saturation at different times and Figure 9-11 shows the pore-water pressure at the same times. Figure 9-12 shows the total stress and the void ratio distribution in the symmetry plane after 320 years, while Figure 9-13 shows history plots of the degree of saturation for a number of points in a bentonite ring and the pellet filling.

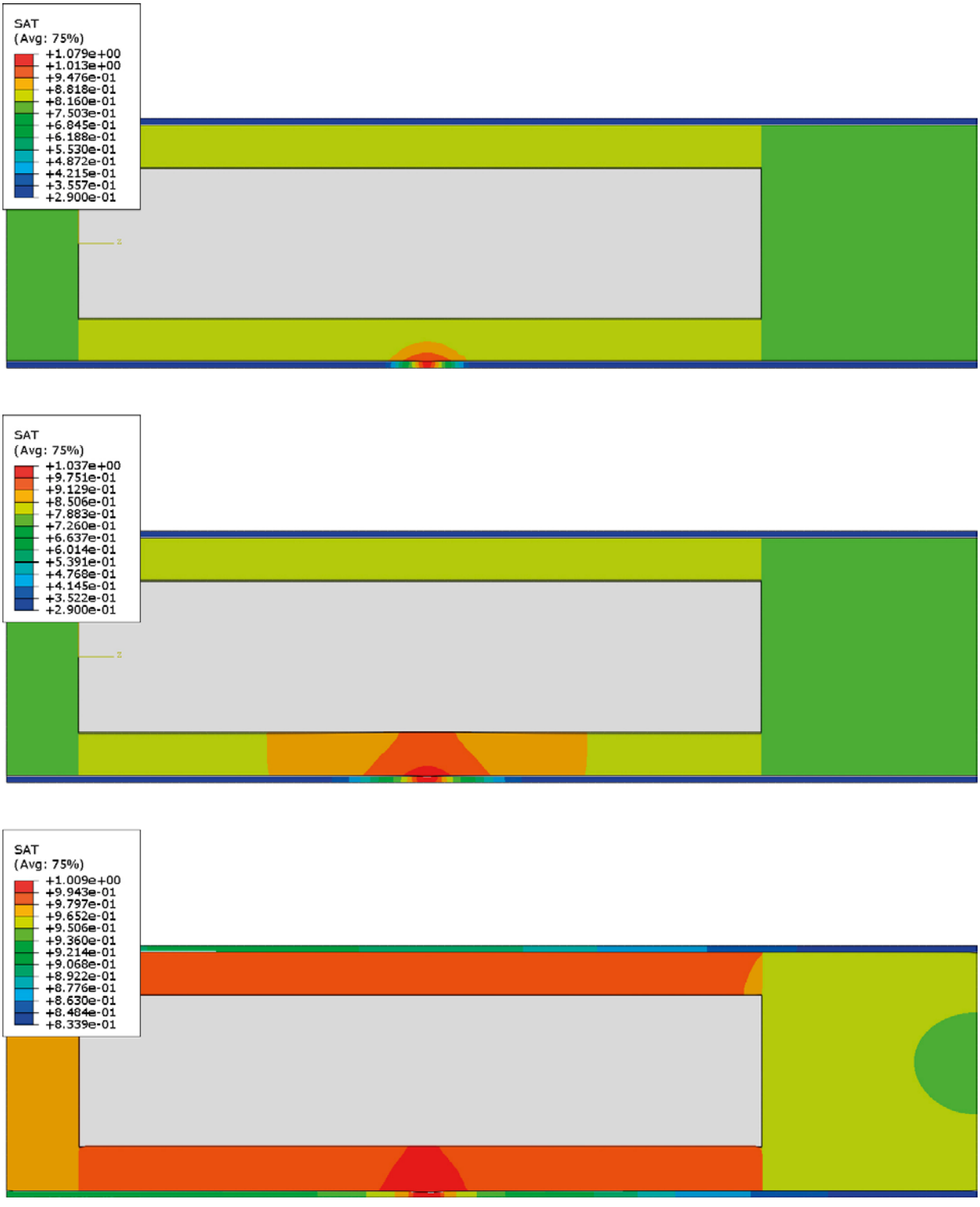

Figure 9-10. *HM-modelling of an entire deposition hole with the point inflow rate of 0.0001 L/min. Degree of saturation after 0.32 years (upper), 3.2 years (middle) and 320 years (lower).*

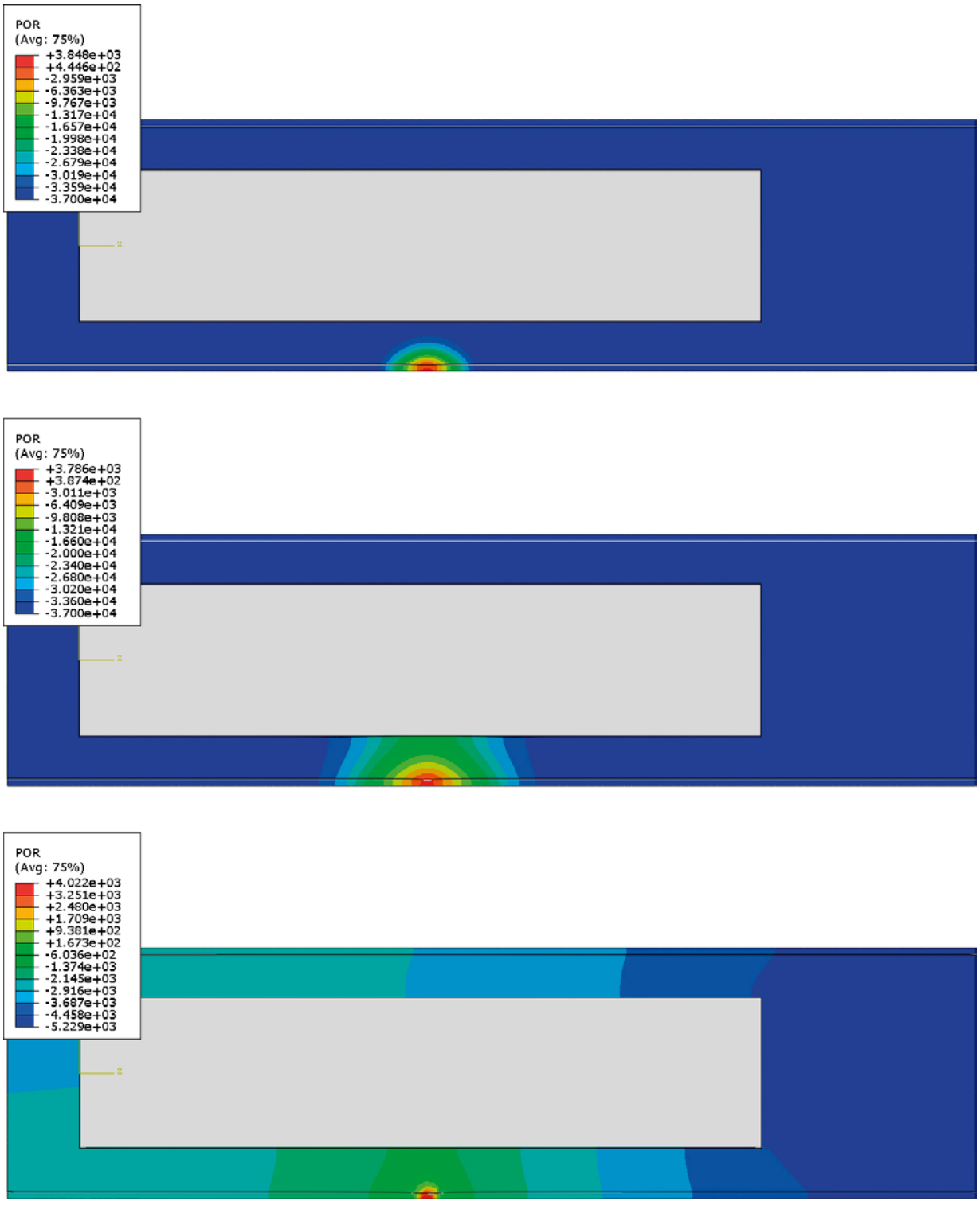

Figure 9-11. *HM-modelling of an entire deposition hole with the point inflow rate of 0.0001 L/min. Pore-water pressure (kPa) after 0.32 years (upper), 3.2 years (middle) and 320 years (lower).*

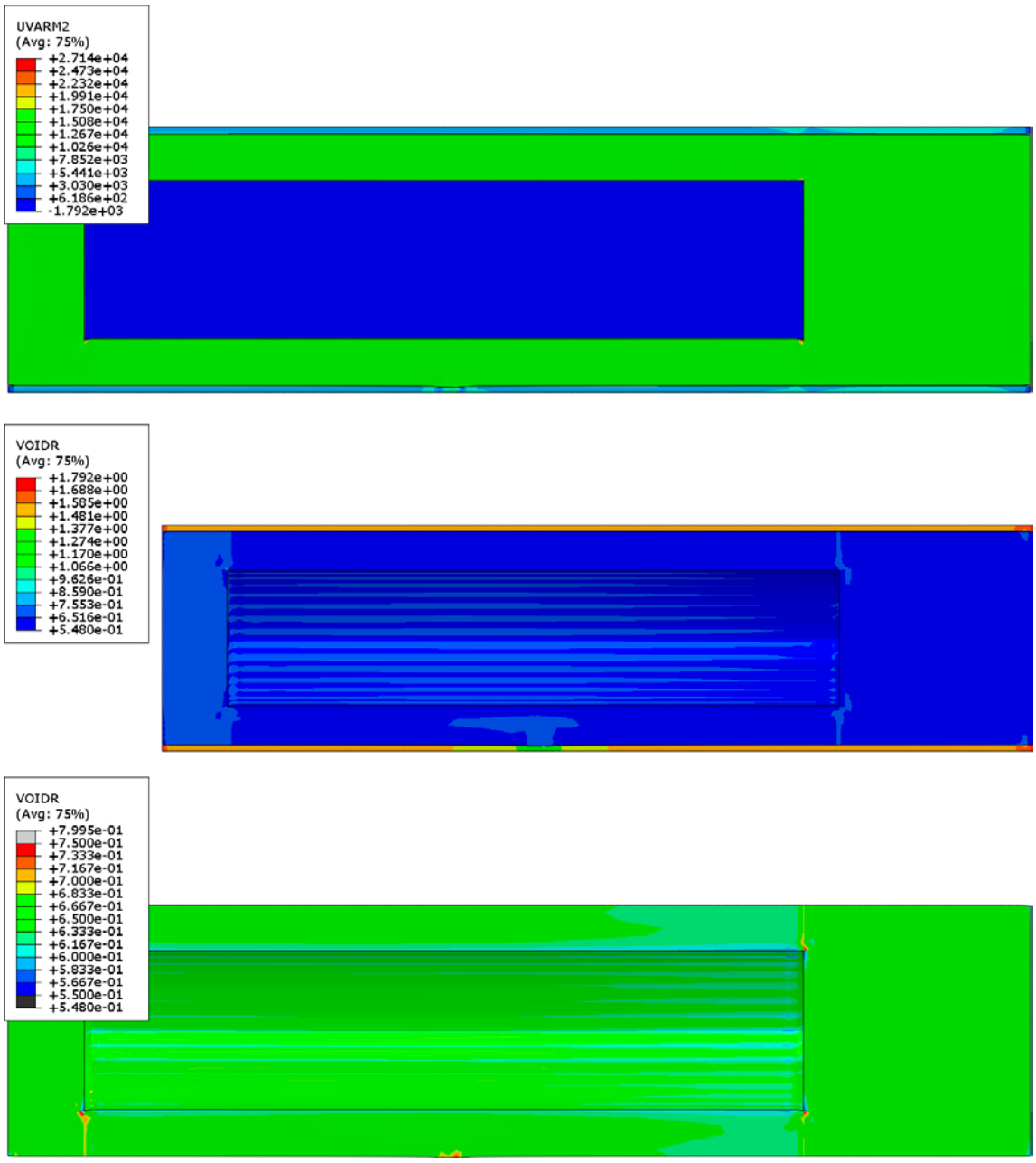

Figure 9-12. *HM-modelling of an entire deposition hole with the point inflow rate of 0.0001 L/min. Total stress (kPa) (upper) and void ratio (lower) after 320 years. The lower picture shows the void ratio in the blocks and rings only and at another scale.*

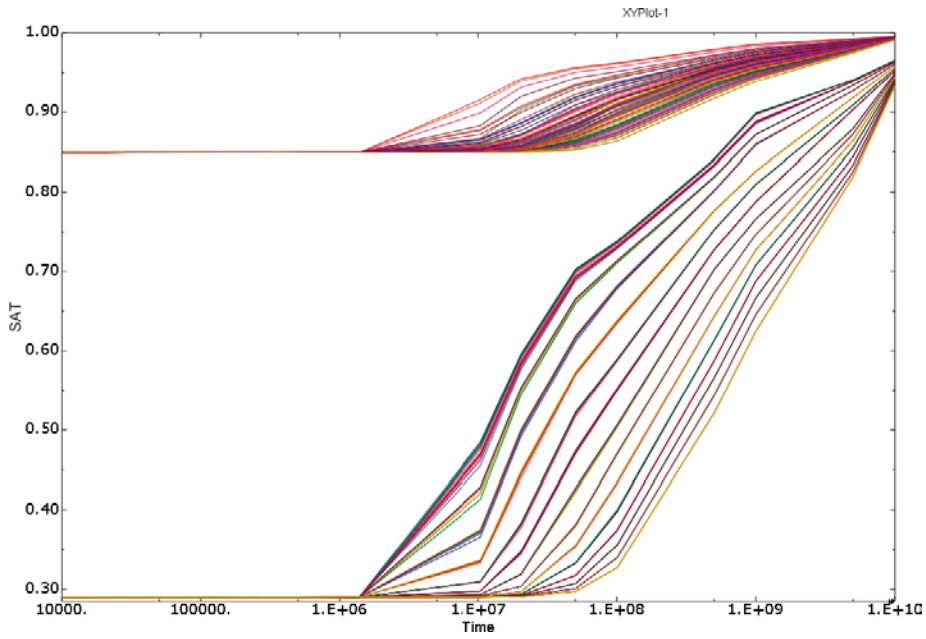

Figure 9-13. *HM-modelling of an entire deposition hole with the point inflow rate of 0.0001 L/min. History plots of degree of saturation for different points in the bentonite rings (upper curves) and the pellet filling according to view 1 and view 2 in Figure 9-9.*

This model leads to a number of different observations:

After 320 years almost the entire bentonite in the blocks and rings have a degree of saturation larger than 95 %, while only a small part of the pellet filling has such a high degree of saturation. The reason for this difference is that the pore-water pressure (suction) is the same in the blocks/rings and the pellet filling in almost all horizontal sections, which yields different degree of saturation due to the difference in density.

There is a large gradient in pore-water pressure in the pellet filled slot during the entire saturation period since the water transport rate in the pellets is slow compared to the inflow rate.

The pore-water pressure is very high in the inflow point during the entire period, which yields a choking of the inflow rate according to Equation 4-1. The water pressure is much higher than the pellet filling can be expected to withstand.

Extrapolation of the history curves leads to an estimated time to full saturation of about 1 500 years. This is about 50 times longer than the time it would take to saturate the buffer meaning that the average inflow rate is only about 2×10^{-6} L/min instead of 10^{-4} L/min.

The inflow rate is thus much lower than the intended inflow rate due to the choking of the inflow. The results are thus probably not representative for the inflow rate 10^{-4} L/min but may be used to study the homogenisation at an inflow rate of about 2×10^{-6} L/min if the pellet filling is not able to prevent water inflow by piping. The degree of saturation and the pore-water pressure plots (Figure 9-10 and Figure 9-11) show that in the beginning after 3.2 years the wetting is very uneven, but after long time (320 years) the wetting has been more evenly distributed and takes place from the entire pellet filling although there are still large gradients in the pellet filling. The void ratio distribution after 320 years, when the degree of saturation in almost all the high density part (blocks and rings) is more than 95 %, is not very inhomogeneous as shown in Figure 9-12. The influence is very local around the inflow point with lower void ratio in the pellet filling and higher in the neighbouring parts of the bentonite rings. It should though be noted that the simulation was not run to complete water saturation.

HM-calculation of the entire deposition hole with fixed nodes of the pellet filled slot – inflow 0.0001 L/min.

Since the calculation in the previous section was not completed due to convergence problems a new model, identical to the previous one but with all nodes of the pellet filling fixed, was made. The problems of convergence, which are often related to deformed elements, could in this way be overcome.

The same history curves of degree of saturation as shown in Figure 9-13 are shown for the fixed nodes calculation in Figure 9-14. The figure shows that the buffer is saturated after 5×10^{10} seconds corresponding to 1 585 years, which was also concluded for the calculation without fixed nodes.

H-calculations of only the pellet filled slot

In order to study the flow behaviour in a pellet-filled slot a number of calculations have been done with the rest of the model excluded. Results from the models described in Table 9-6 will be shown:

Figure 9-15, Figure 9-16, Figure 9-17 and Figure 9-18 illustrate the results and the differences for the calculations with the inflow rate 10^{-4} L/min. The results from all three models are shown and compared in each figure.

The pore pressure distribution after 3.2 years and 32 years are shown in Figure 9-15 and Figure 9-16. The degree of saturation after 32 years is show in Figure 9-17. In Figure 9-18 the calculated total inflow is plotted as function of time.

Table 9-6 Calculations with pellets filled slot only.

Model	See Table	Inflow rate	Remark
Reference model	Table 9-3	10^{-4} L/min	
Alternative model 1	Table 9-4	10^{-4} L/min	Increased K at $S_r > 90$ %; $K_{max} = 10^{-6}$ m/s
Alternative model 2	Table 9-4	10^{-4} L/min	Increased K at $S_r > 90$ %; $K_{max} = 1$ m/s
Alternative model 2	Table 9-4	10^{-6} L/min	Increased K at $S_r > 90$ %; $K_{max} = 1$ m/s

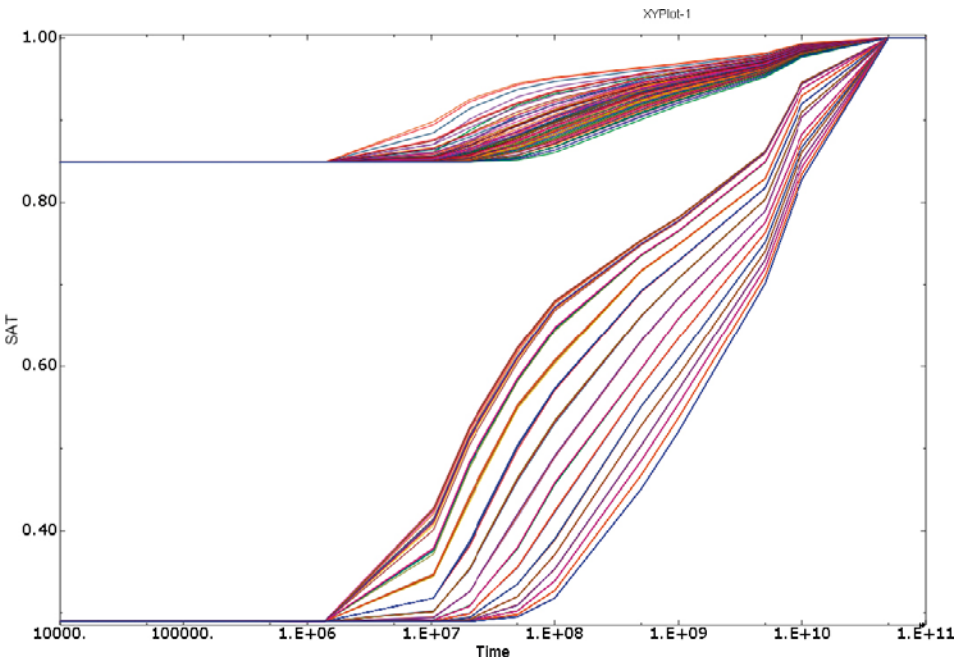

Figure 9-14. *HM-modelling of an entire deposition hole with the point inflow rate of 0.0001 L/min in the model with fixed nodes of the pellet filling. History plots of degree of saturation for different points in the bentonite rings and the pellet filling.*

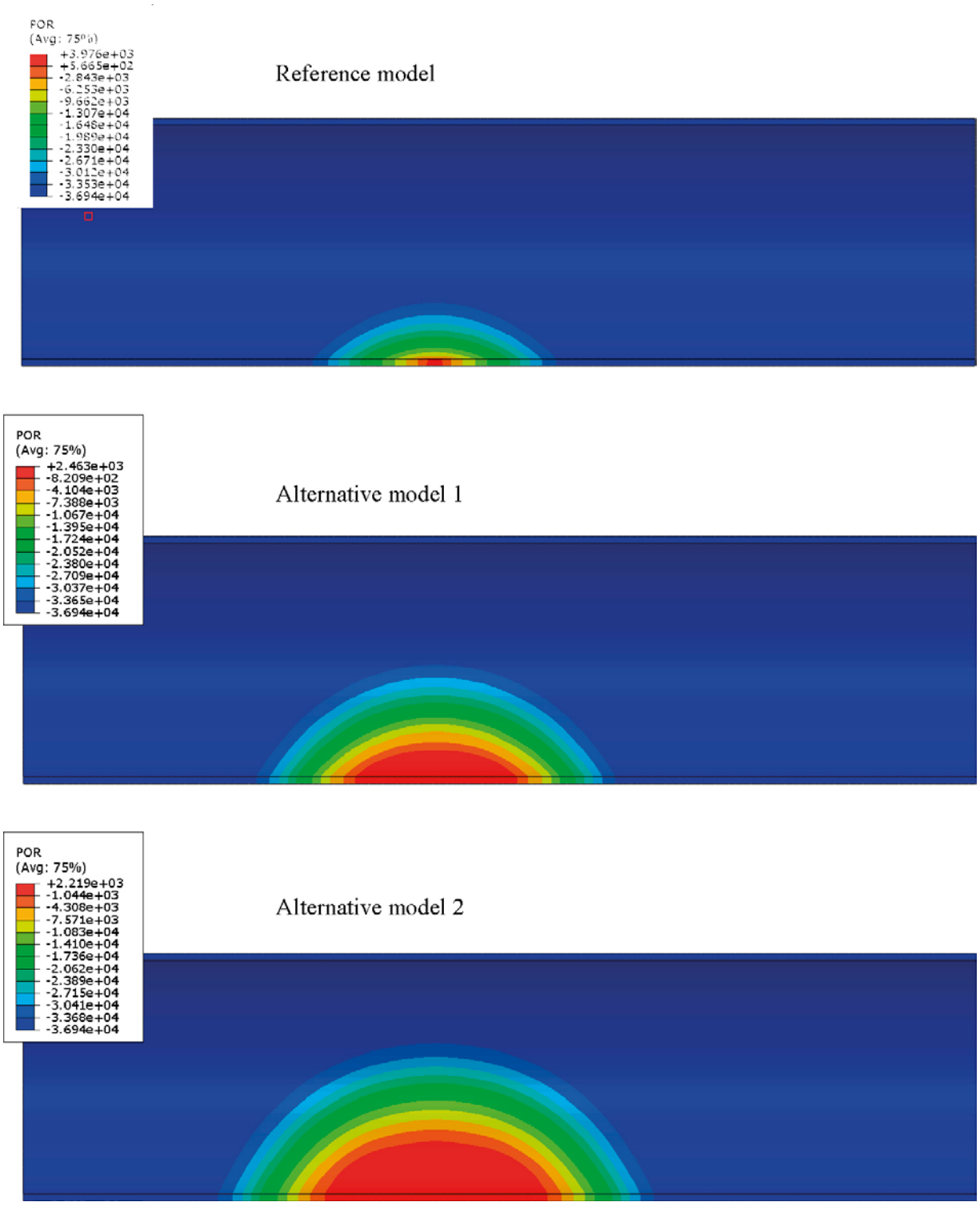

Figure 9-15. *H-modelling of pellet filled slot only with the point inflow rate of 0.0001 L/min. Pore-water pressure (kPa) after 3.2 years.*

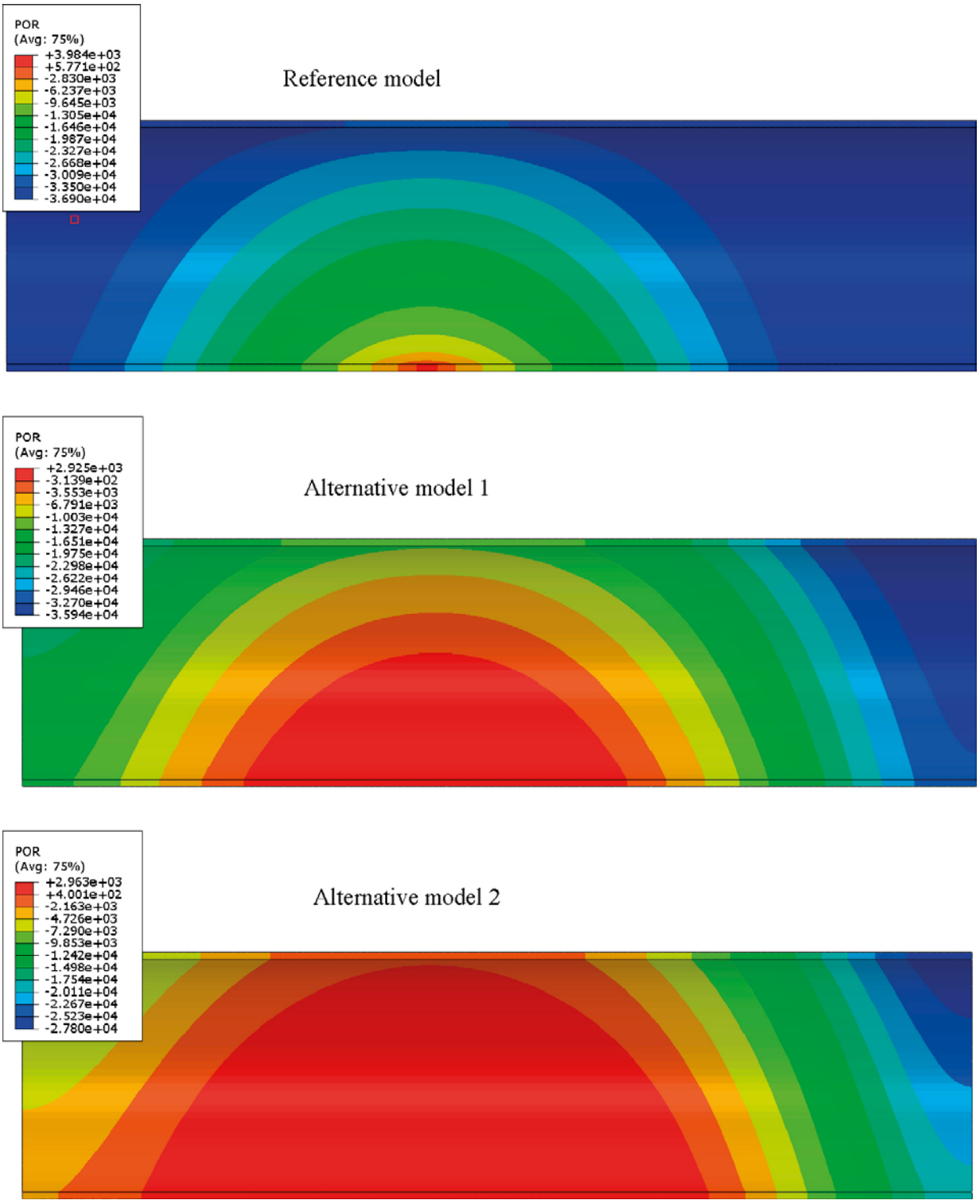

Figure 9-16. *H-modelling of pellet filled slot only with the point inflow rate of 0.0001 L/min. Pore-water pressure (kPa) after 32 years.*

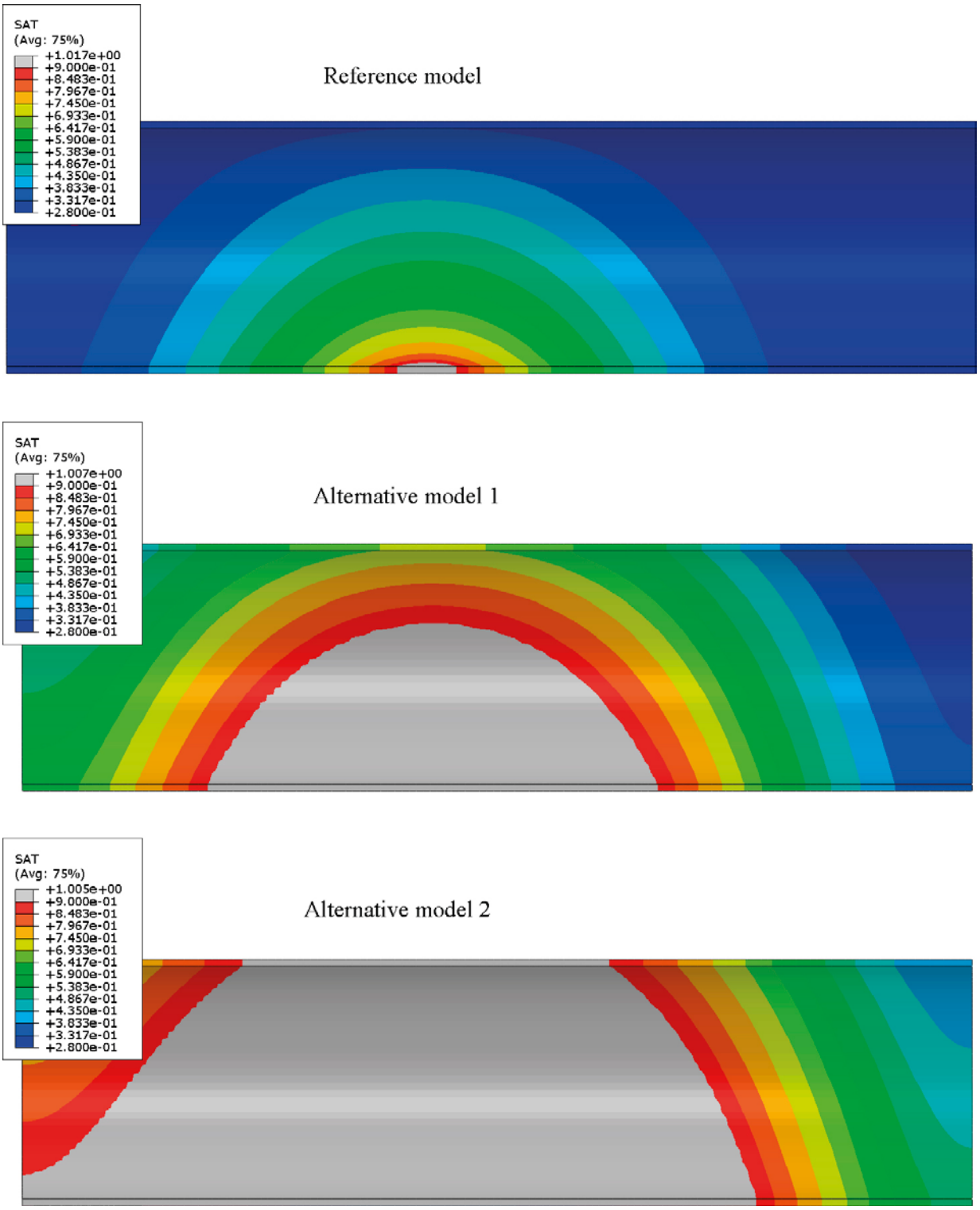

Figure 9-17. *H-modelling of pellet filled slot only with the point inflow rate of 0.0001 L/min. Degree of saturation after 32 years.*

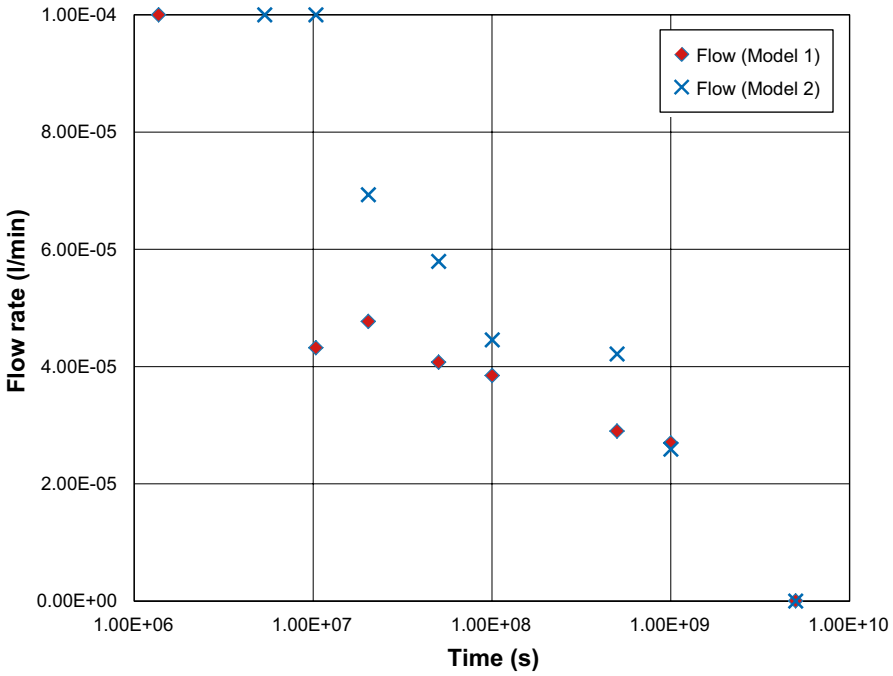

Figure 9-18. *Inflow rate as function of time for alternative models 1 and 2.*

The attempts to better model the inflow distribution with the alternative models yields some obvious results. The pore pressure at the inflow point is reduced but still too high. The propagation of the pore water into the pellet filled slot is faster. The time to full saturation is about 5×10^9 seconds ($\approx$150 years) for the alternative models and 10 times longer for the reference model. It is, however, still 10 times longer than the theoretical time to fill up the slot if the inflow rate was constant 0.0001 L/min, which means that the actual average inflow rate in the alternative models is 10 times lower. There is also some difference between the alternative models with faster wetting in model 2 due to the higher hydraulic conductivity adapted at $S_r > 90$ %.

The results from the calculation with the inflow rate 10^{-6} L/min are shown in Figure 9-19 to Figure 9-21. Figure 9-19 shows the pore-water pressure at three different times, Figure 9-20 shows the degree of saturation at the same times and Figure 9-21 shows the inflow rate and the pore pressure in the inflow points as function of time.

The figures show that the wetting is rather slow. The pore pressure in the inflow points is always negative meaning that the pellet filling can take more water than the inflow. The inflow rate is constant during almost the entire calculation since it has been set at 10^{-6} L/min according to the condition in Equation 9-25. After 3×10^{10} seconds (950 years), the inflow is reduced since the pore pressure gets positive. Some strange irregularities occur after that time but the inflow decreases and full saturation is reached after 1 500–2 000 years whereupon the pore pressure is 4 MPa and the inflow zero.

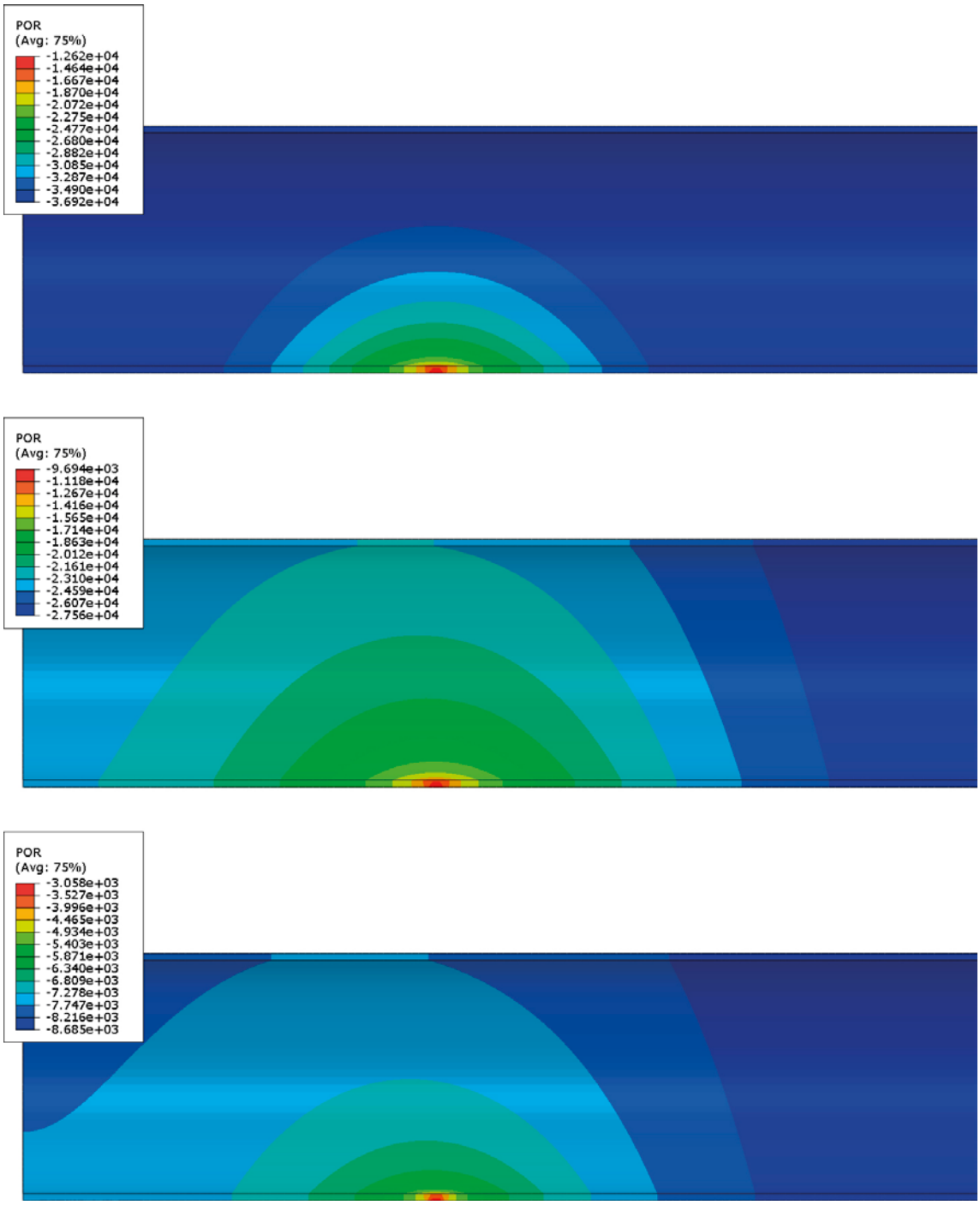

Figure 9-19. *H-modelling of pellet filled slot only with the point inflow rate of 10^{-6} L/min. Pore-water pressure (kPa) after 32 years, 320 years and 950 years.*

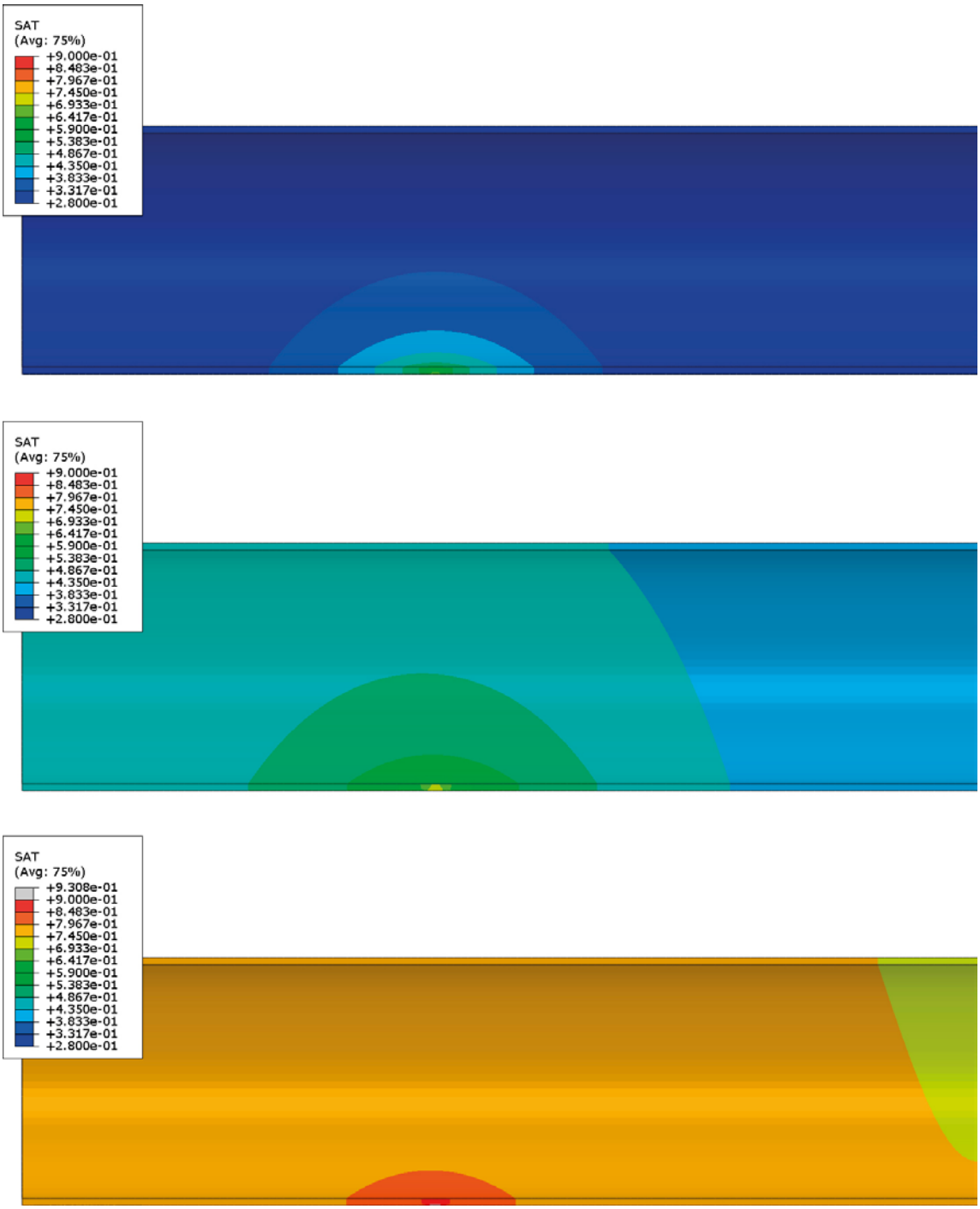

Figure 9-20. *H-modelling of pellet filled slot only with the point inflow rate of 10^{-6} L/min. Degree of saturation after 32 years, 320 years and 950 years.*

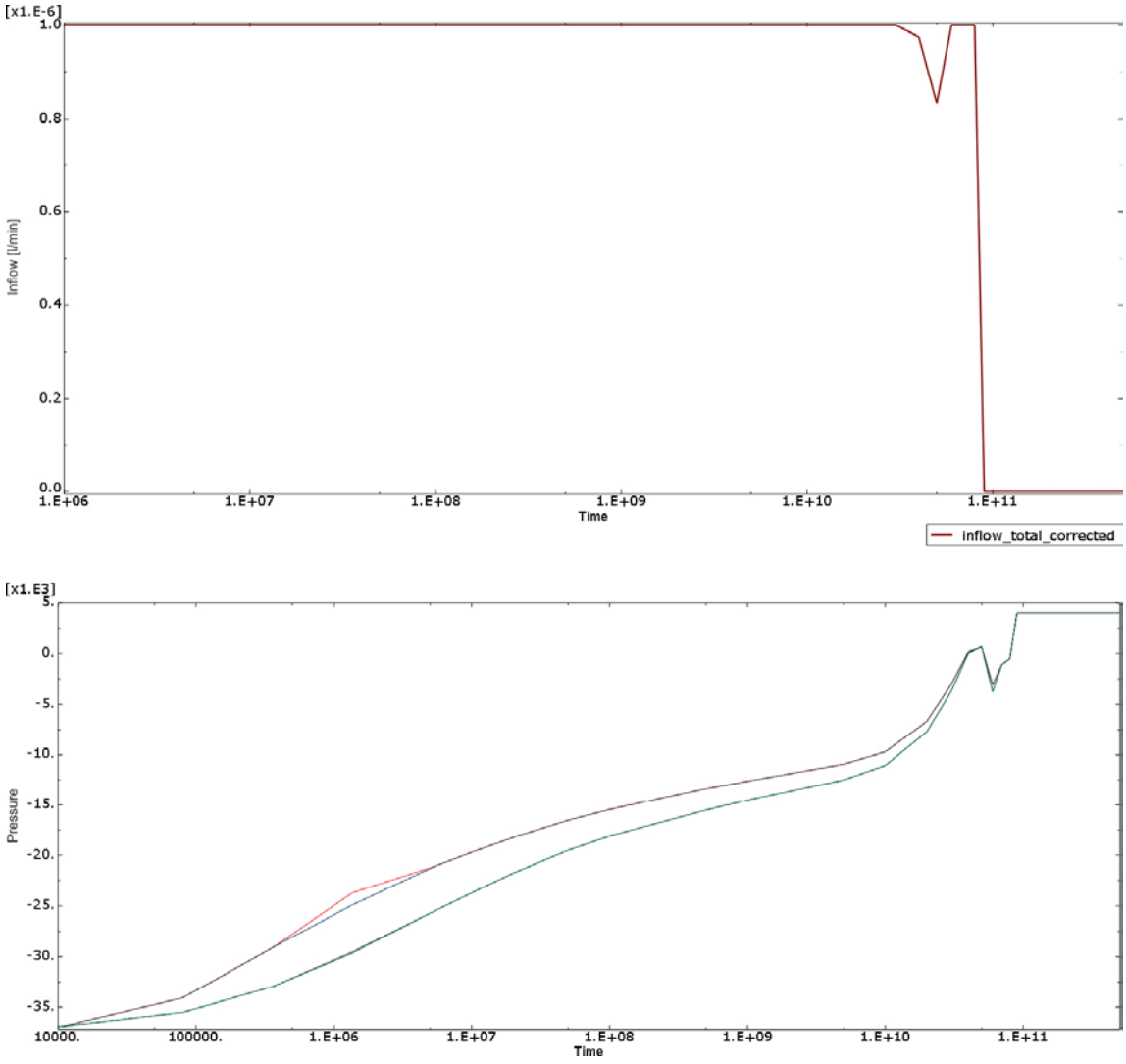

Figure 9-21. *H-modelling of pellet filled slot only with the point inflow rate of 10^{-6} L/min. Total inflow (upper) and pore pressure (kPa) in the inflow points as function of time (s).*

9.4.7 Modelling results – constant water pressure

General

Four simulations with constant water pressure were also run. In two of them the inflow was located in one point as the simulations shown in Sections 9.4.4–9.4.6. In the other two the flow was instead located as a line source. Since there were large problems with convergence each simulation were also at first run with fixed nodes in the pellet filling. Unfortunately only the point inflow simulations yielded results that can be used.

Point inflow and fixed nodes of the pellet filling

This simulation was identical to the one shown in Section "HM-calculation of the entire deposition hole with fixed nodes of the pellet filled slot – inflow 0.0001 L/min", with the only difference that a constant inflow rate was changed to constant water pressure $u = 0$ kPa.

Figure 9-22 shows history plots of the pore-water pressure in a number of points in the pellets and the bentonite rings. Figure 9-23 shows the water inflow rate as function of time and Figure 9-24 and Figure 9-25 show the pore-water pressure and the degree of saturation after 320 years and 3 200 years.

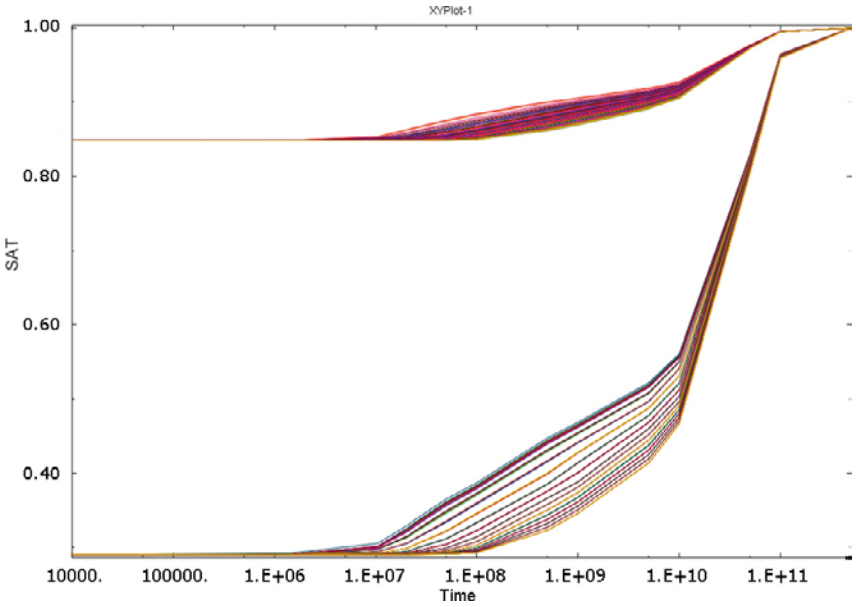

Figure 9-22. *HM-modelling of an entire deposition hole with point inflow and constant pore-water pressure in the model with fixed nodes of the pellet filling. History plots of degree of saturation for different points in the bentonite rings and the pellet filling.*

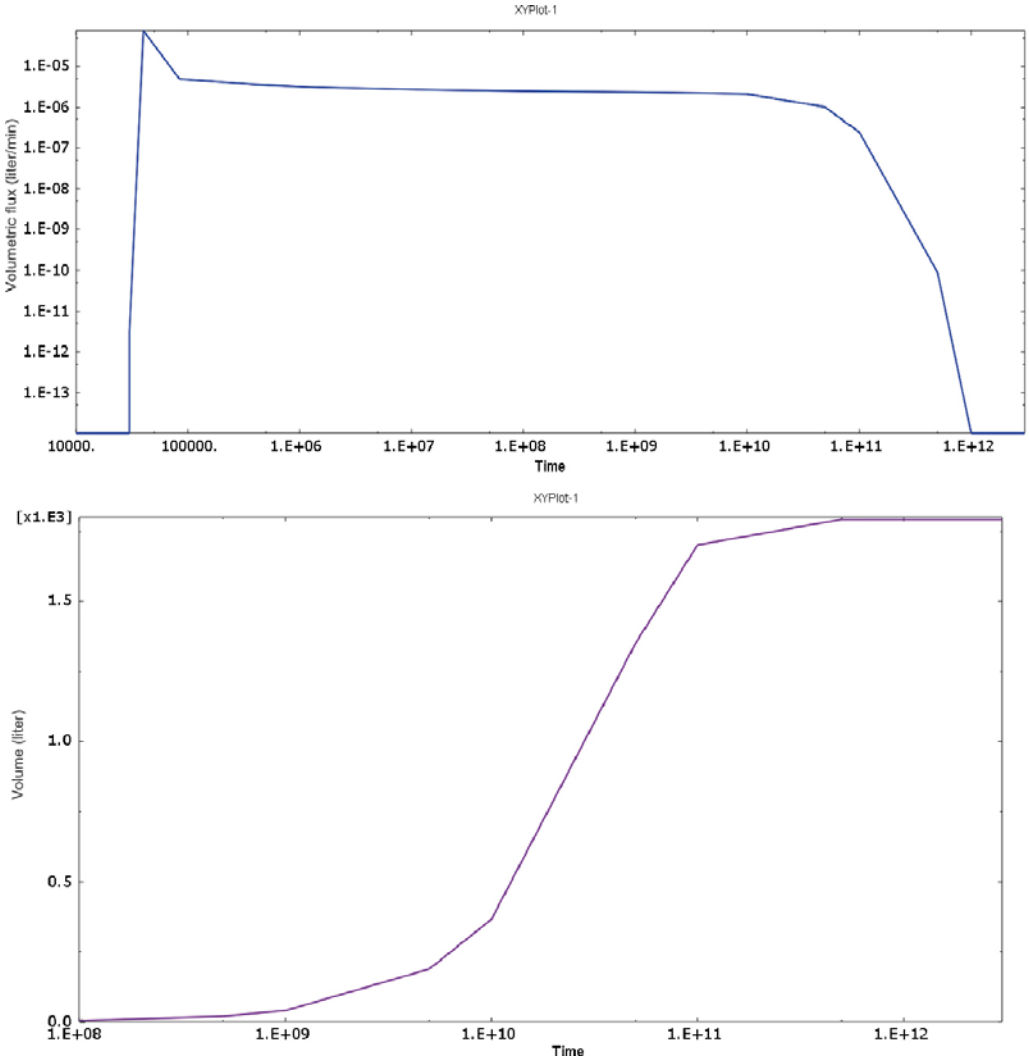

Figure 9-23. *HM-modelling of an entire deposition hole with point inflow and constant pore-water pressure in the model with fixed nodes of the pellet filling. Water inflow rate (upper) and total water inflow as a function of time (s).*

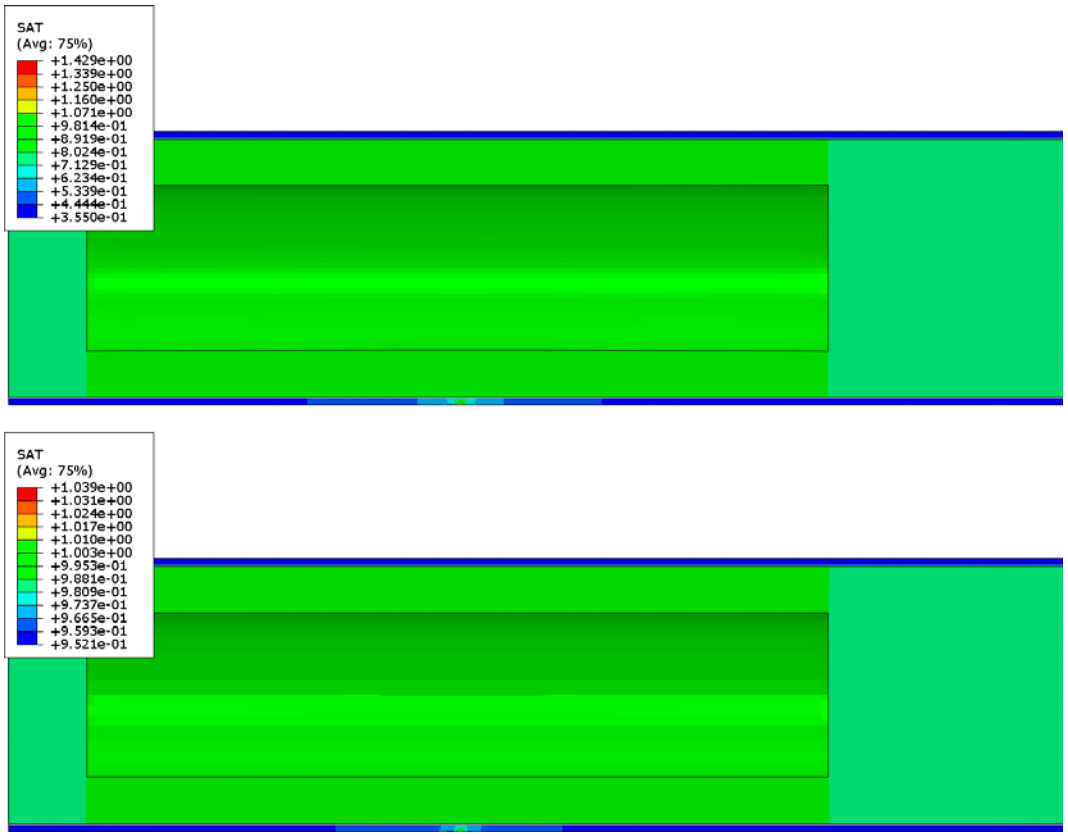

Figure 9-24. *HM-modelling of an entire deposition hole with point inflow and constant pore-water pressure in the model with fixed nodes of the pellet filling. Degree of saturation after 320 years (upper) and 3 200 years (lower).*

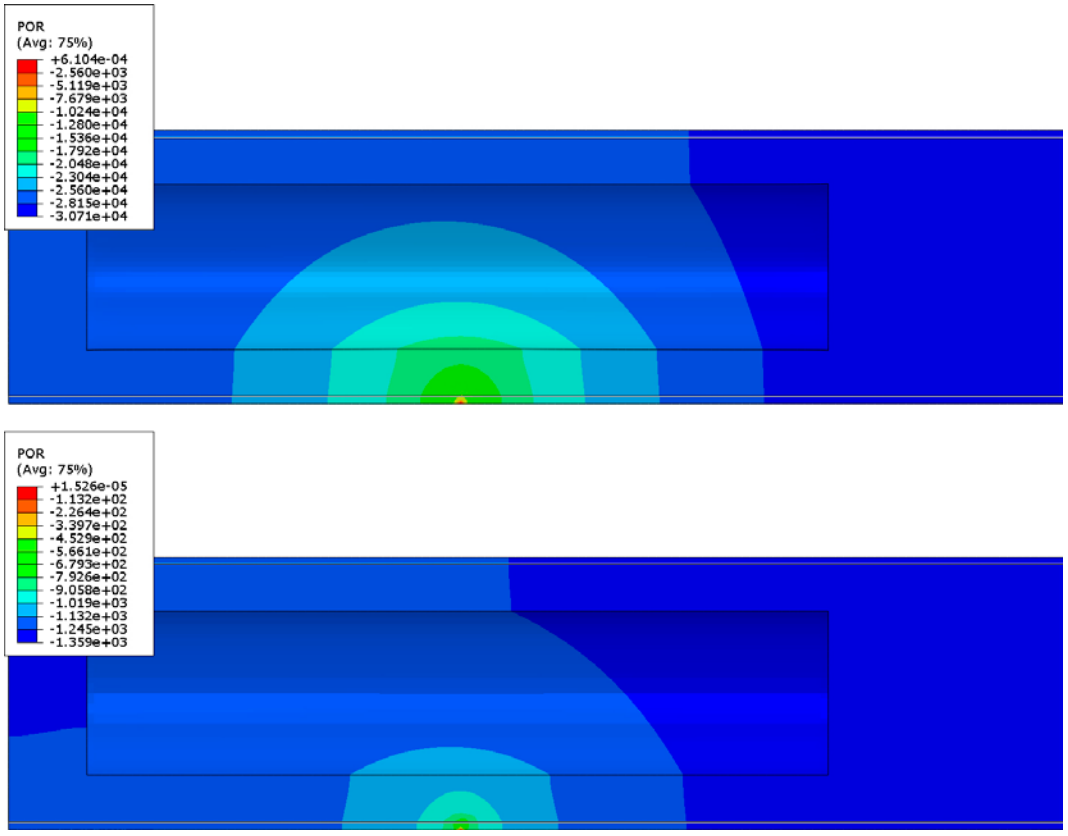

Figure 9-25. *HM-modelling of an entire deposition hole with point inflow and constant pore water pressure in the model with fixed nodes of the pellet filling. Pore-water pressure (kPa) after 320 years (upper) and 3 200 years.*

The results show that the entire buffer is water saturated after between about 5 000 years and 15 000 years (1.5×10^{11}–4.5×10^{11} seconds). The water inflow rate is between 10^{-5} and 10^{-6} L/min up until about 1 500 years (5×10^{10} s) where after it decreases rapidly.

The wetting is rather inhomogeneous in the beginning, with large gradients in pore-water pressure in the pellet filling after 320 years with still very high suction of 30 000 kPa in large parts. With time the wetting gets more homogeneous and after 3 200 years the pore-water pressure gradient is reduced to about 4 % of the original (highest suction about 1 350 kPa).

Point inflow and free nodes of the pellet filling

Because of convergence problems, only results up to about 1 600 years are available. The results are similar to the results of the simulation with fixed pellet nodes, with exception of the void ratio distribution. Figure 9-26 and Figure 9-27 show some contour plots of the situation after 1 600 years.

Figure 9-26. shows that the pore-water equilibrium has gone rather far and that the degree of saturation is everywhere higher than 96 %. In spite of that the simulation is not completed the results can be used to some extent.

Figure 9-27 shows the mechanical consequences with the void ratio distribution and the total displacements. The results show that there is no strong inhomogeneity except from the large difference in void ratio of the block/ring parts and the pellet part, which indicate that the pellet filling is too stiff. The displacement plot shows that the canister has moved about 4 mm away from the water inlet side due to the inhomogeneous wetting.

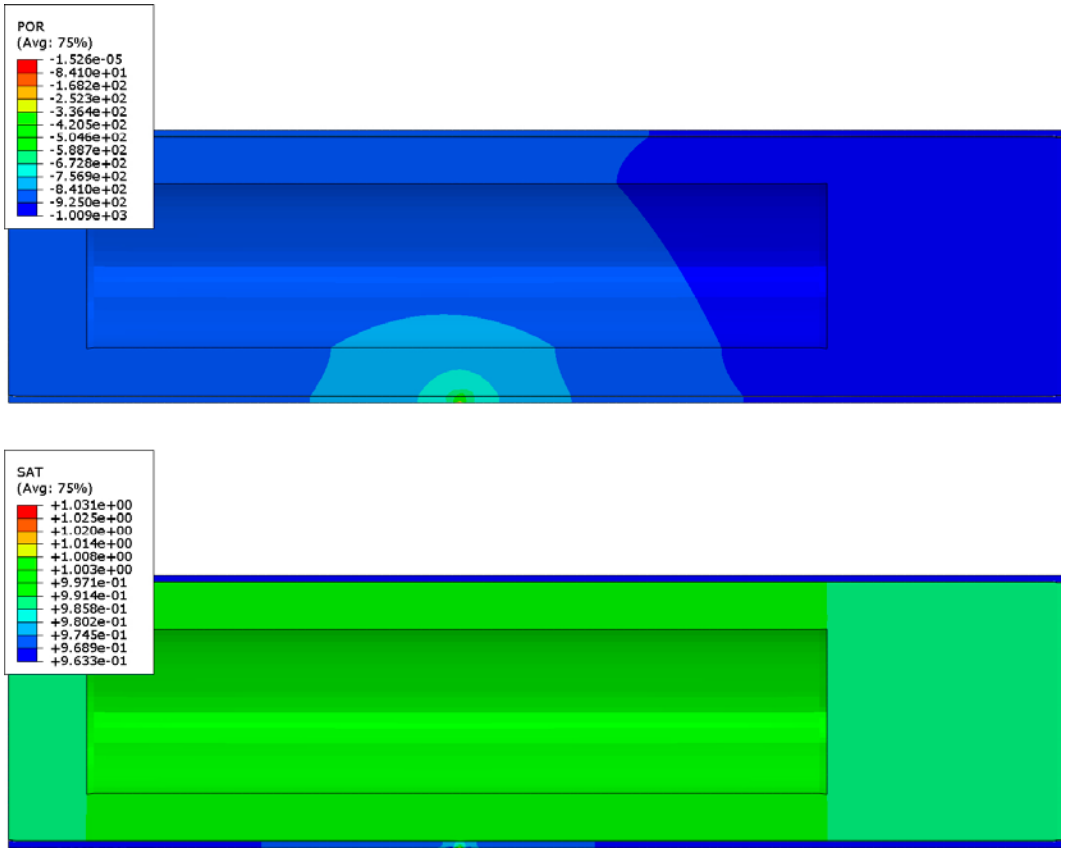

Figure 9-26. *HM-modelling of an entire deposition hole with point inflow and constant pore-water pressure in the model with free nodes of the pellet filling. Pore-water pressure (kPa) and degree of saturation after 1 600 years.*

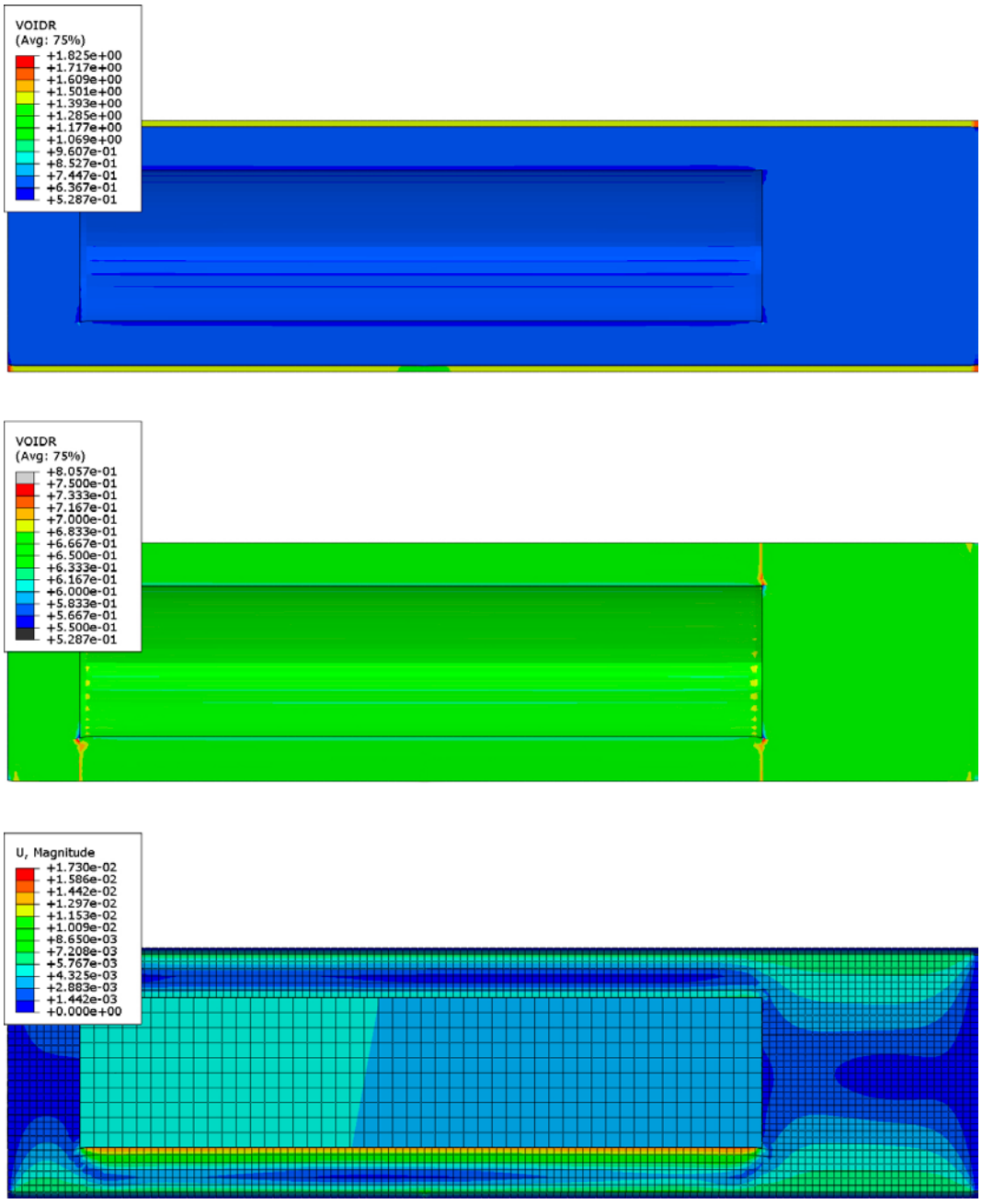

Figure 9-27. *HM-modelling of an entire deposition hole with point inflow and constant pore-water pressure in the model with free nodes of the pellet filling. Void ratio of the entire buffer (upper), void ratio of the blocks and rings (middle) and displacements after 1 600 years (lower).*

9.5 Risks and consequences

In spite of problems with convergence and uncertainties of how water inflow into a pellet filling can be modelled, an analysis of the risks and consequences can be done.

Since uneven wetting will only occur when the inflowing water mainly comes in local spots, the contribution from the rock matrix must be small otherwise there will be a simultaneous homogeneous wetting. As concluded in Section 9.2.1 the matrix hydraulic conductivity is in the range between 10^{-12} m/s and 10^{-13} m/s. If the lower value is used the time to complete water saturation from the rock matrix alone will be about 1 500 years according to the analyses referred to in Section 9.2.2. This means that if a point inflow rate yields a longer time to full saturation of the buffer than about 1 500 years there will be no uneven wetting of the buffer.

According to the volume calculations shown in Section 9.2.3 the time to fill up all empty pores in the buffer is 3 500 years at the point inflow rate 10^{-6} L/min and 350 years at the point inflow rate 10^{-5} L/min. The conclusion is thus that there will only be uneven wetting of the buffer if the point inflow rate is higher than between 10^{-5} L/min and 10^{-6} L/min or about 5×10^{-6} L/min.

On the other hand, if the point inflow rate is so high that the pellet filling is water filled before the buffer rings have been water saturated close to the inflow point, there will not be an uneven wetting either. As shown in Table 9-2 it will take 1.55 years to fill up the pellet voids at the inflow rate 10^{-3} L/min. The time to saturate the bentonite rings if water is freely available in the pellet filling is about 2 years (Åkesson et al. 2010b). This means that if the inflow rate is higher than 10^{-3} L/min, there will not be an uneven wetting since the pellet filling will be filled and give even wetting in the entire buffer. The requirement for this conclusion is that the water filling of the pellets are equally distributed. This is the case when the inflow rate is lower than 10^{-3} L/min – 10^{-4} L/min as shown in Figure 9-2. For 10^{-3} L/min, the water will seek its way upwards and form a wetting path with water available along a vertical line as shown in Figure 9-2.

The conclusion is thus that uneven wetting can only take place for the following cases:

1. At an inflow rate of about 10^{-3} L/min when water is freely available along a vertical line in the rock surface
2. At inflow rates (into an open deposition hole) between about 5×10^{-4} L/min – 5×10^{-6} L/min when water is available at a point in the rock surface

According to Joyce et al. (2013), the number of holes with an expected inflow rate between 5×10^{-6} L/min and 10^{-3} L/min is about 500 out of 6 916 i.e. every 14:th deposition hole may have uneven wetting.

The simulations yield that a water inflow rate of 10^{-5} L/min – 10^{-6} L/min can be taken by the pellet filling without yielding a high water pressure or a high suction at the inflow point. If the inflow rate is higher, the absence of capability to model piping will cause water pressure in the numerical simulation so high that the inflow cannot be taken by the pellet filling. The calculations that either prescribe or yield water inflow rate of between 10^{-5} L/min and 10^{-6} L/min are thus probably relevant.

The first case above corresponds to the calculation with line inflow. Unfortunately this simulation did not lead to any results. The second case corresponds mainly to the calculations shown in Section 9.4.6 with water pressure dependant inflow rate and to the point inflow calculation with constant water pressure shown in Section 9.4.7. Both these latter calculations have an effective inflow rate of between 10^{-5} L/min and 10^{-6} L/min.

The results of the mechanical simulations of these cases indicate that the inhomogeneity of the buffer caused by the uneven wetting is rather small, although some horizontal displacement of the canister can be expected as well as some local inhomogeneity around the inflow point.

The overall conclusion is thus that the inhomogeneous wetting will not take place in dry holes but in a spectrum of holes (about 500) that have an inflow rate of between 5×10^{-6} L/min and 10^{-3} L/min and that the influence on the density distribution of the buffer and thus also the swelling pressure on the canister is very limited.

It must though be pointed out that there are several uncertainties about the simulations and analyses made and the main ones being the following two:

The mechanical model of the dry pellet filling in the simulations is not verified and calibrated and it turned out to be a little stiffer than what can be expected after full saturation, which thus underestimates the displacements. However, making it softer would make the convergence more difficult.

The hydraulic model of the dry pellet filling has been made with a number of assumptions that have not been verified. The theoretical analysis (Section 9.3) and the numerical model (Section 9.4) yield similar results but need to be investigated and verified in laboratory tests.

10 Analysis of how a buffer with brittle shear properties may affect the rock shear case

Lennart Börgesson, Clay Technology AB
Jan Hernelind, 5T Engineering AB

10.1 Introduction

Tests on bentonite that has been affected by high temperatures have shown tendencies of brittle failure during shear in contrast to unaffected bentonite, which has smooth or no decrease in strength after peak shear stress. Figure 10-1 shows example of such results.

The general conclusions from the tests were that the shear strength is not affected but the failure may be brittle i.e. have an abrupt decrease in shear resistance after reaching maximum shear stress. Similar behaviour has been observed in field tests at temperatures below 100 °C (Dueck et al. 2011).

The effect of a rock shear through a deposition hole has been investigated with both laboratory tests that have been the bases for a material model of the buffer and by a large number of finite element calculations that have studied the effect of different rock shear cases on the stresses in the canister. The material models of the buffer and the copper and the calculation technique have been verified by modelling three laboratory tests of a rock shear scaled 1:10. These studies are reported in several technical reports and articles. See e.g. Dueck et al. (2010), Börgesson et al. (2010), Börgesson and Hernelind (2010), Hernelind (2010) and Dueck (2010).

The influence of having a buffer that show brittle failure on the stresses in the canister after a rock shear has been studied with a series of finite element calculations.

10.2 Finite element model

The material model of the bentonite is the same as used in the referred documents. The bentonite is modelled as an elastic-plastic material with strain rate dependant stress-strain relations. Four different calculations have been done, one reference calculation with unaltered bentonite, two calculations with brittle bentonite and a fourth calculation with brittle bentonite and with the shear plane of the buffer removed in order to simulate that the shear strength has been completely lost in that zone. The material model for the reference case is identical to the material model of the bentonite used for SR-Site. The model is described in Börgesson et al. (2010).

Figure 10-2 shows the stress-strain relations for the models.

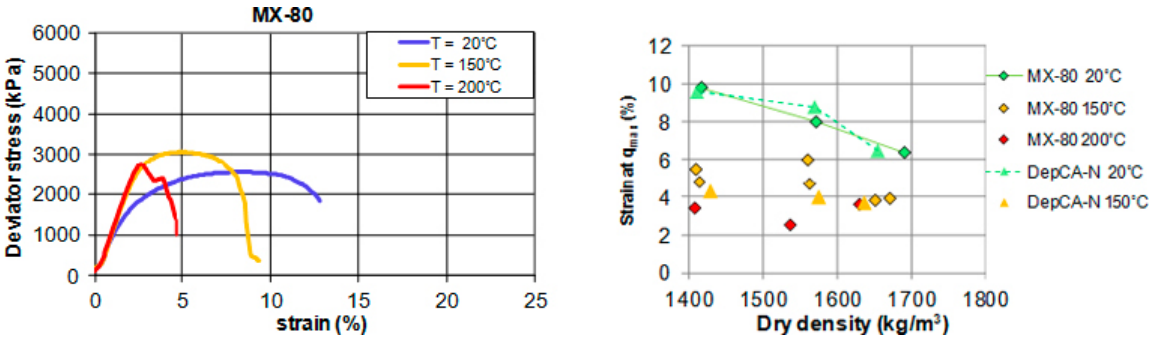

Figure 10-1. *Example of brittle failure. The left figure shows example of stress strain relations at uni-axial testing of specimen of bentonite that have been exposed to different temperatures. The right figure shows measured strain until failure as function of dry density for specimen exposed to different temperature.*

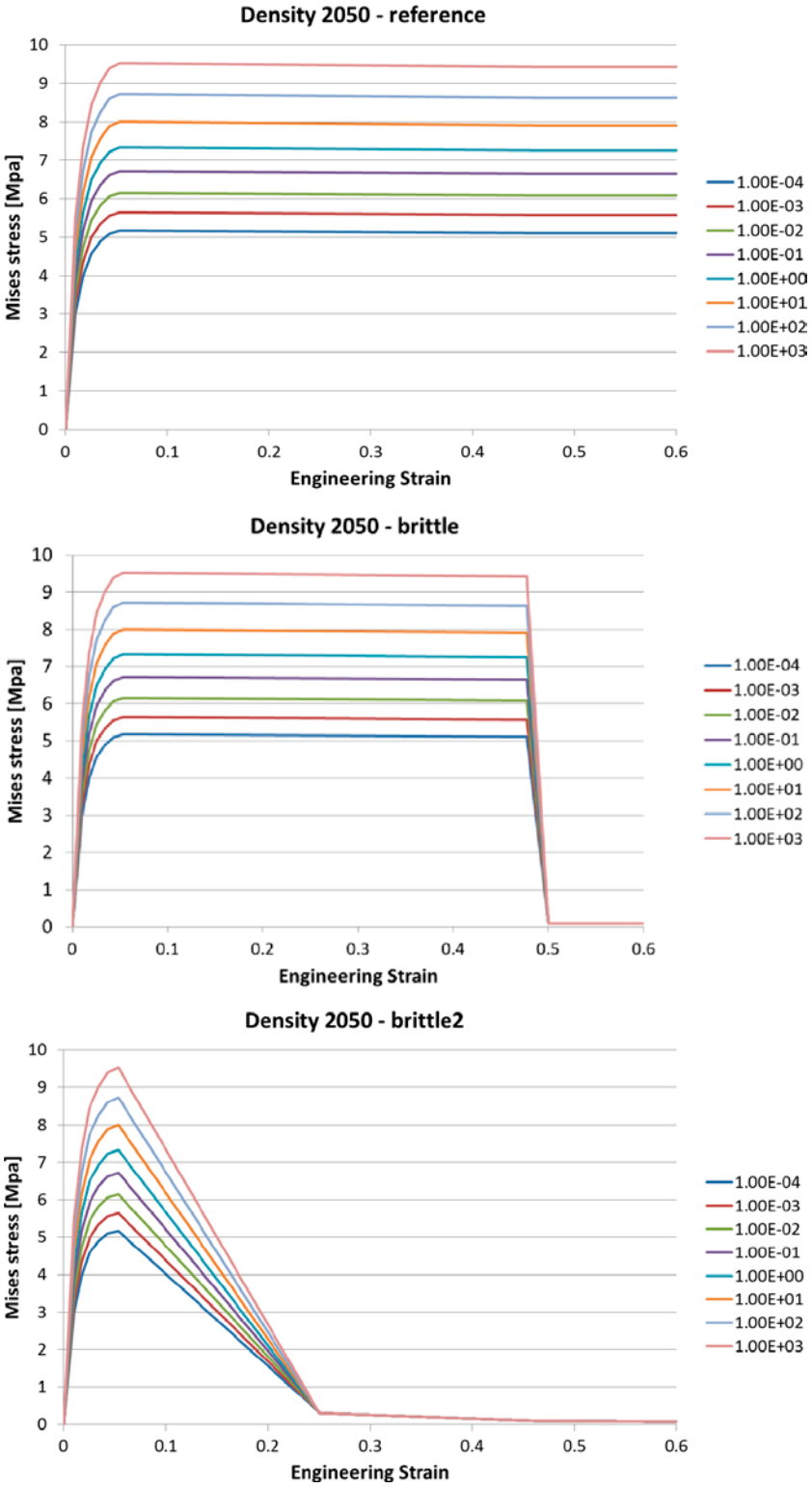

Figure 10-2. *Stress-strain relations of the bentonite in the calculations – see Table 10-1.*

The geometry of the canister consists of the insert (made of iron), the insert lid (made of steel) and the copper shell surrounded by buffer material (bentonite). The geometry is based on CAD-geometries received from SKB, "Ritningsförteckning för kapselkomponenter" (Hultgren 2014) and should therefore correspond to the current design.

The copper and cast iron were modelled in an identical way as the calculations made for SR-Site. These models are in detail described in Hernelind (2010).

The finite element mesh with horizontal shear at the ¼ point of the canister was used for the calculations since this case had proved to be the most critical that yields the highest stresses in the canister. The mesh is described in Hernelind (2010) and shown in Figure 10-3, Figure 10-4 and Figure 10-5.

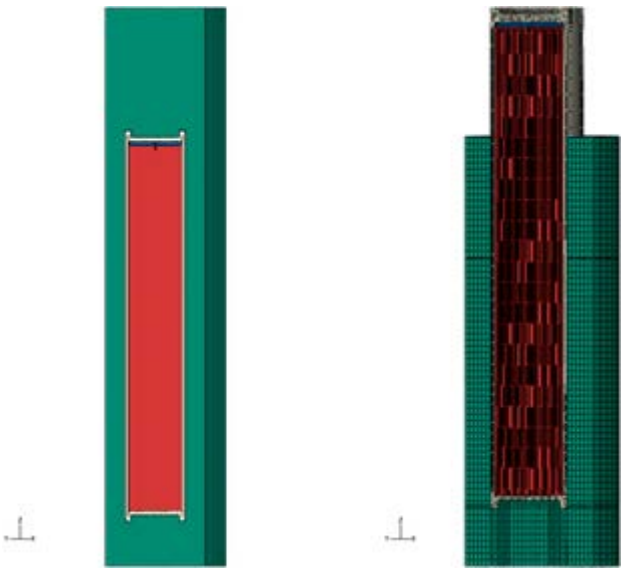

Figure 10-3. *Plot of geometry for rock shear perpendicular to axis of canister (left) with the ¼ shearing part removed (right).*

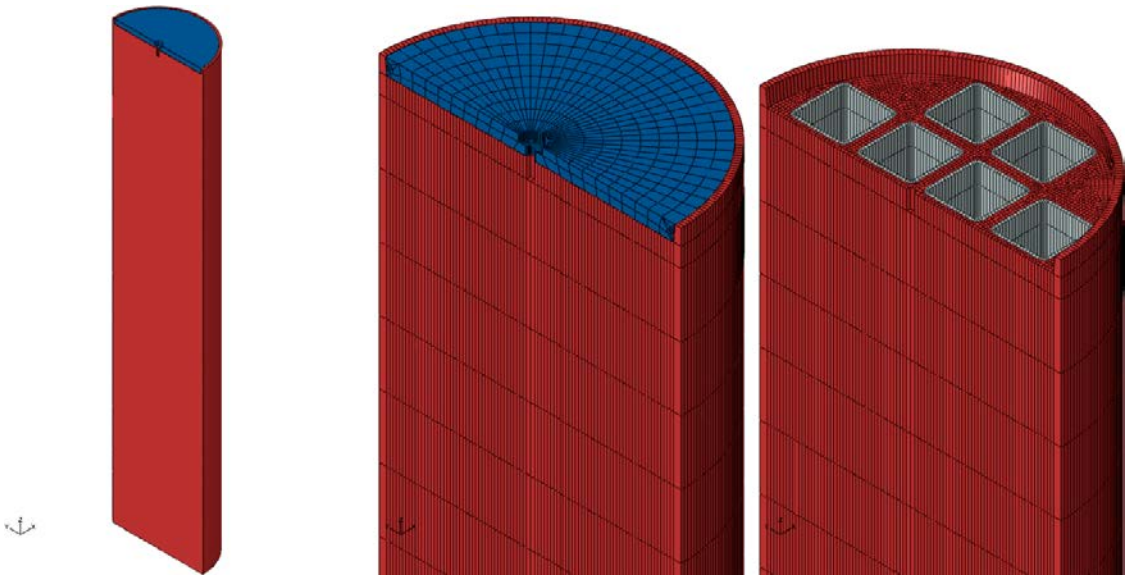

Figure 10-4. *Insert BWR geometry (left), mesh with lid (mid) and without lid (right).*

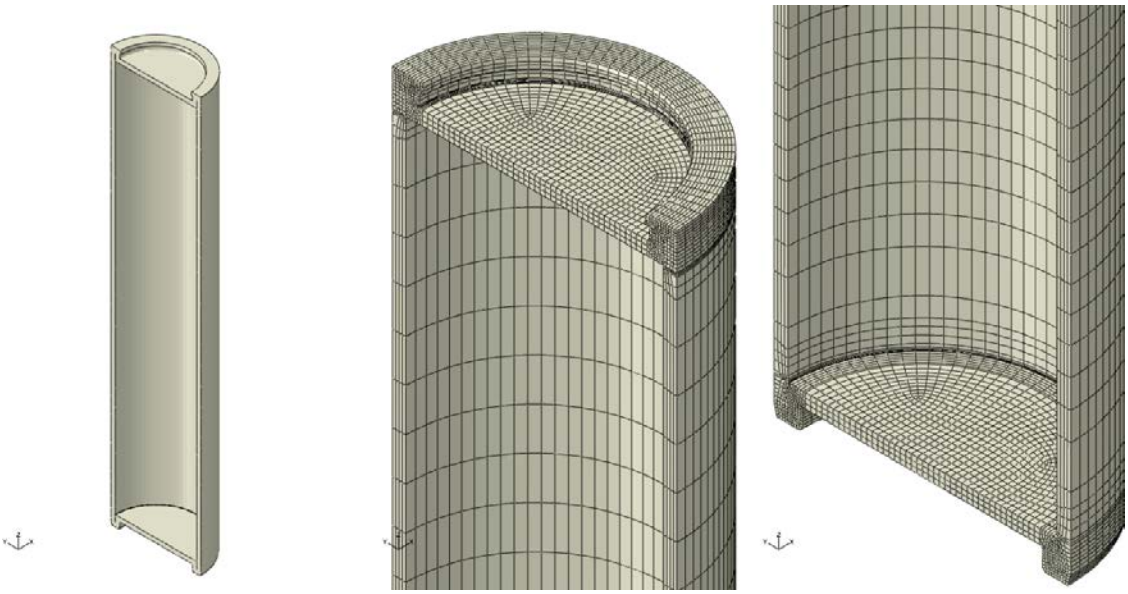

Figure 10-5. *Copper shell geometry (left), mesh top (mid) and mesh bottom (right).*

10.3 Calculations

The calculation technique of the reference case was done with a static procedure and used damping (Stabilize) in order to reach convergent solutions, which is identical to the technique used for SR-Site and described in Hernelind (2010). The calculations with the brittle bentonite were made with a dynamic procedure (quasi-static) and don't need artificial damping.

A large number of calculations have been performed but with severe convergence problems. All attempts with a material model of the bentonite with a fast drop in strength, which directly after reaching maximum deviator (Mises stress) stress goes to zero after a few per cent strain, failed to converge. The most brittle like behaviour that succeeded were the two shown in Figure 2. One (Density 2050 brittle) had a very long plastization before the strength was rapidly reduced while the other one (Density 2050 brittle2) had a rather slow decrease in strength that started early at about 5 % strain. In order to simulate that the shear strength has been completely lost a fourth calculation was done with brittle bentonite and with the shear plane of the buffer removed in the shear zone of the bentonite. Table 10-1 shows the different models.

The calculations have been run to a total shear displacement of 5 cm and the results compared. Calculation 3 was though only possible to run to 4.5 cm displacement, but it is so close to 5 cm that the results can be used for comparison.

Table 10-1 Calculations presented in this section.

Calculation	Model	Remarks
1 model6g_normal_quarter_2050ca3	bentonite_2050ca3	Reference case
2 model6g_normal_quarter_2050ca3_brittle_quasi	bentonite_2050ca3_**brittle**	brittle
3 model6g_normal_quarter_2050ca3_brittle_quasi2e	bentonite_2050ca3_**brittle2**_old5	brittle2
4 model6g_normal_quarter_2050ca3_brittle_quasi2_removed2	bentonite_2050ca3_**brittle2**_old5	D:o+Buffer shear plane removed

10.4 Results

The results of the four calculations are shown as the stresses in the buffer, copper shell and cast iron insert.

Figure 10-6 and Figure 10-7 show the plastic strain in the buffer. Figure 10-6 shows the entire buffer while Figure 10-7 shows a part of the shear plane.

The figures show that the plastic strain in the buffer in the brittle cases differs quite a lot from that in the reference case, except for calculation 2, which has a rather late decrease in shear strength that does not start until after almost 50 %. The difference is especially pronounced in calculation 4 where the shear plane is removed, which is natural since the strains will be concentrated to that plane and the stresses released in the surrounding of the shear plane.

Figure 10-8 shows the plastic strain in the copper. The most obvious difference occurs in calculation 4 with the buffer shear plane removed, where the stress (or plastic strain) concentration close to the shear plane is larger than in the other cases. Otherwise the difference between the different cases is small.

Figure 10-9 and Figure 10-10 show the plastic strain in the iron insert. The difference between the calculations is not strong but especially the calculation with the buffer shear plane removed shows slightly higher plastic strain in the centre of the insert although the maximum plastic strain in the insert is lower than in the reference case.

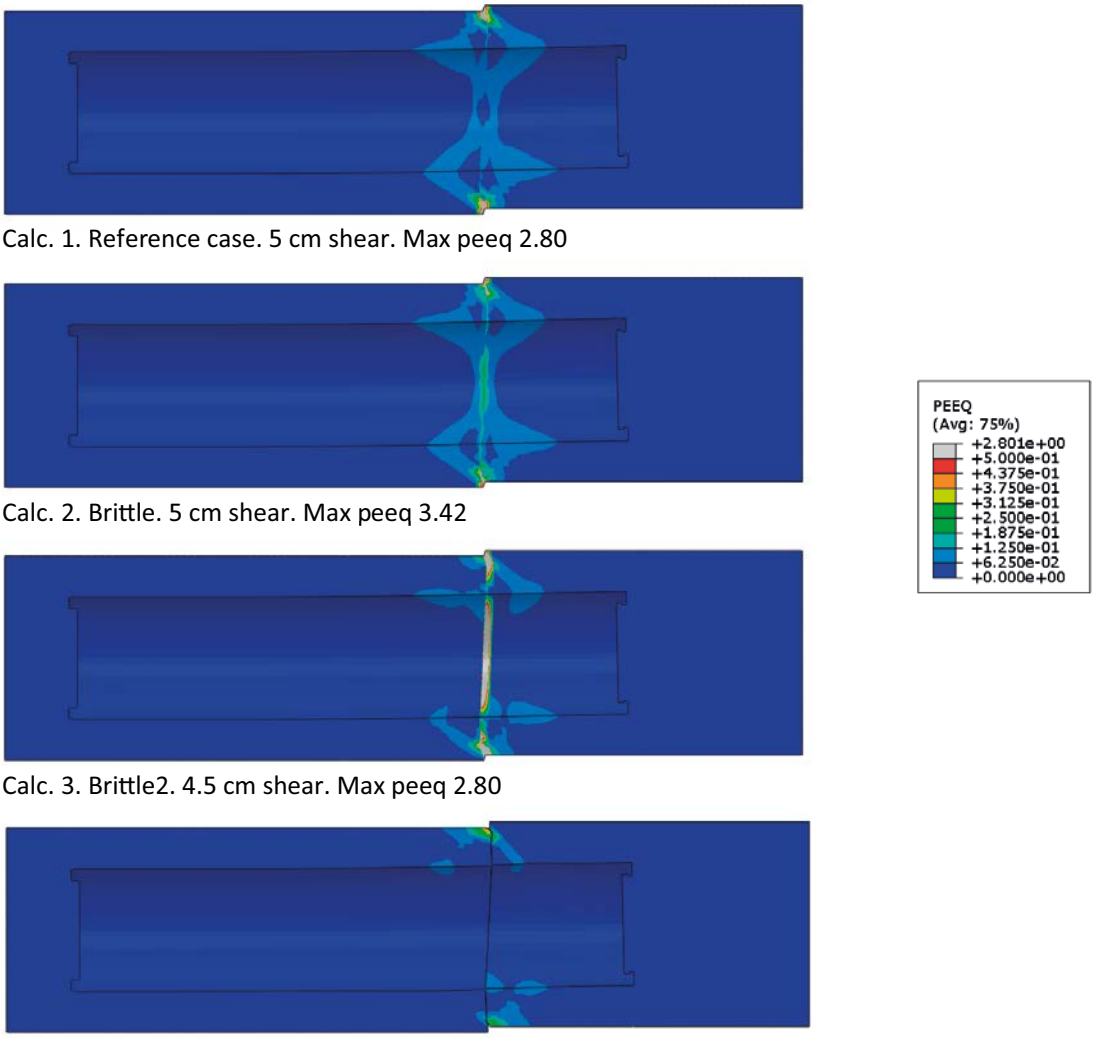

Figure 10-6. *Plastic strain (peeq) in the buffer.*

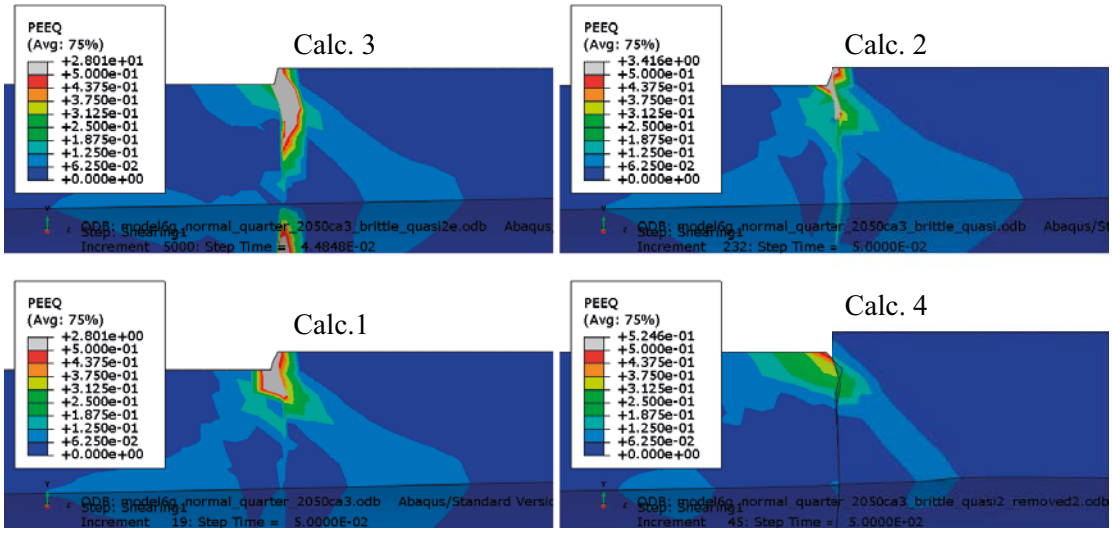

Figure 10-7. *Plastic strain (peeq) in the buffer close to the shear plane.*

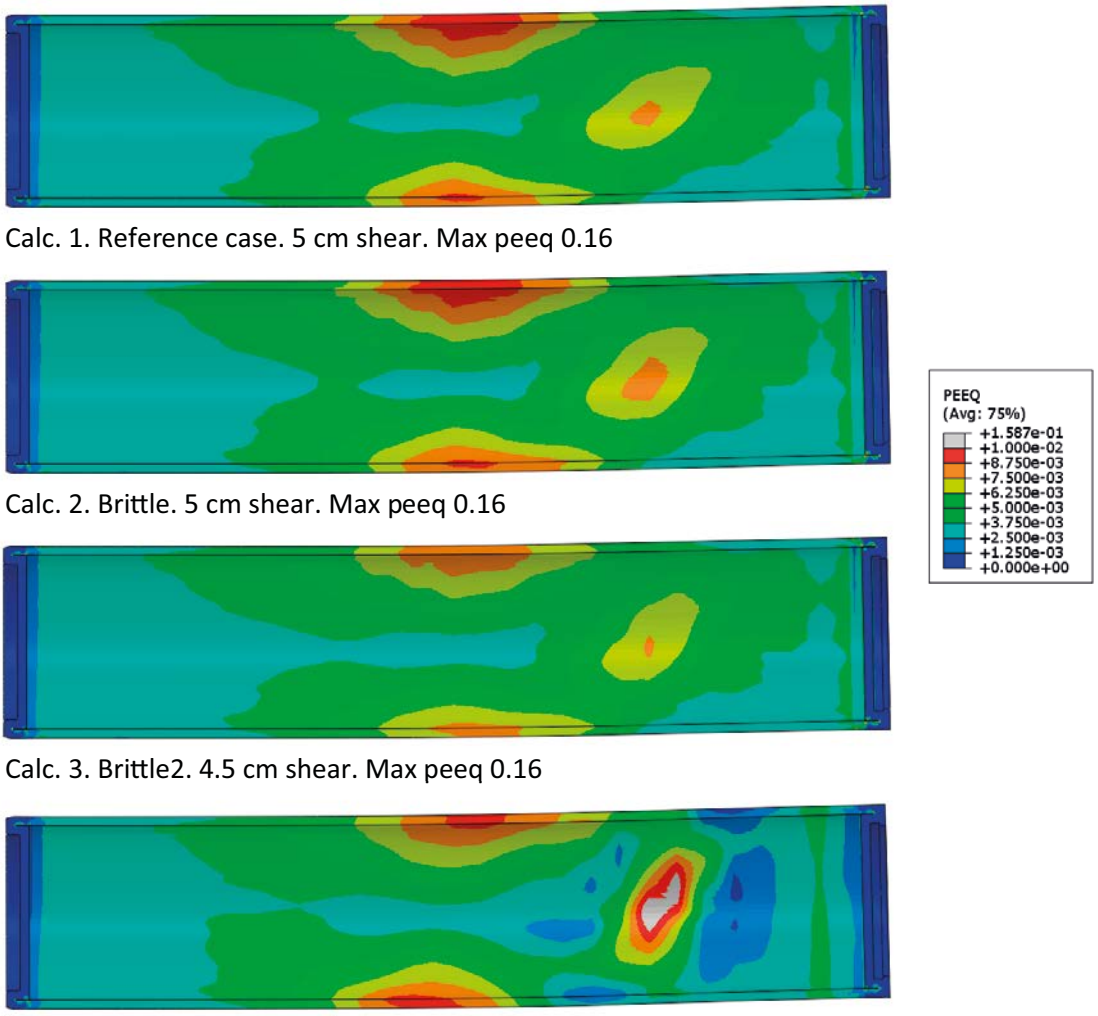

Calc. 1. Reference case. 5 cm shear. Max peeq 0.16

Calc. 2. Brittle. 5 cm shear. Max peeq 0.16

Calc. 3. Brittle2. 4.5 cm shear. Max peeq 0.16

Calc. 4. Brittle2. Shear plane removed. 5 cm shear. Max peeq 0.15

Figure 10-8. *Plastic strain (peeq) in the copper.*

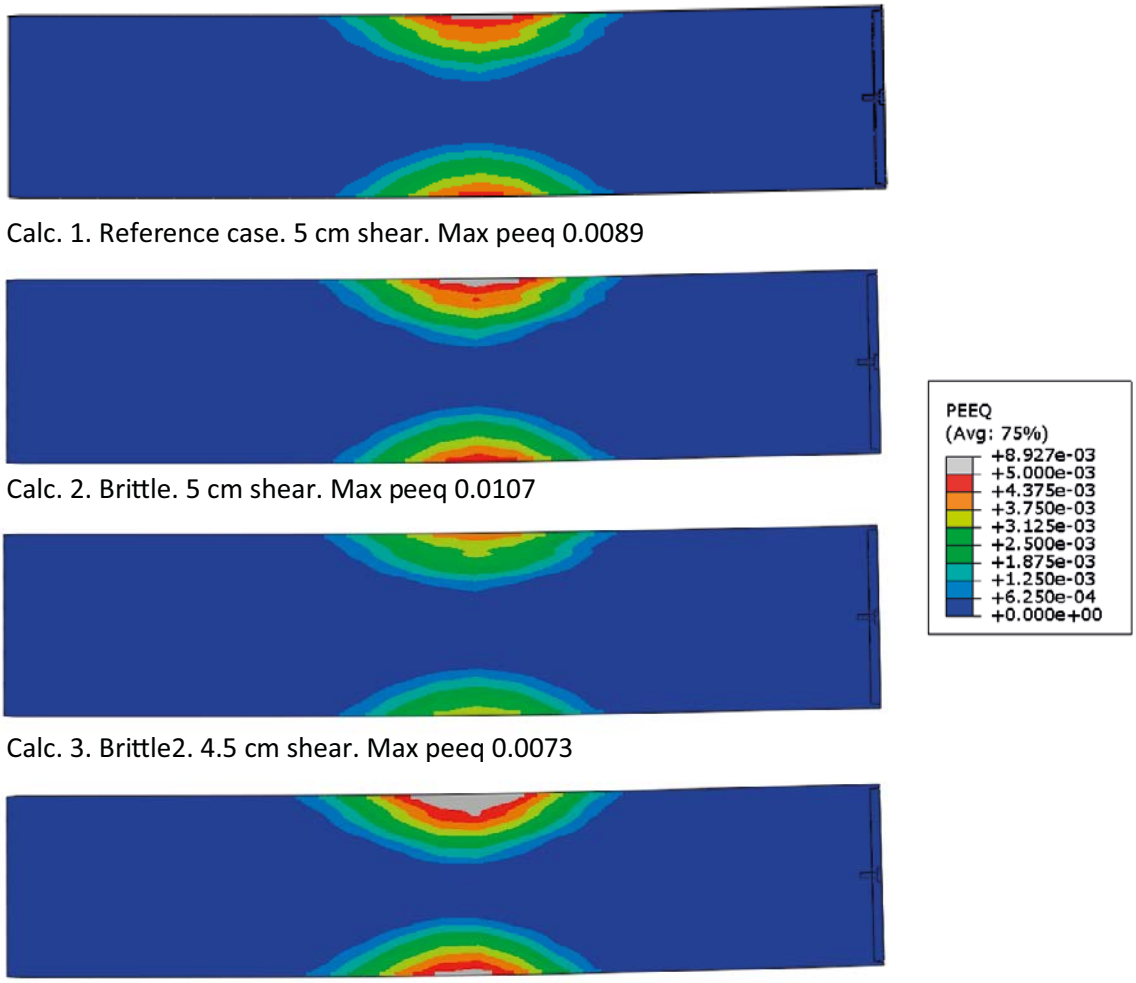

Calc. 1. Reference case. 5 cm shear. Max peeq 0.0089

Calc. 2. Brittle. 5 cm shear. Max peeq 0.0107

Calc. 3. Brittle2. 4.5 cm shear. Max peeq 0.0073

Calc. 4. Brittle2. Shear plane removed. 5 cm shear. Max peeq 0.0066

Figure 10-9. *Plastic strain (peeq) in the insert.*

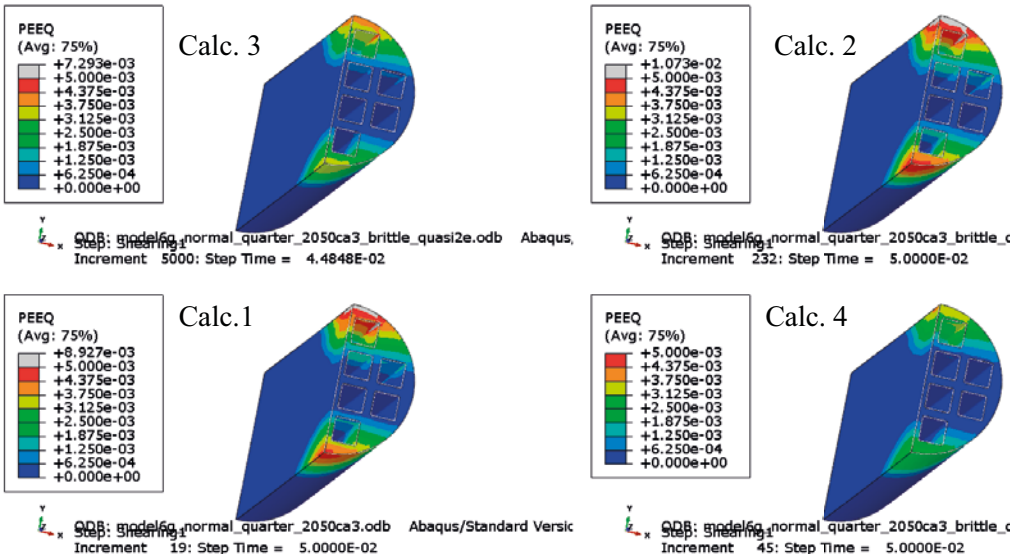

Figure 10-10. *Plastic strain (peeq) in the iron insert. The insert is cut at a horizontal central section.*

10.5 Conclusions

Three rock shear calculations with a buffer that shows brittle behaviour have been performed and compared to the reference case with the same buffer properties as used for SR-Site. The influence on the plastic strain in the copper shell was small but the extreme case with the buffer shear plane removed showed clearly higher plastic strain at a point located adjacent to the shear plane. The influence on the plastic strain in the iron insert was also very small and the total plastic strain was not for any case higher than about 1 %.

The overall conclusion is thus that brittle failure behaviour of the buffer will not have a strong effect on the consequences of a rock shear. This is a logical conclusion since brittle failure does not mean increased shear strength but decreased shear strength with strain, i.e. the shear resistance of the buffer will decrease and all previous calculations show that higher shear resistance of the buffer means larger stresses in the canister.

11 Assessment of the extent to which slow re-saturation can exacerbate deterioration of the material properties of the buffer due to chemical and structural transformations in comparison with a case of rapid re-saturation – Available observations and ongoing studies

Ola Karnland, Martin Birgersson, Ann Dueck

11.1 Background

The bentonite in the buffer consists of mainly of the clay mineral montmorillonite together with a minor proportion of common used minerals such as quartz, feldspar, gypsum etc. The sealing properties of the bentonite are essentially linked to the montmorillonite, mainly through interaction between montmorillonite counter-ions and water. Common counter-ions in natural bentonite are mainly Ca^{2+}, and Na^{+}. At high water content (low material density), sealing properties are affected by which counter-ion that dominates, while sealing properties are similar at low water content (high material density). The buffer density is therefore planned to be sufficiently high for the sealing properties to be independent of which counter-ion dominates (Karnland 2010).

General studies of bentonite alteration in various contexts, e.g. general sedimentology and oil exploration have been going on for a long time and extensive general knowledge is described in the literature. A summary of the state of art regarding the buffer in a KBS-3 repository is reported in Karnland and Birgersson (2006). SKB, in cooperation with Nagra and Posiva, has subsequently conducted further investigations, and the work on an updated summary of the knowledge situation is ongoing (now published as Leupin et al. 2014).

Studies of bentonite materials under full water saturation have strongly dominated the general research efforts, as this is the common condition in natural systems. Studies for final repositories have also mainly considered a water saturated buffer. However, a few studies specifically relating to structural and/or mineralogical conversion of bentonite under unsaturated conditions have been conducted. Some studies have also touched on the special conditions, with elevated temperature and varying degrees of saturation, which may be prevailing in a final repository. Slow water saturation generally causes transient conditions and gradients to prevail for a longer period than in the case of a rapid water saturation. Qualitative differences may also occur during slow water saturation, e.g. about the intake and hence the distribution of water in the buffer and tunnel backfill is faster than the supply of water from the rock, which in some respects leads to less pronounced gradients. This is discussed and investigated in both laboratory tests and field tests.

11.2 Current research at SKB (2013)

SKBs nuvarande forskning som helt eller delvis rör långtidseffekter av långsam vattenmättnad innefattas huvudsakligen i det följande.

SKB's current research, which relates to or in part to long-term effects of slow water saturation, is mainly included in the following.

11.2.1 The PEBS project (EC-project, www.pebs-eu.de)

The project involves laboratory tests focusing on changes in bentonite material with respect to physical properties such as shear strength, shear elongation, swelling pressure and hydraulic conductivity as a result of short-term exposure to elevated temperature (up to 150 °C) for materials with varying mineral composition. The test series thus also includes various counter-ions in the bentonite. The tests have been completed and reporting is ongoing. Preliminary results relevant to slow water saturation can be summarized in the following bullets:

- Tendency to increased shear strength has been measured after short-term hydrothermal treatment under saturated conditions. In samples that were hydrothermally treated without water pressure, the effects were similar or less pronounced.
- Significant changes in strain on failure due to short-term hydrothermal treatment at saturated conditions. In samples that were hydrothermally treated without water pressure, the effects were similar or less pronounced.
- Unchanged swelling pressure due to short-term hydrothermal treatment regardless of treatment regardless of if the sample was exposed to water pressure or not.
- Unchanged hydraulic conductivity due to short-term hydrothermal treatment regardless of if the sample was exposed to water pressure or not.
- Slightly extended water saturation time for unsaturated samples exposed to hydrothermal treatment.
- Significantly reduced shear strength in old fractures/shear surfaces even after water absorption to full water saturation.

A general conclusion is that the effects on shear and sealing properties due to temperature impact are equivalent, or less pronounced, in samples hydrothermally treated without water pressure as compared to samples that have been completely water-saturated.

11.2.2 The Bastu Project

The project included laboratory experiments with bentonite pellets in temperature and/or relative humidity gradients. The aim was to qualitatively, and to some extent also quantitatively, study water absorption and sealing ability of a pellet filling. The tests showed that vapour condensed under all investigated conditions, and that water from condensation totally dominated water adsorption compared to adsorption directly from vapour. In all experiments, the condensation started at a point from which all further uptake of water occurred through condensation along the edges of the moist area. All tests showed that water adsorption decreased over time, indicating that the pellet system sealed and that vapour transport declined over time. The tests have been completed and a report is available (Birgersson and Goudarzi 2013).

11.2.3 Montmorillonite stability project

The dry conditions in Forsmark make it interesting to study montmorillonite alteration under unsaturated conditions. Couture (1985) reported that bentonite exposed to heated water vapor lost a large part of its swelling ability. However, no mineralogical changes were identified. Therefore, temperature experiments with montmorillonite that have varying degrees of water saturation are conducted to determine if water vapour has a particular effect on the swelling properties. If so, the effect will be quantified for different exposure times and temperatures. Furthermore, the work involves attempts to identify the mechanism behind such a vapour impact.

A part of the project includes test series with materials that were briefly (7 days) exposed to temperatures of up to 200 °C at different water saturation levels. The test series comprise of ten different bentonites, which represent different excavation sites and hence suppliers, as well as various counter-ion compositions. Also tests were made with four different purified montmorillonites as completely ion-exchanged into calcium, sodium and potassium respectively. The water saturation rate has been controlled according to two principles; partly passively via the added amount of water in a closed system, and partly through external control of water activity. The results show no clear differences as a result of hydrothermal treatment between unsaturated and water-saturated samples with respect to swelling capacity (Figure 11-1). On the other hand, significant differences in sedimentation behavior of bentonites/montmorillonites that contain calcium as a counter-ion, probably due to structural changes. Furthermore, there are large expected differences between samples dominated by sodium as counter-ion and samples dominated by calcium. Generally, differences in measured swelling properties due to hydrothermal treatment are negligible in comparison to the differences between sodium dominated and calcium-dominated materials. The effects of short-term vapour exposure on free swelling are therefore not considered to be a problem for a KBS-3 repository. Laboratory trials have been completed and reported as Leupin et al. (2014).

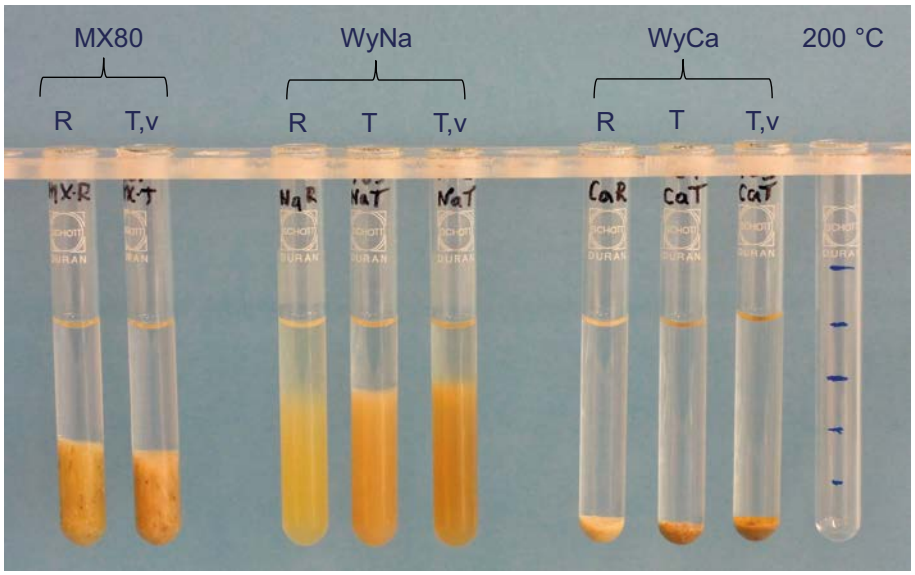

Figure 11-1. *Result from free swelling tests. All test tubes contain 1.00 grams of material expanded to the maximum volume. MX-80 bentonite was the starting material for all samples purified for some experiments and ion exchanged into sodium (WyNa) and calcium form (WyCa) respectively. R indicates reference material; T indicates material hydrothermally treated at full water saturation, and T, v indicates material hydrothermally treated in unsaturated state.*

11.3 From SKB independent publications with relevant studies

In addition to SKB's studis of conditions relevant to slow water saturation of the buffer in a KBS-3 storage, the following publications are available with relevant studies.

11.3.1 Article by Couture

Couture (1985) exposed a number of bentonites for a short-term hydrothermal treatment, and then measured the volume at maximum swelling. The results showed that the water ratio (mass of water/mass of bentonite) in hydrothermal treatment was of major importance for the subsequent swelling (Figure 11-2). Absolutely dry samples (w = 0) and very high water ratio (w = 20) samples were less affected than medium water samples (w = 0.08 to w = 1.14). Exposure of samples with a 0.15 water ratio at 150 °C for 7 days reduced the maximum volume to less than 50 % of the expansion of the reference materials. At 250 °C, swelling capacity decreased to just over 10 %. Couture concluded that the measured changes in bentonite properties are important for sealing ability, and that the effect must be taken into account in a safety assessment. Limited mineralogical investigations were conducted on hydrothermally treated materials, but no chemical/mineralogical changes could be identified in relation to untreated reference materials. In all of the investigations, the bentonite swelled to significantly higher water ratios than what is necessary for the function of a KBS-3 repository. The most extreme reduction of swelling ability (4 cm^3/gram of clay) corresponds to a water ratio of 3.64, comparable to the lowest nominal water ratio (w = ~0.31) in the buffer in a KBS-3 storage. The measured reduction of maximum expansion even at as high a temperature as 250 °C is therefore considered to be of no importance to the buffer in a KBS-3 repository.

11.3.2 Technical report by Haas et al. (1999)

The study included geotechnical and mineralogical studies of the two bentonite materials Montigel (Ca^{2+}-dominated) and MX-80 (Na^{+}-dominated) exposed to various forms of vapour treatment. Cyclic vapour treatment of the Montigel bentonite led to a reduction of swelling pressure by as much as 50 % of measured pressure for untreated material. The swelling pressure was recovered after ultrasonic treatment, drying and grinding, and in some cases higher pressure was also measured than for the reference material. Shrinkage tests, liquid limit test, sedimentation experiments and water adsorption

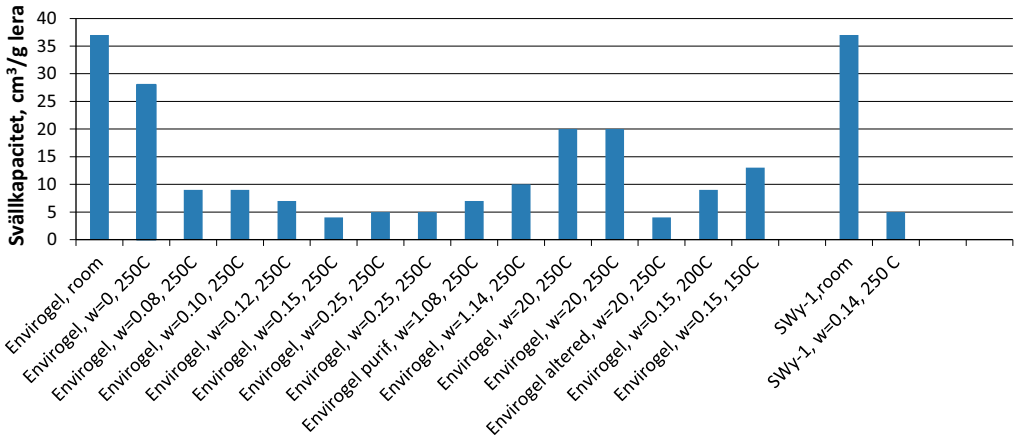

Figure 11-2. *Swelling capacity of hydrothermally treated material from Couture (1985). The labels indicate clay type, water ratio and temperature at hydrothermal treatment.*

tests with vapour treated materials showed no or insignificant changes to reference materials. The mineralogical investigations included cation exchange capacity, base plane distance (XRD) and BET surface area. All studies showed minor or insignificant differences compared to reference materials regardless of temperature and exposure time.

11.3.3 Article by Oscarson and Dixon (1990)

The study included experiments with bentonite at different degree of water saturation (0, 50, 85 and 100 %) exposed to temperatures up to 150 °C. After hydrothermal treatment, the samples were saturated and swelling pressure and hydraulic conductivity was determined both at elevated temperature and at room temperature. In no case was any significant change found in the properties compared to reference materials. Morphological and mineralogical analyses using scanning electron microscopy and X-ray diffraction were performed, and cation exchange capacity was determined. However, no changes compared to reference materials could be detected.

11.4 Summary of studies relevant to slow water saturation of the buffer

In the study material-mentioned in this section there are indications of structural changes due to short-term exposure of certain hydrothermal treatment, especially when calcium is the dominant counter-ion, which possibly may affect swelling or sedimentation properties of the bentonite. However, there is nothing in the described study materials suggesting mineralogical changes in montmorillonite as a result of short-term exposure to dry or semi-dry conditions at temperatures up to 250 °C.

The transport capacity of dissolved species is generally lower at low water content, which can thus be expected to reduce the extent of most known alteration processes under unsaturated conditions. However, specific processes not studied in the described experiments, due to gradients in temperature, water content and salinity, may result in transport in partially saturated bentonite buffer, which can thus lead to precipitations. Uneven distribution in the buffer of chlorine from groundwater, and redistribution of relatively easily soluble secondary minerals in the buffer, e.g. gypsum, has been observed in field test where a high temperature and/or water saturation gradient has persisted, for example in LOT tests (Muurinen 2003, Karnland et al. 2011). The relative high solubility of the redistributed minerals means that the reactions are generally reversible, and that any precipitated minerals will dissolve and the concentrations equilibrate when water saturation increases. Such precipitations are therefore not expected to affect the long term function of the buffer.

References

SKB's (Svensk Kärnbränslehantering AB) publications can be found at www.skb.com/publications.

Alonso E E, Alcoverro J, 2005. Decovalex III project. Modelling of FEBEX in-situ test. Task 1 Final report. SKI Report 2005:20, Swedish Nuclear Power Inspectorate.

Alonso E E, Gens A, Josa A, 1990. A constitutive model for partially saturated soils. Géotechnique 40, 405–430.

Alonso E E, Alcoverro J, Coste F, Malinsky L, Merrien-Soukatchoff V, Kadiri I, Nowak T, Shao H, Nguyen T S, Selvadurai A P S, Armand G, Sobolik S R, Itamura M, Stone C M, Webb S W, Rejeb A, Tijani M, Maouche Z, Kobayashi A, Kurikami H, Ito A, Sugita Y, Chijimatsu M, Börgesson L, Hernelind J, Rutqvist J, Tsang C-F, Jussila P, 2005. The FEBEX benchmark test: case definition and comparison of modelling approaches. International Journal of Rock Mechanics & Mining Sciences 42**,** 611–638.

Bear J, 1972. Dynamics of fluids in porous media. New York: Dover.

Benbow S, Metcalfe R, Watson C, Bond A, 2012. SR-Site independent modelling of engineered barrier evolution and coupled THMC: Contribution to the initial review phase. Technical Note 2012:18, Swedish Radiation Safety Authority.

Birgersson M, Goudarzi R, 2013. Studies of vapor transport from buffer to tunnel backfill (Sauna effects). SKB R-13-42, Svensk Kärnbränslehantering AB.

Birgersson M, Karnland O, Nilsson U, 2010. Freezing of bentonite. Experimental studies and theoretical considerations. SKB TR-10-40, Svensk Kärnbränslehantering AB.

Börgesson L, 2001. Äspö Hard Rock Laboratory. Compilation of laboratory data for buffer and backfill materials in the Prototype repository. SKB IPR-01-34, Svensk Kärnbränslehantering AB.

Börgesson L, Hernelind J, 2010. Earthquake induced rock shear through a deposition hole. Modelling of three model tests scaled 1:10. Verification of the bentonite material model and the calculation technique. SKB TR-10-33, Svensk Kärnbränslehantering AB.

Börgesson L, Johannesson L-E, Sandén T, 1999. Djupförvarsteknik. Canister Retrieval Test. Konstgjord bevätning av bufferten. SKB TD-99-50, Svensk Kärnbränslehantering AB. (In Swedish.)

Börgesson L, Dueck A, Johannesson L-E, 2010. Material model for shear of the buffer – evaluation of laboratory test results. SKB TR-10-31, Svensk Kärnbränslehantering AB.

Börgesson L, Åkesson M, Kristensson O, Dueck A, Hernelind J, 2016. EBS TF – THM modelling. BM 2 – Large scale field tests. SKB TR-13-07, Svensk Kärnbränslehantering AB.

Carslaw H S, Jaeger J C, 1959. Conduction of heat in solids. 2nd ed. Oxford: Clarendon.

Claesson J, 2007. Selected models for key processes in a nuclear waste repository. Temperature field – bentonite drying/resaturation. SKI Report 2008:47, Swedish Nuclear Power Inspectorate.

Couture R A, 1985. Steam rapidly reduces the swelling capacity of bentonite. Nature 318, 50–52.

Crank J, 1975. The mathematics of diffusion. 2nd ed. Oxford: Clarendon.

Cuss R J, Harrington J F, Noy D J, 2010. Large scale gas injection test (Lasgit) performed at the Äspö Hard Rock Laboratory. Summary report 2008. SKB TR-10-38, Svensk Kärnbränslehantering AB.

De Groot S R, Mazur P, 1984. Non-equilibrium thermodynamics. New York: Dover.

Dixon D, Chandler N, Graham J, Gray M N, 2002. Two large-scale sealing tests conducted at Atomic Energy of Canada's underground research laboratory: the buffer–container experiment and the isothermal test. Canadian Geotechnical Journal 39, 503–518.

Dueck A, 2004. Hydro-mechanical properties of a water unsaturated sodium bentonite: laboratory study and theoretical interpretation. PhD thesis. Lund University, Sweden.

Dueck A, 2007. Results from suction controlled laboratory tests on unsaturated bentonite – verification of a model. In Schanz T (ed). Experimental unsaturated soil mechanics. Berlin: Springer. (Springer proceedings in physics 112), 329–335.

Dueck A, 2010. Thermo-mechanical cementation effects in bentonite investigated by unconfined compression tests. SKB TR-10-41, Svensk Kärnbränslehantering AB.

Dueck A, Nilsson U, 2010. Thermo-Hydro-Mechanical properties of MX-80. Results from advanced laboratory tests. SKB TR-10-55, Svensk Kärnbränslehantering AB.

Dueck A, Börgesson L, Johannesson L-E, 2010. Stress-strain relation of bentonite at undrained shear. Laboratory tests to investigate the influence of material composition and test technique. SKB TR-10-32, Svensk Kärnbränslehantering AB.

Dueck A, Johannesson L-E, Kristensson O, Olsson S, Sjöland A, 2011. Hydro-mechanical and chemical-mineralogical analyses of the bentonite buffer from a full-scale field experiment simulating a high-level waste repository. Clay and Clay Minerals 59, 595–607.

Gens A, Sánchez M, Guimarães L Do N, Alonso E E, Lloret A, Olivella S, Villar M V, Huertas F, 2009. A full-scale in situ heating test for high-level nuclear waste disposal: observations, analysis and interpretation. Géotechnique 59, 377–399.

Green R E, Corey J C, 1971. Calculation of hydraulic conductivity: a further evaluation of some predictive methods. Proceedings of the Soil Society of America 35, 3–8.

Haas R, Teysseire P, Bucher F, 1999. Einfluss von Wasserdampf auf Quellpotential von Bentonit. Nagra Report NAB 99-31, Nagra, Switzerland.

Hernelind J, 2010. Modelling and analysis of canister and buffer for earthquake induced rock shear and glacial loads. SKB TR-10-34, Svensk Kärnbränslehantering AB.

Hultgren J, 2014. Ritningsförteckning för kapselkomponenter. SKBdoc 1203875 ver 2.0, Svensk Kärnbränslehantering AB.

Hökmark H, Lönnqvist M, Kristensson O, Sundberg J, Hellström G, 2009. Strategy for thermal dimensioning of the final repository for spent nuclear fuel. SKB R-09-04, Svensk Kärnbränslehantering AB.

Hökmark H, Lönnqvist M, Fälth B, 2010. THM-issues in repository rock. Thermal, mechanical, thermo-mechanical and hydro-mechanical evolution of the rock at the Forsmark and Laxemar sites. SKB TR-10-23, Svensk Kärnbränslehantering AB.

Johannesson L-E, 2007. Äspö Hard Rock Laboratory. Canister Retrieval Test. Dismantling and sampling of the buffer and determination of density and water ratio. SKB IPR-07-16, Svensk Kärnbränslehantering AB.

Johannesson L-E, Börgesson L, 2002. Äspö Hard Rock Laboratory. Laboratory tests on Friedland Clay. Friedland Clay as backfill material. Results of laboratory tests and swelling/compression calculations. SKB IPR-02-50, Svensk Kärnbränslehantering AB.

Johannesson L-E, Sandén T, Dueck A, 2008. Deep repository – engineered barrier system. Wetting and homogenization processes in backfill materials. Laboratory tests for evaluating modeling parameters. SKB R-08-136, Svensk Kärnbränslehantering AB.

Johannesson L-E, Sandén T, Dueck A, Ohlsson L, 2010. Characterization of backfill candidate material, IBECO-RWC-BF. Baclo project – Phase 3. Laboratory tests. SKB R-10-44, Svensk Kärnbränslehantering AB.

Joyce S, Simpson T, Hartley L, Applegate D, Hoek J, Jackson P, Swan D, Marsic N, Follin S, 2010. Groundwater flow modelling of periods with temperature climate conditions – Forsmark. SKB R-09-20, Svensk Kärnbränslehantering AB.

Joyce S, Swan D, Hartley L, 2013. Calculation of open repository inflows for Forsmark. SKB R-13-21, Svensk Kärnbränslehantering AB.

Kahr G, Kraehenbuehl F, Müller-Vonmoos M, Stoeckli H F, 1986. Wasseraufnahme und Wasserbewegung in hochverdichtetem Bentonit. Nagra Technischer Bericht 86-14, Nagra, Switzerland. (In German.)

Kahr G, Kraehenbuehl F, Stoeckli H F, Müller-Vonmoos M, 1990. Study of the water–bentonite system by vapour adsorption, immersion calorimetry and X-ray techniques: II. Heats of immersion, Swelling pressures and Thermodynamic properties. Clay Minerals 25, 499–506.

Karnland O, 2010. Chemical and mineralogical characterization of the bentonite buffer for the acceptance control procedure in a KBS-3 repository. SKB TR-10-60, Svensk Kärnbränslehantering AB.

Karnland O, Birgersson M, 2006. Montmorillonite stability. With special respect to KBS-3 conditions. SKB TR-06-11, Svensk Kärnbränslehantering AB.

Karnland O, Olsson S, Nilsson U, 2006. Mineralogy and sealing properties of various bentonites and smectite-rich clay materials. SKB TR-06-30, Svensk Kärnbränslehantering AB.

Karnland O, Olsson S, Sandén T, Fälth B, Jansson M, Eriksen T E, Svärdström K, Rosborg B, Muurinen A, 2011. Long term test of buffer material at the Äspö HRL, LOT project. Final report on the A0 test parcel. SKB TR-09-31, Svensk Kärnbränslehantering AB.

Leupin O X (ed), Birgersson M, Karnland O, Korkeakoski P, Sellin P, Mäder U, Wersin P, 2014. Montmorillonite stability under near-field conditions. Nagra Technical Report 14-12, Nagra, Switzerland.

Martin P L, Barcala J M, 2005. Effects of over-heating on the performance of the engineering clayed barriers of the mock-up test. In Alonso E E, Ledesma A (eds). Advances in understanding engineered clay barriers: proceedings of the International Symposium on Large Scale Field Tests in Granite, Sitges, Barcelona, Spain, 12–14 November 2003. Rotterdam: Balkema, 391–412.

Mitchell J K, 1993. Fundamentals of soil behavior. New York: Wiley.

Muurinen A, 2003. Chemical conditions in the A0 parcel of the long-term test of buffer material in Äspö (LOT). Posiva Working Report 2003-32, Posiva Oy, Finland.

Nield D A, Bejan A, 2006. Convection in porous media. 3rd ed. New York: Springer.

Oscarson D W, Dixon D A, 1990. The effect of heating unsaturated bentonite on the swelling and hydraulic properties of subsequently saturated clay. Proceedings of the Annual Conference and 1st Biennial. Environmental Speciality Conference of the Canadian Society of Civil Engineering, Hamilton, Ontario, Volume 11-1, 312–323.

Sánchez M, Gens A, 2006. FEBEX Project, Final report, Final report on thermo-hydro-mechanical modelling. ENRESA publicación técnica 05-2/2006, ENRESA, Spain.

Sánchez M, Villar M V, Lloret A, Gens A, 2007. Analysis of the expansive clay hydration under low hydraulic gradient. In Schanz T (ed). Experimental unsaturated soil mechanics. Berlin: Springer. (Springer proceedings in physics 112), 309–318.

Sandén T, Börgesson L, 2010. Early effects of water inflow into a deposition hole. Laboratory tests results. SKB R-10-70, Svensk Kärnbränslehantering AB.

Sandén T, Olsson S, Andersson L, Dueck A, Jensen V, Hansen E, Johnsson A, 2014. Investigation of backfill candidate materials. SKB R-13-08, Svensk Kärnbränslehantering AB.

SKB, 2006. Buffer and backfill process report for the safety assessment SR-Can. SKB TR-06-18, Svensk Kärnbränslehantering AB.

SKB, 2010a. Design, production and initial state of the backfill and plug in deposition tunnels. SKB TR-10-16, Svensk Kärnbränslehantering AB.

SKB, 2010b. Design, construction and initial state of the underground openings. SKB TR-10-18, Svensk Kärnbränslehantering AB.

SKB, 2011. Long-term safety for the final repository for spent nuclear fuel at Forsmark. Main report of the SR-Site project. SKB TR-11-01, Svensk Kärnbränslehantering AB.

SKB, 2013. Svar till SSM på begäran om komplettering rörande lång återmättnadsfas. SKBdoc 1385067 ver 3.0, Svensk Kärnbränslehantering AB.

Svensson D, Dueck A, Nilsson U, Olsson S, Sandén T, Lydmark S, Jägerwall S, Pedersen K, Hansen S, 2011. Alternative buffer material. Status of the ongoing laboratory investigation of reference materials and test package 1. SKB TR-11-06, Svensk Kärnbränslehantering AB.

Svensson U, Follin S, 2010. Groundwater flow modelling of the excavation and operational phases – Forsmark. SKB R-09-19, Svensk Kärnbränslehantering AB.

Thomas H R, Cleall P J, Chandler N, Dixon D, Mitchell H P, 2003. Water infiltration into a large-scale in-situ experiment in an underground research laboratory. Géotechnique 53, 207–224.

Thomas H R, Clear P J, Dixon D, Mitchell H P, 2009. The coupled thermal-hydraulic-mechanical behavior of a large-scale in situ heating experiment. Géotechnique 59, 401–413.

Thorsager P, Börgesson L, Johannesson L-E, Sandén T, 2002. Äspö Hard Rock Laboratory. Canister Retrieval Test. Report on installation. SKB IPR-02-30, Svensk Kärnbränslehantering AB.

Tsang C-F, Stephansson O, Jing L, Kautsky F, 2009. DECOVALEX Project: from 1992 to 2007. Environmental Geology 57, 1221–1237.

UPC, 2012. CODE_BRIGHT, User's guide. Universitat Politècnica de Catalunya. Available at: https://www.etcg.upc.edu/recerca/webs/code_bright/code_bright.

Vilks P, 2007. Forsmark site investigation. Rock matrix permeability measurements on core samples from borehole KFM01D. SKB P-07-162, Svensk Kärnbränslehantering AB.

Villar M V, 2002. Thermo-hydro-mechanical characterization of a bentonite from Cabo de Gata. A study applied to the use of bentonite as sealing material in high level radioactive waste repositories. ENRESA publicación técnica 04/2002, ENRESA, Spain.

Villar M V, Gòmez-Espina R, 2007. Retention curves of two bentonites at high temperature. In Schanz T (ed). Experimental unsaturated soil mechanics. Berlin: Springer. (Springer proceedings in physics 112), 267–274.

Zheng L, Samper J, 2008. A coupled THMC model of FEBEX *mock-up* test. Physics and Chemistry of the Earth, Parts A/B/C 33, 508–515.

Åberg A, 2009. Effects of water inflow on the buffer – an experimental study. SKB R-09-29, Svensk Kärnbränslehantering AB.

Åkesson M, Börgesson L, Kristensson O, 2010a. SR-Site data report. THM modelling of buffer, backfill and other system components. SKB TR-10-44, Svensk Kärnbränslehantering AB.

Åkesson M, Kristensson O, Börgesson L, Dueck A, Hernelind J, 2010b. THM modelling of buffer, backfill and other system components. Critical processes and scenarios. SKB TR-10-11, Svensk Kärnbränslehantering AB.

Appendix 1

Volume calculations

Location: ”Administrativa dokument on”:\Projekt\ SR-Site SSM-frågor\data\modeller\Task_1.2\ Water_volume*

MathCad-document
‘Estimate of water in CRT 2.xmcd’

Excel-documents	* in Location given above
‘Sammanst C2.xls’	\Block C2
‘Sammanst C3.xls’	\Block C3
‘Sammanst C4.xls’	\Block C4
‘Sammanst R6.xls’	\Block C6
‘Sammanst C7.xls’	\Block C7
‘Sammanst C8.xls’	\Block C8
‘Sammanst C9.xls’	\Block C9
‘Sammanst C10.xls’	\Block C10

Calculate initial water volume

$$\rho_w := 1000 \qquad r_o := \frac{1.64}{2} \qquad r_i := \frac{1.07}{2} \qquad \Delta r := 0.061$$

Cylinders	$H_C := 0.504$	$\rho_C := 1991$	$w_C := 0.172$
Rings	$H_R := 0.510$	$\rho_R := 2087$	$w_R := 0.171$
Bricks	$H_B := 0.123$	$\rho_B := 1883$	$w_B := 0.165$
Pellet slot	$H_P := 4 \cdot H_C + 10 \cdot H_R$	$\rho_P := 1101$	$w_P := 0.1$

$$V_{w\_init\_cylinders} := H_C \cdot r_o^2 \cdot \pi \cdot \frac{1}{1 + \frac{1}{w_C}} \cdot \frac{\rho_C}{\rho_w}$$

$$V_{w\_init\_rings} := H_R \cdot \left(r_o^2 - r_i^2\right) \cdot \pi \cdot \frac{1}{1 + \frac{1}{w_R}} \cdot \frac{\rho_R}{\rho_w}$$

$$V_{w\_init\_bricks} := H_B \cdot r_i^2 \cdot \pi \cdot \frac{1}{1 + \frac{1}{w_B}} \cdot \frac{\rho_B}{\rho_w}$$

$$V_{w\_init\_pellet} := H_P \cdot \left[\left(r_o + \Delta r\right)^2 - r_o^2\right] \cdot \pi \cdot \frac{1}{1 + \frac{1}{w_P}} \cdot \frac{\rho_P}{\rho_w}$$

$$V_{w\_init} := 4 \cdot V_{w\_init\_cylinders} + 10 \cdot V_{w\_init\_rings} + V_{w\_init\_bricks} + V_{w\_init\_pellet}$$

$$V_{w\_init} = 3.392$$

Program calculating water volume from density and water content data

$$
\begin{aligned}
&\text{vol}(\text{DATA}, \Delta r_{min}, H) := \\
&\quad \text{sum} \leftarrow 0 \\
&\quad \text{row} \leftarrow 0 \\
&\quad j \leftarrow 0 \\
&\quad \text{while } \text{row} \le \text{rows}(\text{DATA}) - 1 \\
&\qquad r_{start_j} \leftarrow \text{DATA}_{\text{row},0} \\
&\qquad r_{end_j} \leftarrow r_{start_j} \\
&\qquad \rho_j \leftarrow 0 \\
&\qquad w_j \leftarrow 0 \\
&\qquad i \leftarrow 0 \\
&\qquad \text{while } \text{row} \le \text{rows}(\text{DATA}) - 1 \wedge \text{DATA}_{\text{row},0} - r_{start_j} \le \Delta r_{min} \\
&\qquad\quad r_{end_j} \leftarrow \text{DATA}_{\text{row},0} \\
&\qquad\quad \rho_j \leftarrow \rho_j + \text{DATA}_{\text{row},3} \\
&\qquad\quad w_j \leftarrow w_j + \text{DATA}_{\text{row},2} \\
&\qquad\quad i \leftarrow i + 1 \\
&\qquad\quad \text{row} \leftarrow \text{row} + 1 \\
&\qquad \rho_j \leftarrow \frac{\rho_j}{i} \\
&\qquad w_j \leftarrow \frac{w_j}{i} \\
&\qquad \text{sum} \leftarrow \text{sum} + \frac{\rho_j}{1 + \frac{1}{w_j}} \cdot \left[\left(\frac{r_{end_j}}{1000} \right)^2 - \left(\frac{r_{start_j}}{1000} \right)^2 \right] \\
&\qquad j \leftarrow j + 1 \\
&\qquad \text{row} \leftarrow \text{row} - 1 \quad \text{if } \text{row} \le \text{rows}(\text{DATA}) - 1 \\
&\quad \text{volume} \leftarrow \frac{\text{sum} \cdot H \cdot \pi}{\rho_w} \\
&\quad \begin{pmatrix} \text{volume} \\ r_{start} \\ r_{end} \\ \rho \\ w \end{pmatrix}
\end{aligned}
$$

Calculate final water volume

$C4\_sol := vol(C4, 50, H_C)$ $\quad C4\_sol_0 = 0.502$

$C3\_sol := vol(C3, 60, H_C)$ $\quad C3\_sol_0 = 0.491$

$C2\_sol := vol(C2, 65, H_C)$ $\quad C2\_sol_0 = 0.512$

$R10\_sol := vol(R10, 50, H_R)$ $\quad R10\_sol_0 = 0.495$

$R9\_sol := vol(R9, 60, H_R)$ $\quad R9\_sol_0 = 0.322$

$R8\_sol := vol(R8, 60, H_R)$ $\quad R8\_sol_0 = 0.323$

$R7\_sol := vol(R7, 50, H_R)$ $\quad R7\_sol_0 = 0.324$

$R6\_sol := vol(R6, 55, H_R)$ $\quad R6\_sol_0 = 0.324$

$$V_{w\_final} := \left(C4\_sol_0 + C3\_sol_0 + 2 \cdot C2\_sol_0 + R10\_sol_0 + R9\_sol_0 + R8\_sol_0 + R7\_sol_0 + 6 \cdot R6\_sol_0\right)$$

$$V_{w\_final} = 5.428$$

Calculate added water volume and compare with measurement

$\Delta V_{w\_calc} := \left(V_{w\_final} - V_{w\_init}\right)$ $\quad \Delta V_{w\_calc} = 2.036$

$\Delta V_{w\_measured} := 1.620$

$$\Delta V_{w\_calc} - \Delta V_{w\_measured} = 0.416$$

$$\frac{\Delta V_{w\_calc} - \Delta V_{w\_measured}}{\Delta V_{w\_measured}} = 0.257$$

Calculate initial avaliable pore volume

Cylinders $e_C := 0.636$

Rings $e_R := 0.56$

Bricks $e_B := 0.72$

Pellet slot $e_P := 1.778$

$H_{swell} := 0.034$

$\Delta r_{slot} := 0.01$

$$V_{av\_init\_cylinders} := H_C \cdot r_o^{\,2} \cdot \pi \cdot \frac{e_C}{1 + e_C} \cdot \left(1 - \frac{\rho_s}{\rho_w} \cdot \frac{w_C}{e_C}\right)$$

$$V_{av\_init\_rings} := H_R \cdot \left(r_o^{\,2} - r_i^{\,2}\right) \cdot \pi \cdot \frac{e_R}{1 + e_R} \cdot \left(1 - \frac{\rho_s}{\rho_w} \cdot \frac{w_R}{e_R}\right)$$

$$V_{av\_init\_bricks} := H_B \cdot r_i^{\,2} \cdot \pi \cdot \frac{e_B}{1 + e_B} \cdot \left(1 - \frac{\rho_s}{\rho_w} \cdot \frac{w_B}{e_B}\right)$$

$$V_{av\_init\_pellet} := H_P \cdot \left[\left(r_o + \Delta r_{pellets}\right)^2 - r_o^{\,2}\right] \cdot \pi \cdot \frac{e_P}{1 + e_P} \cdot \left(1 - \frac{\rho_s}{\rho_w} \cdot \frac{w_P}{e_P}\right)$$

$$V_{av\_init\_slot} := \left(10 \cdot H_R - H_B\right) \cdot \left[r_i^{\,2} - \left(r_i - \Delta r_{slot}\right)^2\right] \cdot \pi$$

$$V_{av\_init\_swell} := H_{swell} \cdot \left(r_o + \Delta r_{pellets}\right)^2 \cdot \pi$$

$$V_{av\_init} := 4 \cdot V_{av\_init\_cylinders} + 10 \cdot V_{av\_init\_rings} + V_{av\_init\_bricks} + V_{av\_init\_pellet}$$

$$V_{av\_init} := V_{av\_init} + V_{av\_init\_slot} + V_{av\_init\_swell}$$

$V_{av\_init} = 2.264$

Calculate estimate of water volume added at installation

$w_{P\_wet} := 0.572$

$$\Delta V_{init\_pellet\_wet} := H_P \cdot \left[\left(r_o + \Delta r_{pellets}\right)^2 - r_o^{\,2}\right] \cdot \pi \cdot \frac{e_P}{1 + e_P} \cdot \left(\frac{\rho_s}{\rho_w} \cdot \frac{w_{P\_wet}}{e_P} - \frac{\rho_s}{\rho_w} \cdot \frac{w_P}{e_P}\right)$$

$\Delta V_{init\_pellet\_wet} = 1.096$

$V_{av\_init\_slot} = 0.166$

$\Delta V_{init\_pellet\_wet} + V_{av\_init\_slot} = 1.261$

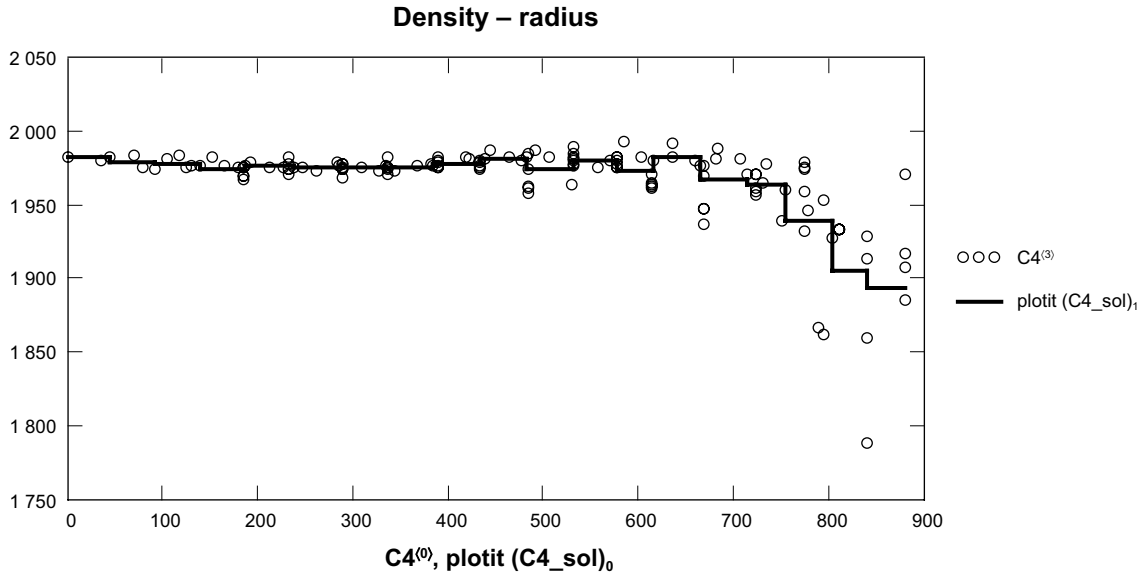
Density – radius
2 050
2 000
1 950
1 900
1 850
1 800
1 750
0
100
200
300
400
500
600
700
800
900
C4(3)
plotit (C4_sol)1
C4⟨0⟩, plotit (C4_sol)0

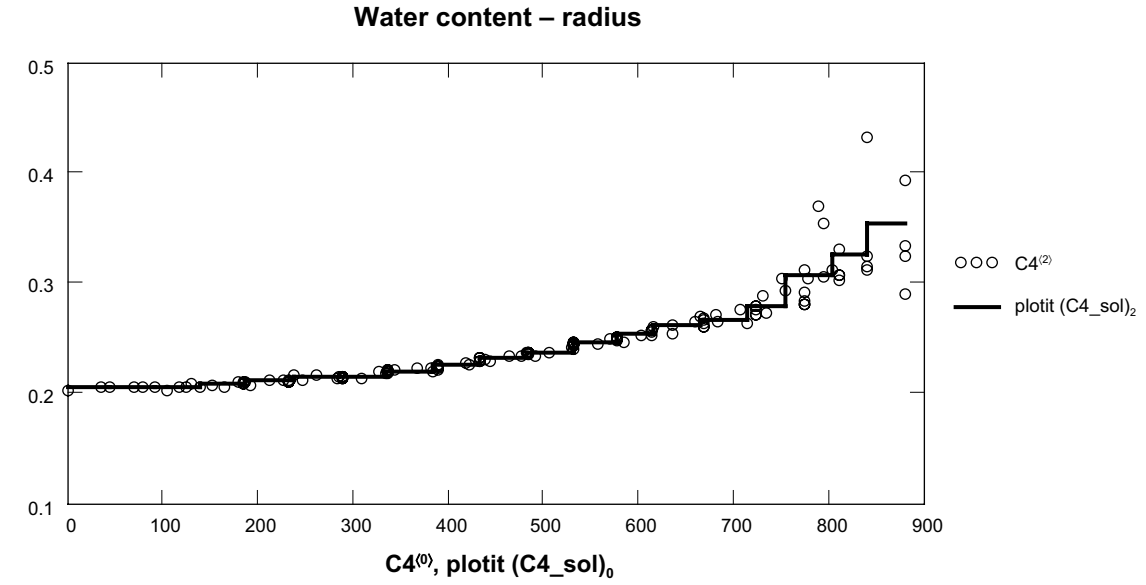
Water content – radius
0.5
0.4
0.3
0.2
0.1
0
100
200
300
400
500
600
700
800
900
C4(2)
plotit (C4_sol)2
C4⟨0⟩, plotit (C4_sol)0

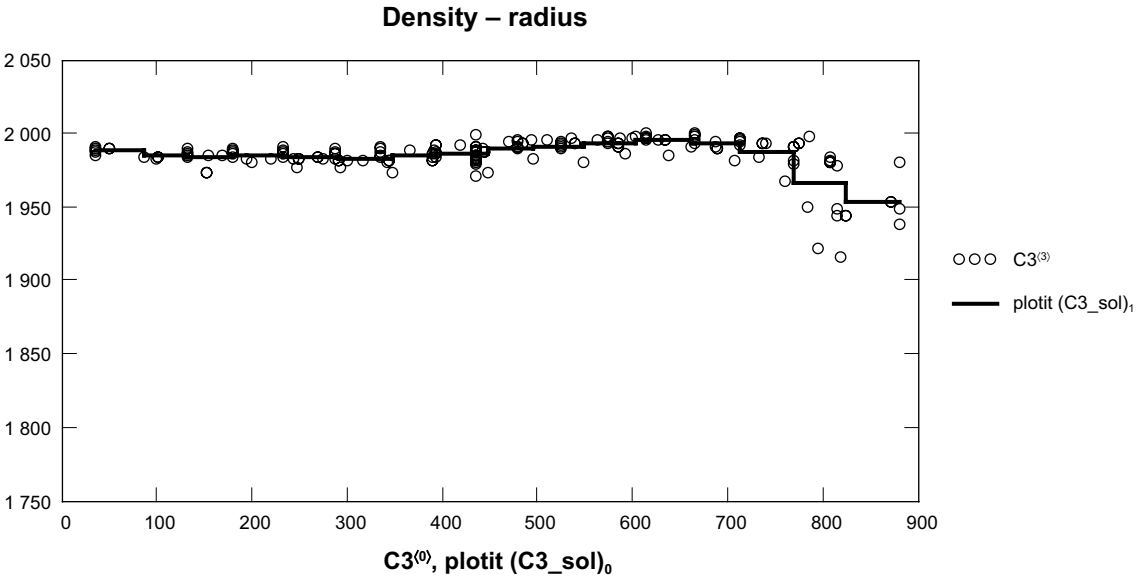
Density – radius
2 050
2 000
1 950
1 900
1 850
1 800
1 750
0
100
200
300
400
500
600
700
800
900
C3⟨0⟩, plotit (C3_sol)0
C3⟨3⟩
plotit (C3_sol)1

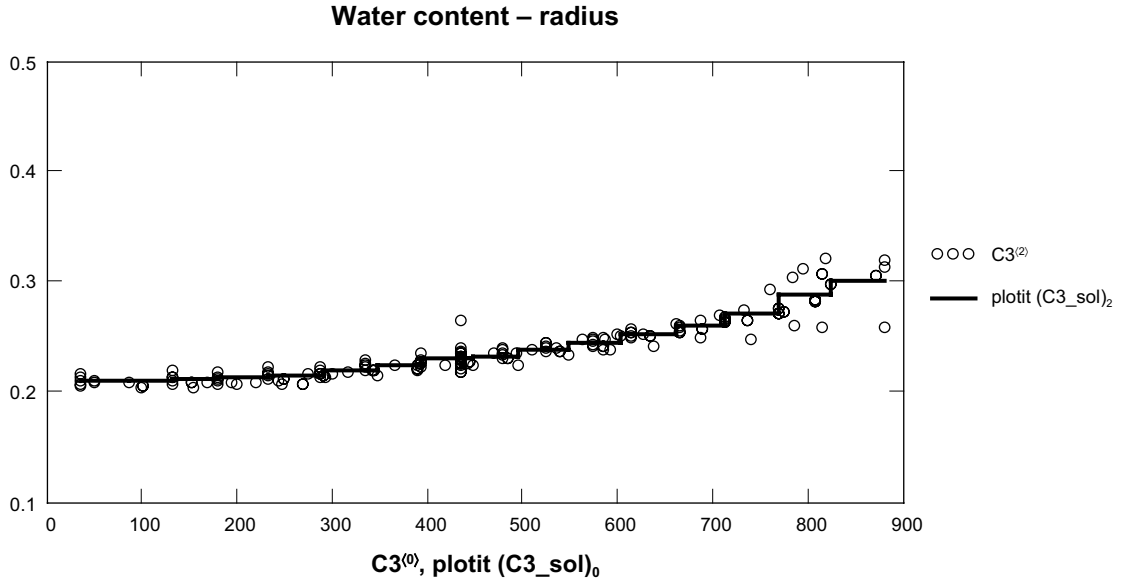
Water content – radius
0.5
0.4
0.3
0.2
0.1
0
100
200
300
400
500
600
700
800
900
C3⟨0⟩, plotit (C3_sol)0
C3⟨2⟩
plotit (C3_sol)2

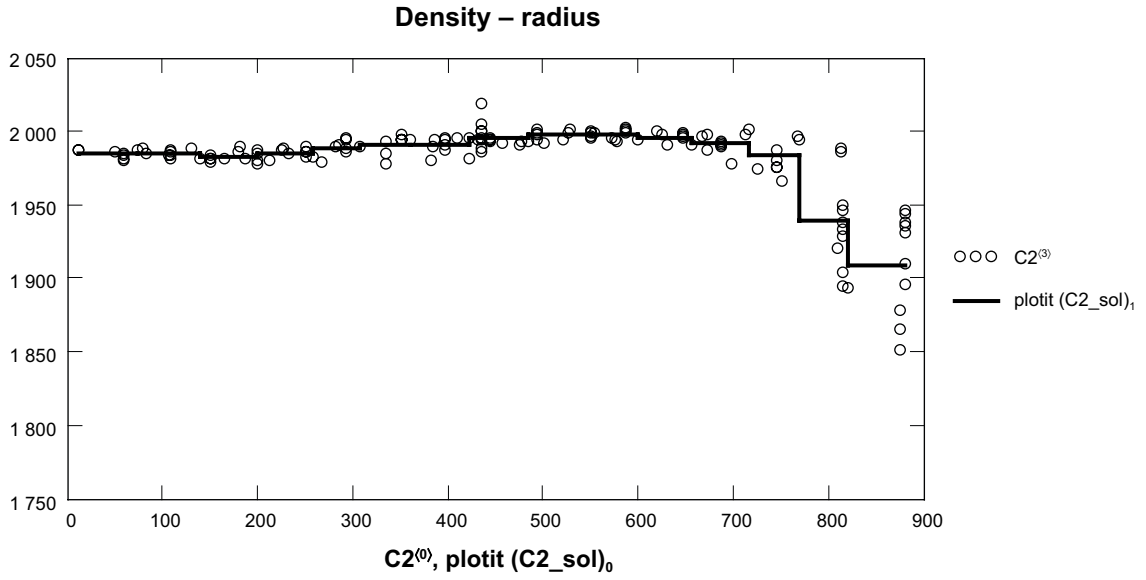
Density – radius
2 050
2 000
1 950
1 900
1 850
1 800
1 750
0
100
200
300
400
500
600
700
800
900
C2(0), plotit (C2_sol)0
C2(3)
plotit (C2_sol)1

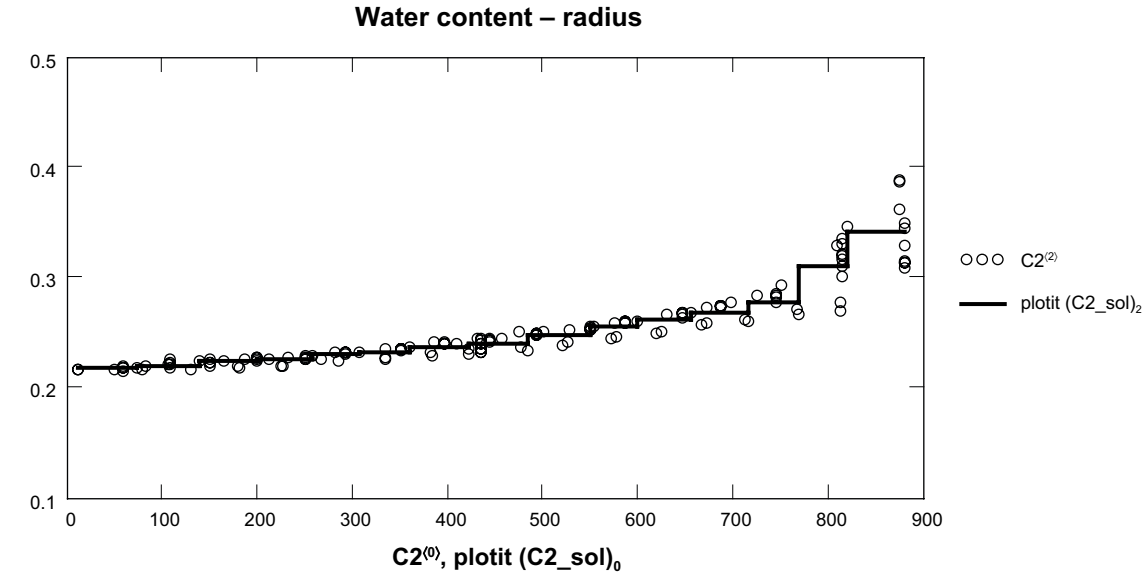
Water content – radius
0.5
0.4
0.3
0.2
0.1
0
100
200
300
400
500
600
700
800
900
C2(0), plotit (C2_sol)0
C2(2)
plotit (C2_sol)2

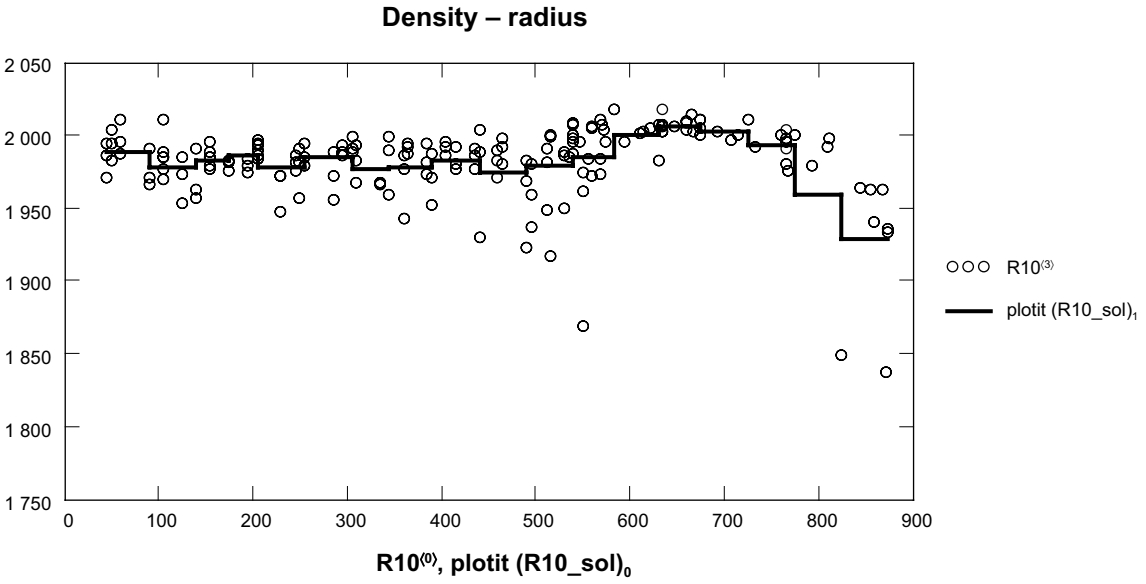
Density – radius
2 050
2 000
1 950
1 900
1 850
1 800
1 750
0
100
200
300
400
500
600
700
800
900
R10(3)
plotit (R10_sol)1
R10(0), plotit (R10_sol)0

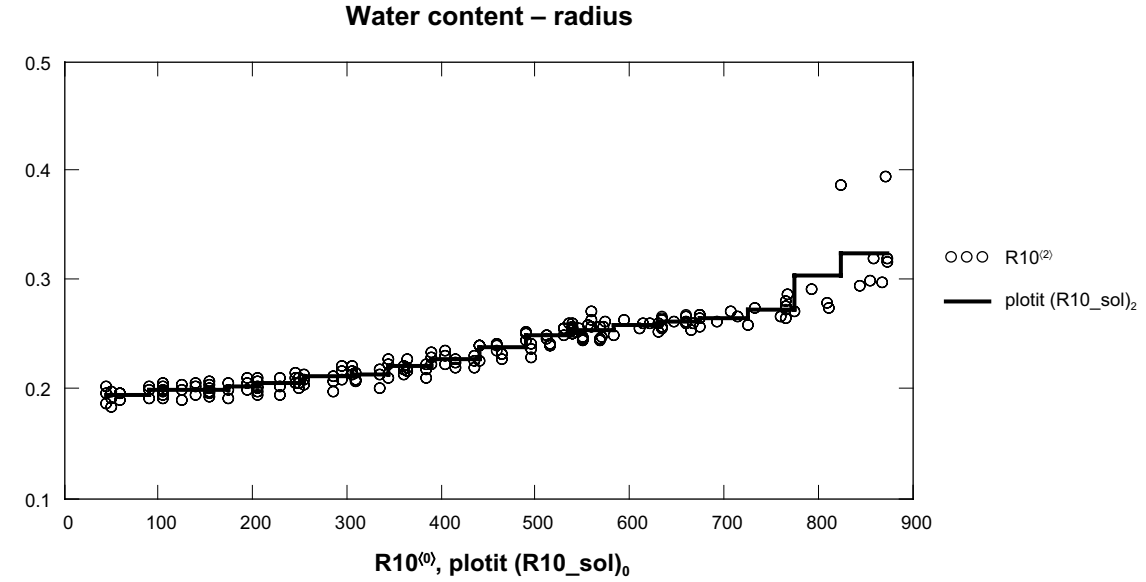
Water content – radius
0.5
0.4
0.3
0.2
0.1
0
100
200
300
400
500
600
700
800
900
R10(2)
plotit (R10_sol)2
R10(0), plotit (R10_sol)0

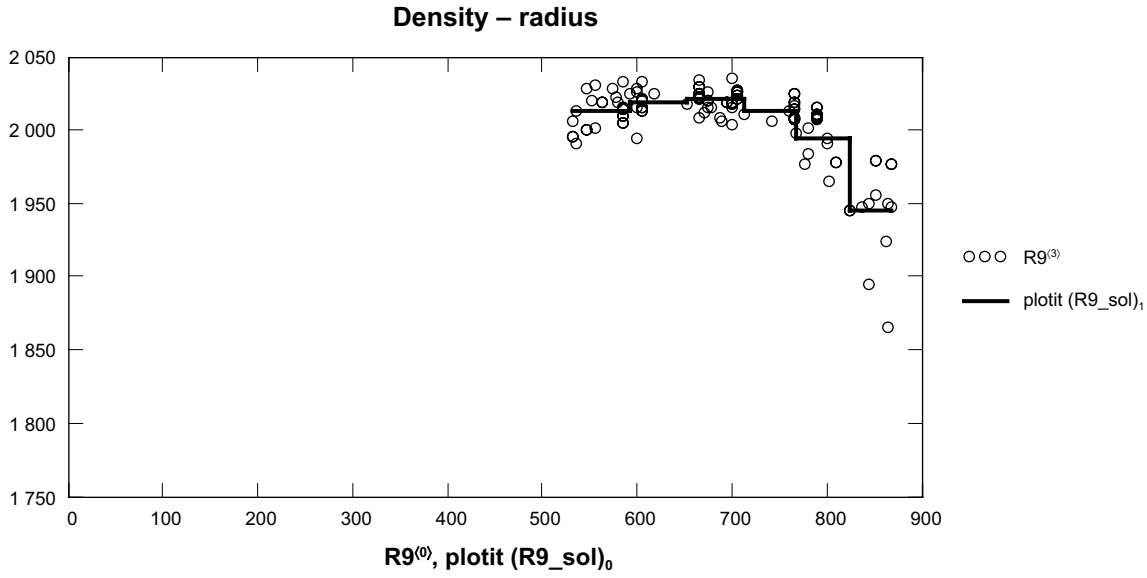
Density – radius
2 050
2 000
1 950
1 900
1 850
1 800
1 750
0
100
200
300
400
500
600
700
800
900
R9(0), plotit (R9_sol)0
R9(3)
plotit (R9_sol)1

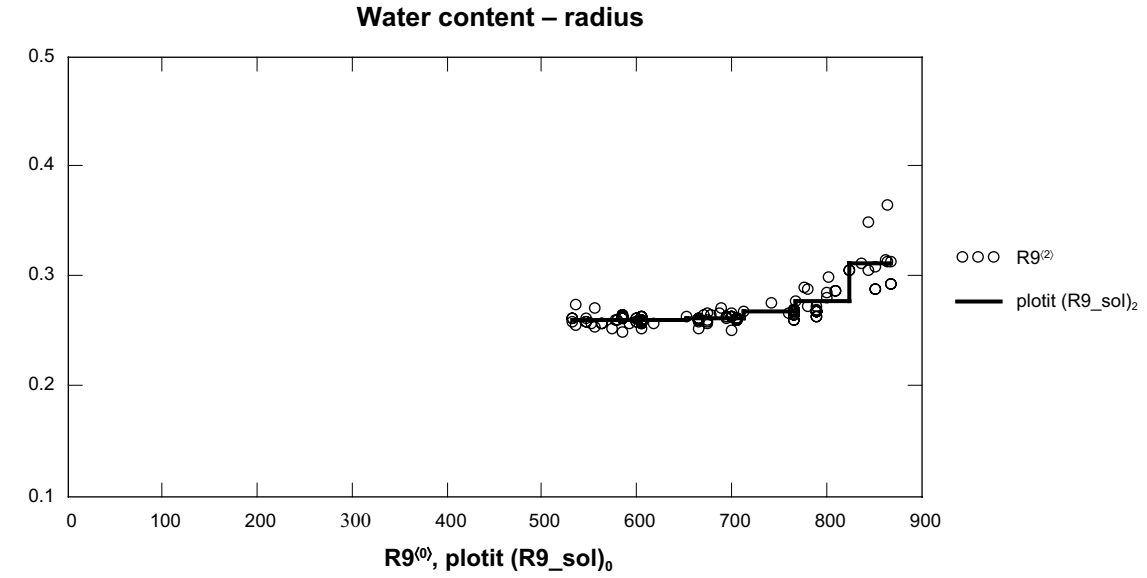
Water content – radius
0.5
0.4
0.3
0.2
0.1
0
100
200
300
400
500
600
700
800
900
R9(0), plotit (R9_sol)0
R9(2)
plotit (R9_sol)2

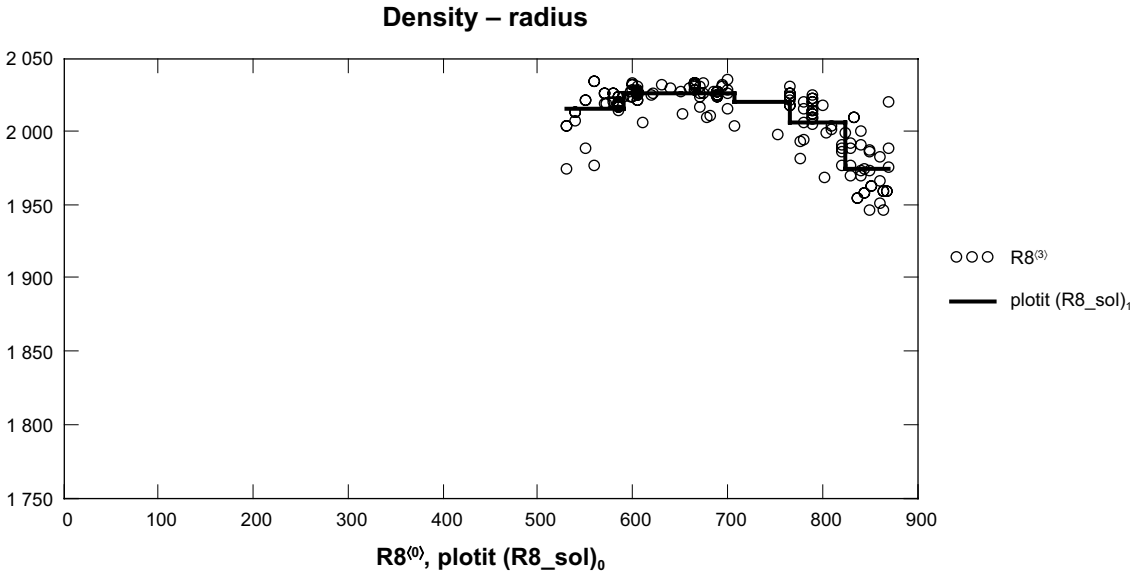
Density – radius
2 050
2 000
1 950
1 900
1 850
1 800
1 750
0
100
200
300
400
500
600
700
800
900
R8⟨0⟩, plotit (R8_sol)0
R8(3)
plotit (R8_sol)1

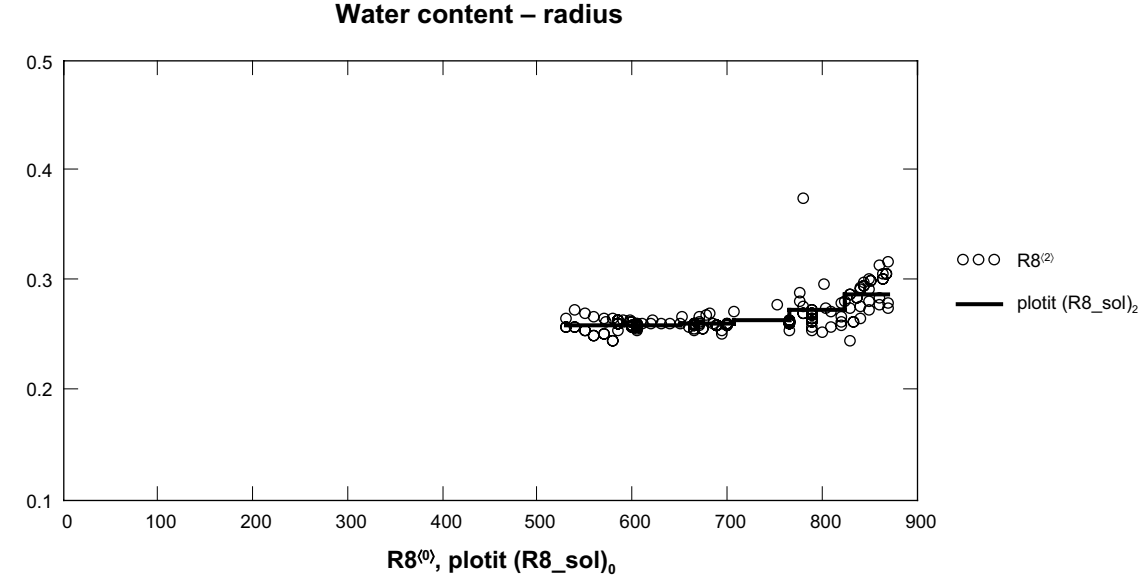
Water content – radius
0.5
0.4
0.3
0.2
0.1
0
100
200
300
400
500
600
700
800
900
R8⟨0⟩, plotit (R8_sol)0
R8(2)
plotit (R8_sol)2

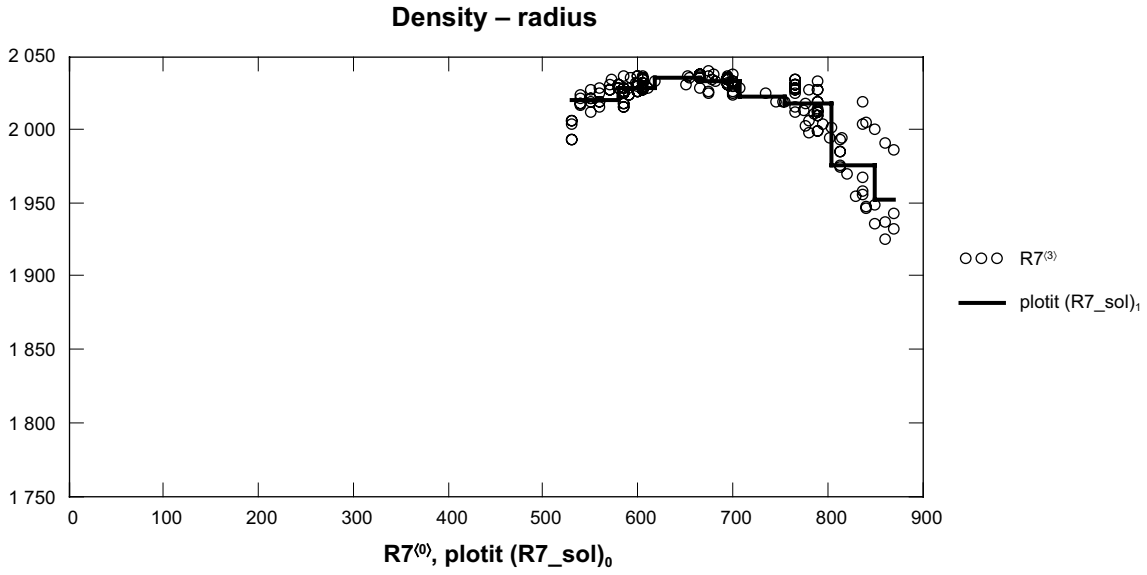
Density – radius
2 050
2 000
1 950
1 900
1 850
1 800
1 750
0
100
200
300
400
500
600
700
800
900
R7(0), plotit (R7_sol)0
R7(3)
plotit (R7_sol)1

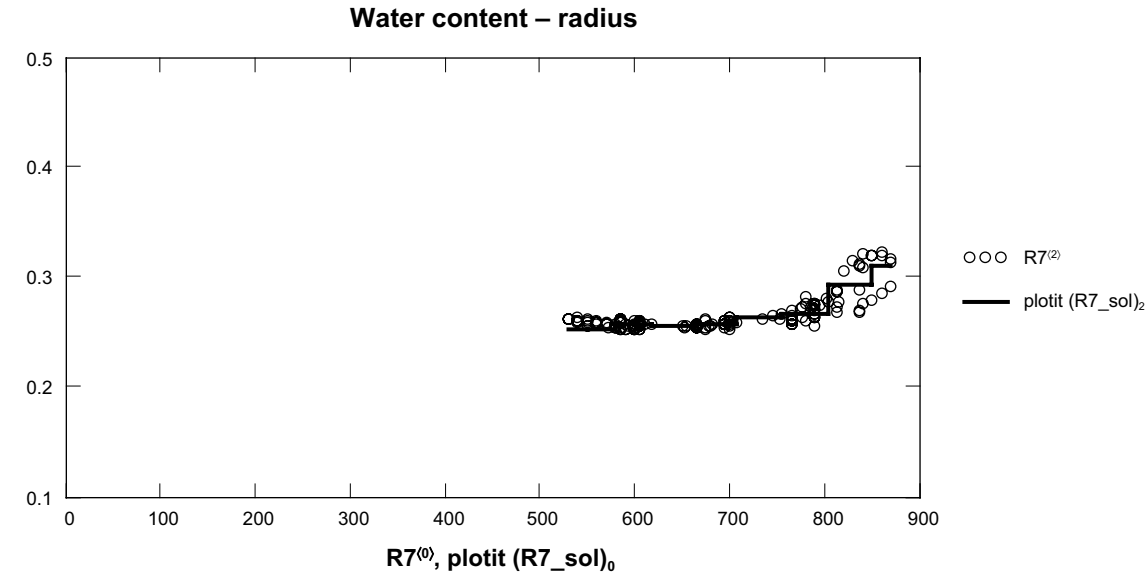
Water content – radius
0.5
0.4
0.3
0.2
0.1
0
100
200
300
400
500
600
700
800
900
R7(0), plotit (R7_sol)0
R7(2)
plotit (R7_sol)2

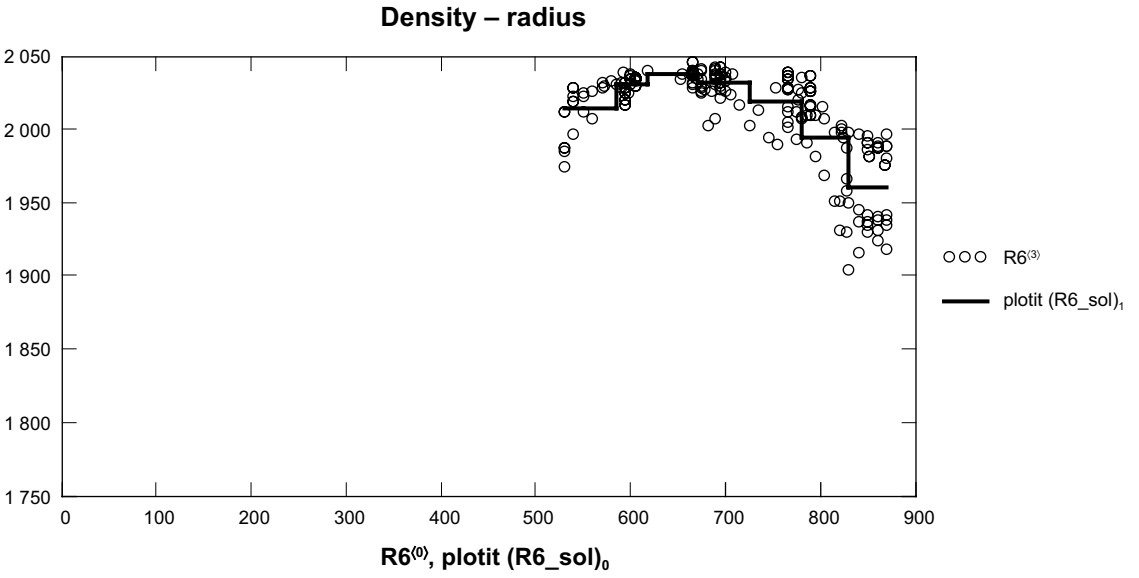
Density – radius
2 050
2 000
1 950
1 900
1 850
1 800
1 750
0
100
200
300
400
500
600
700
800
900
R6(0), plotit (R6_sol)0
R6(3)
plotit (R6_sol)1

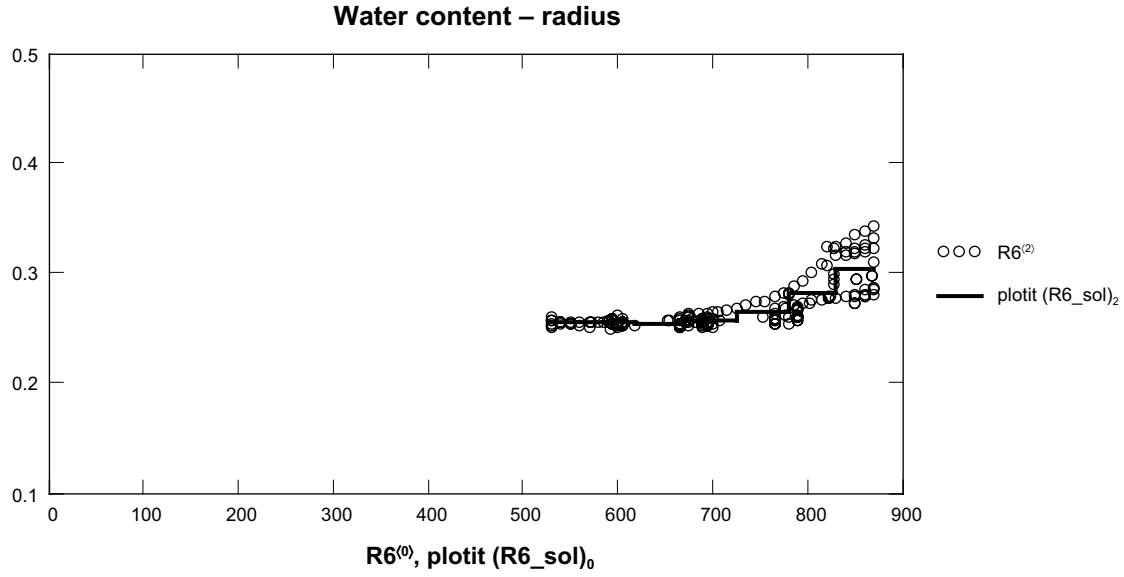
Water content – radius
0.5
0.4
0.3
0.2
0.1
0
100
200
300
400
500
600
700
800
900
R6(0), plotit (R6_sol)0
R6(2)
plotit (R6_sol)2

Appendix 2

Water-uptake tests with Febex bentonite

A.1 General

Water uptake tests were performed in order obtain data on moisture diffusivity for Febex bentonite from independent measurements.

A.2 Test description

The tests were performed as follows:

- Bentonite material with a water content of 14.3 % was compacted into cylinders (ø = 50 mm and h = 50 mm) with a dry density of 1 551 ± 1 kg/m^3 (void ratio = 0.76 and water content at saturation = 28 % if ρ_s set to 2 735 kg/m^3, see Svensson et al. 2011)
- The specimens had access to de-ionized water from the bottom during a specified time. The water was not pressurized (less than 10 kPa pressure). During the water uptake the sample was prevented to expand (Figure A.1).
- After the water uptake phase the specimen was removed from the cylinder and the density and water content of the material were determined. The determinations were made on every 10 mm of the specimen. The results from the measurements were plotted as function of the distance from the water inlet.
- Two tests were performed. Test 1 and Test 2 were allowed to take up water during 14 and 21 days, respectively.

A.3 Test results

Results concerning water content and void ratio are shown in Figure A.2 as a function of distance from the water inlet i.e. from the bottom of the specimens. The water content profiles demonstrate that a significant part of the available pore space was filled with water already after the time span of the Test 1.The void ratio distribution confirms that the specimen were fairly homogenously compacted, although the overall void ratio level suggests that the specimen had expanded slightly during the dismantling.

A.4 Final remarks

The tests showed that the Febex bentonite displayed a fairly high capacity for water uptake. The results also showed that the bentonite adjacent to the water inlet tended to expand and therefore displayed relatively high void ratio and water content.

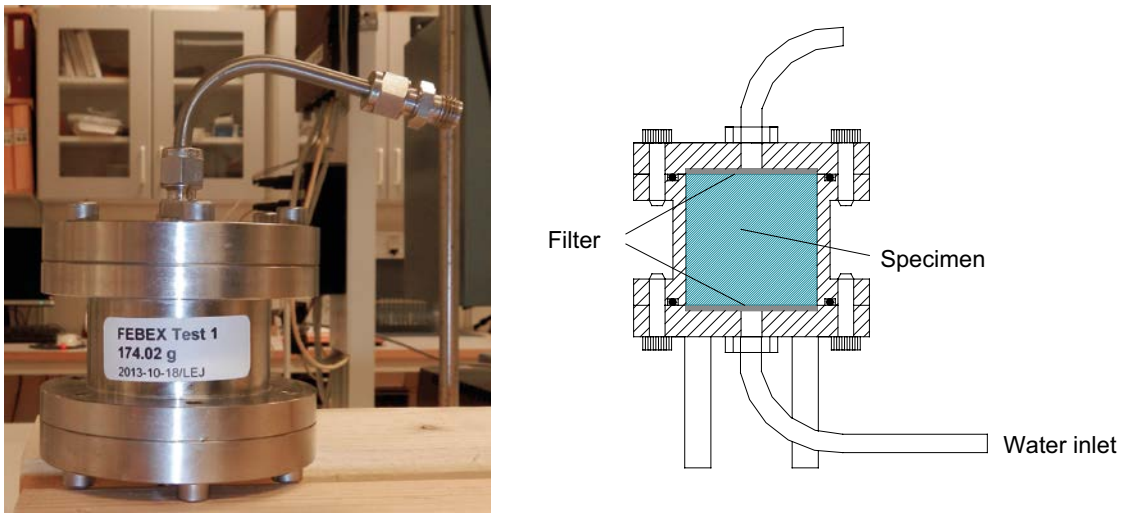

Figure A2-1. *Equipment used for the tests.*

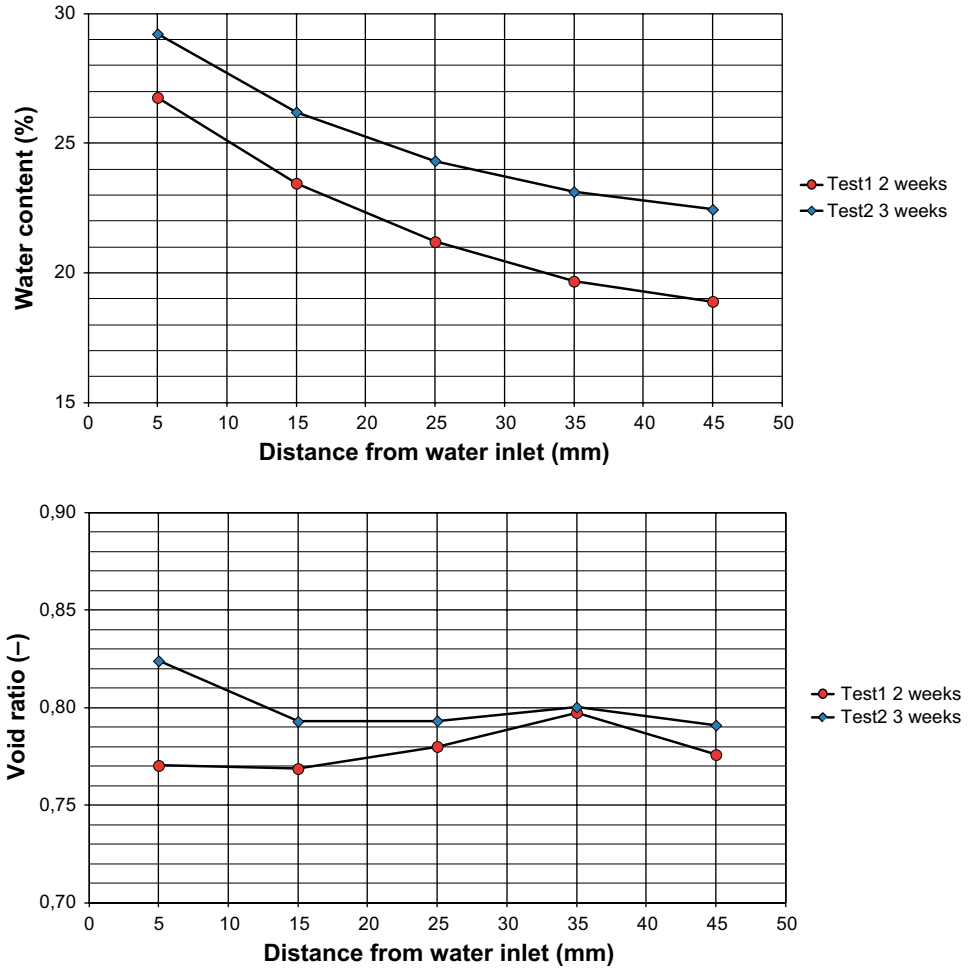

Figure A2-2. *Tests results regarding water content (upper) and void ratio (lower).*

Appendix 3

Calculation of the average available pore volume in the deposition tunnel (MathCad excerpt)

Bentonite solid density: $\rho_s := 2.78 \cdot \frac{kg}{m^3}$

Liquid density: $\rho_l := 1.00 \cdot \frac{kg}{m^3}$

Void ratio - porosity relationship: $n(e) := \frac{e}{1 + e}$

Saturation - Water content relationship: $S_l(w, e) := \frac{w \cdot \rho_s}{\rho_l \cdot e}$

Available pore volume at installation - Deposition hole

DH - Buffer ring-shaped blocks - Available pore volume:

Cross-section area : $A_R := \pi\left[(0.815 \cdot m)^2 - (0.525 \cdot m)^2\right] = 1.221 \cdot m^2$

Height: $h_R := 4.75 \cdot m$

Void ratio: $e_R := 0.571$

Water content: $w_R := 0.17$

Available pore volume: $V_{p\_R} := A_R \cdot h_R \cdot n(e_R) \cdot (1 - S_l(w_R, e_R)) = 363.216 \cdot L$

DH - Buffer cylinder-shaped blocks - Available pore volume:

Cross-section area : $A_C := \pi\,(0.815 \cdot m)^2 = 2.087 \cdot m^2$

Height: $h_C := 3.4 \cdot m$

Void ratio: $e_C := 0.626$

Water content: $w_C := 0.17$

Available pore volume: $V_{p\_C} := A_C \cdot h_C \cdot n(e_C) \cdot (1 - S_l(w_C, e_C)) = 669.343 \cdot L$

DH - Buffer pellets - Available pore volume:

Cross-section area : $A_P := \pi\left[(0.875 \cdot m)^2 - (0.815 \cdot m)^2\right] = 0.319 \cdot m^2$

Height: $h_P := 8 \cdot m$

Void ratio: $e_P := 1.78$

Water content: $w_P := 0.13$

Available pore volume: $V_{p\_P} := A_P \cdot h_P \cdot n(e_P) \cdot (1 - S_l(w_P, e_P)) = 1.3 \times 10^3 \cdot L$

Total DH available pore volume: $V_{p\_DH} := V_{p\_R} + V_{p\_C} + V_{p\_P} = 2.333 \times 10^3\,L$

Available pore volume - Tunnel

Average tunnel length: $L_T := 252 \cdot m$

Average number of deposition holes per tunnel: $n_{DH} := \frac{6916}{207} = 33.411$

Backfill blocks (including inner slot)

Cross-section area $A_{TB} := 16.8 \cdot m \cdot 1.02 \cdot m = 17.136\,m^2$

Void ratio: $e_{TB} := \frac{\frac{2780}{1700}}{1.02} - 1 = 0.668$

Water content: $w_{TB} := 0.17$

Available pore volume: $V_{p\_TB} := L_T \cdot A_{TB} \cdot n(e_{TB}) \cdot (1 - S_l(w_{TB}, e_{TB})) = 5.059 \times 10^5 \cdot L$

Backfill pellets

Cross-section area $A_{TP} := 22.7 \cdot m^2 - 17.1 \cdot m^2 = 5.6\,m^2$

Void ratio: $e_{TP} := \frac{2780}{1000} - 1 = 1.78$

Water content: $w_{TP} := 0.17$

Available pore volume: $V_{p\_TP} := L_T \cdot A_{TP} \cdot n(e_{TP}) \cdot (1 - S_l(w_{TP}, e_{TP})) = 6.637 \times 10^5 \cdot L$

Total tunnel backfill available pore volume

$$V_{p\_T} := V_{p\_TB} + V_{p\_TP} = 1.17 \times 10^5\,L$$

Total tunnel available pore volume (incl. deposition holes):

$$V_p := V_{p\_T} + n_{DH} \cdot V_{p\_DH} = 1.247 \times 10^6\,L$$

Appendix 4

Mesh dependence investigation

When increasing the number of elements in the radial direction by a factor of three in the block and pellet slot, no significant change could be seen in the responses. This indicates that the coarser discretization is fine enough for the used element type.

Table A1-1. Models used in the mesh dependence study.

Model name	No. of elements radially		
	Open slot	Block	Pellet slot
TEP_new_12	1	30	5
TEP_new_12_fine	1	90	15

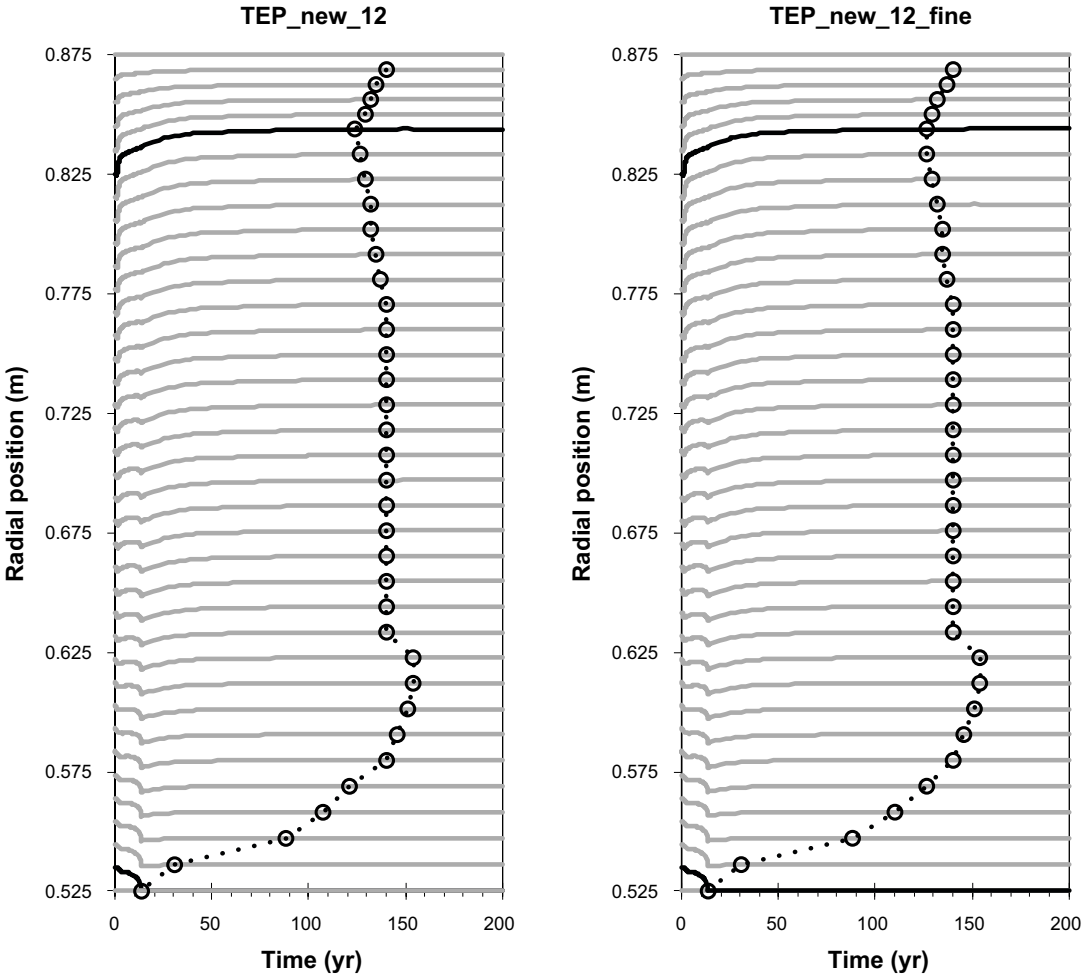

Figure A4-1. *Local models deformation evolution (solid lines) and isoline consisting of pairs (time, position) for which the deformation is 0.99 of the final is indicated (hatched),i.e.* $t(|u_r|) \approx 0.99 \times |u_r(t = 200)|$.

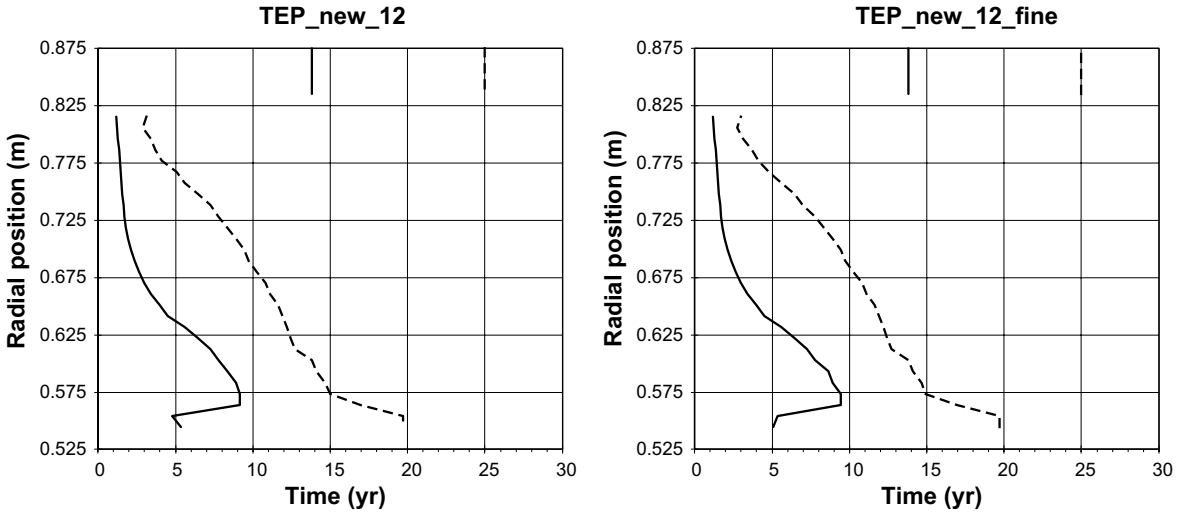

Figure A4-2. *Local model isolines consisting of pairs* **(***t,r*$_0$**)** *for which p ≈ 1 MPa (solid) and p ≈ 2 MPa (hatched)***.**

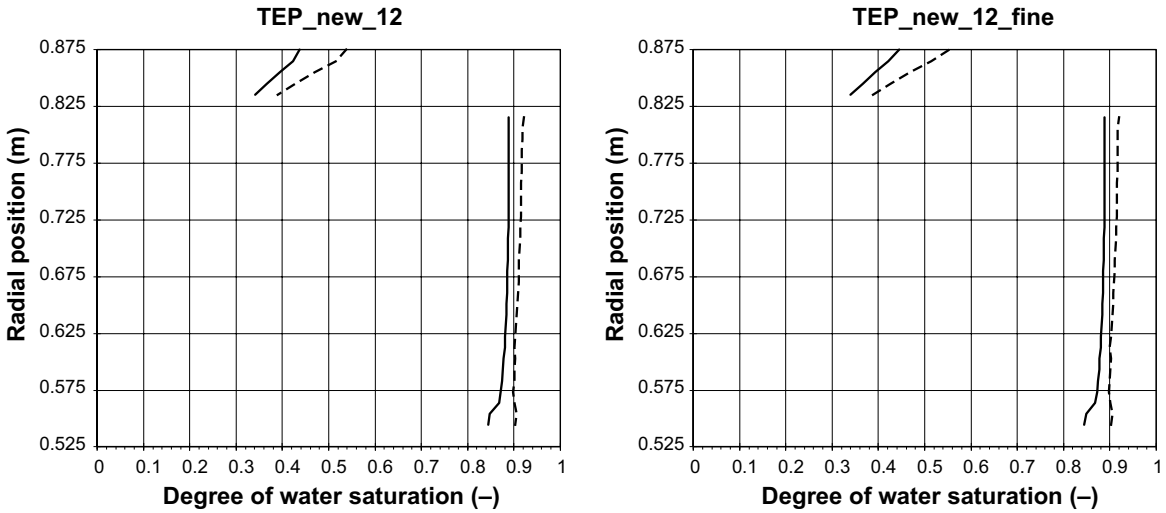

Figure A4-3. *Local model isolines consisting of pairs (*S_l*,*r_0*) for which p ≈ 1 MPa (solid) and p ≈ 2 MPa (hatched).*

Appendix 5

Model catalogue

Location: ”Administrativa dokument on”:\ Projekt\ SR-Site SSM-frågor\data\modeller\ Task_3.1*

Table A2-1. Local models used in this study.

Model name	GiD-directory
TEP_new_12	TEP_new_12.gid
TEP_new_14	TEP_new_14.gid
TEP_new_12_fine	TEP_new_12_fine.gid

Table A2-2. Global models used in this study.

Model name	GiD-dir.
2I	THsat13.gid
2H	THsat14.gid
8I	THsat20I2.gid
8H	THsat20H4.gid

Arkitektkopia AB, Bromma, 2018

SKB is responsible for managing spent nuclear fuel and radioactive waste produced by the Swedish nuclear power plants such that man and the environment are protected in the near and distant future.

skb.se